RESEARCH

2007-08

Strength and Stability of Prestressed Concrete Through-Girder Pedestrian Bridges Subjected to Vehicular Impact

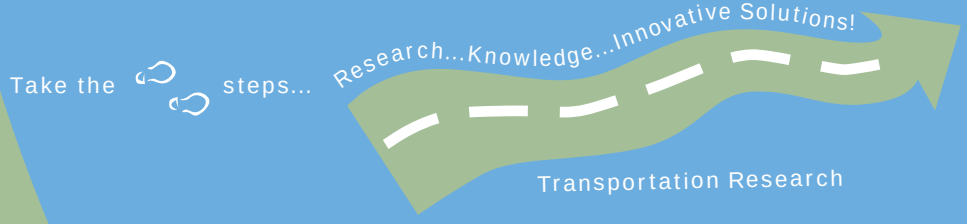

Technical Report Documentation Page

1. Report No.	2.	3. Recipients Accession No.
MN/RC-2007-08		

4. Title and Subtitle	5. Report Date
Strength and Stability of Prestressed Concrete Through-Girder Pedestrian Bridges Subjected to Vehicular Impact	January 2007
	6.

7. Author(s)	8. Performing Organization Report No.
Eray Baran, Arturo E. Schultz, Catherine W. French	

9. Performing Organization Name and Address	10. Project/Task/Work Unit No.
Department of Civil Engineering University of Minnesota 500 Pillsbury Drive SE Minneapolis, MN 55455	11. Contract (C) or Grant (G) No. (c) 81655 (wo) 69

12. Sponsoring Organization Name and Address	13. Type of Report and Period Covered
Minnesota Department of Transportation 395 John Ireland Boulevard Mail Stop 330 St. Paul, Minnesota 55155	14. Sponsoring Agency Code

15. Supplementary Notes
http://www.lrrb.org/PDF/200708.pdf

16. Abstract (Limit: 200 words)

Two issues regarding the prestressed concrete through-girder pedestrian bridge system are investigated. The first issue concerns the ductility of prestressed concrete girders in these bridges because the section that is typically used may be considered to be over-reinforced according to AASHTO LRFD Bridge Specifications. Response of the section, including neutral axis location, strand stress at ultimate capacity, and moment capacity, predicted by AASHTO Standard and AASHTO LRFD Specifications are compared with the sectional response determined from nonlinear strain compatibility analyses. Modifications are proposed to the AASHTO LRFD procedure to rectify the errors in predicting sectional response.

The second issue that was investigated concerns the strength and stability of prestressed concrete through-girder pedestrian bridges when subjected to impact by over-height vehicles. Three-dimensional finite element models of entire bridges and subassemblages were used to evaluate the strength, stiffness, and ductility characteristics of the bridge system and connection details. Accurate representation of the bridge details in the finite element models were assured by utilizing experimentally determined load-deformation characteristics for the connections. Results showed that significant improvements in the lateral load-deflection behavior of the bridge system could be obtained by implementing alternate connection schemes, and that concrete side-walls should be provided at girder ends.

17. Document Analysis/Descriptors		18. Availability Statement
Damage, ductility, Finite Element Analysis, LRFD, prestressed girders	impact, mechanical anchors, pedestrian bridge, precast concrete,	No restrictions. Document available from: National Technical Information Services, Springfield, Virginia 22161

19. Security Class (this report)	20. Security Class (this page)	21. No. of Pages	22. Price
Unclassified	Unclassified	244	

Strength and Stability of Prestressed Concrete Through-Girder Pedestrian Bridges Subjected to Vehicular Impact

Final Report

Prepared by:
Eray Baran
Arturo E. Schultz
Catherine W. French

Department of Civil Engineering
University of Minnesota

January 2007

Published by:

Minnesota Department of Transportation
Research Services Section
395 John Ireland Boulevard, MS 330
St. Paul, Minnesota 55155-1899

Acknowledgements

The work on this project was conducted under the sponsorship of the Minnesota Department of Transportation (Mn/DOT). Appreciation is expressed to the members who served on the Mn/DOT Technical Advisory Panel for their input and assistance. The support provided by the University of Minnesota Graduate School in the form of Doctoral Dissertation Fellowship is also acknowledged. Appreciation is also acknowledged to the Minnesota Supercomputing Institute for allocating their resources and technical support.

Table of Contents

List of Tables

List of Figures

Executive Summary

Prestressed concrete through-girder pedestrian bridge systems consist of two prestressed concrete girders that support reinforced concrete cast-in-place floor beams at their bottom flange and a reinforced concrete cast-in-place deck placed on top of the floor beams. Mn/DOT Type 63 girder cross section is used on these bridges with a typical span of 125-135 ft. and a typical spacing of 12-15 ft. between the two girders.

Two issues have recently been raised regarding the prestressed concrete through-girder pedestrian bridge system, which has been widely used in the State of Minnesota. The first issue was related with the ductility of prestressed concrete girders used in these types of bridges. The girders are reinforced with large amounts of prestressing strands in order to satisfy the deflection requirements with the relatively large span lengths (125-135 ft.). Moreover, the girders do not have a composite deck on top that would help to resist the relatively large internal tensile force caused by the prestressing strands. As a result, the section used in these bridges (Mn/DOT Type 63 section) is considered to be over-reinforced, according to the AASHTO LRFD Bridge Specifications, and fails to meet the required flexural strength.

A nonlinear strain compatibility analysis of the Mn/DOT Type 63 section was performed in order to identify the design procedures that accurately predict the section behavior. Response of the section, including the neutral axis location, strand stress at ultimate capacity, and the moment capacity of the section, predicted by the AASHTO Standard and AASHTO LRFD Specifications, was compared with the sectional response determined from the strain compatibility analyses. Based on the analysis results, modifications were proposed to the procedure used by the LRFD Specifications in order to rectify the errors in predicting the sectional response.

The second issue that was investigated in the study was regarding the strength and stability of prestressed concrete through-girder pedestrian bridges when subjected to striking by over-height vehicles. Three-dimensional full-scale finite element models of an entire bridge-system as well as bridge subassemblages were used to evaluate the strength, stiffness, and ductility characteristics of the bridge system and connection details. Accurate representation of the bridge details in the finite element models were assured by utilizing the experimentally determined load-deformation characteristics of these connections in the finite element models.

Three series of laboratory tests were conducted in order to investigate the performance of currently used and proposed details to be used in the future construction for prestressed concrete through-girder bridges. Results from these tests were either directly incorporated in modeling of the behavior of the components in the finite element models or the experimental data was used to calibrate the subassemblage finite element models.

Performance of a typical prestressed concrete through-girder pedestrian bridge system was analyzed through three sets of finite element analyses using the models of an entire bridge

system. Each of these three sets of analyses aimed at studying a different aspect of the bridge system behavior.

The pull-out tests performed on steel inserts indicated that the type of inserts currently being used in prestressed concrete bridge girders in the State of Minnesota has the ability to undergo significant amounts of plastic deformation without a reduction in the load capacity. The ductile behavior of the steel inserts used in prestressed concrete girders was also confirmed by the results from the connection subassemblage tests. The connection subassemblage tests also revealed that the behavior of these inserts is significantly affected by the construction method followed during the fabrication of prestressed concrete girders. Results obtained from the girder end detail specimens indicated two types of horizontal load resisting mechanisms depending on the type of detail. During testing of the girder end detail specimens, large values of lateral displacements following the peak load capacities were measured with some level of residual load capacity.

The static lateral load finite element analyses indicated significantly different bridge response depending on whether or not the flexibility of the girder supports were included in the models. It was also determined that the load transfer mechanism among the bridge components depends on whether the girders were loaded at the exterior or interior face. Results from these analyses also showed that the lateral load and deformation capacities of the bridge system could be improved by increasing the ductility and strength of the connection between the girders and floor beams.

The dynamic lateral impact analyses that were performed in an attempt to determine the demand that would occur on the bridge system indicated relatively small impact durations. The dynamic analyses revealed a different deformation pattern of the bridge system than the deformation patterns observed in the static analyses. The damage in the bridge caused by the impacting body was observed to remain highly localized near the impact location for approximately half of the impact duration. As a result, the support flexibility of the girders did not have much effect on the dynamic behavior of the bridge, as opposed to the behavior observed in the static lateral load analyses. The Equivalent Static Force (ESF) values determined from the dynamic analyses were smaller than the static lateral load capacity of the bridge for the cases with flexible girder supports, while for the rigid supports the ESF values were still larger than the static lateral load capacities.

Results of the stability analyses indicated that the local girder damage that would occur in prestressed concrete through-girder pedestrian bridges due to striking of over-height objects may cause the failure of the bridge depending on the extent of damage that the girders would be subjected to. The bridge was determined to be more susceptible to failure when the impact damage occurs near the girder midspan than the girder ends. When only one of the girders was impacted, failure of the bridge would require slightly larger amount of damage in the girder section for failure than the damage level required for failure when both girders are damaged. The amount of “additional capacity” between the cases of single girder versus the both girders being damaged is due to load redistribution from the impacted girder to the other girder. Analysis results showed that the in the case of both girders being impacted,

failure of the bridge would occur when approximately 15 percent to 40 percent of the girder web, depending on the location of impact, was damaged in addition to the entire bottom flange.

Chapter 1
Introduction and Literature Review

1.1. Background

Each year a large number of concrete bridges are subjected to impact by over-height vehicles or vehicles carrying over-height objects, causing not only structural damage, but in many cases leading to injuries and sometimes even fatalities. Most state departments of transportation in the United States are concerned with the increasing trend of bridges impacted by over-height vehicles, and have tried to deal with the problem by taking simple precautions, such as placing larger warning signs and under-reporting the bridge clearances by several inches, or by taking more costly measures, such as increasing required bridge clearances. However, none of these precautions can ensure the avoidance of vehicular impacts, and the resistance of bridges to lateral impact loads needs to be studied.

1.1.1 Statement of Problem

There are a limited number of studies available in the literature dealing with the experimental and numerical investigation of the behavior of highway bridges under lateral impact loads. Results from these studies have shown the ability of highway bridges to redistribute and transfer the locally-applied impact loads to other parts of the bridge to create alternate load paths [1-3]. Different from highway bridges, pedestrian bridges are of lighter construction and they do not have the high degree of redundancy exhibited by highway bridges. These characteristics make pedestrian bridges more vulnerable to collapse than highway bridges in the case of vehicular impact.

The American Association of State Highway and Transportation Officials (AASHTO) also recognize the vulnerability of pedestrian bridges to collapse in the case of over-height vehicle impact. In the publication titled "A Policy on Geometric Design of Highways and Streets", a minimum of 17 ft. clearance was specified for pedestrian overpasses and sign trusses because of "their lesser resistance to impacts", while a 16 ft. minimum clearance was specified for highway bridges [4].

Even though they are more vulnerable to collapse, pedestrian bridges under transverse impact loads have not been studied to date, and this study seeks to bridge this gap. The investigation is limited to the evaluation of the behavior of a specific type of pedestrian bridge system (i.e., prestressed concrete through-girder pedestrian bridge) that has been widely used in the State of Minnesota.

1.1.2. Description of Prestressed Concrete Through-Girder Bridge System

As shown in Fig. 1.1(a), in a typical through-girder type pedestrian bridge, two prestressed concrete girders support cast-in-place reinforced concrete floor beams at their bottom flange, and a reinforced concrete cast-in-place deck is placed on top of the floor beams. Mn/DOT Type 63 girder cross section, shown in Fig. 1.1(b), is typically used in the State of Minnesota for these types of bridges. The span length of the prestressed concrete girders is on the order of 125-135 ft. with a typical spacing between the two girders of 12-15 ft. End floor beams are placed between girders at both ends of the girders, and intermediate floor beams are typically spaced at 14-17 ft.

in between the two end floor beams. The floor beams are 12 in. wide and have a depth of 20-22 in. The reinforced concrete deck has a minimum thickness of 6-7 in.

The girders are restrained at one end ("fixed" end) and are free to move transversely at the other end ("expansion" end). At the end of the girders, steel curved plates are connected to steel sole plates, which are embedded in the girders, through two 1-1/2 in. diameter pintles. The curved plates themselves are welded to steel bearing plates, which rest on elastomeric bearing pads. Similar types of curved plate-bearing plate-elastomeric pad details are used for both ends, except at the fixed end the elastomeric pads are thinner and the bearing plates are bolted down to the bridge seat through 1-1/2 in. diameter anchor rods as shown in Figs. 1.2(a) and 1.2(b). In the case of single-span bridges, the girder ends are fixed at one abutment and free at the other abutment. In double-span bridges, the girder ends are fixed at the pier and free at the abutments. The bridges have parapets placed on outside faces of the prestressed concrete bridges at the piers, while at the abutments these parapets, which are called "maskwalls", are provided in only some of the bridges. These parapets and maskwalls can be used as supports for preventing excessive lateral movement of the girders under transverse loads given that adequate reinforcement is provided to resist the associated transverse forces.

In this type of construction, there is no connection between the deck and the prestressed concrete girders, and the only connection between the floor beams and the girders is through steel inserts embedded in the girders during fabrication (see Figs. 1.1(b) through 1.1(d)). In such a bridge system, depending on the impact location, the connections between the girders and the floor beams might be subjected to large forces during the transfer of impact loads from the impacted girder to other parts of the bridge. Failure of these connections would reduce the structural integrity of the bridge, which compromises the stability of the structure. Another failure mode of these bridges under transverse impact loads might be the sliding of the entire bridge from the supports if the details used at the girder ends do not have sufficient strength to transfer the impact loads from the girders to the abutments or the piers.

The second concern regarding these types of bridges is related to the ductility of the prestressed concrete girders used in these bridges. The relatively large span length of the girders requires the use of a large number of strands to control deflections. In addition, the Mn/DOT Type 63 section used in these bridges has a relatively narrow top flange. Because neither a composite deck nor a wide top flange is provided to help carry the compressive part of the internal force couple, the neutral axis is located within the web of the section in order to satisfy the internal force equilibrium. This results in the section being considered as over-reinforced according to some of the code specifications, and failing to meet the required flexural strength.

1.2. Literature Review

Currently there are no studies available reporting the analysis of concrete pedestrian bridges under lateral impact loads. The available literature on behavior of bridges under lateral loading mostly deals with highway bridges. Related studies found in the literature are summarized below and cover topics including strength and ductility of prestressed concrete girders, bridge impact statistics and damage evaluation in prestressed concrete bridges, analysis of vehicle crashes with highway structures, performance of various diaphragm types under lateral loads, impact

characteristics of concrete beams and slabs, and behavior of concrete anchors under axial and shear loading.

1.2.1. Strength and Ductility of Prestressed Concrete Girders

In most structural design codes, flexural ductility of sections is attained by introducing a limit on the maximum amount of tensile reinforcement in a section to ensure the member has sufficient plastic deformation capacity prior to collapse. For prestressed concrete, different codes define this limit in terms of different parameters. Versions of the ACI Code until 2002 [5-7] and the AASHTO Standard Specifications [8] have used the reinforcement index ω to define the limit, while the AASHTO LRFD Specifications [9] use the *c/d* ratio to limit the amount of maximum tensile reinforcement. Sections not satisfying the maximum tensile reinforcement limits are termed "over-reinforced" sections. Use of over-reinforced prestressed concrete sections is penalized in the codes by limiting the moment capacity that the section can be assumed to provide.

The differences among the procedures used by the different structural codes to predict the nominal strength of prestressed concrete sections, and the effect of those differences on the decision of whether the section is over-reinforced or not, has been discussed in the literature [10-16]. These studies revealed that the procedure used by the AASHTO LRFD Specifications overpredicts the neutral axis location, which, in turn, causes some sections to be considered over-reinforced.

The concept of limiting the maximum tensile reinforcement in flexural members dates back to the 1971 edition of the ACI Code. In ACI 318-71, the value of 0.30 was introduced as the limit on the maximum reinforcement index of prestressed concrete flexural members [5]. Originally, the limit of 0.30 on the maximum reinforcement index first appeared in the 1958 report titled "Tentative Recommendations for Prestressed Concrete" by the ACI-ASCE Joint Committee 323 [17]. This limit was intended "to avoid approaching the condition of over-reinforced beams for which the ultimate flexural strength becomes dependent on concrete strength…" This issue was further investigated by Warwaruk et al. with an extensive experimental and analytical study on flexural strength of prestressed concrete beams [18]. It was stated that for smaller amounts of longitudinal tensile reinforcement, small variations in the reinforcement ratio or in the concrete strength do not cause significant changes in strand stress at ultimate load. However, if the section has a large amount of tensile reinforcement, then the strand stress, and hence the moment capacity are affected significantly by the marginal changes, which can be accidental, in the concrete strength or the reinforcement ratio. Based on the strand strain at ultimate of 0.01 and the maximum usable concrete strain of 0.003, the authors proposed the limit of $\rho(f_{ps} / f'_c) \leq 0.25$ on the maximum reinforcement.

Thompson and Park investigated the effect of amount of prestressing steel on the moment-curvature characteristics of rectangular sections [19]. Based on the results obtained from an analytical study, the authors stated that the moderately ductile behavior that the 0.30 limit on the reinforcing index in the ACI Code produces is sufficient for gravity loading. Cohn and Bartlett studied the effect of several parameters, including the total amount of longitudinal steel, proportion of the prestressing steel area to the total steel area and the degree of prestressing on the ductility of partially prestressed concrete sections [20]. It was stated that the limiting value of

0.30 on the reinforcing index is adequate in terms of flexural ductility as it guarantees a ductility factor (ratio of curvatures corresponding to ultimate capacity of the section and yielding of the mild steel reinforcement) of 2.

Mattock conducted a study to investigate the accuracy of the f_{ps} equation given in ACI 318-77, and proposed an equation, which is currently being used by ACI 318-02 and the AASHTO Standard Specifications, to estimate the stress in the prestressing steel at ultimate capacity [21]. Mattock related the limit on the maximum amount of tensile steel to the stress in the prestressing strand at ultimate load and stated that the limit of 0.30 on the reinforcing index is a good approximation to the point of $f_{ps}=f_{py}$ for low concrete strengths. However, the reinforcing index corresponding to $f_{ps}=f_{py}$ decreases significantly as the concrete strength increases. Based on these results, the new limit on the reinforcing index was proposed to be $0.36\beta_1$, instead of 0.30. In the 1983 edition of ACI Code (ACI, 1983), The limiting value of 0.30 in ACI 318-77 was changed to $0.36\beta_1$ "so as to account for the effect of increase in concrete strength." Naaman et al. stated that in partially prestressed sections, the limit of $0.36\beta_1$ on the reinforcement index yields a curvature ductility factor of 1.5 to 3 [22]. A ductility factor of at least 4 is obtained with the limit of 0.2 on the reinforcement index.

Harajli and Naaman investigated, both experimentally and analytically, the stress in the prestressing steel at ultimate capacity, f_{ps}, in partially prestressed concrete beams [23]. Based on the results, the authors indicated that the equation given in ACI 318-83 for f_{ps} may be unconservative for T-sections in some cases. A new equation, which included the c/d_u factor, was recommended to replace the ACI Code Equation. The d_u term in the equation is the depth to the center of the tensile force carried by the mild steel reinforcement and prestressing steel together, assuming yield strength for the mild steel reinforcement and ultimate strength for the prestressing steel. The equation proposed by the authors was modified by Naaman, and is currently being used by the AASHTO LRFD Bridge Design Specifications to predict the strand stress at ultimate [24].

Skogman, Tadros and Grasmick conducted a study on the ductility of prestressed concrete beams, and proposed the unified expression $c/h \le 120\varepsilon_{cu}$ to be used as a minimum ductility requirement for both reinforced and prestressed concrete sections [25]. Cohn and Riva stated that ensuring ductility through the use of c/d and c/h factors as a limit is inconvenient, as the neutral axis depth is unknown before the calculation of moment capacity [26]. Instead, they proposed a new form of reinforcement index that is based on the ultimate strengths of the prestressing strands and the mild steel bars. In the document titled "Unified Design Recommendations for Reinforced, Prestressed, and Partially Prestressed Concrete Bending and Compression Members," Naaman recommended a new provision of $c/d_e \le 0.42$ in order to limit the maximum tensile reinforcement [24]. In this equation, d_e is the depth to the center of the tensile force carried by the mild steel reinforcement and the prestressing steel at the nominal resistance of the section. Another major difference that was recommended by Naaman was the treatment of overhanging portions of the top flange when computing the internal compressive force. In the formulas given by Naaman for the flexural strength of T-sections, the contribution of the flange overhangs was reduced by the factor β_1. It was assumed that T-section behavior starts when the depth of the neutral axis, c, exceeds the depth of the top flange.

Mast recommended "Unified Design Provisions for Reinforced and Prestressed Concrete Flexural and Compression Members," in which he introduced the concepts of "compression controlled" and "tension controlled" sections [27]. This approach was later adopted by ACI 318-02 [28]. Together with compression and tension controlled sections, new capacity reduction factors, which change with the maximum steel strain, were also defined. With this proposed method, reinforced and prestressed concrete sections having steel in excess of what is limited by the previous codes are also permitted, but with a more severe strength reduction factor.

1.2.2. Damage Evaluation in Prestressed Concrete Bridges

According to the recent Federal Highway Administration National Bridge Inventory 617,800 bridges exist in the United States [29]. This number is increasing steadily as new bridges are being constructed each year. The increase in the demand on highway transportation together with the addition of new bridges constitutes the reason for the increasing trend of over-height vehicle and bridge collisions [30]. Feldman et al. reported that according to a survey conducted between 1987 and 1992, the occurrence of impact damage only in the State of Texas has risen to approximately 50 incidents in a year. According to a recent Maryland State Highway Administration study, approximately one out of every five overpasses in Maryland has been struck by an over-height vehicle during its lifetime [31]. According to the report, one-half of these bridges suffer from minor scrapes only, while one-third sustained minor damage and one-sixth sustained damage that required repairs.

In order to obtain the statistical data for bridge collisions over the nation, Harik et al. studied the bridge failures in the United States between 1951 and 1988, and Wardhana and Hadipriono studied those that occurred between 1989 and 2000. According to Harik et al., there were 114 reported failures of bridges, 89 of which were total collapses and 25 of which were partial collapses, between 1951 and 1988 [32]. Among 89 incidents of total collapse, 33 of them were due to collision of a vehicle. In the partial collapse category, 16 of 25 incidents were due to vehicle collision. Wardhana and Hadipriono reported 503 cases of bridge failures, including distress, that occurred in the United States from 1989 until 2000 [33]. Among 503 incidents, 59 of them were due to collision of a vehicle with the bridge, and 14 of these cases included trucks striking the bridge.

According to a National Cooperative Highway Research Program study the average number of prestressed concrete bridges damaged each year is 200, approximately 80 percent of which are caused by impact from over-height vehicles or loads [34]. It was stated that prestressed concrete box girders are not susceptible to vehicle impact damage as much as the prestressed I-beams, T-beams, bulb tees, and multi-web tees. Possible reasons that were given for this include fewer box girder bridges, greater vertical clearance in box girder bridges due to falsework requirements, and greater capacity against impact damage without loss of structural capacity due to the inherent stiffness of the box girder bridges.

A study aimed at the assessment of the over-height vehicle collision problem and the identification of probable remedies was conducted by the University of Maryland, Bridge Engineering Software and Technology Center [31]. This study was prompted by the accident in 1999, where an excavator on a flatbed trailer struck a prestressed concrete pedestrian bridge over the Baltimore Beltway. The impact led to the collapse of the bridge, killing one motorist and

injuring three others. According to a nationwide survey, standard bridge clearances in the United States range from 14 to 17 ft., and some states post the actual vertical clearance on warning signs while other states under-report the clearance by 6 in. It was stated that prior to the Beltway accident, the truck passed under several other bridges; all of which had greater clearance than the pedestrian bridge. After the accident, a new policy was adopted in Maryland such that the recently constructed pedestrian bridges over freeways would have equal or greater clearance than the adjacent highway bridges.

After an incident, the decision to repair or replace a damaged member is often times based on a simple evaluation performed under time pressure in order to restore the bridge to service as quickly as possible. The lack of guidelines for a systematic damage assessment may sometimes result in decisions that are not always appropriate for particular damage cases. Assessment techniques for concrete bridge damage due to vehicle impact have been proposed in a National Cooperative Highway Research Program report [34]. The report divides the assessment of damage in three categories; damage to prestressing strands, damage to concrete, and concerns about the structural integrity of the bridge. Four general damage categories, namely minor damage, moderate damage, severe damage, and critical damage, have been established. Minor damage corresponds to damage in concrete portions of prestressed concrete girders only, with no exposed steel. The moderate damage category includes extensive concrete spalling exposing prestressing strands without strand fractures. In the severe damage category, there is major loss of concrete in the bottom flange and in the web with visibly deformed and/or fractured strands. There is also the potential for horizontal misalignment of the bottom flange in this category. In the case of critical damage, excessive lateral and vertical misalignment in the girders with excessive deformation is observed in the entire section.

Feldman et al. also conducted a study on impact-damaged prestressed concrete bridges [30]. The damage in prestressed concrete bridges was classified as minor damage, moderate damage, or severe damage. According to a national survey conducted by the authors that included a total of 241 damaged bridges, 61 percent of the damaged bridges studied had minor damage, 25 percent had moderate damage, and 14 percent had severe damage. It was proposed that in the case of severely damaged girders, a structural analysis of the bridge incorporating the girders in their damaged state with possible losses in the prestressing force due to fractured strands and losses in the shear capacity due to fractured stirrups should be performed. The authors also indicated that even if one or more of the girders were damaged, the structural performance of the entire bridge might not be affected adversely due to possible load redistribution among different members.

1.2.3. Vehicle Crashes with Highway Structures

The magnitude of the impact load exerted on a bridge during a vehicular collision is difficult to determine as there is a complex interaction between the vehicle and the bridge during the impact. AASHTO LRFD Bridge Design Specifications recommend the use of equivalent static force in the design of bridge components subjected to vehicular collision [9]. It was stated in the AASHTO Specifications that, unless protected by an embankment or a barrier, the abutments and piers of highway bridges located within a certain distance to the roadway or railway track should be designed for an equivalent static force of 400 kips acting horizontally in any direction. The commentary states that the value of 400 kips is based on information from analysis of truck and train collision cases, and this load could be applied as a point load or could be distributed

over an area “deemed suitable for the size of the structure and the anticipated impacted vehicle…”

El-Tawil et al. performed finite element crash simulations of two different types of trucks with two different types of bridge piers [35]. Highly-detailed finite element models with nonlinear material properties were used for the 3-kip and 15-kip trucks used in the crash simulations. One type of square section and one type of circular section reinforced concrete piers were used to investigate the interaction between the piers and the colliding vehicles. The piers were modeled using beam elements and included linear elastic material properties. The foundation for the piers consisted of beam elements simulating the piles and lateral inelastic spring elements to model the pile-structure interaction. The impact speeds used in the analyses varied between 35 mph and 85 mph. The three quantities used by the authors to compare the impact analyses were the peak dynamic force (PDF), the equivalent static force (ESF), and the peak 50 ms average force (PFMA). It was reported that the PFMA values obtained from the analyses were not as reliable as the other two methods, because of its arbitrary definition. The PDFs and the ESFs for both pier models were found to increase with increasing impact speeds with the rate of increase being larger for the PDFs. The PDFs and the ESFs were larger for the square pier than for the circular pier, mainly because of the larger stiffness and larger contact area of the square piers. Even though one of the trucks used in the analyses was five times heavier that the other truck, the PDFs and ESFs for this truck was less than five times the values for the other truck. The authors compared the ESF values obtained from their analyses with the 400-kip load specified by the AASHTO LRFD Specifications [9]. The authors’ ESF values were larger than the AASHTO LRFD design force of 400 kips for the majority of the cases studied. For the highest impact speed considered, the analyses indicated approximately 70 percent larger ESF than the AASHTO Design force for the 3-kip truck. For the 15-kip truck, the ratio between the authors’ ESF and the AASHTO LRFD design force was 4.9 for the highest impact speed.

AASHTO LRFD Bridge Design Specifications also include provisions regarding vessel-induced impact loads exerted on bridges crossing waterways [9], and these provisions were adopted from AASHTO Guide Specification and Commentary for Vessel Collision Design of Highway Bridges [36]. It was stated that in a previous study investigating a deckhouse collision of a ship with the superstructure of a bridge, 1200 kips of load was reported to develop for a 1000 DWT (Deadweight Tonnage) ship. Based on this data, an empirical relationship was given in the AASHTO Specifications to determine impact forces on bridge superstructures for deckhouse collision.

Tests of vehicle crashes with overhead sign structures were conducted by Ivey et al. [37]. Ten tests including different weight vehicles crashing at one of the four supports of a steel sign bridge at different impact speeds and angles were performed. Weight of the vehicles varied between 2100 and 5170 lb, with initial speeds of 25.7 to 75.3 mph. The reductions in the speed of the vehicles after the collision varied between 3.1 and 12.2 mph. The maximum two impact forces occurred in the tests including 5150 and 5170 lb vehicles colliding with the bridge with 75.3 and 72 mph speeds, respectively. For these two cases, the peak vehicle decelerations were measured to be 17.6g and 22.4g, corresponding to a peak force of 90.6 and 115.8 kips, respectively. The average vehicle decelerations and forces for these two cases, respectively, were 6.9g and 8.8g,

and 35.5 and 45.5 kips. The impact durations measured during the tests were about 0.06 to 0.07 second, and the peak decelerations were observed to occur at approximately 0.05 second.

In a series of tests performed by Cook and Bodocsi, crashes of "standard-size" automobiles with steel-channel sign supports were analyzed [38]. The maximum peak vehicle decelerations determined during these tests were around 9g with average accelerations on the order of 2g to 3g.

There are numerous studies available in literature reporting collision tests of vehicles with other vehicles [39-42]. These studies have shown that duration of a collision, which is defined as the time duration at which the acceleration of the colliding vehicle returns to zero, is generally in the range of 50 to 200 milliseconds. Kerkhoff et al. also stated that as the initial velocity of the colliding vehicle increases, the progressive structural yield of the body of the vehicle results in longer impact durations [39].

1.2.4. Performance of Concrete Diaphragms under Lateral Loads

Effects of diaphragms on the performance of prestressed concrete bridges under static, dynamic and lateral impact loads was experimentally studied by Sengupta and Breen [1]. Four 1:5.5 scale model bridges, each having six prestressed concrete girders, were tested with the major experimental variables being the skew angle and the location and number of concrete diaphragms. Two of the bridges, one with 45-degree skew and one with no skew, were subjected to lateral impact loading with and without diaphragms. The span length of the bridges was either 107 or 172 in. and the diaphragms were located either at 1/3 points or at midspan. The impact load was applied by a pendulum at the bottom flange of the girders at the midspan section. It was reported that the damage on the impacted girder was considerably larger with the diaphragms in place. The maximum crack widths in the impacted girders were measured to be approximately 2 in. and 1/16 in., respectively, with and without diaphragms. It was also reported that in cases with diaphragms, not only the impacted girders were more highly damaged but also the forces transferred through the diaphragms caused diagonal shear cracks at the bottom flange of the next girder. The measured loads and lateral displacements at the impact locations showed that the presence of diaphragms reduced the lateral deflection of the bottom flange of the impacted girder and increased the impacting force. Similar observations were made for bridges with and without skew. It was concluded that the diaphragms make the prestressed concrete girders more rigid when resisting lateral impacts and reduce energy absorption capacity, which in turn, makes the girders more susceptible to damage under lateral impact loading.

Effects of various types and locations of intermediate diaphragms on the behavior of prestressed concrete bridges subjected to lateral loading were studied by Abendroth et al. [2]. The types of diaphragms studied included reinforced concrete, structural steel channel, and steel X-brace diaphragms with and without a horizontal strut. A full-scale three-girder single-span prestressed concrete bridge model incorporating different diaphragm configurations was tested under statically applied loads. The model included three 38 ft. long Iowa A38 girders spaced at 6 ft. with a 4 in. thick reinforced concrete deck at the top. The girders were supported at the ends by 1 in. thick elastomeric bearing pads, and the girder ends were encased in full-depth reinforced concrete end diaphragms. Use of four types of steel and one type of reinforced concrete intermediate diaphragms was investigated with the model. Vertical (upward) and/or horizontal loads were applied at the bottom flange of the girders at different locations along the length of

the model. The magnitude of the applied loads was adjusted such that the girders remained uncracked during testing so that several different cases could be studied with the same model. A linear finite element analysis of the bridge model was also carried out. Results from the finite element models indicated that the vertical load distribution among the girders was independent of the diaphragm type and location. A difference in vertical load distribution factors of approximately 10 percent is reported between the cases with perfectly pinned and fixed girder end conditions. In the case of horizontal loading, the amount of load distribution among the girders was dependent on the type of diaphragms with the reinforced concrete diaphragm and X-brace steel diaphragm with a bottom horizontal strut providing the largest distribution from the loaded girder to the other girders. The girder deflection and strain values measured during testing of the bridge model verified the findings of the finite element study.

Andrawes conducted a finite element study as a continuation of the research described above by Abendroth et al. [3]. A more detailed finite element model of the bridge model tested by Abendroth et al. was prepared in an attempt to better predict the response with different types and configurations of intermediate diaphragms. The models included the same geometric details of the model bridge and utilized linear-elastic material models. The girder displacement and strain values obtained from the refined models were reported to compare well with the measured response of the bridge model. Having verified the accuracy of the finite element model of the test bridge, finite element models of two existing prestressed concrete highway bridges were prepared to study the performance of different diaphragm types under lateral impact loading. These models included linear material properties and were subjected to horizontal impact loads with a duration of 0.1 sec applied at several locations along the length of one of the outside girders. The impact loading was applied at the diaphragm locations as well as at locations in between two diaphragms. The lateral displacements of the girders were observed to increase gradually until the load was removed at time t=0.1 sec. The girder strains, on the other hand, were maximum around t=0.01 sec, and remained constant until t=0.1 sec, when the load was removed. Results of the analyses suggested that the location of the maximum principal tensile strains was the same for all diaphragm types studied, which was at the bottom flange of each girder at the locations where the diaphragms were connected to the girders. The effect of the impact was observed to be more localized with the concrete diaphragms than it was with steel X-braced and K-braced diaphragms. The results also suggested that the degree of load transfer from the loaded girder to the other girders was larger with the concrete diaphragms than with the steel diaphragms. The dynamic load factor, which is the ratio between the extreme principal tensile strains produced under dynamic and static loads, was reported to be between 1.15 and 1.2.

1.2.5. Impact Characteristics of Concrete Beams and Slabs

The available literature on the behavior of reinforced and prestressed concrete members subjected to dynamic loads mostly deals with local impact loading in nuclear power plant structures that may be caused by an airplane crash or by internal projectiles such as pumps and turbine blades in case of an accident. The majority of these studies were performed in Europe and Japan. Ito and Ohnuma conducted impact tests on reinforced concrete and prestressed concrete beams and slabs, where the impact loading was applied by a steel cylinder weighing 154 lbs and with a maximum impact velocity of 164 ft/sec accelerated using compressed gas [43]. It was found that the residual deflection following the impact in prestressed concrete beams was smaller than in reinforced concrete beams. This difference was attributed to deflection

recovery due to prestressing. It was also reported that the level of prestress did not have an effect on measured beam strains and failure mode of the beams.

Eibl et al. performed impact tests on reinforced concrete beams and slabs to investigate the effect of reinforcement type [44]. The specimens were subjected to the impact of a rigid mass weighing 225 to 270 lbs running in steel guide tubes with impact velocities ranging from 17.4 ft/sec to 70.5 ft/sec. The results indicated that beams reinforced with low-strength plain bars performed better than those reinforced with high-strength deformed bars. The superior bond characteristics of high-strength deformed bars generated high local strains in the reinforcement. In those cases, failures were characterized by rupture of the reinforcement. Results from the slab tests showed the effectiveness of stirrups in reducing impact damage. It was found that at low impact velocities, stirrups increased the resistance of the specimens considerably by changing the failure mechanism from local punching failure into overall bending failure. At high impact velocities, however, the concrete in the vicinity of the point of impact was destroyed completely irrespective of the amount of reinforcement provided.

Ishikawa et al. studied bonded and unbonded prestressed concrete beams under impact loading [45]. Experimental results obtained from weight dropping tests performed on bonded and unbonded prestressed concrete beams revealed that both beams exhibited similar failure modes of prestressing tendon fracture. It was also noted that the dropping height that caused the failure of the unbonded prestressed concrete beam was 1.7 times larger than that of bonded beams, while the ultimate displacement was approximately 3 times larger.

In order to investigate the shear failure of reinforced concrete beams, Ando et al. conducted falling-weight impact tests, using 661 lb steel weights with impact velocities ranging from 3.3 to 19.7 ft/sec, on twenty-seven beams without shear reinforcement and with two different longitudinal reinforcement ratios [46]. Beams with almost equal static shear and bending capacities were observed to undergo flexural failure at lower-velocity impacts, and shear type failure at high-velocity impacts. Impact forces were observed to follow a half-sine wave with approximately 10 msec duration for an impact velocity of 3.3 ft/sec. For higher impact velocities, on the other hand, the impact forces showed a sudden linear increase after the impact and then a gradual decrease after reaching a maximum value. The impact durations were measured to be approximately 10 msec irrespective of the magnitude of impact velocity.

Hughes and Speirs conducted weight-drop tests on ninety-two reinforced concrete beams with different amounts of tension reinforcement, stirrups, and boundary conditions in order to validate the applicability of simple beam vibration theory to predict the dynamic response of beams subjected to impact loading [47]. Their results showed that the equivalent static force approach can predict the behavior of the beams with an acceptable accuracy for pulses that can be considered roughly sinusoidal with pulse durations of at least 2.5 times the natural period of the beam. For other cases, a proper dynamic analysis was recommended.

1.2.6. Behavior of Concrete Anchors

Description of Design Approaches

Several procedures are recommended in different resource documents to predict the capacity of headed anchors in concrete under shear and tensile loads [48-53]. The failure of a steel anchor

loaded in tension, shear or a combination of both will be due to either the failure of the concrete or the failure of the anchor steel. For the cases where failure is due to steel, the ultimate loads predicted by different methods are in close agreement with each other. In the case of concrete failure, on the other hand, there might be significant differences among the failure loads determined by the different procedures considered here. Two approaches used in the development of methods to determine the anchor capacity are (1) assumption of an average concrete tensile stress acting on a failure area (2) regression analysis of experimental data. In the case of tensile loading, a failure surface in the form of a cone (or prism) with an inclination angle of 30-45 degrees with the head of the cone coinciding with the head of the anchor is generally accepted. Among the procedures that use concrete tensile stress acting on a failure area to determine the capacity, there are two distinct approaches: the capacity is computed based on either the actual surface area of the failure cone times an average uniform stress or a pseudo area times an average uniform stress.

In ACI 349-85 Appendix B, the strength in tension of an anchor when the failure is due to the concrete is based on a uniform tensile stress of $4\sqrt{f'_c}$ acting on an effective stress area which is the projected circular area of the failure cone that assumes a 45-degree angle [50]. The value of the uniform tensile stress of $4\sqrt{f'_c}$ comes from averaging the principal stress distribution along the failure plane. The tensile stress changes linearly from $6\text{-}7\sqrt{f'_c}$ at the anchor head to zero at the concrete surface, constituting an average stress of approximately $4\sqrt{f'_c}$ acting on the projected circular area. A restriction on the minimum edge distance necessary to prevent lateral bursting of the concrete around the anchor head is also included in ACI 349. The provisions of ACI 349 on tensile strength of anchors are only applicable to those satisfying the restriction on edge distance.

The shear strength of anchors governed by concrete failure in ACI 349 is based on a uniform tensile stress of $4\sqrt{f'_c}$ acting on an effective area of a half-circle defined by projecting the 45-degree half-cone on the side of the concrete [50]. The influence of the edge and group effects on the tensile and shear strengths of anchors is considered by computing the effective projected stress areas accordingly.

ACI 349 indicates that the 45-degree failure angle changes at later stages of loading [50]. As the crack propagates from the side of the anchor head toward the concrete surface, bending of the uncracked portion around the cracked concrete causes compression around the perimeter, which is termed disc action. This additional compression of the concrete reduces the inclination angle as the cracking progresses. The effect caused by disc action is more significant in anchors with shallow embedments (less than 5 in.). It was also stated in ACI 349 that the existence of transverse stress causes changes in the inclination angle of the failure plane. Biaxial compression in the plane of the concrete block increases the inclination angle, making the cracks steeper. It is noted that the mode of failure of the concrete in this case approaches direct shear.

A method for determining the strength of bolt-type fastenings was developed in the early 1980s in Germany and is termed the κ-method [51,52]. In this method, the expressions used to determine the capacity of an isolated anchor, in the case of concrete failure, are based on regression analysis of experimental data. The κ-method implicitly assumes a failure plane inclination of 30-40 degrees, and the effects of edge distance and group action are included in the capacity with the use of κ-factors. For example, for the effect of anchor spacing, the two extreme

cases considered were (1) when the spacing between two anchors is sufficiently large (based on an inclination angle of approximately 35 degrees), in which case the capacity of the group is the summation of the individual capacities, and (2) when the spacing between the anchors is zero, in which case the total capacity is that of a single anchor. A linear interpolation between these two cases was adopted to determine the κ-factor that multiplies the capacity of an individual anchor to determine the capacity of the group including the effect of anchor spacing. The effect of limited edge distance is taken care of by another κ-factor obtained in a similar way. For combined tension and shear loading, the κ-method uses a tri-linear interaction expression.

The method used by the PCI Handbook [48] is based on the studies by Shaikh and Yi [54] for capacity in tension, and Eligehausen and Fuchs [52] for capacity in shear. The concrete capacity of an isolated anchor in tension is determined by multiplying the surface of the failure cone, with 45-degree inclination angle, by the factor of $(4/\sqrt{2})\sqrt{f'_c}$. In this approach, the $4\sqrt{f'_c}$ term is the average uniform stress acting along the concrete failure area, while the $1/\sqrt{2}$ factor was required so that the predicted anchor capacities would correspond to lower bound of the available test data. If the anchor is placed near a free edge, then this capacity is reduced by the ratio of the edge distance to the embedment depth. For a group of anchors, the failure surface is assumed to occur along a truncated pyramid rather than a cone, and the tensile capacity in this case is determined by multiplying the average uniform stress with the total surface area of the truncated pyramid. In case of shear strength, the effects of edge distance and anchor spacing are considered by multiplying the capacity of an isolated anchor with adjustment factors. For the anchors under combined tension and shear, a circular interaction equation is adopted.

The most recent approach for the design of post-installed anchors and cast-in-place studs or bolts, termed the concrete capacity design (CCD) approach, was developed by Fuchs, Eligehausen, and Breen [53], and is based on the κ-method. As the foundation of the CCD method is the κ-method, the capacities predicted by the two methods are similar. The concrete capacity of a single fastener in the CCD method is calculated based on a 35-degree inclination angle between the failure surface and the surface of the concrete, and the rate of change of concrete capacity with embedment depth (or with edge distance in case of shear loading) varies with the power of 1.5, similar to the κ-method. One of the principal advantages of the CCD method over the others is that it uses the simpler geometry based on a rectangular failure prism in order to include the edge distance and group effects. In the CCD method, the reduction in tensile capacity of anchors with limited edge distance is divided into two parts: the first part of the reduction is due to the reduction in the surface area of the failure plane, and the second part is due to the "disturbance of radial symmetric stress distribution." The first part of the reduction is considered by multiplying the capacity of an isolated anchor by the ratio of the projected rectangular areas with and without limited edge distance. The capacity is further reduced by a multiplier, which depends on edge distance, to account for the disturbance of symmetry in the original stress distribution. A similar approach is applied when determining the shear capacity of single anchors and anchor groups with limited edge distance.

The 2002 and 2005 versions of ACI 318 includes information on the behavior and design of cast-in-place and post-installed anchors in Appendix D [28,49]. The procedure used by ACI 318-02 and 318-05 regarding the assessment of the strength of anchors was developed from the CCD method with the design strength of the concrete limited to 10,000 psi for cast-in-place anchors.

In addition to concrete breakout failure in tension and shear, ACI 318-02 and 318-05 also consider anchor pullout and concrete side-face blowout failures under tension, and concrete pryout failure under shear. A 35-degree inclination of the failure planes under tension and shear loads is adopted with the assumption that failure of the concrete occurs along the surfaces of a prism. Similar to the CCD method, simple shapes of rectangular projected stress areas are used in order to include the effects of limited edge distance and anchor spacing in the calculated strength. One of the major differences between the ACI 318 approach and the others is that in the ACI approach the capacity of the anchor in cracked concrete is determined first, and if no cracking is expected then this capacity is multiplied by a factor that accounts for the absence of cracking. Depending on the type of failure, this factor ranges between 1.2 and 1.4 for cast-in-place anchors. In the case of concrete breakout failure in shear, the factor used to magnify the strength of anchors in uncracked concrete also accounts for the presence and the amount of reinforcement. The provisions used in ACI 318-02 and 318-05 regarding the behavior of anchors in cracked concrete are based on the paper by Eligehausen and Balogh [55]. For the anchors subjected to combined tension and shear loads, a tri-linear interaction approach is adopted which has no reduction in shear or tension capacity for small values of the second force.

Among the documents summarized above, only Shaikh and Yi mention wire-formed inserts specifically [54]. They indicated the applicability of this equation to different types of concrete inserts by stating that "Although the paper focuses on welded headed studs, the design equations would also apply to nut/washer anchor bolts and other similar inserts, such as loop inserts and expansion anchors." As mentioned earlier, this document forms the basis of the procedure used by the PCI Design Handbook. Both the third and fourth editions of the PCI Design Handbook include a section on concrete breakout strength of wire-formed inserts, and it is recommended that the equation given for the capacity of headed studs be used to predict the breakout capacity of wire-formed inserts [56,57]. The fifth edition of the PCI Design Handbook, on the other hand, does not mention the capacity of wire-formed inserts, nor does it mention whether the concrete breakout capacity equation given for headed studs can be used for wire-formed inserts [48].

Comparison of Different Approaches with Experimental Data

Rodriguez et al. investigated the dynamic behavior of tensile anchors. Different types of anchors used in nuclear power plants, including ¾ in. diameter cast-in-place A325 bolts with shallow embedment (4 in.) were tested under static and dynamic loads [58]. Dynamic tensile capacity of all types of anchors tested in the study significantly exceeded the static tensile capacity, with the margin being 27 percent for the cast-in-place anchors in uncracked concrete. In cracked concrete, the dynamic capacity of the cast-in-place anchors was more than 50 percent higher than the static capacity. Gross et al. reported results of static and dynamic shear tests performed as part of the same research project [59]. The shear tests were performed on specimens including single and double anchors in cracked and uncracked concrete, with and without hairpin reinforcement. The dynamic shear capacity of cast-in-place anchors exceeded the static capacity by approximately 20 percent with and without hairpin reinforcement. The static shear capacity of anchors in cracked concrete was approximately 18 percent less than that in the uncracked specimens. It was also reported that the reduction in capacity due to the existence of cracks in concrete was lower for dynamic loading than for static loading. This was attributed to lower additional crack opening under dynamic loading compared to static loading. The hairpin reinforcement was reported to substantially increase the shear capacity of near-edge anchors. The increase in capacity was

greater for static loading than for dynamic loading. Hairpin reinforcement placed directly against the anchors increased the concrete cone breakout capacity 1.9 to 3.0 times.

Behavior of cast-in-place bolts in high-strength concrete under tensile loads was investigated by Primavera et al. [60]. Sixty tests on two types of anchor bolts (A490 heavy hex bolts, and Richmond SAE3 anchors) with 4, 6, and 8 in. embedments were tested in 7500 and 12,000 psi concrete. Failure in all of the tests was due to failure of the concrete along a cone-shaped surface. All anchors, except for A490 bolts with 4 in. embedment were observed to experience an increase in capacity with increasing concrete strength. Increasing the concrete strength from 7500 psi to 12,000 psi resulted in load-deflection curves that were more linear with higher initial stiffness and with a well-defined ultimate load. Results from the tests also indicated that embedment was the most important parameter for increasing the capacity for a given concrete strength. For all anchors tested, the inclination of the failure planes ranged between 21 and 28 degrees. This observation contradicts the assumptions of 35- and 45-degree failure plane inclinations utilized in the current design methods, but supports the statement of the ACI 349 Commentary that shallower failure planes might occur due to disc action. It was stated by the authors that the shallow failure plane inclinations observed even with 6 and 8 in. embedment depths extend the validity of ACI 349 statement to embedment depths up to at least 8 in. Another important observation reported was that the CCD method over-predicted the capacity of cast-in-place anchors tested in this study, with the degree of over-prediction increasing with the concrete strength (4 percent for 7500 psi concrete and 20 percent for 12000 psi concrete).

Tension tests on several types of anchors, including cast-in-place headed anchors (Richmond SAE-3 anchors, Richmond DB-SAE-3 anchors, and threaded rod with end nut assembly) and wire-formed anchors (Richmond TY anchors and Richmond TY Loop anchors), with 8 to 19 in. embedments were conducted at Bucknell University by Carrato et al. [61]. Five of the cast-in-place headed anchors and one of the cast-in-place wire-formed anchors exhibited concrete failures. For the nominal embedment depth of 8 in. and with similar concrete strengths, the cast-in-place headed anchors were observed to have 20 percent to 62 percent more concrete capacity than the cast-in-place wire-formed anchor.

Eligehausen and Balogh studied the behavior of fasteners in cracked and uncracked concrete under tensile loading [55]. It was reported that, even though a concrete cone failure was exhibited in both cases, the pre-existence of cracks in the concrete caused the load-displacement plot of cast-in-place headed anchors to be flatter than that of the anchors in initially uncracked concrete by reducing the failure load and increasing the displacement at failure. Analysis of data from several experimental studies indicated that for an average crack width of approximately 0.012 in., the concrete cone failure load of cast-in-place headed anchors in cracked concrete is about 75 percent of the value in uncracked concrete. If the anchors are located at the intersection of two cracks, the concrete cone failure load is further reduced by approximately 20 percent. The reason for the reduction in capacity when a crack is present was indicated to be the disturbance of axi-symmetric stress distribution, which, in turn, reduces the surface area over which the tensile stresses are transferred.

Static, fatigue, and impact tensile tests were performed by Collins on short, cast-in-place anchor bolts [62]. Anchors with 4.75 in. and 7 in. embedment lengths with 60 ksi and 120 ksi anchor

strengths, respectively, were tested. In all of the specimens, the embedment lengths were large enough such that the full tensile capacity of the anchor steel was developed. All of the static tests resulted in fracture of steel without any relative slip between the anchors and the surrounding concrete. Fatigue tests revealed that 1 million cycles of fatigue loading with a maximum load corresponding to 60 percent of the yield strength of the anchors had no effect on anchor strength. After the fatigue tests, a slight reduction in stiffness was observed due to deterioration of the bond between the concrete and anchor steel. Impact loading with a maximum pulse magnitude corresponding to the yield strength of the anchor steel had no effect on anchor strength. It was stated that "required embedment lengths for all types of anchors in this study subjected to impact loads can be estimated using the same criteria for anchors under static loads." Regarding design of anchor bolts, the author concluded that cast-in-place anchors can be designed to behave in a ductile manner using the embedment length criteria of ACI 349 Appendix B.

Using the results of available tension tests performed previously by other researchers, Klingner and Mendonca compared the experimentally obtained nominal capacities of short anchor bolts to strengths predicted by different procedures used in the U.S. including the PCI and ACI 349 procedures [63]. Results of 90 tests, including 37 of which the failure was governed by the concrete, were investigated. It was concluded that the tensile capacities governed by steel failures were predicted with reasonable accuracy by all methods. As a result of the small scatter in the ratio of the predicted-to-measured capacities, the authors proposed a capacity reduction factor of 0.90 to be used in the design of anchors governed by steel failures. For the cases governed by concrete failures, all procedures except the ACI 349 procedure significantly overestimated the capacity for the majority of the tests. The main reason the ACI 349 procedure performed better than the other methods was attributed to its bursting criteria for large-diameter anchors placed at small edge distances. Because of the large variation in the ratio of the predicted-to-measured capacity of anchors governed by concrete failure, it was stated that a smaller capacity reduction factor (0.65) be used for these types of failures.

Klingner et al. studied the effect of reinforcing details on the shear resistance of anchor bolts under monotonic and reversed cyclic loading [64]. The anchors tested were ¾ in. diameter A307 bolts embedded to a depth of 8 in. The aim of the study was to develop reinforcing details that would bring the shear capacity of an edge anchor to that of an anchor located away from an edge. It was concluded that for good ultimate load performance, hairpin reinforcement should be placed directly against the anchor, and the best performance was obtained when an additional hairpin was placed at the base of the anchor.

McMackin et al. performed tension, shear, and combined tests on headed steel anchors to develop a tension-shear interaction relationship [65]. Anchors with 3/4 in. and 7/8 in. diameter were tested at 4 in., 7 in., and 8 in. embedment depths in normal-weight and light-weight concrete. An elliptical tension-shear interaction relation with a power of 5/3 was found to best fit the test data.

1.3. Objectives and Scope

The objective of this research was to study the strength and ductility characteristics of prestressed concrete through-girder pedestrian bridges using experimental analyses integrated

with numerical simulations. There were two primary issues requiring investigation to ensure the safety of prestressed concrete through-girder pedestrian bridges.

The first issue is related to the ductility of prestressed concrete girders used in these bridges. Strain compatibility analyses with nonlinear material properties were performed for the Mn/DOT Type 63 section in order to identify the inconsistencies between the American State Highway and Transportation Officials (AASHTO) LRFD [9] and AASHTO Standard Specifications [8] procedures, and to investigate the accuracy of both specifications in predicting the flexural response of prestressed concrete flanged sections. Sectional response from strain compatibility analyses was compared to those predicted by the AASHTO LRFD Specifications, the AASHTO Standard Specifications, and a procedure obtained by modifying the equations in the AASHTO LRFD Specifications to rectify the errors in the determination of the top flange contribution. Measured flexural strengths of prestressed concrete I-beams found in the literature were also used for comparison with the predictions from the specifications and the strain compatibility analyses.

The second issue regarded the stability of the entire bridge system under lateral loading caused by over-height vehicle impact. As the impact loads are transferred to other parts of the bridge, the connections between different bridge members are subjected to large forces. Failure of these connections reduces the structural integrity of the bridge, which compromises the stability of the structure. Numerical and experimental analyses were performed to investigate the adequacy of the strength and ductility of connection details currently used in prestressed concrete through-girder pedestrian bridges.

Three series of laboratory tests were conducted to investigate the performance of currently used and proposed details, as well as to obtain information to be used in the entire-bridge finite element models. The laboratory tests included (1) pull-out tests on steel inserts used for the floor beam to girder connections, (2) tests on floor beam and girder connection subassemblages, and (3) tests on the girder end details. Results obtained from the tension pull-out tests on steel inserts were incorporated in the entire-bridge finite element models in modeling of the connectors between the floor beams and the girders. Similarly, results obtained from the girder end detail tests were used in modeling the girder boundary conditions in the entire-bridge finite element models. Calibration of the finite element models was performed using the data obtained from the tests on connection subassemblage specimens.

Three-dimensional full-scale finite element models of an entire prestressed concrete through-girder bridge system were used to study the behavior of bridge under statically applied transverse loads. These models included both material nonlinearities, such as cracking and crushing of concrete, and geometric nonlinearities, such as bearing and friction between contact surfaces of different bridge members in order to accurately represent the behavior of the bridge. The three sets of analyses performed using the full bridge models were lateral static analysis, lateral dynamic impact analysis, and stability analysis under bridge self-weight. Effects of parameters, such as location of load application, connection details, and girder end details on the strength and ductility of the bridge were studied in these analyses. The effectiveness of several modified connection details on the performance of the bridge system were also investigated with these analyses.

1.4. Organization of Report

Chapter 2 presents the results of the nonlinear strain compatibility analyses conducted to determine and rectify the inconsistencies between the sectional response of Mn/DOT Type 63 section predicted by the AASHTO LRFD [9] and AASHTO Standard Specifications [8].

Chapter 3 describes the tension pullout tests performed on steel inserts that were currently used in prestressed concrete girders fabricated in Minnesota and proposed for future construction.

Chapter 4 summarizes the experimental an numerical investigation of the behavior of typical girder-floor beam connection details used in the prestressed concrete through-girder pedestrian bridges constructed in Minnesota. The investigation included load testing of subassemblage specimens as well as a companion finite element study.

In Chapter 5, a description of the static load tests performed to determine the lateral stiffness and strength of end details used for prestressed concrete girders is given.

Results from the finite element analyses of a typical prestressed concrete through-girder pedestrian bridge system, including static lateral load analyses, dynamic lateral impact analyses, and stability analyses under gravity loading, are presented in Chapter 6.

Chapter 7 provides a summary of the results and recommendations for retrofitting existing bridges and for new construction.

Table 1.1 Prestressed Concrete Through-Girder Pedestrian Bridge Dimensions

Bridge #	# of spans	Span length	Skew angle	Girder depth	Girder spacing	Min slab thickness	End floor beams	Intermediate floor beams		Sidewalls?	
								Type	Spacing	At abutment	At pier
62582	2	125’-0”	0°	63”	12’-6”	7”	Conc. 12” wide	Conc. 12”wide	14’-0”	Yes	Yes
71522	2	135’-0”	16°	63”	14’-0”	6-½”	Conc. 12” wide	Conc. 12”wide	14’-9”	Yes	Yes
02565	1	135’-0”	0°	63”	14’-0”	6-½”	Conc. 12” wide	Conc. 12”wide	16’-6”	Yes	N/A
27A26	1	135’-0”	35°	63”	14’-6”	6”	Conc. 12” wide	Conc. 12”wide	14’-6”	No	N/A
82515	1	135’-0”	20°	63”	14’-6”	7”	Conc. 12” wide	Conc. 12”wide	14’-9”	No	N/A

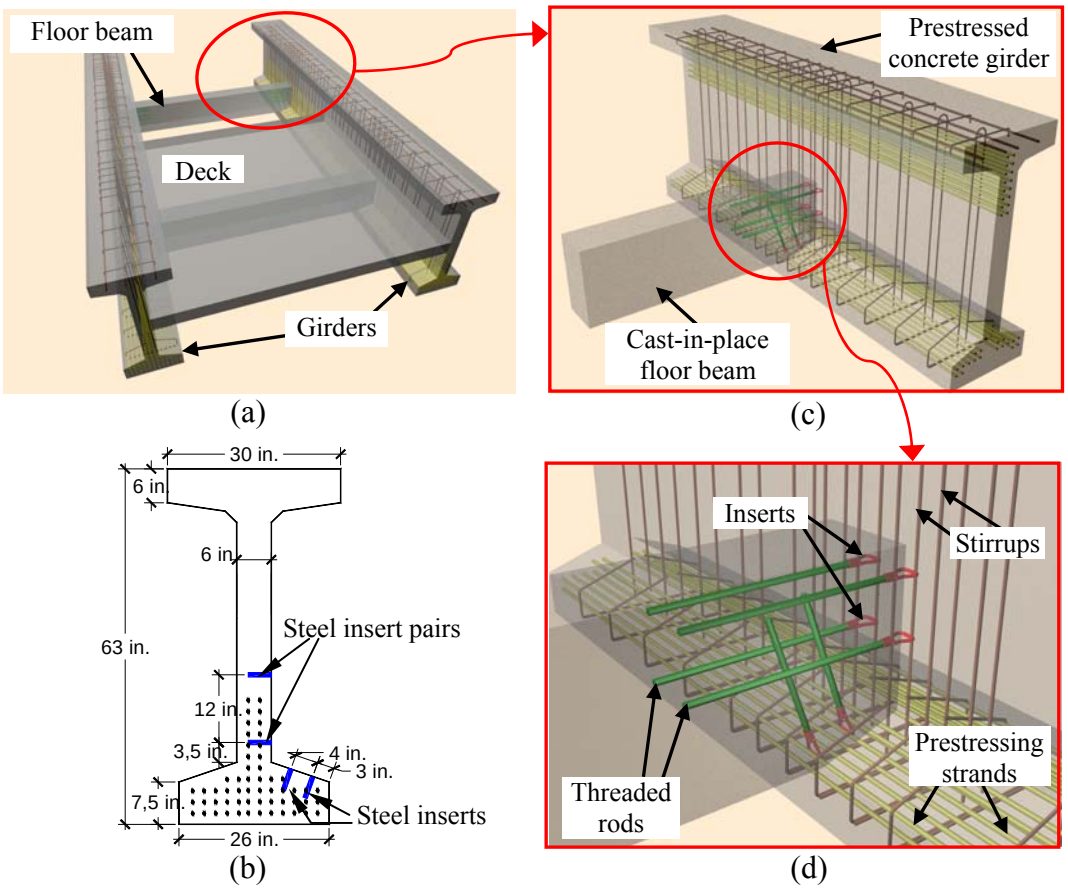

Fig. 1.1. Relation between prototype and test specimens: (a) geometry of a typical prestressed concrete through-girder pedestrian bridge; (b) Mn/DOT Type-63 section; (c) girder-floor beam connection subassembly; (d) close-up of connection region.

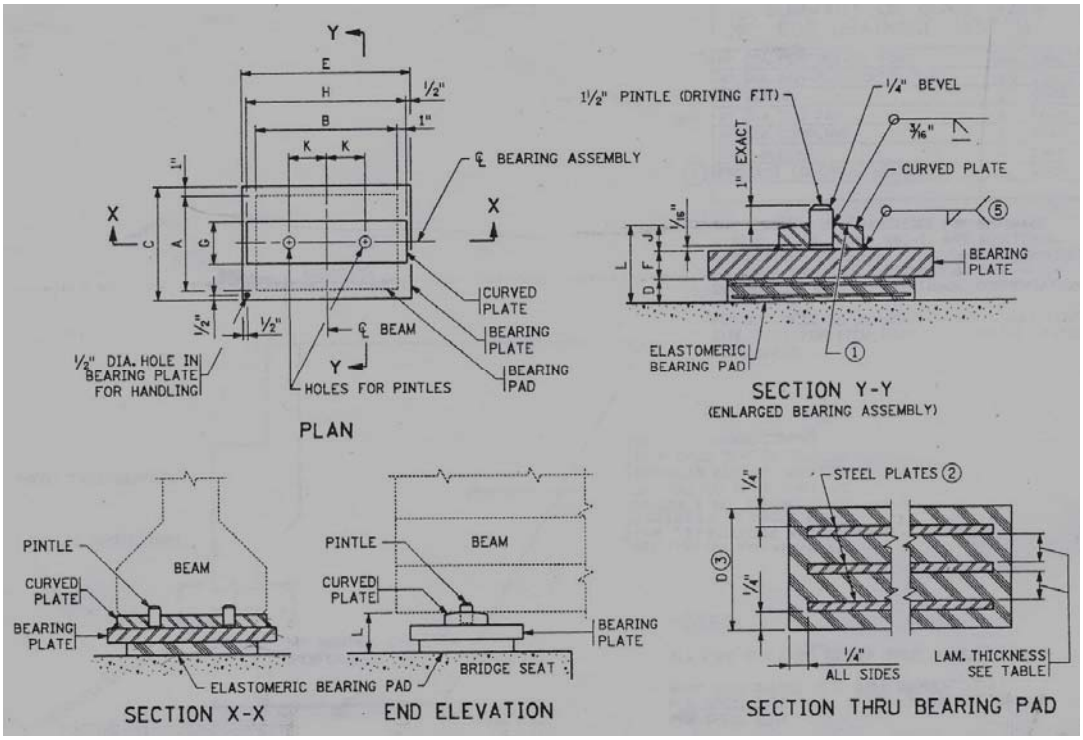

(a)

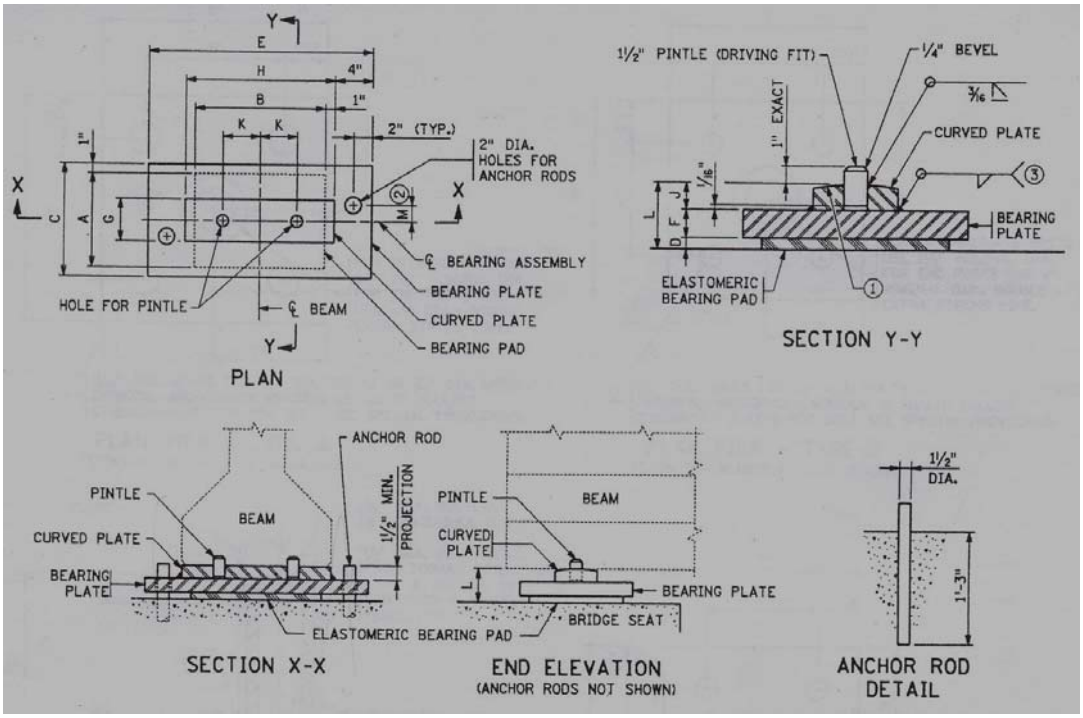

(b)

Fig. 1.2. Support details used at girder ends: (a) expansion end; (b) fixed end.

Chapter 2
Strength and Ductility of Prestressed Concrete Girders

Inconsistencies in the sectional response of prestressed concrete flanged sections predicted by the AASHTO LRFD [9] and AASHTO Standard Specifications [8], including maximum reinforcement limits, arises due to different interpretations of the equivalent rectangular stress block idealization. In an effort to identify design procedures that more accurately represent the actual behavior of prestressed concrete flanged sections, provisions of the AASHTO LRFD and AASHTO Standard Specifications are compared to the results from strain compatibility analyses of such sections using realistic stress-strain models for the constituent materials.

2.1. Background on AASHTO Specifications

2.1.1. Reinforcement Limits

In order to provide adequate ductility of prestressed concrete sections, the ACI Code (1999 and earlier versions) [5-7], AASHTO Standard Specifications [8], and AASHTO LRFD Specifications [9] use the amount of tensile reinforcement in the section as the control variable. For prestressed concrete, the three specifications define the maximum reinforcement limit in terms of different parameters. The AASHTO Standard Specifications [8] control the maximum amount of tensile reinforcement by placing a limit on reinforcement index, ω. This limitation can be expressed by the following relationship:

$$\omega = \frac{A_{sr} f_{ps}}{b_w d f'_c} \le 0.36\beta_1 \qquad \text{Eq. (2.1)}$$

Versions of the ACI Code up to 2002 utilized a similar expression in order to limit the maximum tensile reinforcement [5-7]. The AASHTO LRFD Specifications [9], on the other hand, limit the maximum amount of tensile reinforcement by imposing the following limit on the ratio of neutral axis depth, c, to effective depth, d_e:

$$\frac{c}{d_e} \le 0.42 \qquad \text{Eq. (2.2)}$$

Even though the Standard and LRFD Specifications define the maximum reinforcement limit using different criteria, the two parameters (the reinforcement index ω and the c/d_e ratio) are related to each other through equilibrium of internal tensile and compressive forces. This relation can be shown by substituting the compression force capacity of the web, $0.85f'_c\beta_1 c b_w$, for the tensile force in the portion of the prestressing steel, $A_{sr}f_{ps}$, equilibrating the compressive force in the web into Eq. (2.1):

$$\frac{0.85 f'_c \beta_1 c b_w}{b_w d f'_c} \le 0.36\beta_1 \qquad \text{Eq. (2.3a)}$$

and after simplification

$$\frac{c}{d} \le \frac{0.36}{0.85} = 0.42 \qquad \text{Eq. (2.3b)}$$

Eq. (2.3b) is identical to Eq. (2.2) when d in Eq. (2.3b) equals d_e (as in Eq. (2.2)), in other words, when the section does not contain any non-prestressed tension reinforcement.

In the AASHTO Specifications [8,9] the sections with tensile reinforcement exceeding the maximum reinforcement limit are termed “over-reinforced.” By preventing the use of the full

flexural capacity of over-reinforced sections, the specifications impose an additional safety margin to account for the limited ductility of those sections. In other words, the specifications permit the use of prestressed concrete sections with steel amounts exceeding the maximum limit, but with a usable flexural strength that is less than the actual strength of the section. The reduction in usable flexural strength is achieved in the Standard Specifications and LRFD Specifications by placing an upper limit on the ultimate moment capacity of over-reinforced sections. In the 2002 version of the ACI Code [28], on the other hand, the reduction in usable flexural strength of over-reinforced sections is achieved through the use of strength reduction factors that decrease with decreasing strand strain at ultimate capacity.

Limiting the maximum tensile reinforcement in flexural members dates back to the 1971 edition of the ACI 318, which placed an upper limit of 0.30 on the reinforcement index, ω, which is directly proportional to the amount of tensile reinforcement [5]. The first appearance of a limit on the reinforcement index equal to 0.30 is found in the report titled "Tentative Recommendations for Prestressed Concrete" by the ACI-ASCE Joint Committee 323 [17]. The justification for such a limit was expressed as the need "To avoid approaching the condition of over-reinforced beams for which the ultimate flexural strength becomes dependent on the concrete strength…"

2.1.2. Ductility Considerations

Warwaruk, Sozen, and Siess conducted an extensive experimental and analytical study on the flexural strength of prestressed concrete beams [18]. It was stated that for smaller amounts of longitudinal tensile reinforcement, small variations in the reinforcement ratio or concrete strength do not cause significant changes in strand stress at ultimate load. However, if the section has a large amount of tensile reinforcement, then the strand stress, and hence the moment capacity, are affected significantly by marginal changes to the concrete strength or the reinforcement ratio, which can be accidental.

The idea behind a limitation on the maximum amount of longitudinal reinforcement was explained as follows: "…a beam should be proportioned to have a low value of longitudinal reinforcement to concrete strength ratio primarily because changes in the concrete strength will then affect the strength only negligibly; a policy which has long been followed in the design of ordinary reinforced concrete beams." Based on the strand strain at ultimate equal to 0.01, and a maximum usable concrete strain equal to 0.003, the authors proposed the limit $\rho(f_{ps} / f'_c) \le 0.25$ for sections with a rectangular compression zone and without any nonprestressed reinforcement.

This limit was obtained in a similar way as the limits on the maximum reinforcement index in the ACI-ASCE Joint Committee 323 report [17] and the AASHTO Standard Specifications [8]. When computing the 0.30 limit on the reinforcement index in the ACI-ASCE Joint Committee 323 report, the maximum usable concrete strain was assumed to be 0.004 with an assumed strand strain at ultimate of 0.01.

The maximum longitudinal reinforcement limits recommended by ACI-ASCE Joint Committee 323 and by Warwaruk, Sozen, and Siess were changed to $0.36\beta_1$ by Mattock in order to account for variations in concrete compressive strength [21]. Mattock also used the condition $f_{ps} = f_{py}$ to

define the limit on the maximum tensile reinforcement. The 1999 edition of the ACI Code indicates that the ASTM specified yield strength of low-relaxation Grade270 strands is f_{py}= 0.90f_{pu}, which corresponds to a strain of 0.01 for strands with a typical stress-strain behavior. In addition, the AASHTO Standard Specifications state that "Prestressed concrete members shall be designed so that the steel is yielding as ultimate capacity is approached."

Mast recommended using the net tensile strain in the extreme tension steel at nominal strength in order to determine if the section is compression-controlled or tension-controlled [27]. Mast proposed steel strain $\geq$ 0.005 for tension-controlled sections, and steel strain $\leq$ 0.0025 for compression-controlled sections. It should be noted that these limits apply to the net steel strain, i.e., they do not include the steel strain due to effective prestress. This approach is currently used by ACI 318-02 and 318-05 [28,49] with the strain limits of 0.005 and 0.002, respectively for the tension and compression-controlled bounds.

For the type of sections (rectangular, I, T, and box) that are typically used for prestressed concrete bridge girders, regular designs include a composite deck that carries the major part of the internal compressive force. For these cases, the maximum tensile reinforcement limits are easily met. But, for the cases in which neither a composite deck nor a wide top flange exist to help carry the compressive component of the internal couple, the neutral axis may be located in the web of the section. For these cases, the increased neutral axis depth, c, can lead to over-reinforced sections.

2.1.3. Strength Considerations

Both the AASHTO Standard [8] and the AASHTO LRFD Specifications [9] approximate the nonlinear concrete compressive stress distribution at nominal capacity (Fig. 2.1(a)) with the Whitney rectangular stress block that has an average compressive stress of 0.85f'_c "uniformly distributed over an equivalent compression zone bounded by the edges of the cross section and a line parallel to the neutral axis at a distance $a=\beta_1 c$ from the extreme compression fiber." However, in the implementation of the equivalent rectangular compression block, the LRFD Specifications neglect the contribution of the bottom of the top flange overhangs (i.e., area below $\beta_1 h_f$) to the internal compression force. The differences in the way the two specifications treat the overhanging portions of the top flange of nonrectangular sections lead to inconsistencies in the determination of whether or not the section is considered over-reinforced, as well as in the resulting flexural capacity.

The AASHTO Standard Specifications use the procedure that has been used by the ACI Building Code since the 1983 Edition [6,7,28,49]. These standards assume that T-section behavior exists when the depth of the equivalent rectangular compressive stress block, $a=\beta_1 c$, drops below the top flange of the section, and that once T-section behavior begins, the full depth of the top flange carries compressive stress with an assumed uniformly constant stress intensity of 0.85f'_c. In this case, the depth of the neutral axis of flanged sections can be calculated using the expression:

$$a = \beta_1 c = \frac{A_{sr} f_{ps}}{0.85 f'_c \, b_w} \qquad \text{Eq. (2.4a)}$$

which can be re-written as:

$$0.85 f'_c \, \beta_1 c b_w = A_{sr} f_{ps} \qquad \text{Eq. (2.4b)}$$

where, A_{sr} is defined as:

$$A_{sr} = A_{ps} - A_{sf} = A_{ps} - \frac{0.85 f'_c (b - b_w) h_f}{f_{ps}} \quad \text{Eq. (2.4c)}$$

Combining Eqs. (2.4b) and (2.4c):

$$(0.85 f'_c)(\beta_1 c) b_w + (0.85 f'_c) h_f (b - b_w) = A_{ps} f_{ps} \quad \text{Eq. (2.4d)}$$

Eq. (2.4d) is the expression for the internal equilibrium of the compressive force in the concrete and tensile force in the prestressing steel. As seen in the second term of the left hand side of Eq. (2.4d), the Standard Specifications allow the full flange depth of h_f to contribute to the total compressive force carried by the section. In this case, the contribution of the top flange overhangs to the total internal compressive force is $0.85 f'_c (b - b_w) h_f$ as illustrated in Fig. 2.1(b).

The AASHTO LRFD Specifications [9], on the other hand, consider the section to be a T-section if the depth of the neutral axis, c, exceeds the depth of the top flange, h_f. The LRFD Specifications use the following equation to determine the depth of the neutral axis of prestressed concrete sections with T-section behavior and without any mild reinforcement:

$$c = \frac{A_{ps} f_{pu} - 0.85 f'_c \beta_1 h_f (b - b_w)}{0.85 f'_c \beta_1 b_w + k A_{ps} \dfrac{f_{pu}}{d_p}} \quad \text{Eq. (2.5a)}$$

which can be re-written as:

$$(0.85 f'_c)(\beta_1 c) b_w + (0.85 f'_c)(\beta_1 h_f)(b - b_w) = A_{ps} f_{pu} \left(1 - k \frac{c}{d_p}\right) \quad \text{Eq. (2.5b)}$$

where the term following A_{ps} on the right hand side is the expression given in the LRFD Specifications for the predicted average stress in the prestressing steel. As a result, Eq. (2.5b) is the expression for the internal equilibrium of the compressive force in the concrete and tensile force in the prestressing steel. As seen in the second term of the left hand side of the equilibrium expression, the LRFD Specifications limit the depth of the equivalent rectangular stress block acting on the overhanging portions of the flange of a T-section to $\beta_1 h_f$ (Fig. 2.1(c)). This implicitly means that, in the case of a T-section, the full depth of the top flange never contributes to the total compressive force when the equivalent rectangular stress block assumption is used, regardless of the magnitude of c. This assumption results in an overestimation of the neutral axis depth, c, for the LRFD Specifications in comparison with the Standard Specifications, as the web contribution must increase to compensate for the portion of the top flange that is being neglected.

Due to the differences in these two interpretations of the Whitney equivalent rectangular stress block assumption, there can be cases for which the AASHTO LRFD Specifications indicate that the section is over-reinforced while the AASHTO Standard Specifications indicate that the same section is not over-reinforced.

2.1.4. Strand Stress

The LRFD and Standard Specifications use different procedures to predict the stress in the prestressing steel at nominal flexural capacity. In the procedure used by the Standard

Specifications [8], the strand stress is predicted by Eq. (2.6), which is independent of the neutral axis depth:

$$f_{ps} = f_{pu}\left[1-\left(\frac{\gamma}{\beta_1}\right)\left(\rho\frac{f_{pu}}{f'_c}\right)\right] \qquad \text{Eq. (2.6)}$$

In the LRFD procedure [9], on the other hand, location of the neutral axis is determined first with Eq. (2.5a), which implicitly includes an assumed value for the strand stress. With this estimate of neutral axis location, strand stress is computed using Eq. (2.7):

$$f_{ps} = f_{pu}\left(1-k\frac{c}{d_p}\right) \qquad \text{Eq. (2.7)}$$

2.1.5. Nominal Moment Capacity

Both the AASHTO Standard and AASHTO LRFD Specifications use formulae for computing the flexural strength of over-reinforced sections that differ from those used for under-reinforced sections. The AASHTO Standard and LRFD Specifications use Eqs. (2.8) and (2.9), respectively, for the calculation of moment capacity of under-reinforced prestressed concrete sections:

$$M_n = A_{sr}f_{ps}d\left[1-0.6\left(\frac{A_{sr}f_{ps}}{b_w d f'_c}\right)\right]+0.85f'_c\left(b-b_w\right)h_f\left(d-0.5h_f\right) \qquad \text{Eq. (2.8)}$$

$$M_n = A_{ps}f_{ps}\left(d_p-\frac{a}{2}\right)+0.85f'_c\left(b-b_w\right)\left(\beta_1 h_f\right)\left(\frac{a}{2}-\frac{h_f}{2}\right) \qquad \text{Eq. (2.9)}$$

For the moment capacity of over-reinforced sections, on the other hand, the Standard and LRFD Specifications recommend using Eqs. (2.10) and (2.11), respectively:

$$M_n = \left(0.36\beta_1-0.08\beta_1^{\,2}\right)f'_c\,b_w d^2+0.85f'_c\left(b-b_w\right)h_f\left(d-0.5h_f\right) \qquad \text{Eq. (2.10)}$$

$$M_n = \left(0.36\beta_1-0.08\beta_1^{\,2}\right)f'_c\,b_w d_e^{\,2}+0.85f'_c\left(b-b_w\right)\left(\beta_1 h_f\right)\left(d_e-0.5h_f\right) \qquad \text{Eq. (2.11)}$$

The last two equations are obtained by substituting into Eqs. (2.8) and (2.9), respectively, the maximum amount of tensile reinforcement allowed by Eqs. (2.1) and (2.2). Through the use of Eqs. (2.10) and (2.11), in effect, the flexural strength of over-reinforced sections is limited to the value of the moment capacity corresponding to the maximum limit of tensile reinforcement. Any additional capacity that may be provided by having more steel than allowed by the reinforcement limits is neglected. This limitation on moment capacity is intended to ensure that sections with limited ductility have reserve moment capacity.

Even though the specifications penalize the use of over-reinforced sections by making a trade-off between the ductility and strength, Provision 5.7.3.3.1 of the AASHTO LRFD Specifications states that "Over-reinforced sections may be used in prestressed and partially prestressed members only if it is shown by analysis and experimentation that sufficient ductility of the structure can be achieved." This statement effectively penalizes the design and use of prestressed and partially prestressed over-reinforced sections more severely than provisions that simply limit the flexural resistance, as is done in the Standard Specifications.

The discrepancies described above concerning the two AASHTO specifications, as well as those of the ACI 318 approach, should be rectified to ensure that consistent levels of safety are achieved regardless of the choice of design procedure.

2.2. Methodology

Strain compatibility analyses were conducted using RESPONSE-2000 [66], a sectional analysis program by Bentz and Collins incorporating a nonlinear stress-strain material model. The model used for the concrete was proposed by Popovics, Thorenfeldt, and Collins [67], and the steel model was the modified Ramberg-Osgood as implemented by Mattock [68]. The tensile strength of the concrete was neglected in the analyses. Typical stress-strain relations used in the strain compatibility analyses for the concrete and prestressing steel are shown in Fig. 2.2.

A computer code utilizing internal force equilibrium and strain compatibility between steel and concrete was also developed using Mathcad [69] to verify the results obtained using RESPONSE-2000 [66]. The material models used in the code for concrete and steel were the same as those used in RESPONSE-2000. The Mathcad uses an iterative numerical solution procedure to determine the sectional response. The nonlinear analysis procedure includes incremental changes (increasing from zero) in the top fiber concrete strain of the section. For each value of top fiber concrete strain, internal force equilibrium is satisfied by changing the location of the neutral axis, and for each equilibrium point, the neutral axis depth, the strand stress, and the bending moment values are calculated and stored in a matrix. This procedure is repeated until the maximum value of the bending moment is reached.

Results of sectional analyses performed using RESPONSE-2000 were used to make comparisons between the sectional responses predicted by the AASHTO Specifications. So, when the term "strain compatibility" is used, it refers to the strain compatibility analyses performed using RESPONSE-2000 with nonlinear material models for the concrete and the steel. A comparison of the sectional responses predicted by RESPONSE-2000 and the nonlinear Mathcad code is also presented in the following sections.

The Mn/DOT Type 63 section was studied in order to illustrate the discrepancies that exist in the response of the sections predicted by the specifications, including the neutral axis locations, ultimate flexural capacity, and the strand stress at ultimate capacity [70]. Predictions of these quantities were obtained from the AASHTO Standard Specifications [8], AASHTO LRFD Specifications [9] and the strain compatibility analyses. In addition, analytical results were compared to the test results of prestressed concrete I-beams found in the literature [71], which were identified as over-reinforced and as having neutral axis depths within the web at nominal strength.

The amounts of prestressing steel that would just cause the Mn/DOT Type63 section to be over-reinforced according to the strain compatibility analyses were compared to those given by the limits in the specifications. The criterion used to determine the amount of steel from the strain compatibility analyses that would produce an over-reinforced section was the amount associated with a total steel strain (including strain due to effective prestress) of 0.01 at the centroid of the strands when ultimate moment capacity of the section was reached, as was done previously by other researchers [17,18,21].

2.3. Analysis of Section Behavior

The Mn/DOT Type 63 section, shown in Fig. 2.3 was analyzed assuming 8.2 ksi concrete compressive strength, which is the concrete strength specified on through-girder pedestrian bridge plans for prestressed concrete girders, and ½ in. diameter strands with an effective prestress of 162 ksi ($0.60f_{pu}$). The number of strands varied from 20 to 60, and the strands were placed in the typical pattern used for this type of section, that is, spaced 2 in. on center in the horizontal and vertical direction. Thus, the depth to the center of gravity of strands decreased as the number of strands increased. The location of the neutral axis depth, the strand stress, and the moment capacity were determined according to the LRFD Specifications [9], the Standard Specifications [8], and strain compatibility analysis. The results of the analyses are shown in Figs. 2.4(a) – 2.4(c).

The change in the neutral axis depth is shown in Fig. 2.4(a). As mentioned earlier, the LRFD Specifications [9] assume that T-section behavior starts when c exceeds h_f, and, as shown in the figure, the LRFD Specifications begin to overestimate the neutral axis depth when there are 20 strands in the section. The Standard Specifications [8], on the other hand, indicate almost the same neutral axis location as the strain compatibility analysis until the number of strands is increased to 32. For this amount of prestressing steel, the Standard Specifications begin to treat the section as a T-section, and overestimate c as compared to the strain compatibility analyses. Similar results were obtained earlier by Badie and Tadros using strain compatibility analysis with the Whitney equivalent rectangular stress block assumption for the concrete [10].

The change in strand stress at ultimate flexural capacity of the section is shown in Fig. 2.4(b). As illustrated, the LRFD Specifications [9] underestimate the strand stress compared to the strain compatibility analysis because of overestimation in neutral axis depth, while the Standard Specifications [8] slightly overestimate it because of the approximate nature of the equation (i.e., in the Standard Specification equation, there is no direct relation between strand stress and neutral axis depth). Note that the strand stress values on the y-axis start from 200 ksi to better show the difference among the values obtained from the different methods.

Fig. 2.4(c) shows how the nominal bending resistance calculated according to the LRFD Specifications [9], Standard Specifications [8], and strain compatibility analyses change with amount of prestressing steel. Once T-section behavior begins (i.e., when there are 20 strands according to the LRFD Specifications) the LRFD Specifications begin to underestimate bending capacity. As the number of strands increases, the depth of the web participating in the internal compressive force increases until the section becomes over-reinforced at 38 strands. Subsequently, Eq. (2.11) is used to compute LRFD nominal bending resistance. This equation is independent of the amount of steel in the section. As seen in the equation, only the geometric properties of the section and the concrete compressive strength were used to determine the capacity of over-reinforced sections. As a result, the moment capacity of the section does not change with the amount of steel in the section as it becomes over-reinforced, and the plot of moment capacity versus the amount of steel in the section is expected to be a straight line. The reason that the plots of moment capacity against the number of strands shown in Fig. 2.4(c) are not straight lines is related to the way that the prestressing strands in the Mn/DOT Type 63 section were placed in the analyses. Both the LRFD and the Standard Specifications use the distance from the extreme compression fiber to the centroid of the strands to compute the

moment capacity of over-reinforced sections, and this distance decreases with increasing number of strands as the strands were distributed through the depth of the Mn/DOT Type 63 section. As a result, once the section became over-reinforced, the moment capacity computed according to Eq. (2.11) started to decrease with increasing number of strands.

As evident in Fig. 2.4(c), the Mn/DOT Type 63 section becomes over-reinforced according to the LRFD Specifications [9] when there are 38 strands in the section. Once the section became over-reinforced, the LRFD Specifications grossly underestimated the moment capacity of the section. According to the Standard Specifications [8], the maximum reinforcement limit was reached at 44 strands. For the number of strands between 38 and 44, the LRFD Specifications indicate that the section is over-reinforced while the Standard Specifications indicate otherwise.

The inconsistency described above severely limits practitioners' choices, as the LRFD Specifications [9] penalize the use of these so-called "over-reinforced" sections in two ways: (1) by placing a conservative limit on nominal bending resistance, and (2) by requiring additional analyses and experimentation to show that there is sufficient ductility. Therefore, the AASHTO LRFD Specifications' procedure was modified as explained in the following section so that the LRFD and Standard Specifications [8] would result in consistent designs.

2.4. Modification of LRFD Procedure

As noted earlier, there are two reasons that the LRFD Specifications [9] overestimate the neutral axis depth; the first reason is the use of $c=h_f$ as the limit for T-section behavior, and the second reason is the use of $\beta_1 h_f$ limit for the maximum flange overhang contribution to the internal compressive force once the T-section behavior begins (Figs. 2.1(b) and 2.1(c)). A modification, that overcomes both of these problems, is proposed to the procedure outlined in the LRFD Specifications to indicate T-section behavior initiates when $a = \beta_1 c = h_f$ rather than when $c=h_f$. This modification also fixes the second problem mentioned above by enabling the entire flange depth to become effective when $a \geq h_f$.

Because the neutral axis depth and moment capacity of under-reinforced sections and the moment capacity of over-reinforced sections depend on the amount of flange overhang contribution to the internal compressive force, the corresponding equations in the LRFD Specifications [9] (Eqs. 5.7.3.1.1-3, 5.7.3.2.2-1, and C5.7.3.3.1-2) were also modified to remove the $\beta_1 h_f$ limit on the contribution of the flange overhangs. After modification, Eqs. 5.7.3.1.1-3, 5.7.3.2.2-1, and C5.7.3.3.1-2 in the LRFD Specifications (Eqs. (2.5), (2.9), and (2.11), respectively, in this document) take the forms of Eqs. (2.12), (2.13), and (2.14), respectively.

$$c = \frac{A_{ps} f_{pu} - 0.85 f'_c (b - b_w) h_f}{0.85 f'_c \beta_1 b_w + k A_{ps} \dfrac{f_{pu}}{d_p}} \qquad \text{Eq. (2.12)}$$

$$M_n = A_{ps} f_{ps} \left(d_p - \frac{a}{2} \right) + 0.85 f'_c (b - b_w) h_f \left(\frac{a}{2} - \frac{h_f}{2} \right) \qquad \text{Eq. (2.13)}$$

$$M_n = \left(0.36\beta_1 - 0.08\beta_1^2 \right) f'_c b_w d_e^2 + 0.85 f'_c (b - b_w) h_f \left(d_e - 0.5 h_f \right) \qquad \text{Eq. (2.14)}$$

The procedure in the LRFD Specifications using Eqs. (2.12), (2.13), and (2.14) instead of Eqs. 5.7.3.1.1-3, 5.7.3.2.2-1, and C5.7.3.3.1-2 is referred to as the "modified LRFD procedure" in the remainder of this document. This procedure uses the strand stress equation from the LRFD Specifications while the rest of the equations are from the Standard Specifications.

The neutral axis depth values for the Mn/DOT Type 63 section were computed with the modified LRFD procedure and are shown in Fig. 2.4(a). The figure reveals that there is better agreement between the values computed with the modified LRFD approach and the strain compatibility results than there is with either the Standard [8] or the LRFD Specifications [9]. As seen, with the modified LRFD procedure, the T-section behavior starts when there are 32 strands in the section, similar to the AASHTO Standard Specifications. For the number of strands investigated, a maximum error of 36 percent occurred in the modified LRFD procedure predictions compared to the strain compatibility analysis results. This compares with maximum errors in neutral axis depths calculated according to the AASHTO Standard and LRFD Specifications of 83 percent and 134 percent, respectively.

The strand stress valuesat nominal moment capacity of the Mn/DOT Type 63 section with increasing number of strands predicted by the modified LRFD procedure are superimposed on the plots in Fig. 2.4(b). As shown, there is a good agreement between the predictions of the modified LRFD procedure and the results from the strain compatibility analyses.

As shown in Fig. 2.4(c), modifying the AASHTO LRFD [9] procedure improved the prediction of the moment capacity of the Mn/DOT Type 63 section. It should be noted that once the section became over-reinforced according to the Standard Specifications [8] and the modified LRFD procedure, both specifications indicated the same moment capacity values for increasing number of strands, even though the strand stress values predicted by the two specifications were different. This was so because, according to both procedures, moment capacity of over-reinforced sections is computed based solely on the compressive portion of the internal couple and once the β_1 factor was removed from the flange overhang contribution in the LRFD equations, both the LRFD and Standard Specifications have the same equation for the moment capacity of over-reinforced sections.

It is evident from the above observations that the modified LRFD procedure provides a better estimate of the response of the section than the LRFD [9] and Standard Specifications [8]. The two reasons for the improved accuracy of the modified LRFD procedure are: (1) rectification of the error associated with the contribution of flange overhangs in the LRFD Specifications, and (2) better strand stress characterization in the LRFD procedure (as it takes into account the changes in neutral axis location due to changes in both the flange depth and the strand area) than the equation used in the Standard Specifications.

2.4.1. Validation with Experimental Data

Thirty-eight 12 in. deep prestressed concrete I-beams tested in flexure by Hernandez [71] were used to validate the strain compatibility analysis results. Twenty-one of the beams were reported to have failed in flexure. The measured flexural strengths were compared to those predicted by the AASHTO specifications [8,9] and the strain compatibility analyses. Reported material properties were used for each beam and the tensile strength of the concrete was neglected. In the

experimental study, two different reinforcement ratios were used with two different cross sections, as shown in Fig. 2.5. Even though the nominal dimensions of all of the beams were the same, the web and flange dimensions varied slightly. In the analyses, the reported measured dimensions were used.

Figs. 2.6 and 2.7 provide a comparison of the predicted and measured moment capacities that are tabulated in Table 2.1. The moment values plotted in Fig. 2.6 were computed according to the specifications with no consideration of maximum reinforcement limits. In other words, in computing the moment capacities, the equations provided in the specifications for under-reinforced sections (Eqs. (2.8), (2.9), and (2.13) for Standard Specifications [8], LRFD Specifications [9], and the modified LRFD procedure, respectively) were used, even though some of the beams would be classified as over-reinforced according to some of the specifications. In this way, the relation between the measured moment capacities and the capacities predicted by the specifications can be investigated without considering the artificial limitation placed on sections that were considered over-reinforced.

Moment capacities predicted by the strain compatibility analysis were in good agreement with the test results, as shown in Fig. 2.6. The mean value of the ratio of the predicted to measured values was 1.02 with a coefficient of variation of 0.03. Such close agreement between the predicted and measured capacities was expected because (a) nonlinear material properties were used in the strain compatibility analysis, and, (b) even though the tensile strength of concrete was neglected in the analysis, the contribution of the concrete tensile strength to the moment capacity was insignificant.

There was also good agreement between the moment capacities predicted by the AASHTO Standard Specifications [8] and the measured capacities. The mean value of the predicted to measured moment capacities for the Standard Specification results was 0.97 with a coefficient of variation of 0.03.

The LRFD Specifications [9] underestimated the moment capacity of the beams compared to the measured capacities, as seen in Fig. 2.6. The mean value of the predicted to measured moment capacities in the case of LRFD Specifications was 0.93 with a coefficient of variation of 0.06. When the modified LRFD procedure was used, the predicted moment capacities approached the measured values, with a mean value of 0.96 and a coefficient of variation of 0.04. As indicated in Table 2.1, there were three beams (G8, G27, G30) for which the LRFD Specifications indicated T-section behavior at ultimate moment capacity while the Standard Specifications and the strain compatibility analyses indicated rectangular section behavior. Modifying the LRFD procedure, as explained previously, resolved this inconsistency.

It should be noted that the data analyzed included beams with rectangular section behavior at ultimate moment capacity (i.e., depth of the compression block was within the flange) as well as beams with flanged section behavior. Even though the response of the sections that behaved as rectangular sections was accurately predicted by both the Standard [8] and LRFD Specifications [9] (i.e., error in T-beam definition does not come into play), these data were included for the sake of comparison. The computed values for mean and coefficient of variation in Table 2.1 also include the results of the beams with rectangular section behavior at ultimate bending moment.

The behavior type (rectangular versus T-section) can be distinguished by the symbols plotted in Figs. 2.6 and 2.7.

In Fig. 2.7, moment capacities predicted by the specifications subjected to the maximum reinforcement limit provisions (using Eqs. (2.10), (2.11), and (2.14)) are plotted against the measured moment values. As shown, the data points for sections with rectangular compression zones at ultimate moment capacity did not change as compared to Fig. 2.6. Because these beams were lightly-reinforced (reinforced with four wires), they were under-reinforced according to both the LRFD [9] and Standard Specifications [8], and were unaffected by the maximum reinforcement provisions.

The beams reinforced with eight wires were considered over-reinforced according to both specifications. Fig. 2.7 shows the safety margin that the specifications place on the computed moment capacity of the over-reinforced sections by limiting the maximum tensile reinforcement to be used in computing the moment capacity. In this case, the LRFD Specifications [9] still predict smaller capacities than the Standard Specifications [8]. On the other hand, moment capacities predicted by the Standard Specifications and the modified LRFD procedure for the over-reinforced beams were identical. This agreement in predicted values occurred, because when the β_1 factor used in the LRFD Specifications for the flange overhangs is removed, the equations used to compute the moment capacity of over-reinforced sections in the AASHTO LRFD and Standard Specifications (Eqs. (2.10) and (2.11)) become identical.

Comparison of Figs. 2.6 and 2.7 suggests that the maximum tensile reinforcement limits are inappropriate from the perspective of moment capacity prediction; the purpose of these limits is to compensate for lower ductility of sections with large amounts of tensile reinforcement.

2.5. Defining Maximum Reinforcement Limits

In order to investigate the relation between the maximum reinforcement limits according to the specifications and strain compatibility analyses, the Mn/DOT Type 63 section (see Fig. 2.3) was further studied. The number of prestressing strands was determined at the limit of over-reinforced behavior using the AASHTO Specifications and from the strain compatibility analyses. The criteria used in this study to determine the maximum number of strands from the strain compatibility analyses was a minimum total steel strain of 0.01 at the centroid of the strands at ultimate capacity. As explained earlier, similar values for strand strain at ultimate capacity were used previously by other researchers in order to define maximum reinforcement limits used in various design specifications [17,18,21].

The number of strands needed to make the Mn/DOT Type 63 section over-reinforced according to the Standard Specifications [8], LRFD Specifications [9], modified LRFD procedure, and the strain compatibility analyses are tabulated in Table 2.2 with the corresponding moment-curvature plots given in Fig. 2.8. The results indicate that the AASHTO LRFD Specifications are grossly conservative, and the limit according to the modified LRFD procedure is in best agreement with that from strain compatibility analysis.

The good agreement between the maximum reinforcement limit predicted by the modified LRFD procedure and that from strain compatibility analysis proves the accuracy of the modified LRFD

procedure in predicting not only the flexural response of prestressed concrete sections, but also the limit at which the section should be considered over-reinforced.

2.6. Verification of RESPONSE-2000 Results

As mentioned earlier, RESPONSE-2000 [66] was used to obtain the strain compatibility sectional analysis results used in the comparisons with the predictions by the LRFD Specifications. To verify the results obtained using RESPONSE-2000, a nonlinear sectional analysis code was developed in Mathcad [69]. A brief description of this sectional analysis code is given earlier in this chapter.

Fig. 2.9 provides a comparison of neutral axis depth, c, strand stress at nominal capacity, f_{ps}, and moment capacity, M_n, of the Mn/DOT Type 63 section, predicted by RESPONSE-2000 and the Mathcad code. As shown, results from the two methods agree well, especially for the neutral axis location and the nominal moment capacity.

The small discrepancy between the strand stress values predicted by RESPONSE-2000 and the Mathcad code is related to the maximum concrete compressive strain values used. When performing the analyses with RESPONSE-2000, the user does not have full control on the value of the top fiber concrete strain at failure; consequently, the point of failure as predicted by RESPONSE-2000 was not always clear. In some of the cases studied, the RESPONSE-2000 analyses stopped with very low top fiber concrete strain values (as low as $\varepsilon_c = 0.002$), whereas for the same cases, maximum top fiber strain values obtained from the Mathcad code were in excess of $\varepsilon_c = 0.003$.

As evident in Fig. 2.9, the difference in values for top fiber concrete strains at failure between REPONSE-2000 and the Mathcad code did not have a significant effect on the predicted neutral axis depth and the nominal moment capacity, and the results obtained using REPONSE-2000 can be used with confidence to make comparisons between the sectional responses predicted using the LRFD Specifications.

2.7. Summary and Recommendations

This chapter summarized the strain compatibility analyses of prestressed concrete sections with nonlinear material properties that were performed in order to identify the inconsistencies between the AASHTO LRFD [9] and AASHTO Standard Specifications [8] procedures, and to investigate the accuracy of both Specifications in predicting the flexural response of prestressed concrete sections. Sectional responses from strain compatibility analyses were compared to those predicted by the AASHTO LRFD Specifications, the AASHTO Standard Specifications, and a procedure obtained by modifying the equations in the AASHTO LRFD Specifications to rectify errors in the determination of the flange contribution.

Measured flexural strengths of prestressed concrete I-beams found in the literature were also used for comparison. A parametric study of the flexural behavior of non-rectangular sections was used to demonstrate the shortcomings of the AASHTO LRFD Specifications [9] in the determination of neutral axis depth and flexural capacity, as well as to present the improvements in accuracy of the proposed modifications.

Inconsistencies exist between the AASHTO LRFD [9] and AASHTO Standard Specifications [8] in predicting the response of reinforced and prestressed concrete sections that are nonrectangular because of two reasons: (a) selection of the neutral axis depth at which transition from rectangular section behavior to T-section behavior occurs, and (b) selection of the amount of the top flange overhang contribution to the internal compressive force. Because of the underestimation of the contribution of top flange overhangs, the AASHTO LRFD Specifications overestimate the neutral axis depth of T-sections compared to the AASHTO Standard Specifications and nonlinear strain compatibility analyses. Overestimation of the neutral axis depth according to the AASHTO LRFD Specifications leads to the section being considered as over-reinforced at reinforcement ratios for which the AASHTO Standard Specifications and the strain compatibility analyses indicate otherwise. The tendency to prematurely classify some sections as over-reinforced results in large differences in the moment capacities predicted by the AASHTO LRFD Specifications and the other methods.

It was determined that limiting the maximum amount of tensile reinforcement to be used in determination of the moment capacity, as used in the AASHTO LRFD [9] and Standard Specifications [8], is a means of providing an additional safety margin to account for the poor flexural ductility of sections with large amounts of tensile reinforcement. The provision in the AASHTO Standard Specifications yields similar maximum reinforcement limits as the strain compatibility analyses considering a limiting total prestressing steel strain of 0.01 at nominal capacity. Results of the AASHTO LRFD Specifications are grossly conservative compared to those of the Standard Specifications and the strain compatibility analyses.

The inconsistencies between the sectional response and the maximum reinforcement limits predicted by the AASHTO LRFD Specifications [9] and the other methods (AASHTO Standard Specifications [8] and the strain compatibility analyses) is reduced by modifying the procedure of the AASHTO LRFD Specifications by changing the T-section limit from $c = h_f$ to $a = h_f$. With this modification, the $\beta_1 h_f$ maximum limit for the depth of the top flange overhang contribution to the internal compressive force in the LRFD Specifications is automatically removed.

The procedure outlined in the AASHTO Standard Specifications [8] to determine the stress in the prestressing steel at ultimate moment does not take into account the effect of changes in the neutral axis location caused by changes in top flange depth. In this respect, the LRFD [9] procedure for strand stress provides more realistic estimation of strand stress. Thus, it is proposed that the LRFD strand stress relation be used with the modified procedure.

Based on the findings, it is recommended that the procedure currently used by the AASHTO LRFD Specifications [9] should be modified as explained above in order to more accurately predict the response of flanged prestressed concrete sections at ultimate capacity. This modification will also reduce the inconsistencies currently existing between the AASHTO LRFD and AASHTO Standard Specifications [8].

Validation of numerical results with experimental data was limited to small-scale flanged specimens tested by Hernandez [71] due to scarcity of data in the literature. There is a need for additional large-scale flexural tests on over-reinforced prestressed concrete flanged sections,

especially as more applications of untopped flanged cross sections with large amounts of prestressing strand may occur.

Table 2.1. Measured and Predicted Moment Capacities* [71].

Beam	Measured capacity	AASHTO Standard Specifications			AASHTO LRFD Specifications			Modified LRFD procedure			Strain compatibility analysis	
	M in-kips	c in.	ω_p	M in-kips	c in.	c/d_e	M in-kips	c in.	c/d_e	M in-kips	c in.	M in-kips
G1	296	2.2	0.15	287	2.2	0.21	287	2.2	0.21	287	2.1	294
G2	294	2.1	0.15	290	2.1	0.20	290	2.1	0.20	290	2.0	295
G3	420	8.2	0.59	405 (346)	7.6	0.75	365 (311)	6.9	0.68	391 (346)	6.1	438
G4	466	7.3	0.52	422 (368)	7.0	0.69	383 (331)	6.2	0.62	408 (368)	5.6	455
G8	296	2.9	0.20	270	3.2	0.31	263	2.9	0.28	271	2.6	281
G9	297	2.2	0.16	286	2.2	0.21	286	2.2	0.21	286	2.1	293
G11	295	2.2	0.16	285	2.3	0.22	285	2.3	0.22	285	2.1	292
G12	477	5.2	0.37	446 (409)	5.4	0.53	425 (381)	5.0	0.50	440 (409)	4.7	482
G16	438	5.8	0.41	432 (381)	5.8	0.57	411 (355)	5.5	0.54	425 (381)	5.2	469
G17	452	5.8	0.41	429 (377)	5.9	0.58	408 (351)	5.5	0.55	422 (376)	5.2	466
G18	297	2.4	0.17	282	2.4	0.23	282	2.4	0.23	282	2.2	290
G19	438	5.6	0.40	437 (389)	5.7	0.56	416 (363)	5.3	0.53	430 (383)	5.0	472
G22	484	5.3	0.38	462 (434)	5.6	0.55	426 (391)	4.9	0.48	451 (434)	4.5	495
G23	289	2.6	0.18	278	2.5	0.24	279	2.5	0.24	279	2.3	288
G24	473	6.5	0.46	442 (397)	6.4	0.63	403 (357)	5.7	0.56	429 (397)	5.1	475
G25	288	2.1	0.15	288	2.2	0.21	288	2.2	0.21	288	2.0	293
G27	512	2.9	0.19	525	3.0	0.30	512	2.8	0.28	526	2.7	542
G30	510	2.7	0.18	529	2.8	0.28	521	2.7	0.27	530	2.6	545
G31	469	4.9	0.35	452 (424)	5.1	0.50	432 (396)	4.7	0.47	446 (424)	4.5	486
G32	466	5.6	0.41	450 (416)	5.8	0.58	414 (375)	5.1	0.51	439 (416)	4.7	483
G37	472	4.8	0.34	459 (436)	5.0	0.49	440 (407)	4.6	0.46	454 (436)	4.4	493

* Shaded cells indicate beams with T-section behavior at ultimate. For over-reinforced sections, the moment capacity with no maximum reinforcement limit is reported followed in parentheses by the capacity with reinforcement limit imposed.

Table 2.2. Number of Strands that Makes Mn/DOT Type 63 Section Over-Reinforced.

Method	Over-reinforced section limit
AASHTO Standard Specifications	44 strands
AASHTO LRFD Specifications	38 strands
Modified LRFD Procedure	46 strands
Strain Compatibility Analysis	48 strands

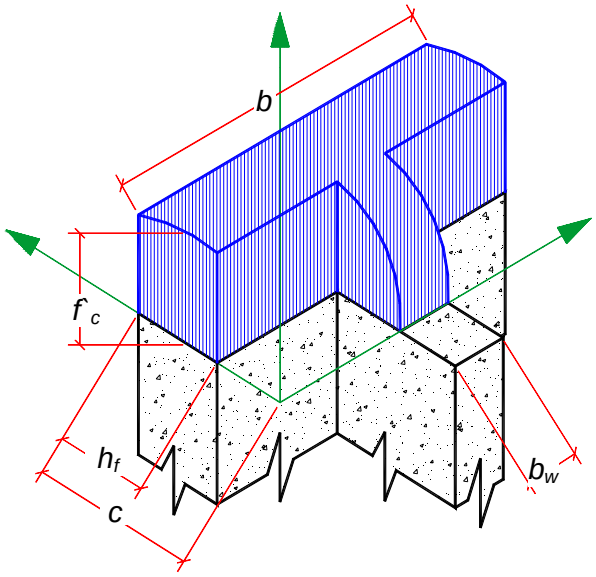

(a) Actual Nonlinear Stress Distribution

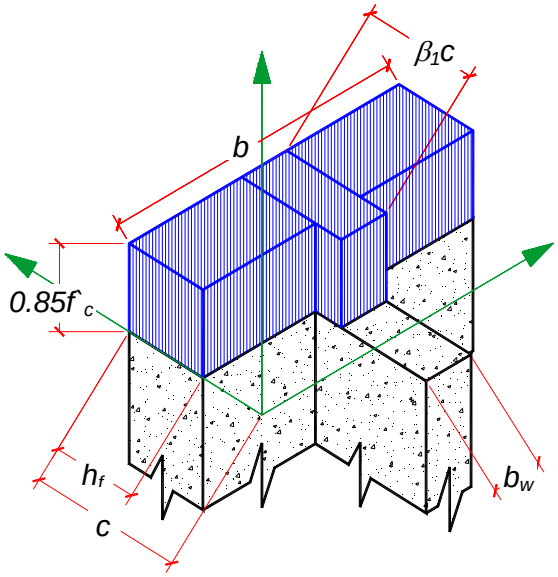

(b) AASHTO Standard Specifications

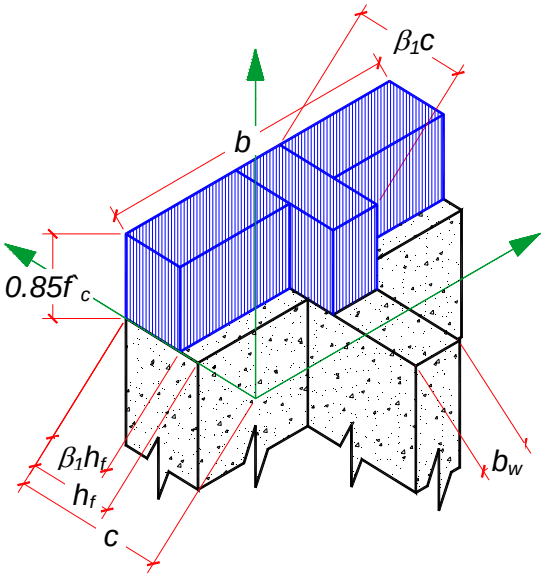

(c) AASHTO LRFD Specifications

Fig. 2.1. Compressive stress distributions for a T-section.

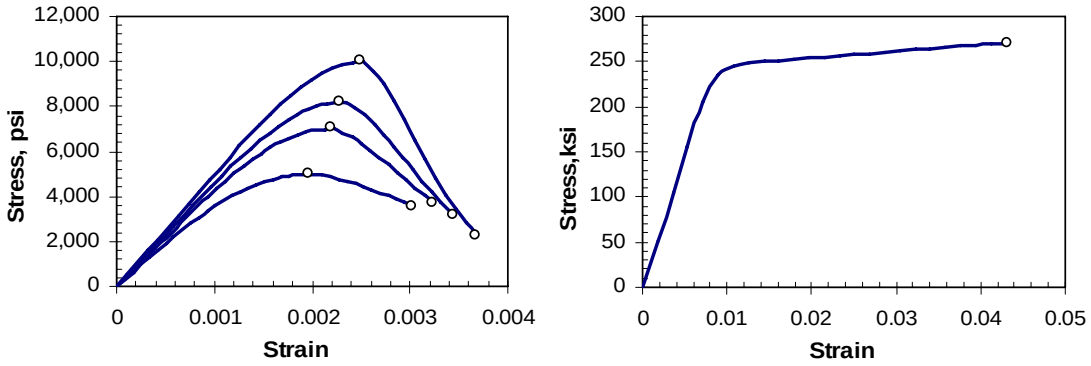

(a) Concrete (b) Steel

Fig. 2.2. Material stress-strain relations used in strain compatibility analyses.

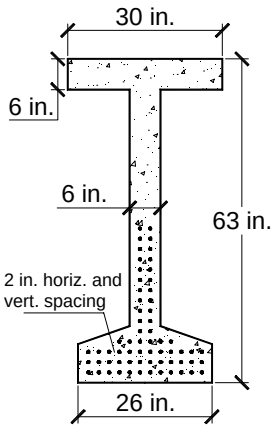

Fig. 2.3. Mn/DOT Type 63 section.

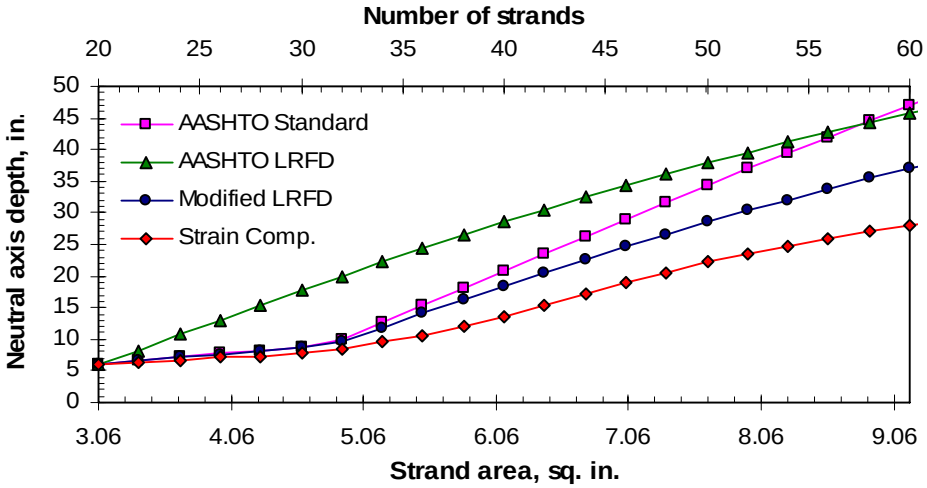

(a) Neutral axis depth, *c*.

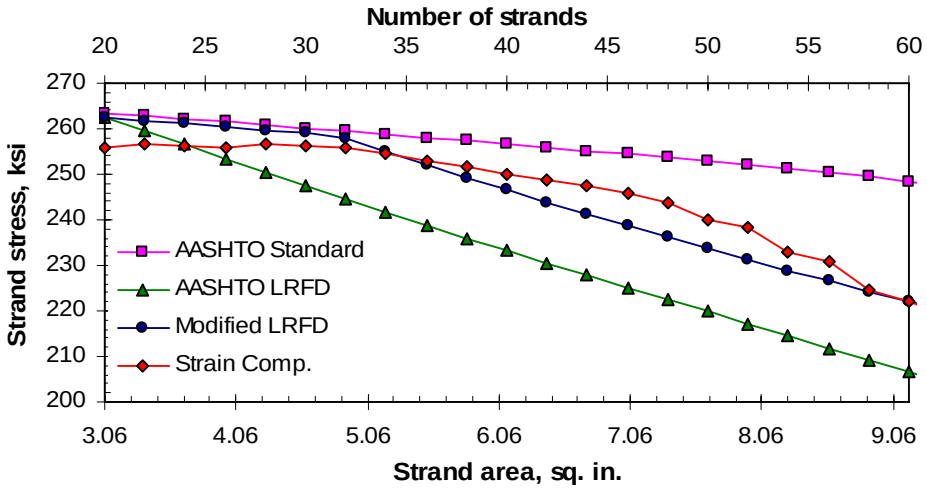

(b) Strand stress at nominal capacity, f_{ps}.

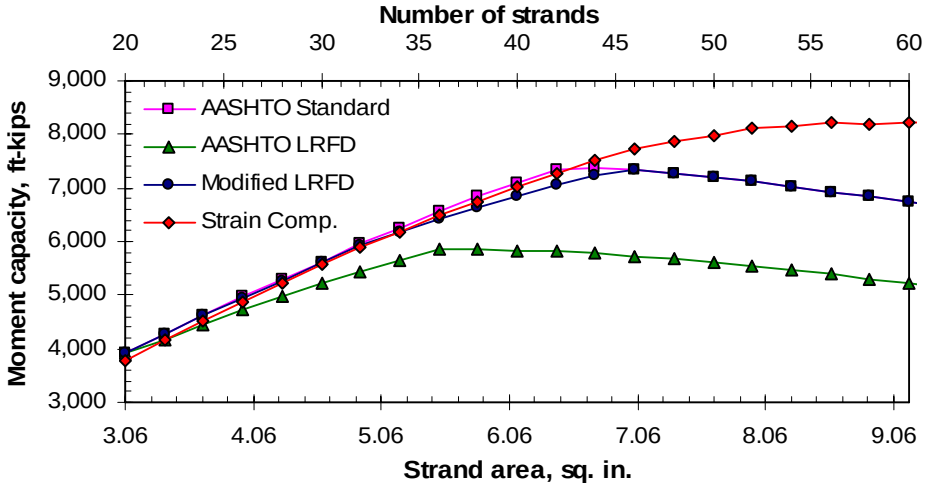

(c) Moment capacity, M_n.

Fig. 2.4. Variation in section response with amount of prestressing steel.

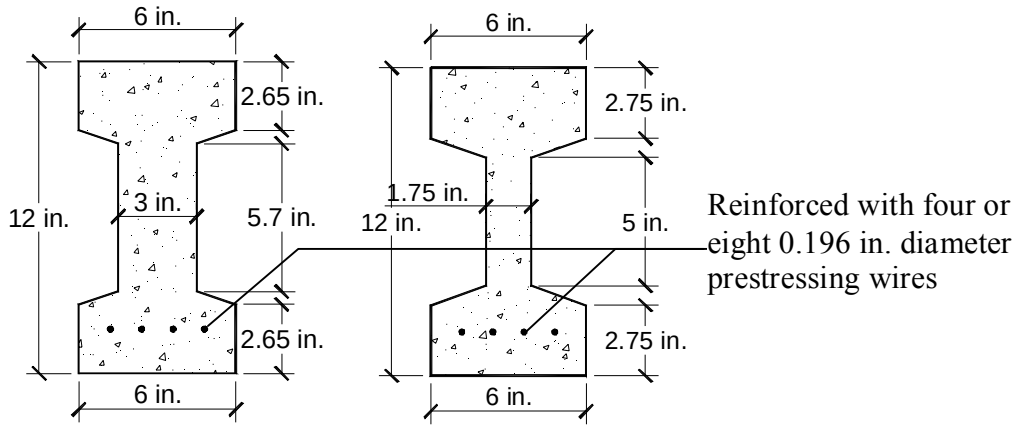

Fig. 2.5. Nominal dimensions of beam sections tested by Hernandez [71].

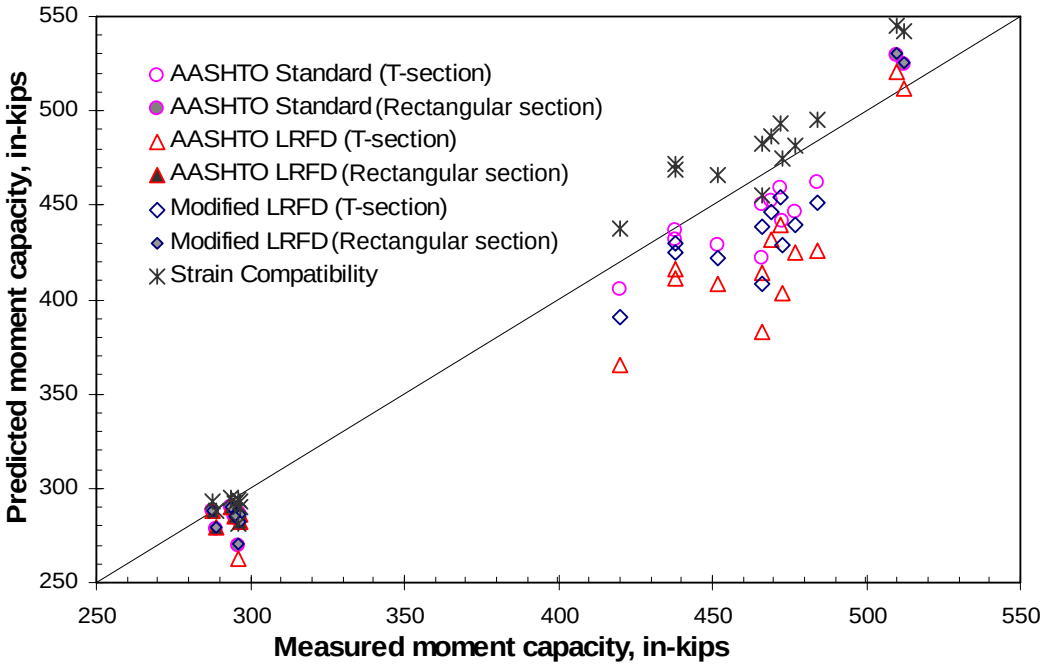

Fig. 2.6. Comparison of predicted and measured [71] moment capacities without maximum reinforcement limit.

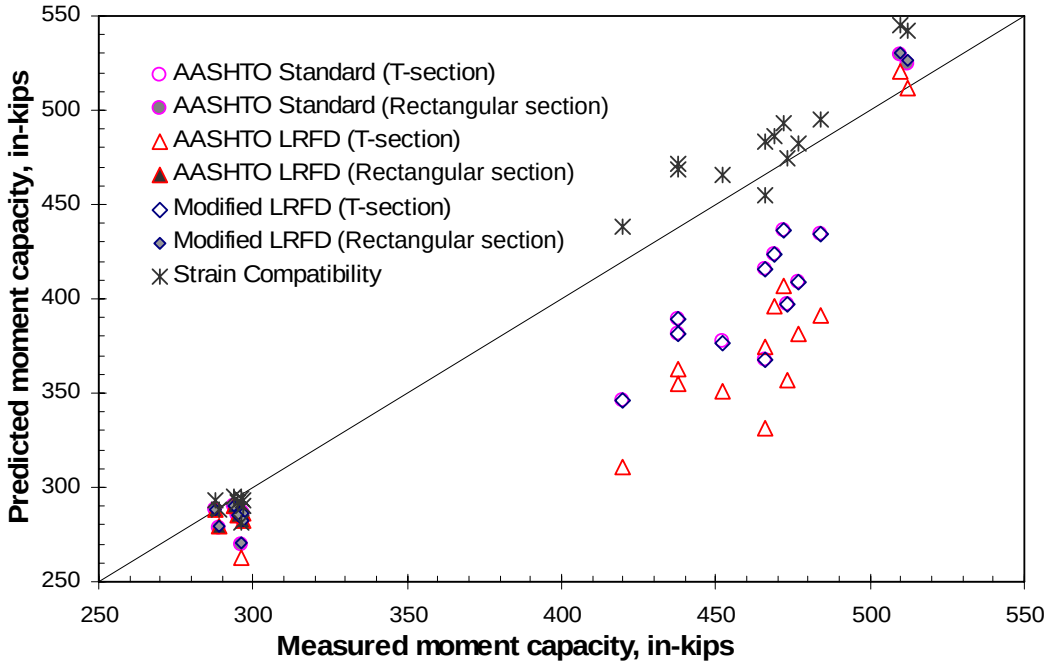

Fig. 2.7. Comparison of predicted and measured [71] moment capacities with maximum reinforcement limit imposed.

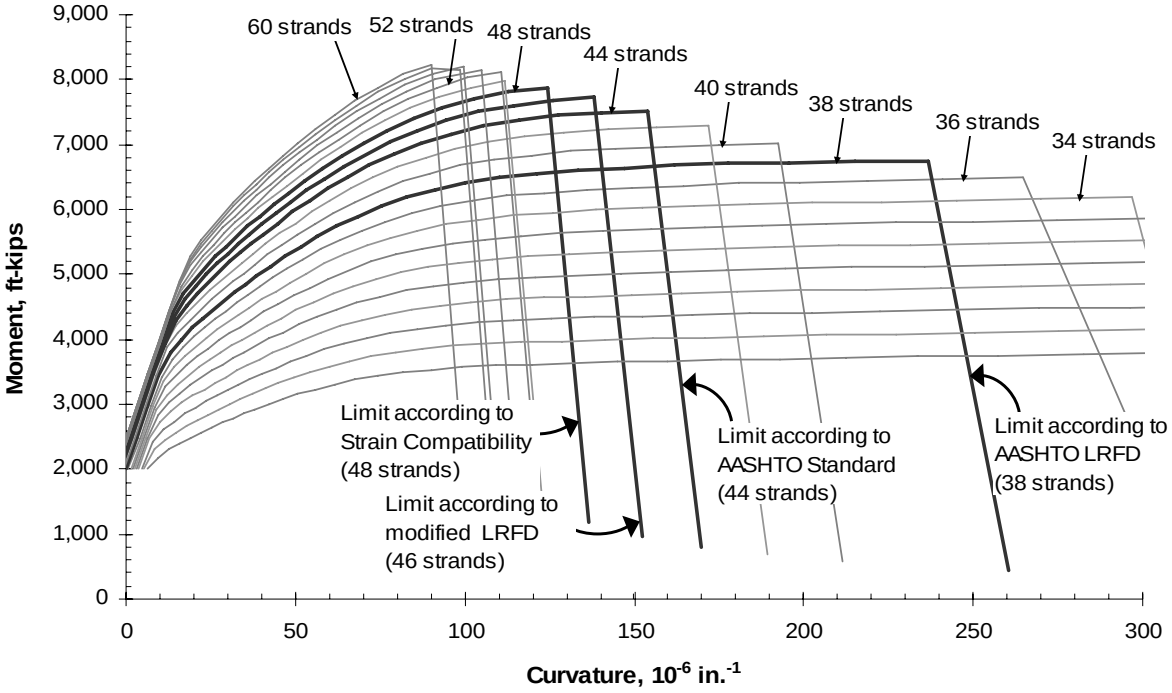

Fig. 2.8. Moment-curvature relations for Mn/DOT Type 63 section.

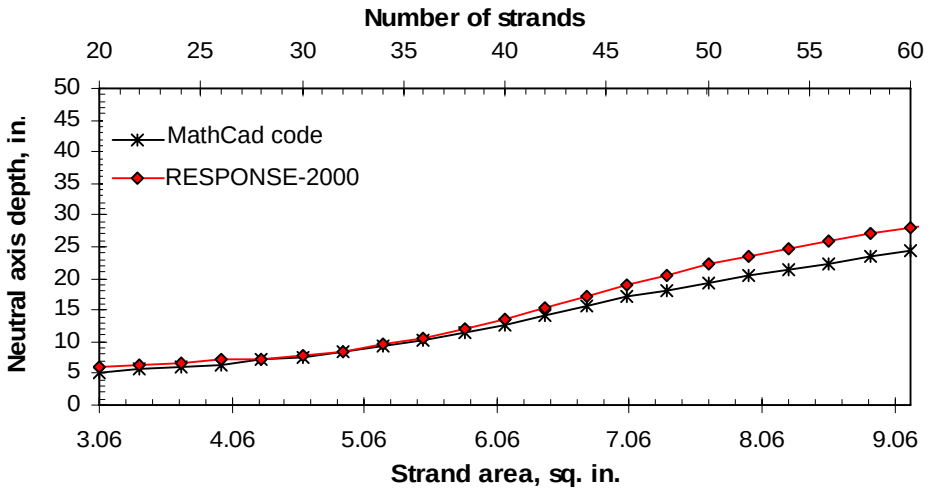

(a) Neutral axis depth, *c*.

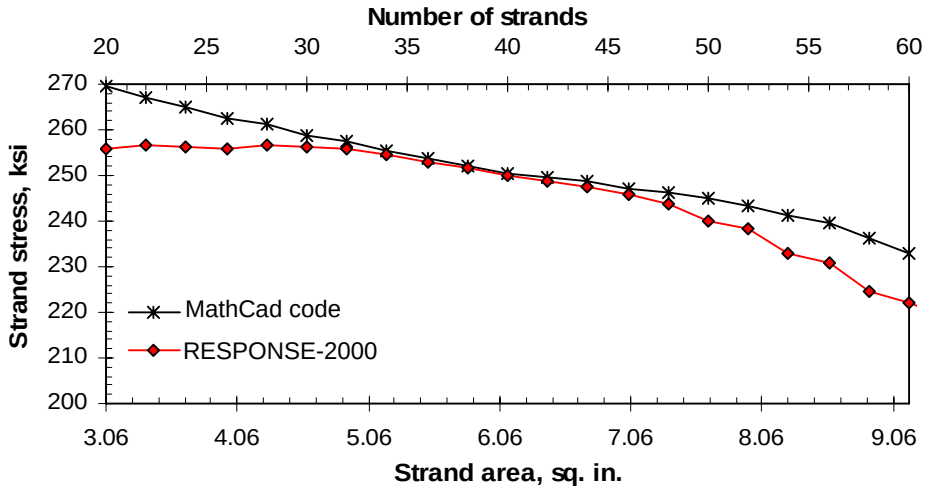

(b) Strand stress at nominal capacity, f_{ps}.

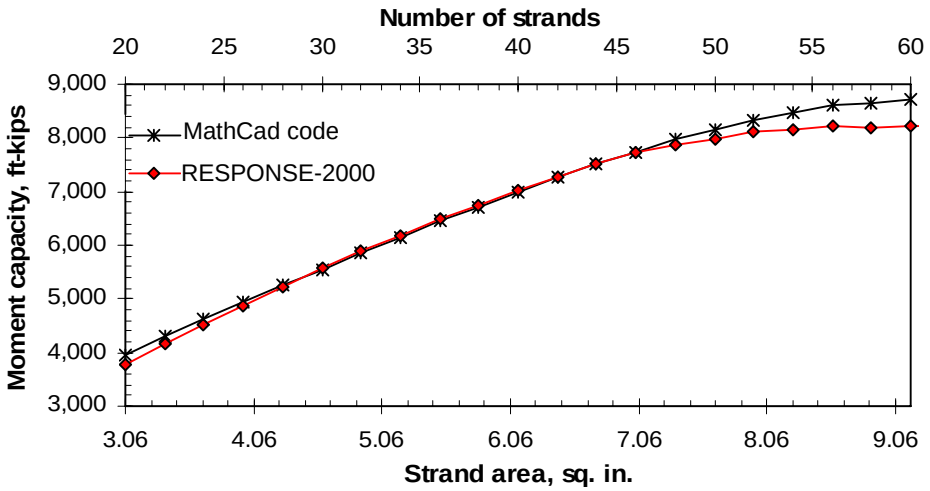

(c) Moment capacity, M_n.

Fig. 2.9. Comparison of section response predicted by RESPONSE-2000 and Mathcad code.

Chapter 3
Pull-Out Tests of Steel Inserts Embedded in Concrete

3.1. Introduction

As mentioned previously, in prestressed concrete through-girder pedestrian bridge construction used in the State of Minnesota, there is no connection between the deck and the prestressed concrete girders, and the only connection between the floor beams and the girders are through wire-formed steel inserts embedded in the girders. In these types of bridges, the connections between the girders and the floor beams are subjected to large forces during the transfer of the loads between the bridge components. As the only connection between the diaphragms and the girders is through these inserts, behavior of the bridge system under vertical and lateral loads is highly dependent on the behavior of the inserts. Moreover, failure of these connections would reduce the structural integrity of the bridge, which compromises the stability of the structure. Despite their important role in transferring loads between different components and keeping the bridge system together, currently there is limited information available on the behavior of cast-in-place wire-formed inserts.

Pullout tests were performed on various types of cast-in-place wire-formed as well as bolt inserts in order to investigate their behavior under circumstances observed in prestressed concrete through-girder pedestrian bridge girders [72]. Analysis and comparison of load and deformation capacities obtained from the tension tests were performed in an attempt to identify the effects of test variables on these quantities. Concrete breakout capacities measured for some of the specimens were also compared to the capacities predicted by the equations of ACI 318-05 Appendix D [49].

3.2. Description of Test Specimens

The experimental investigation consisted of pull-out tests of 32 specimens. Table 3.1 lists the test specimens and associated variables including the type of insert, the location and number of inserts, the presence of axial compression to represent the effect of prestress, and the presence of reinforcement. Each specimen is identified by a combination of letters and numbers, as defined in Fig. 3.1. For example, 2-RC-T-1-6 indicates the specimen that was fabricated in the cast #2 and that had a single thin-slab insert placed in the center of the specimen. This specimen also had longitudinal rods and 6-in. spaced stirrups, and was tested under 1 ksi axial compression stress.

Fig. 3.2 shows the specimen dimensions and placement of inserts and steel reinforcement in the specimens.

3.2.1. Test Variables

Types of Inserts

The four types of inserts tested in this study were: (1) loop insert, (2) thin-slab insert, (3) double-leg insert, and (4) bolt insert. Geometric details of the inserts are given in Fig. 3.3. The first three types of inserts were commercially available, while the bolt insert was fabricated specifically for the pull-out tests, and it consisted of a ¾ in. diameter A490 bolt, coupler, and washer.

Insert F-65 Type L represented a typical insert used in prestressed concrete bridge girders in the State of Minnesota. In addition to the one shown in Fig 3.3(a), there is another type of F-65 Type L insert that is used by the precasters in Minnesota. These two types of loop inserts have identical geometry, with the only difference being in the coupler part of the insert, which provided the connection between the loop wire of the insert and the connector rod. The loop insert included in the pull-out tests had an NC-threaded coupler, while the other type, not included in the pull-out tests, had a coil-type coupler.

The other three types of inserts shown in Figs 3.3(b), 3.3(c), and 3.3(d) represented potential alternatives for the loop-type insert. A criterion that all selected inserts met was the ability to be placed at required positions in the prestressed concrete girders between tensioned prestressing strands spaced at 2 in. on center.

Location and Number of Inserts

Fig. 3.4 shows a detail of a typical connection used in prestressed concrete through-girder construction. As seen, at each floor beam-girder connection location there were six wire-formed inserts, two of which were in the flange and four of which were in the web of the girder. The testing program included inserts placed at the center of the specimen (center-insert specimens) and inserts placed closer to an edge of the specimen (edge-insert specimens). The center-insert specimens were intended to represent the inserts placed in the web of the girder, and inserts placed closer to an edge (edge-insert specimens) were intended to represent the inserts in the bottom flange of the girder. Some of the specimens contained two inserts to investigate the interaction among the failure area of individual inserts.

In the center-insert specimens shown in Fig. 3.2, the inserts were placed at the center of a 20 in. wide concrete block. The specimen width of 20 in. provided 10 in. of distance on either side of the insert to reduce edge effects. The minimum edge distance of 10 in. used in center-insert specimens corresponded to 2.6 to 3.2 times the embedment depth of the four types of inserts used.

The edge-insert specimens had a nominal width of 13.75 in. with the inserts placed at 3.75 in. from the edge of the specimen. The 3.75 in. side distance was used in the edge-insert specimens to approximate the side distance of the inserts embedded in the bottom flange of the prestressed concrete girders used in through-girder construction.

In the double-insert specimens, the inserts were spaced at either 6 or 4 in. on center depending on whether it was a center- or edge-insert specimen. In the double center-insert specimens, a 6-in. insert spacing was used, as this was the spacing between inserts placed in the web of prestressed concrete girders used in through-girder pedestrian bridges. The double edge-insert specimens included 4 in. spaced inserts, as the inserts placed in bottom flange of girders had a 4-in. spacing.

Presence of Axial Compression

The objective of the experiments was to evaluate the behavior of inserts under typical circumstances present in prestressed concrete girders used in through-girder pedestrian bridges. In a typical design, a net compressive stress exists in the bottom flange of such girders. No

studies could be found in the literature regarding the effect, if any, of axial compression on the behavior of embedded inserts.

In this study, compressive stress due to prestress was simulated by a hydraulic testing machine that applied an external axial compressive load to the specimens. As shown in Table 3.1, the majority of the specimens were tested under 1 ksi of axial compressive stress. There were also some specimens tested under 2 ksi compressive stress, as well as others with no axial compression. Considering that the compressive stress at insert locations in a typical prestressed concrete girder in a through-girder pedestrian bridge under the self-weight of the bridge was determined to be between 1.2 and 2.5 ksi, the compressive stress levels used in the tests were representative of those expected in bridges under service loads.

Presence of Reinforcement

In an attempt to simulate the restraining effect that the prestressing strands and transverse reinforcement might have on the behavior of inserts placed in bridge girders, both longitudinal and transverse reinforcement were incorporated into some of the specimens.

The dowel action provided by prestressing strands in a prestressed concrete girder were simulated through ½ in. diameter steel threaded rods that were wrapped in tape and greased to prevent bonding with the surrounding concrete. This enabled the rods to remain unstressed when the effect of prestress was imposed on the test specimens through the application of the external compressive load, as described above. Washers and nuts were placed at the ends of the threaded rods to provide anchorage to concrete so that the dowel action of the rods could be obtained when the tension load on the inserts was transferred to these rods. Fig. 3.5 shows the placement of inserts and reinforcement in the casting forms for the edge-insert specimens.

The location of the longitudinal rods in the center-insert and edge-insert specimens was different as shown in Fig. 3.2, to represent the different strand configurations of the girder web and bottom flange. In the center-insert specimens, the rods were placed in two layers 2 and 4 in. away from the surface of the specimen (Figs. 3.2(b) and 3.2(c)). In the edge-insert specimens, the location of the longitudinal rods was determined based on the relative location of prestressing strands with respect to the top surface of the bottom flange in the prestressed concrete I-girders (Figs. 3.2(d) and 3.2(e)). In the edge-insert specimens with thin-slab inserts, the position of one of the longitudinal rods was modified slightly to position the inserts between the rods.

Transverse reinforcement was provided by No. 4 stirrups. The majority of the specimens had stirrups spaced at 6 in., the typical stirrup spacing used in the vicinity of inserts in through-girder pedestrian bridges in Minnesota. To investigate the influence of the presence and spacing of stirrups, some of the specimens were tested with stirrups at a 4-in. spacing while others were tested without stirrups.

In the remainder of this chapter when the term “reinforced specimen” is used, it refers to the specimens that had both longitudinal rods and stirrups, while the term “unreinforced specimen” refers to the specimens with neither longitudinal rods nor stirrups.

3.2.2. Material Properties

The specimens were fabricated in two separate casts at the Structural Engineering Laboratory of the Department of Civil Engineering at the University of Minnesota using commercial ready-mixed concrete. The designation used for each beam indicates whether the specimen was fabricated in the first or second cast (i.e., "1" denotes first cast, "2" denotes second cast).

The concrete strengths were determined as the average of three 4x8 in. cylinders. The 28-day compressive strengths, f_c', were found to be 9200 psi for the first cast and 8600 psi for the second cast. The 28-day split cylinder strengths, f_{ct}, were 660 and 580 psi for the first and second casts, respectively. The concrete strengths in both casts were fairly representative of those used in typical prestressed concrete bridge girders.

At the time of load tests, the ages of the first-cast specimens were between 139 and 148 days, while the second-cast specimens were tested at ages between 34 and 80 days. Fig. 3.6 shows the change of concrete compressive strength with time, for concrete cylinders from both casts. Because the second-cast specimens were subjected to load tests at early ages, the strengths were determined more frequently for the second cast. Measured splitting strength values are tabulated in Fig. 3.6.

The concrete compressive strength at the time of load testing of specimens was between 10,600 and 10,800 psi (approximately 2 percent difference) for the first-cast specimens and between 9200 and 9500 psi (approximately 3 percent difference) for the second-cast specimens. The small variation in concrete strengths of specimens belonging to the same cast enabled direct comparison of behavior among the same-cast specimens.

3.3. Test Setup, Instrumentation, and Testing

The pull-out test setup shown in Fig. 3.7 was different from that prescribed by ASTM E-488 for tensile anchor tests [73]. In the conventional setup, the load is applied to the anchor by a hydraulic jack that reacts against the specimen through a circular steel reaction ring or a reaction assembly made up of steel sections. In this type of setup, compression struts between the anchor and reaction points on the surface of the specimen might influence the anchor behavior. To eliminate such interaction, the reaction points should be located outside the expected concrete failure area.

The setup used in this study was a modified form of the setup recommended by ASTM E-488 [73] for cyclic tension testing of anchors. In the configuration used in this study, the specimens were placed in a 600-kip capacity MTS universal testing machine. As shown in Fig. 3.7, the axial compression force was applied to the specimen by the testing machine through steel I-sections placed below and above the specimen. Tension load from a horizontally-positioned 77-kip capacity hydraulic actuator was transferred to the insert through a 3/4 in. diameter high-strength steel threaded rod. For the case of double-insert specimens, the tension load was first transferred from the hydraulic actuator to a steel plate through a steel threaded rod, and then transferred to the inserts through two steel threaded rod.

The specimen was supported along the back of the top and bottom surfaces by three 7/8 in. diameter high strength steel threaded rods, which were embedded in the concrete and reacted

against the steel I-sections above and below the specimens. The 7/8 in. diameter threaded rods used to support the specimens were placed behind the inserts, therefore they did not influence the behavior of the inserts.

A detail of the connection used at the top and bottom of the specimens is shown in Fig. 3.7(b). The adapter plates shown in the figure transferred the compression force applied by the testing machine head directly to the concrete while the longitudinal rods representing the dowel effects of the prestressing strands remained stress-free. As mentioned earlier, bond between the longitudinal rods and the concrete was prevented for this purpose, and steel nuts were placed at both ends of the longitudinal rods to prevent slipping of the rods inside the concrete when the inserts were pulled-out during load tests.

Linear Variable Differential Transformers (LVDTs) were used to monitor the insert displacements as well as the displacement of the front and back faces of the concrete blocks. Deformation of the insert was determined by measuring the movement of a point that was approximately 1 in. away from the front face of the specimen on the threaded rod that transferred the tensile load from the hydraulic actuator to the inserts. Location of the point from which the insert displacements were measured is indicated in Fig. 3.7(a). Displacement of this point on the threaded rod was measured relative to a fixed point on the laboratory floor. Displacements recorded by the LVDTs placed at the back face of the specimen were used to correct the insert displacements for tilting of the specimen. Tilting of the specimens during pull-out tests occurred because the bottom of the specimens were connected to the laboratory floor while the top of the specimens were restrained by the head of the 600-kip testing machine, which had finite stiffness. The magnitude of deflections due to tilting of the specimens remained significantly small as compared to the measured insert displacements for all specimens.

Strain gages were placed on the surfaces of two specimens (1-UC-T-0-N and 1-RC-T-1-6) prior to load tests in order to determine whether the distribution of compressive strain in the cross section of the specimens was uniform. The gages were placed on two sides of the specimen with two gages on each side. Strains measured from these gages indicated a uniform compression of the concrete blocks was achieved during the initial application of axial compression load.

Four of the specimens (2-RC-L-1-6, 2-RC-T-1-6, 2-RC-D-1-6, and 2-RC-B-1-6) also had strain gages placed on the longitudinal rods and stirrups near the insert location. As indicated in Fig. 3.8, one strain gage was placed on the top surface of each rod and stirrup. Data from these gages were used to determine the extent to which the longitudinal rods and stirrups were engaged in the load carrying mechanism for each type of insert.

The specimens were also whitewashed with a mixture of lime and water to facilitate visual detection of the cracks during load testing.

The testing sequence included two loading phases. In the first phase, a compressive axial load was applied to the test specimen with the 600-kip capacity universal testing machine operated in force-controlled mode, except for the specimens tested with no axial compression. The vertical load was applied over a span of 5 minutes. After reaching the full load, the loading was paused,

and the amount of vertical load on the specimen was held constant during the second loading phase.

The second loading phase consisted of application of tension load to the insert using the horizontally-positioned 77-kip capacity hydraulic actuator in displacement-controlled mode. A typical loading rate of 0.0833 in./min. was used during this phase of loading until failure of the specimen. During the tests, careful visual inspection of the specimens was conducted to monitor development of surface cracking.

3.4. Test Results

3.4.1. Failure Modes

The failure mode for each specimen is identified in Table 3.2 as either "concrete," "steel," or "weld" type failure. In all but the loop-type insert tests, the specimens experienced concrete failures. Steel failures were observed with many of the loop-type inserts. The common feature of all modes of failure was the formation of radial cracks in the majority of the specimens, which began at the insert location and propagated outwards on the front face of the specimens.

3.4.1.1. Steel and Weld Failure

As indicated in Table 3.2, steel failure occurred in six of the eleven specimens with loop-type inserts (Specimens 1-UC-L-0-N, 1-RC-L-1-6, 2-RC-L-1-6, 2-RC-L-2-6, 2-RE-L-2-6, and 2-RE-L-1-4). In five of these specimens two legs of the loop insert ruptured at the corner locations as shown in Fig. 3.9(a). In the sixth of these specimens, 2-RE-L-1-4, a combination of steel and weld failure occurred. One of the two loop inserts in Specimen 2-RCD-L-1-6 experienced weld failure at the locations where the legs connected to the coupler part of the insert.

In the remaining four specimens with loop-type inserts (Specimens 2-UC-L-0-N, 2-RE-L-1-6, 2-RE-L-0-4, and 2-RED-L-1-6), failure was due to concrete breakout without fracture of the insert itself. However, the loop inserts in these specimens experienced substantial plastic deformation, including necking of the legs, prior to concrete breakout failure.

All specimens with loop-type inserts exhibited considerable ductility prior to failure as compared to rest of the specimens tested. This was attributed to large plastic deformation, and in some cases, fracture of the inserts occurring in these specimens.

Fig. 3.10 shows typical concrete breakout patterns observed in specimens exhibiting steel failure. In these specimens, there was relatively minor damage to the concrete with little or no breakout of concrete cover.

3.4.1.2. Concrete Failure

Specimens with thin-slab, double-leg, or bolt-type inserts experienced concrete failure, as indicated in Table 3.2. These specimens exhibited more brittle behavior than the loop-type insert specimens. Figs. 3.9(b), 3.9(c), and 3.9(d) show typical deformation patterns for these inserts when placed in reinforced specimens. As shown, these inserts also underwent some degree of plastic deformation, but no necking or fracture of the steel was observed, which was the case with the loop-type inserts (see Fig. 3.9(a)).

Specimens that experienced concrete failures exhibited different types of behavior depending on whether or not the specimen was reinforced and the insert location (i.e., center versus edge). These factors affected the load and deformation capacity of inserts, as wells as the concrete failure pattern. In general, failure of unreinforced specimens was characterized by either a regular concrete cone breakout or concrete breakout with radial cracking. Fig. 3.11 shows examples of these two cases.

In the case of reinforced center-insert specimens, concrete breakout occurred with irregularly-shaped failure areas, as shown in Fig. 3.12. In Specimen 1-RC-B-1-6 (Fig. 3.12(b)), splitting of the entire front face of the specimen occurred. In general, concrete breakout depths observed in these specimens were smaller than those observed in unreinforced center-insert specimens. Due to the restraining effects of longitudinal rods, the inserts in these specimens experienced more inelastic deformation than the inserts in unreinforced center-insert specimens. As a result, these specimens exhibited more ductile behavior with larger force capacity than unreinforced center-insert specimens.

Fig. 3.13 illustrates the two distinct concrete breakout patterns observed with edge-insert test specimens. The limited edge distances used in these specimens resulted in concrete edge breakout failures. Some of the specimens in this group exhibited shallow breakout cones (Fig. 3.13(a)), while others exhibited more regular breakout cones (Fig. 3.13(b)).

3.4.1.3. Internal Steel Strains

As mentioned earlier, longitudinal rods and stirrups in the second-cast reinforced center-insert specimens were instrumented with strain gages during fabrication. Strains measured by these gages during the load tests are plotted in Fig. 3.14. For each specimen, strains from one strain gage placed on a stirrup and one placed on a longitudinal rod in the vicinity of inserts were included in the plots.

The reason that the strain gages in Specimen 2-RC-L-1-6 (Fig. 3.14(a)) measured smaller strain values than those in the other three specimens was related to the load carrying mechanism of the loop insert. In Specimens 2-RC-T-1-6, 2-RC-D-1-6, and 2-RC-B-1-6, (Figs. 3.14(b), 3.14(c), and 3.14(d)), part of the forces generated by the inserts were transferred to the longitudinal rods, which were themselves restrained by stirrups, thus causing large tensile strains in these elements at the strain gage locations.

In Specimen 2-RC-L-1-6 (see Fig. 3.14(a)), on the other hand, because of the geometry of the loop insert, there was no direct transfer of load from the insert to the longitudinal rods or the stirrups, which resulted in smaller measured steel strains in this specimen.

As shown in Fig. 3.14, in all four specimens, load versus strain plots for stirrups showed a change in the initial slope at some values of applied load. After the slope change, the stirrup strains increased at a higher rate. The increase in the rate of change of stirrup strains was due to the formation of cracks crossing the stirrups.

The fact that the initiation of cracking was always evident in the stirrup strain measurements, and not in the strains measured on the longitudinal rods might be coincidence that the first cracks

always crossed the stirrups, and not the longitudinal rods. Even though the orientation of the first visual cracks observed during the testing of specimens was arbitrary, the likelihood of these cracks being vertical (crossing the stirrups) is higher due to the existence of vertical axial compressive stresses applied on the specimens. Another reason might be the fact that the longitudinal rods were de-bonded from the surrounding concrete, so the initiation of cracks in the concrete at the gage locations did not cause nearly as much appreciable additional strain in the rods as in the stirrups.

The loads at crack initiation determined using the point of divergence in load versus steel strain plots are identified in Fig. 3.14. The load at crack initiation for Specimens 2-RC-L-1-6, 2-RC-T-1-6, 2-RC-D-1-6, and 2-RC-B-1-6 were 5.2, 8.1, 10.4, and 13.9 kips, respectively. During load testing, radial cracks beginning at the insert location and propagating outwards on the front face of specimens were visually detected at loads of 16 and 30 kips in Specimens 2-RC-T-1-6 and 2-RC-B-1-6, respectively. No radial cracking was visually detected in Specimens 2-RC-L-1-6 and 2-RC-D-1-6.

The cracking load levels determined from the internal steel strains were consistent with observations reported earlier by Stone and Carino [74]. They used the results from testing two large-scale headed insert specimens, heavily instrumented with internal concrete strain gages, to determine the formation and propagation of internal cracking during the pull-out tests. Circumferential cracking was determined to begin near the bottom of the inserts at load levels that were 25 to 35 percent of the ultimate load. It was also reported that radial cracking began at lower load levels.

3.4.2. Load-Deflection Behavior

The load-deflection responses of the specimens obtained during the load tests were evaluated with respect to several variables, such as insert type, insert location, and presence of reinforcement. The load values used in the plots were the tensile loads applied to the inserts by the laterally-positioned hydraulic actuator. The displacement values shown in the plots represent the horizontal movement of the insert as measured by the LVDTs located approximately 1 in. away from the front face of the specimen on the rod transferring the load from hydraulic actuator to the insert (see Fig. 3.7(a)). As mentioned earlier, the insert displacements were corrected for any tilting or movement of specimens using the displacement measurements taken on the back side of the specimen.

3.4.2.1. Unreinforced Specimens

The load-deflection responses of the unreinforced specimens tested with no axial compression are given in Figs. 3.15(a)-3.15(d). Pictures of the specimens and the inserts following the load tests are inset in the plots. There were a total of eight specimens in this group, and the plots are arranged with respect to the insert type. For each insert type, there were two repeat specimens, one of them from the first cast and the other from the second cast. The value of the maximum load carried by each specimen is given in Table 3.2.

As mentioned earlier, there were differences in the measured concrete properties (compressive and split tensile strengths) between the two casts. The deviations observed between the response

of the first cast and the repeat (second cast) specimens were attributed to these differences in concrete strengths.

Splitting tensile strengths of the concrete used in the first cast were as much as 24 percent higher than the tensile strengths of the second cast, while the difference in the measured concrete compressive strengths of specimens from the first and second casts was between 13 and 17 percent. For the three types of inserts that resulted in concrete failure (i.e., thin-slab, double-leg, and bolt-type inserts), specimens from the first cast had larger load capacities than those from the second cast. The ratio of load capacities of the first cast and second cast specimens were 1.13, 1.39 and 1.21, respectively, for thin-slab, double-leg, and bolt-type inserts.

As shown in the plots, specimens with the loop-type insert (Fig. 3.15(a)) exhibited ductile behavior as a result of substantial plastic deformation (necking at several locations on the loop). Indeed, failure of Specimen 1-UC-L-0-N was due to fracture of the insert legs, as shown in the inset. The maximum loads attained by these two specimens were very similar, even though some difference can be observed in the load-deflection plots in early stages of loading.

Different from the loop inserts (Fig. 3.15(a)), the behavior of the thin-slab, double-leg, and bolt-type inserts, as shown in Figs. 3.15(b)-3.15(d), was brittle. These specimens failed shortly after reaching their maximum loads due to the concrete breakout failure before the inserts achieved substantial plastic deformation.

3.4.2.2. Reinforced Center-Insert Specimens

The results of the reinforced specimens tested under 1 ksi axial compressive stress are given in Figs. 3.16(a)-3.16(d). There were small differences between the load-deflection plots of the repeat specimens, even though the general behavior was the same. The scale difference between the plots in Fig. 3.16 and those in Fig. 3.15 should also be noted.

Similar to the unreinforced specimens, first cast specimens had larger load capacities than the second cast specimens for the three types of inserts that resulted in concrete failure (i.e., thin-slab, double-leg, and bolt-type inserts), which was attributed to the difference in concrete strengths between the two casts. The ratio of load capacities of the first-cast and second-cast specimens were 1.21, 1.12, and 1.03, respectively for thin-slab insert, double-leg insert, and bolt insert.

A comparison of reinforced and unreinforced specimens is shown in Figs. 3.17(a)-3.17(d). For each insert type, results from two unreinforced specimens tested with no axial load and two reinforced specimens with an axial compressive stress of 1 ksi are shown in the figure.

As noted earlier, the concrete strengths measured at the time of load testing of specimens differed by 2 percent among the first-cast specimens and by 3 percent among the second-cast specimens. As a result, the effect of concrete strength on the difference in specimen behavior from the same cast remained minimal.

The influence of reinforcement and axial compression is clearly evident for specimens with thin-slab and bolt-type inserts in Figure 3.17. For these specimens, the presence of reinforcement and

axial compression resulted in major increases in the load capacity as well as improvements in ductility. As shown in Figs. 3.17(b) and 3.17(d), the improvement in ductility is more pronounced for the thin-slab insert specimens, while the increase in load capacity is larger for the bolt insert specimens. The average increase in load capacity was 54 percent in the case of the thin-slab insert and 123 percent in the case of the bolt-type insert.

The increases in load capacity and ductility were attributed to two reasons. Part of the improvement was attributed to the restraining effect provided by the longitudinal rods and stirrups, which caused the inserts to undergo large plastic deformations. The presence of longitudinal rods and stirrups also resulted in a larger area of concrete breakout, which increased the load capacity of the inserts. The second possible reason for the increase in insert capacity was due to the axial compression, which delayed the concrete cracking in the direction perpendicular to the axial compression.

The reason that the double-leg inserts were not influenced by the restraining effects of the longitudinal rods and stirrups as much as the thin-slab and bolt-type inserts was probably due to relatively smaller flexural stiffness of the insert legs for the case of the double-leg inserts.

Specimens with loop-type inserts showed similar behavior irrespective of whether or not there was reinforcement and axial compression. As mentioned earlier, with loop-type inserts, the behavior of the specimens was mainly controlled by the plastic deformation of the insert itself. As a result, including reinforcement and axial compression did not have a major effect on the behavior of the specimen. As indicated in Fig. 3.17(a), three of the specimens with loop-type inserts exhibited steel failure, meaning fracture of the inserts. Even though the fourth specimen exhibited concrete failure, substantial plastic deformation of the insert, including pronounced necking of the legs, was observed prior to failure.

Interaction of Multiple Inserts

The effect of the interaction of inserts is presented in Figs. 3.18(a) and 3.18(b), respectively, for the loop and thin-slab inserts. Each plot includes results from one single-insert specimen and one double-insert specimen, both of which were reinforced specimens and tested under 1 ksi axial compressive stress. Only the results from the specimens fabricated in the second cast are included in these plots, even though the similar results were obtained from the first-cast specimens. In this manner, the effect of any difference in concrete properties is minimized.

In the case of the loop insert, the addition of the second insert doubled the load capacity of the single-insert specimen (see Fig. 3.18(a)). This is because of the fact that for both the single-insert and double-insert specimens, failure mode of the specimens was not concrete failure. As indicated in the plot, in the double-insert specimen, premature failure of one of the inserts occurred due to weld fracture, while the failure mode in the single-insert specimen was steel failure.

In contrast to the loop inserts, the thin-slab inserts spaced at 6 in. distance were observed to interact with each other (see Fig. 3.18(b)). The load capacity of the specimen with two thin-slab inserts was determined to be only 46 percent larger than the capacity of the single-insert specimen. This was not an unexpected result, because with thin-slab inserts, failure of the

specimens was due to concrete cone breakout, and interaction of failure cones would occur if there was insufficient spacing between the inserts.

In addition to an increase in load capacity, Specimen 2-RCD-T-1-6 had different overall behavior than Specimen 2-RC-T-1-6, as shown in Fig. 3.18(b). The photographs of the failed specimens shown in Fig. 3.19 help to explain this difference. As shown in Fig. 3.19(b), there was extensive cracking of the double-insert specimen, Specimen 2-RCD-T-1-6, immediately before failure. In Specimen 2-RC-T-1-6, on the other hand, only moderate cracking with almost no radial cracks developed before failure (see Fig. 3.19(a)).

The extensive damage that occurred in Specimen 2-RCD-T-1-6 as compared to Specimen 2-RC-T-1-6 resulted in a drop in the load-carrying ability of the specimen after reaching the maximum load. On the other hand, Specimen 2-RC-T-1-6 exhibited a stable behavior after reaching the maximum load, as this specimen developed only moderate damage while reaching the maximum load.

Influence of Axial Compression

The effect of increasing the axial compressive stress from 1 to 2 ksi on the load-deflection behavior of the loop and thin-slab inserts fabricated in the second cast is shown in Figs. 3.20(a) and 3.20(b), respectively. Doubling the amount of axial compression caused a slight increase in load capacity of the specimens. The increase in load capacity was 26 percent for the loop insert and 11 percent for the thin-slab insert. For the loop inserts, as the behavior was mostly governed by the deformation and failure of the insert, increase in friction between the insert and the surrounding concrete was the likely reason for the increase in capacity with increasing axial compression.

The difference in failure mode may be the reason that the increase in load capacity was less for the thin-slab insert (concrete failure) compared to that of the loop insert specimen (steel failure). Following the formation of the concrete breakout cone in Specimens 2-RC-T-1-6 and 2-RC-T-2-6, the load carrying mechanism was through the inserts reacting against the longitudinal rods. In this mechanism, any increase in friction between the inserts and the surrounding concrete due to the increased axial compressive stress on the specimen would not affect the load capacity. In the case of the loop inserts, on the other hand, the increase in friction resulted in an increase in load capacity, as there was no concrete breakout in Specimen 2-RC-L-2-6 (Fig. 3.20(a)).

3.4.2.3. Reinforced Edge-Insert Specimens

The effects of insert type on the behavior of specimens with limited edge distance are shown in Fig. 3.21. The figure shows the results for the four types of inserts tested with 1 ksi axial compressive stress and with stirrups spaced at 6 in. The general behavior of the reinforced edge-insert specimens was similar to that of the corresponding reinforced center-insert specimens.

The specimen with the loop-type insert (Specimen 2-RE-L-1-6) exhibited a ductile behavior and was able to maintain nearly the maximum load for large values of insert displacement, however, it also had the lowest load capacity. The specimen with the thin-slab insert (Specimen 2-RE-T-1-6) also showed a ductile behavior as compared to the specimens with the double-leg and bolt-type inserts. The specimen with the bolt-type insert had the largest load capacity with the

maximum load carried by this specimen being 78, 42, and 33 percent larger than those carried by specimens with loop, thin-slab, and double-leg inserts, respectively.

Thin-Slab Insert Specimens

Results from all of the thin-slab edge-insert specimens tested are presented in Fig. 3.22. The figure shows the effects of axial compression, stirrup spacing, and the number of inserts. As shown, the specimens all came from the second cast and were tested under three levels of axial compression (2 ksi, 1 ksi, and no compression) with two values of stirrup spacing (6 and 4 in.).

As the load-deflection plots show, the specimen tested with no axial compression (Specimen 2-RE-T-0-4), which had 4 in. stirrup spacing, not only had the smallest load capacity but also experienced a loss in capacity with increasing insert displacement. This specimen also exhibited the most concrete damage compared to the other single edge-insert specimens, as shown in Fig. 3.22(b).

For the thin-slab edge-insert specimens, increasing the axial compressive stress from 1 to 2 ksi while keeping the stirrup spacing at 6 in. (i.e., Specimen 2-RE-T-1-6 vs. Specimen 2-RE-T-2-6) resulted in approximately 11 percent increase in load capacity without changing the shape of the load-deflection curve significantly. Coincidentally, decreasing the stirrup spacing from 6 to 4 in. while keeping the axial compressive stress constant at 1 ksi (Specimen 2-RE-T-1-6 vs. Specimen 2-RE-T-1-4) also resulted in an increase of approximately 11 percent in load capacity with no major change in the shape of the load-deflection curve.

Specimen 2-RED-T-1-6 had two thin-slab inserts with 3.75 and 7.75 in. edge distances. This specimen had 61 percent larger load capacity than Specimen 2-RE-T-1-6, which had a single insert with a 3.75 in. edge distance. The fact that the addition of a second insert resulted only in 61 percent increase in load capacity indicates the occurrence of interaction of the thin-slab inserts spaced at 4 in.

As shown in Fig. 3.22(a), the double-insert specimen suffered from a larger magnitude of loss in load capacity after reaching the maximum load than the single-insert specimens (2-RE-T-1-6, 2-RE-T-2-6, and 2-RE-T-1-4). The reason for the larger loss of capacity in the double-insert specimen was the extensive concrete damage that occurred while testing this specimen. As depicted in the photographs given in Fig. 3.22(b), concrete breakout occurred over the entire face of the double-insert specimen, with the breakout region for one insert intersecting (i.e., disturbing) that of the other insert. This mechanism resulted in deterioration of the load-carrying ability of the inserts after reaching maximum load.

Loop Insert Specimens

Results from the loop insert edge specimens are shown in Fig. 3.23. The variables addressed in this figure are the same as those explained in Fig. 3.22. Similar to what was observed for the center-insert specimens, all of the edge-insert specimens with loop-type inserts exhibited a ductile behavior.

Specimen 2-RE-L-0-4, which had stirrups spaced at 4 in. and was tested with no axial compression, exhibited a slightly different behavior than the other single-insert specimens.

Pictures of the specimens shown in Fig. 3.23(b) also suggest that the failure pattern for Specimen 2-RE-L-0-4 was different from those of the other single-insert specimens. As seen, Specimen 2-RE-L-0-4 had a relatively deep breakout cone with large inclination angles.

Pictures of the other specimens shown in Fig. 3.23(b) reveal a trend that as the axial compressive stress increases, the plan area of the concrete breakout region increases while the angle of inclination decreases (i.e., flattens).

Specimen 2-RED-L-1-6, which had two inserts placed 3.75 and 7.75 in. from an edge, had 118 percent larger load capacity than its counterpart specimen 2-RE-L-1-6, with a very similar load-deflection behavior. It should also be noted that the ultimate failure mode of the double-insert specimen (2-RED-L-1-6) as well as its counterpart single-insert specimen (2-RE-L-1-6) was concrete failure (see Table 3.2 for failure mode of specimens) even though substantial amount of plastic deformation occurred in the inserts during load testing. These observations indicate that interaction of the loop inserts is avoided with an insert spacing of 4 in.

3.4.3. Predicted Specimen Response

For unreinforced center-insert specimens, the inclination angles of the failure cones observed during testing of the specimens were determined. The experimentally determined failure cone inclination angles were compared to those assumed by ACI 318-05 Appendix D [49] and the PCI Design Handbook [48] to predict the concrete breakout capacity of steel anchors. The associated concrete breakout capacities of the unreinforced center-insert specimens predicted by the methods of ACI 318-05 Appendix D and the PCI Design Handbook were also compared to the measured load capacities.

3.4.3.1. Background on ACI and PCI Procedures

In the ACI 318-05 [49], the effective anchor embedment depth, h_{ef}, is defined for anchors that can be considered as wire-formed (e.g., "L" and "J" type anchors), while in provision RD.2.2 it is stated that "The wide variety of shapes and configurations of specialty inserts makes it difficult to prescribe generalized tests and design equations for many insert types. Hence, they have been excluded from the scope of Appendix D." Even though, it is not clear whether the equations given in ACI 318-05 Appendix D are applicable to wire-formed inserts such as the ones tested in this study (i.e., loop, thin-slab, and double-leg inserts), the predicted load capacities are included for the sake of comparison.

In the procedure given in ACI 318-05 [49], which is based on the Concrete Capacity Design (CCD) Method [53], concrete breakout strength of a single anchor with embedments less than 11 in. located away from edges in cracked concrete is calculated with Eq. (3.1) (Eq. (D-7) in the ACI 318-05).

$$N_b = k\sqrt{f_c'}h_{ef}^{1.5} \qquad \text{Eq. (3.1)}$$

where k is taken as 24 for cast-in anchors, f_c' is the compressive strength of concrete, and h_{ef} is the effective anchor depth.

In the cases where no cracking is expected in the region that the anchor is located, the capacities obtained from Eq. (3.1) are multiplied by a factor ($\psi_{C,N}$) that accounts for the absence of cracking. The factor $\psi_{C,N}$ is specified as 1.25 for cast-in anchors.

The equation used in the PCI Design Handbook [48] to calculate the concrete breakout strength of headed studs in tension is based on the work done by Shaikh and Yi [54]. Shaikh and Yi indicated the applicability of this equation to different types of concrete inserts by stating that "Although the paper focuses on welded headed studs, the design equations would also apply to nut/washer anchor bolts and other similar inserts, such as loop inserts and expansion anchors."

Both the third and fourth editions of the PCI Design Handbook [56,57] include a section on concrete breakout strength of wire-formed inserts, and the same equation is recommended for calculating the breakout capacity of both headed studs and wire-formed inserts. The fifth edition of the PCI Design Handbook [48], on the other hand, does not mention the capacity of wire-formed inserts, nor is it mentioned whether the concrete breakout capacity equation given for headed studs can be used for wire-formed inserts.

In the PCI Design Handbook method [48], concrete breakout strength of an anchor in tension is determined by multiplying the surface area of the concrete failure cone assuming a 45º inclination angle with an average uniform tensile stress of $\left(4/\sqrt{2}\right)\sqrt{f_c'}$ acting on the failure surface. Therefore, for a normal weight concrete, the equation is (Eq. (6.5.2) in the fifth edition of the PCI Design Handbook):

$$P_c = A_o\left(2.8\sqrt{f_c'}\right) \qquad \text{Eq. (3.2)}$$

where A_o is the surface area of the 45º failure cone. For a single anchor away from free edges, the failure surface area is:

$$A_o = \sqrt{2}\cdot l_e\pi\left(l_e + d_h\right) \qquad \text{Eq. (3.3)}$$

where l_e and d_h are the embedment depth and head diameter of the anchor, respectively.

The geometric properties of the inserts and the measured concrete strengths used to predict the breakout capacities are given in Table 3.3. The embedment depth and head diameter of the inserts used in Eq. (3.3) were determined based on Fig. 6.5.8 of the fourth edition of the PCI Design Handbook [57]. For loop, thin-slab, and double-leg inserts, the effective depth values used in the calculations were the total embedment depth of the inserts minus the diameter of the wires. For bolt inserts, the effective depth was taken as the depth of the insert to the top of the washer.

Even though ACI 318-05 Appendix D [49] allows using a larger failure area to compute the concrete breakout capacity when there is a washer or plate added at the head of the anchor, the capacity of bolt inserts were determined with Eq. (3.1) without considering this increase in failure area. It was decided that the thickness of the washers added at the head of the bolts was small enough to be neglected in the capacity calculations. The effect of washer was also ignored when computing the capacity according to the PCI Design handbook [48] (i.e., the head diameter of the bolt was used rather than the diameter of the washer in calculations).

3.4.3.2. Failure Cone Inclination Angles

Concrete breakout cone profiles observed in unreinforced specimens are given in Fig. 3.24. The plotted breakout cone profiles are shown for a vertical section passing through the center of the inserts. The figure includes the cone profiles for the four types of inserts tested with two specimens for each insert type.

Specimens with double-leg and bolt-type inserts exhibited consistent breakout cone profiles. The shallow breakout cone observed in Specimen 1-UC-L-0-N was due to the steel failure that occurred in this specimen. The unsymmetrical concrete breakout cone of Specimen 2-UC-T-0-N suggests that in addition to tensile load, some level of downward shear loading might have been exerted on the insert.

Failure cone inclination angles determined using the profiles shown in Fig. 3.24 are tabulated in Table 3.4. The table shows the inclination angles from a horizontal plane determined for the two sides of the profiles, and their average. By excluding Specimen 1-UC-L-0-N, which had a steel failure, the average inclination angles observed in the specimens ranged from 29 to 45 degrees. These inclination angles were consistent with the 30- to 45-degree angles explicitly or implicitly recommended in different references [48-53] to predict the capacity of headed anchors in concrete under tensile loads.

3.4.3.3. Comparison of Measured and Predicted Load Capacities

Concrete breakout strengths of the unreinforced center-insert specimens calculated using Eqs. (3.1) and (3.2) are presented in Table 3.3. Fig. 3.25 shows a bar-chart representation of the comparison between the measured and calculated capacities.

It should be noted that the measured load capacity for Specimen 1-UC-L-0-N was not the concrete breakout capacity, as this specimen experienced steel failure. As a result, the calculated and measured load capacities given in Table 3.3 for this specimen should not be compared.

As shown in Fig. 3.25, the PCI Design Handbook [48] equation (Eq. (3.2)) overestimated the concrete breakout capacity of the specimens, with the level of overestimation being higher for the bolt insert specimens. The average value of the ratio of predicted to measured capacities was 1.25 with a coefficient of variation of 14 percent.

Good agreement was observed between the measured concrete breakout capacities and those calculated using Eq. (3.1) considering the case of cracked concrete. When the $\psi_{C,N}$ factor was applied to account for the uncracked concrete case, the calculated capacities overestimated the measured values. For the case with no $\psi_{C,N}$ factor (i.e., assuming cracked concrete), the ratio of predicted to measured breakout capacities had an average value of 1.02 with a coefficient of variation of 13 percent. When the $\psi_{C,N}$ factor was included in the calculations, the average value of the ratio of predicted to measured breakout capacities became 1.27 with a coefficient of variation of 13 percent, similar to the results of the PCI Design Handbook [48].

The reason that Eq. (3.1) with no $\psi_{C,N}$ factor, which accounts for the absence of cracking, predicted the concrete breakout strength of the test specimens with good accuracy may be related to the test setup used in the study. As mentioned in Section 3.3, the specimens were supported at

the top and bottom of the back side of concrete blocks by embedded threaded rods. In this type of setup, bending of the specimen, which creates tensile stresses at the insert location, occurs as the tensile load is applied to the insert. Even though the specimens were uncracked prior to the load tests, existence of tensile stresses at the insert location due to bending of the specimens may be the reason that there is better agreement between the measured capacities and those predicted assuming cracked concrete rather than uncracked concrete.

Concrete breakout capacities were also calculated for the reinforced specimens tested under 1 ksi of compressive stress. In those cases, the predicted capacities using Eq. (3.1) with the $\psi_{C,N}$ factor of 1.25 underestimated the measured capacities. This is to be expected due to the beneficial effects of the reinforcement and the prestress, which promotes resistance to cracking.

Observations on the Behavior of Loop Insert Specimens

A tension test was performed on a piece of wire cut out from a loop insert in order to measure the steel strength of these inserts. Strength of the wire was measured to be 8.4 kips, which means that without any effect of additional specimen reinforcement and axial compression, the strength of a loop insert in the case of steel failure mode is expected to reach up to 16.8 kips assuming both legs of the loop inserts fail simultaneously. Considering that there is always the possibility of both legs of the insert not fracturing simultaneously, the capacity of the inserts would be expected to range between 8.4 and 16.8 kips due to load sharing. Moreover, during load testing of Specimen 1-UC-L-0-N, fracture of the insert legs at corner locations occurred, which indicates the involvement of bending as well as axial tension in the failure process. As a result, the strength of a loop insert itself is expected to be smaller than that corresponding to the pure tensile strength of the insert legs. The measured strength of 14.9 kips for Specimen 1-UC-L-0-N was consistent with these expectations.

The load-carrying mechanism of loop inserts explained above assumes that there was no concrete contribution to the steel failure capacity. However, because fracture of insert legs occurred inside the concrete, some part of the maximum load reached by the loop insert specimens was due to concrete contribution, even though the final failure of the specimen was due to fracture of the insert. For example, Specimen 1-RC-L-1-6 shown in Figure 3.16(a) reached a maximum load of 17.9 kips during load testing. At this point, breakout of cover concrete occurred with some level of cracking, as shown in the inset picture. Following the breakout of cover concrete, the load carried by the specimen dropped and became stable at approximately 13.5 kips. The breakout of cover concrete caused the part of the load carried by concrete to be transferred to the insert. Therefore, it may be said that the difference between the maximum load and the value of load attained after concrete breakout corresponded to the contribution of concrete to the load capacity of Specimen 1-RC-L-1-6.

In the light of the above discussion on the load carrying mechanism, it can be said that in the case of steel failure mode (i.e., fracture of insert legs), the load capacity of loop inserts might be higher than the total tensile strength of the insert legs in the presence of reinforcement and axial compression. The presence of reinforcement and axial compression would increase the resistance against cracking of concrete, and delays the initiation of cracking around the insert location. The delayed initiation of cracking, and hence breakout of cover concrete, would result in an increase in the maximum load, even though the load at which the insert fracture occurs might remain

unchanged. As a matter of fact, an analysis of the test results given in Table 3.2 indicates that for specimens with a loop insert, the load capacity of specimens increased slightly with increasing axial compressive stress and decreasing stirrup spacing even for the specimens that had steel and weld failures.

Among the loop insert specimens that had steel failure, the load capacity of Specimens 1-RC-L-1-6 and 2-RC-L-2-6 corresponded to 107 percent of the total tensile strength of the insert legs (16.8 kips). This observation supports the theory explained above that the load capacity of the loop inserts might be higher than the total tensile strength of the insert legs in the presence of reinforcement and axial compression. For Specimen 1-UC-L-0-N, which had no reinforcement and was tested with no axial compression, the ratio of measured capacity to the total tensile strength of the insert legs remained at 89 percent.

3.5. Summary, Conclusions, and Recommendations

Concrete, steel, and weld failures were observed during load testing of the insert specimens. Concrete failures occurred in all specimens with thin-slab, double-leg, and bolt-type inserts. Considerable plastic deformation, including necking at several locations, was observed to occur in specimens with loop-type inserts. The majority of the specimens (seven specimens out of eleven) with the loop-type insert experienced failures featuring the fracture of steel wires and/or welds.

Specimens with loop inserts exhibited stable behavior with almost no degradation of load carrying capacity after reaching the peak load. As the behavior of these specimens was governed by the deformation (and eventual fracture, in the majority of cases) of the inserts, the presence of longitudinal reinforcement and axial compression resulted in slight increases in load capacities without changing the global behavior of the specimens.

The test results also indicated no significant effect of limited edge distance on specimens with loop inserts. The capacity of single loop insert specimens doubled with the addition of a second insert for both the center-insert and edge-insert cases. It was concluded that loop-type inserts were the most reliable and robust of the four types tested, however, they also demonstrated the lowest tensile force capacities for reinforced specimens.

The load capacities of loop insert specimens that exhibited steel failure were generally observed to be smaller than the total tensile strength of the legs of the loop insert. Two reasons for this reduction in load capacity were: (1) both legs of the loop insert did not fracture simultaneously and (2) potential bending of the wire, in addition to axial tension (wire fractures occurred at the corner locations). On the other hand, the beneficial effects of the presence of reinforcement and axial compression resulted in some of the loop insert specimens exhibiting steel failures after achieving loads as much as 7 percent higher than the total tensile strength of the insert legs.

The behavior of the specimens with thin-slab, double-leg, and bolt-type inserts was influenced by the presence of reinforcement. Unreinforced specimens exhibited brittle behavior with limited deformation taking place before failure. The addition of reinforcement resulted in some level of improved ductility, based on the type of insert.

Significant increases in capacity were noted in reinforced bolt-insert specimens as compared to the unreinforced specimens. In specimens with thin-slab, double-leg, and bolt-type inserts, slight increases in strength were associated with increasing amounts of axial compression. Reducing the stirrup spacing resulted in similar effects to increasing the axial compression. Interaction of failure surfaces was also determined to occur in double-insert specimens with thin-slab inserts.

Failure cone inclination angles observed in the unreinforced specimens (i.e., ranging from 29 to 45 degrees) were consistent with the inclination angles assumed by several sources to predict the concrete breakout strength of cast-in-place headed anchors [48-53].

The measured concrete breakout capacities were found to be in good agreement with the capacities predicted by Equation (3.1) (i.e., Equation (D-7) of ACI 318-05 Appendix D [49]) when the factor to account for the absence of concrete cracking was not used. The reason that the measured capacities agreed better with the breakout capacity in cracked concrete than the capacity in uncracked concrete was due to tensile stresses created on the front face of specimens due to possible bending of the specimens during testing.

Based on this portion of the study, the following recommendations can be offered:

- If the maximum tensile force demands for the inserts are known a priori, it is possible to select a bolt insert configuration, or possibly thin-slab or double-leg insert configurations, to meet the design requirements. The bolt-type insert, given its high tensile force capacity in reinforced concrete also offers the option to select connector strength (i.e., steel threaded rod or reinforcing bar that is connected to the insert) such that the connector yields before the bolt insert would exhaust its capacity. However, maximum loads for inserts are seldom known with accuracy, in which case the loop insert may offer a better choice given its ductile behavior and insensitivity to edge distance, presence and detailing of reinforcement, and amount of axial compression.

- In the case of steel failure of loop inserts, the load capacity of the insert may be estimated to be 80-90 percent of the total tensile strength of the insert legs. In the presence of reinforcement and axial compression, the insert capacity might be increased up to 100-110 percent of the total tensile strength of the insert legs, or for more conservative estimates, the beneficial effects of reinforcement and axial compression might be ignored.

- PCI Design Handbook equation (i.e., Eq. (6.5.2) in the fifth edition of the PCI Design Handbook [48]) should not be used to predict the concrete breakout capacity of the types of inserts tested in this study, as this equation resulted in unconservative estimates of the measured insert capacities.

- Eq. (D-7) of ACI 318-05 Appendix D [49] may be used to predict the concrete breakout capacity of the types of inserts tested in this study. However, care must be exercised in using the $\psi_{C,N}$ factor to account for the absence of cracking in the concrete. Even though the inserts may be placed in uncracked regions, the concrete breakout capacity of inserts may be better predicted by the breakout capacity in cracked concrete if tensile stresses are likely to develop during loading at the insert locations. It should be assumed that tensile

stresses are likely to develop at insert locations if there is not a reliable and sustained compression field present in the concrete, such as that from prestress.

Table 3.1. Summary of Pull-Out Test Variables.

Specimen designation	Insert type	Insert location	Number of inserts	Axial compression	Longitudinal reinforcement	Stirrup spacing
1-UC-T-0-N	Thin-slab	Center	1	0	Unreinforced	N/A
1-UC-L-0-N	Loop	Center	1	0	Unreinforced	N/A
1-UC-D-0-N	Double-leg	Center	1	0	Unreinforced	N/A
1-UC-B-0-N	Bolt	Center	1	0	Unreinforced	N/A
2-UC-T-0-N	Thin-slab	Center	1	0	Unreinforced	N/A
2-UC-L-0-N	Loop	Center	1	0	Unreinforced	N/A
2-UC-D-0-N	Double-leg	Center	1	0	Unreinforced	N/A
2-UC-B-0-N	Bolt	Center	1	0	Unreinforced	N/A
1-RC-T-1-6	Thin-slab	Center	1	1 ksi	Reinforced	6 in.
1-RC-L-1-6	Loop	Center	1	1 ksi	Reinforced	6 in.
1-RC-D-1-6	Double-leg	Center	1	1 ksi	Reinforced	6 in.
1-RC-B-1-6	Bolt	Center	1	1 ksi	Reinforced	6 in.
2-RC-T-1-6	Thin-slab	Center	1	1 ksi	Reinforced	6 in.
2-RC-L-1-6	Loop	Center	1	1 ksi	Reinforced	6 in.
2-RC-D-1-6	Double-leg	Center	1	1 ksi	Reinforced	6 in.
2-RC-B-1-6	Bolt	Center	1	1 ksi	Reinforced	6 in.
2-RC-T-2-6	Thin-slab	Center	1	2 ksi	Reinforced	6 in.
2-RC-L-2-6	Loop	Center	1	2 ksi	Reinforced	6 in.
2-RCD-T-1-6	Thin-slab	Center	2	1 ksi	Reinforced	6 in.
2-RCD-L-1-6	Loop	Center	2	1 ksi	Reinforced	6 in.
2-RE-T-1-6	Thin-slab	Edge	1	1 ksi	Reinforced	6 in.
2-RE-L-1-6	Loop	Edge	1	1 ksi	Reinforced	6 in.
2-RE-D-1-6	Double-leg	Edge	1	1 ksi	Reinforced	6 in.
2-RE-B-1-6	Bolt	Edge	1	1 ksi	Reinforced	6 in.
2-RE-T-2-6	Thin-slab	Edge	1	2 ksi	Reinforced	6 in.
2-RE-L-2-6	Loop	Edge	1	2 ksi	Reinforced	6 in.
2-RE-T-1-4	Thin-slab	Edge	1	1 ksi	Reinforced	4 in.
2-RE-L-1-4	Loop	Edge	1	1 ksi	Reinforced	4 in.
2-RE-T-0-4	Thin-slab	Edge	1	0	Reinforced	4 in.
2-RE-L-0-4	Loop	Edge	1	0	Reinforced	4 in.
2-RED-T-1-6	Thin-slab	Edge	2	1 ksi	Reinforced	6 in.
2-RED-L-1-6	Loop	Edge	2	1 ksi	Reinforced	6 in.

N/A: No stirrup.

Table 3.2. Summary of Pull-Out Test Results.

Specimen designation	Failure type	Failure load kips	Testing date[+]
1-UC-T-0-N	Concrete	15.3	9/21/04
1-UC-L-0-N	Steel	14.9	9/20/04
1-UC-D-0-N	Concrete	17.0	9/23/04
1-UC-B-0-N	Concrete	17.1	9/24/04
2-UC-T-0-N	Concrete	13.6	10/6/04
2-UC-L-0-N	Concrete	14.2	10/7/04
2-UC-D-0-N	Concrete	12.2	10/8/04
2-UC-B-0-N	Concrete	14.1	10/9/04
1-RC-T-1-6	Concrete	24.5	9/27/04
1-RC-L-1-6	Steel	17.9	9/28/04
1-RC-D-1-6	Concrete	20.1	9/28/04
1-RC-B-1-6	Concrete	35.5	9/29/04
2-RC-T-1-6	Concrete	20.3	10/12/04
2-RC-L-1-6	Steel	14.3	10/13/04
2-RC-D-1-6	Concrete	17.9	10/15/04
2-RC-B-1-6	Concrete	34.3	10/15/04
2-RC-T-2-6	Concrete	22.5	10/18/04
2-RC-L-2-6	Steel	18.0	10/19/04
2-RCD-T-1-6	Concrete	29.6	11/18/04
2-RCD-L-1-6	Weld	28.6	11/21/04
2-RE-T-1-6	Concrete	16.8	10/21/04
2-RE-L-1-6	Concrete	13.5	10/22/04
2-RE-D-1-6	Concrete	18.1	10/25/04
2-RE-B-1-6	Concrete	24.0	10/26/04
2-RE-T-2-6	Concrete	18.6	11/6/04
2-RE-L-2-6	Steel	14.8	11/8/04
2-RE-T-1-4	Concrete	18.6	10/28/04
2-RE-L-1-4	Steel & Weld	14.1	10/29/04
2-RE-T-0-4	Concrete	14.4	11/9/04
2-RE-L-0-4	Concrete	13.2	11/9/04
2-RED-T-1-6	Concrete	27.1	11/12/04
2-RED-L-1-6	Concrete	28.6	11/16/04

[+] Fabrication date of first-cast specimens was 5/4/04 and second-cast specimens was 9/2/04.

Table 3.3. Measured and Predicted Concrete Breakout Capacities for Unreinforced Specimens.

Specimen designation	h_{ef}, l_e in.	d_h in.	Concrete strength psi	Measured capacity kips	Capacity predicted by Eq. (1) kips		Capacity predicted by Eq. (2) kips
					Cracked	Uncracked	
1-UC-T-0-N	3.3	1	10,600	*15.3*	14.8	18.5	18.2
1-UC-L-0-N[+]	3.8	0	10,600	*14.9*	18.3	22.9	18.5
1-UC-D-0-N	3.1	1.125	10,600	*17.0*	13.5	16.9	16.8
1-UC-B-0-N	3.7	1.25	10,600	*17.1*	17.6	22.0	23.5
2-UC-T-0-N	3.3	1	8700	*13.6*	13.4	16.8	16.5
2-UC-L-0-N	3.8	0	8850	*14.2*	16.7	20.9	16.9
2-UC-D-0-N	3.1	1.125	9000	*12.2*	12.4	15.5	15.5
2-UC-B-0-N	3.7	1.25	9150	*14.1*	16.3	20.4	21.8

[+] Steel failure (breakout strength is not applicable).

Table 3.4. Failure Cone Inclination Angles Observed in Unreinforced Specimens.

Specimen designation	Top angle	Bottom angle	Average angle
1-UC-L-0-N[+]	21º	16º	19º
2-UC-L-0-N	39º	42º	41º
1-UC-T-0-N	33º	34º	34º
2-UC-T-0-N	40º	18º	29º
1-UC-D-0-N	26º	31º	29º
2-UC-D-0-N	31º	28º	30º
1-UC-B-0-N	47º	42º	45º
2-UC-B-0-N	31º	44º	38º

[+] Steel failure.

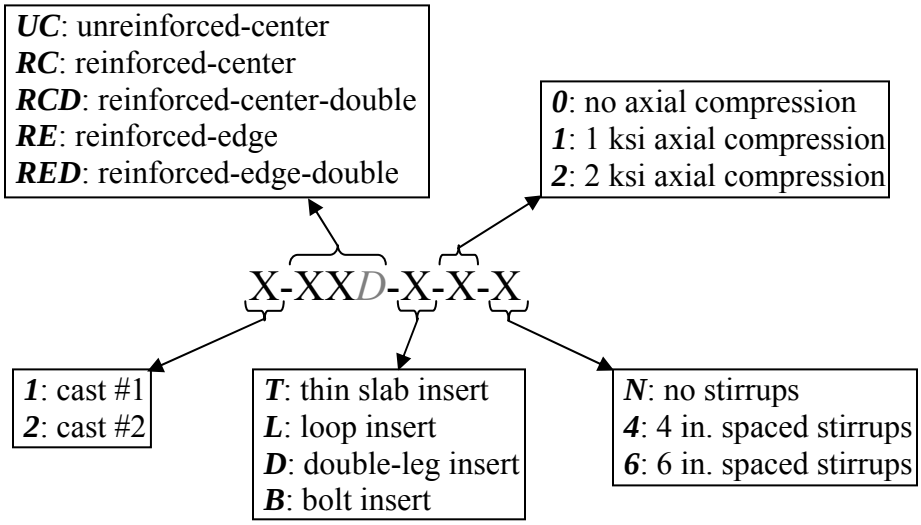

Fig. 3.1. Designation used to identify pull-out specimens.

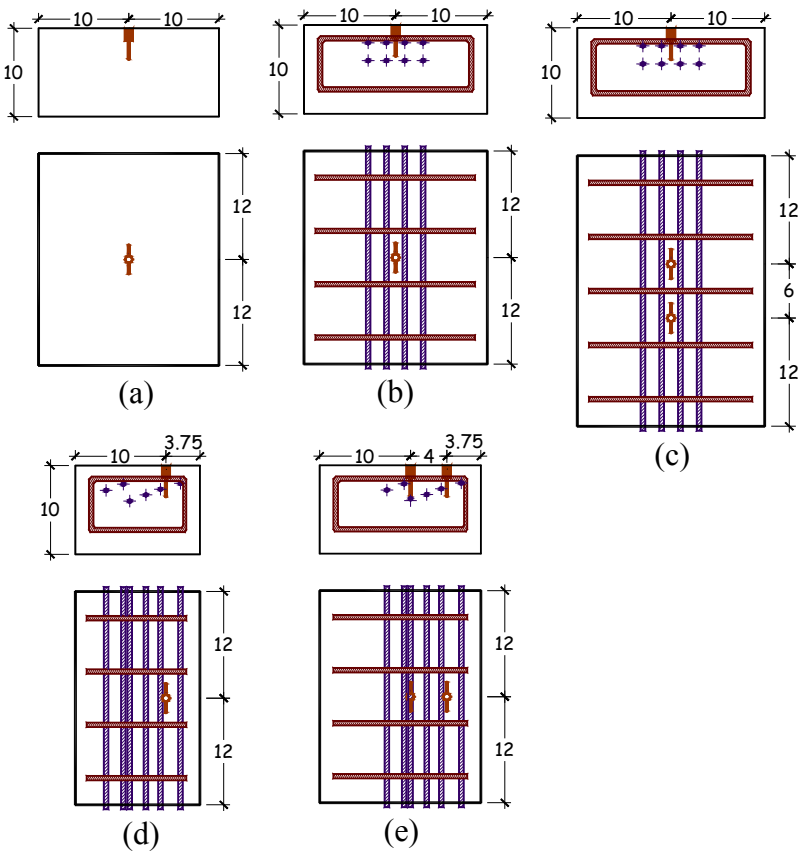

Fig. 3.2. Specimen dimensions and location of inserts.

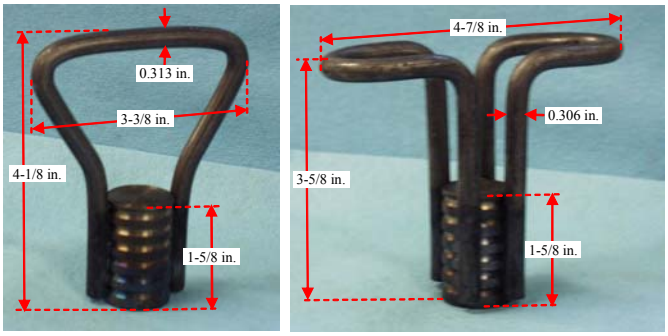

a) Loop insert b) Thin slab insert

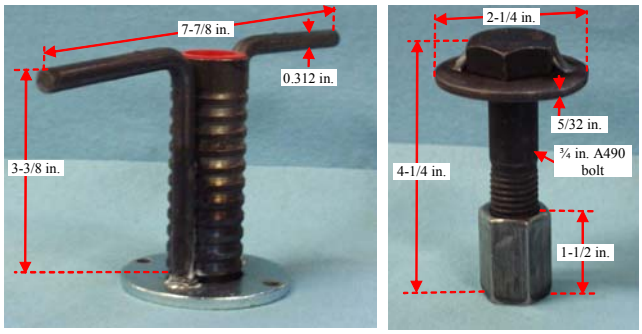

c) Double-leg insert d) Bolt –type insert

Fig. 3.3. Inserts used in the pull-out tests.

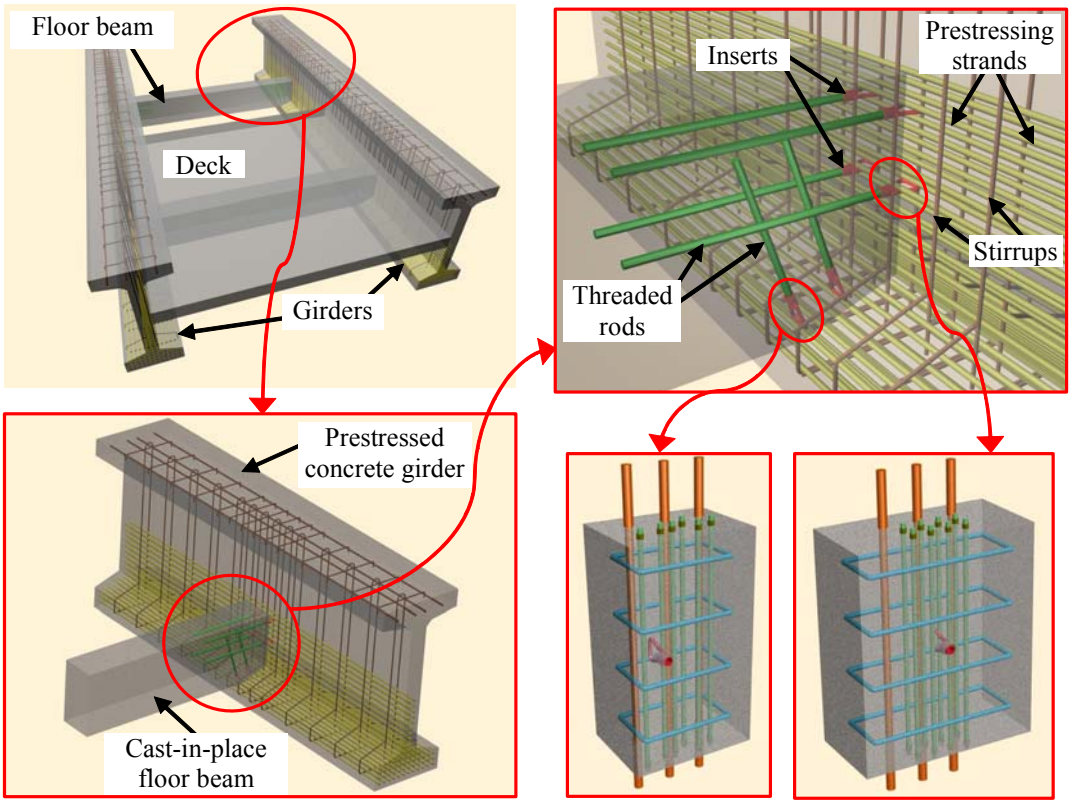

Fig. 3.4. Relationship between prototype and pull-out specimens.

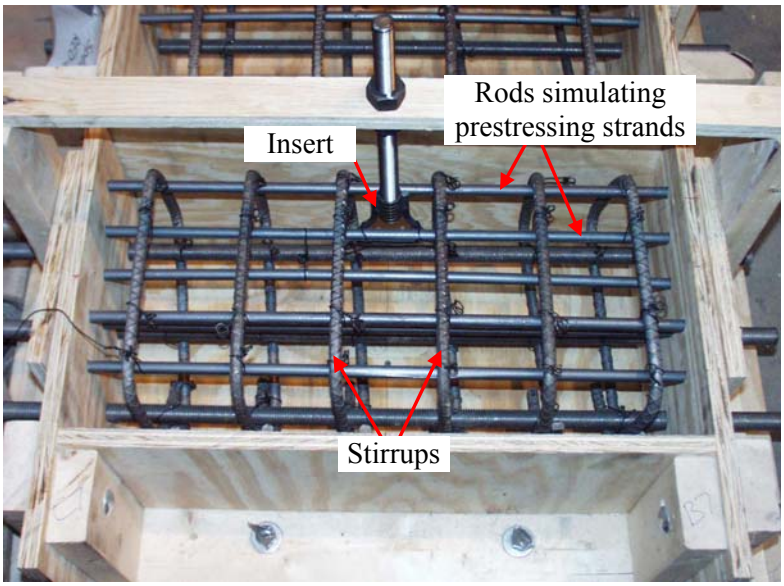

Fig. 3.5. Placement of insert and reinforcement in edge-insert specimens.

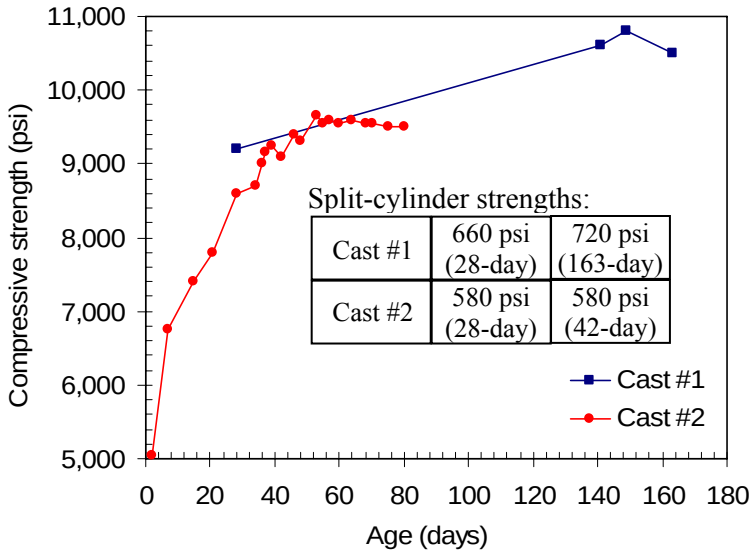

Fig. 3.6. Change in concrete compressive strength with time.

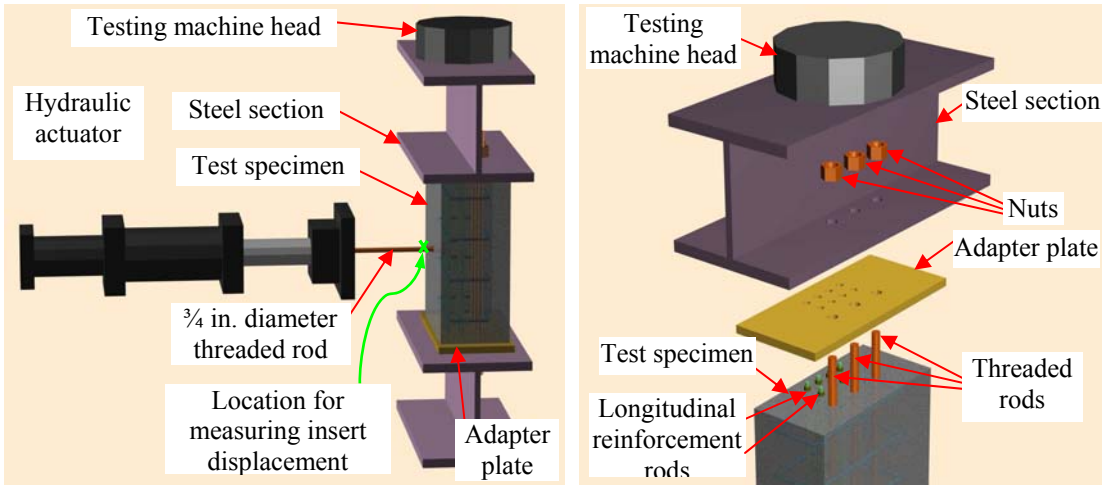

(a) (b)

Fig.3.7. Pull-out test setup: (a) overall view; (b) top connection detail.

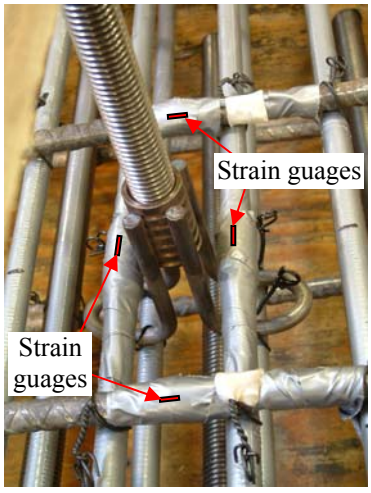

Fig. 3.8. Strain gages placed on longitudinal rods and stirrups.

(a) (b) (c) (d)

Fig. 3.9. Typical deformation patterns for the inserts in reinforced pull-out tests specimens: (a) loop insert; (b) thin-slab insert; (c) double-leg insert; (d) bolt-type insert.

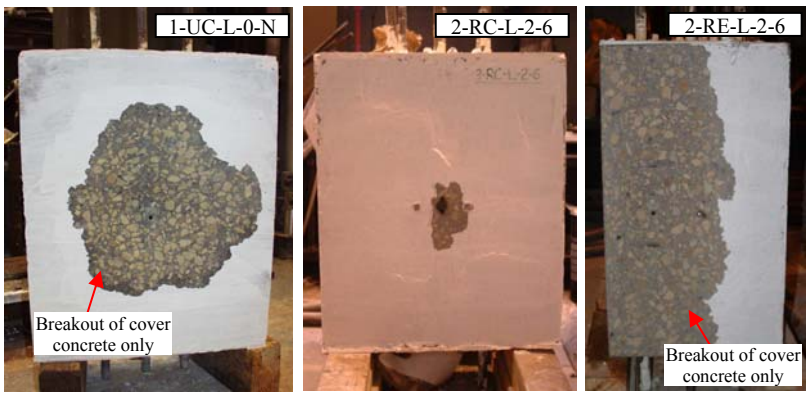

Fig. 3.10. Concrete breakout patterns for cases of steel failure.

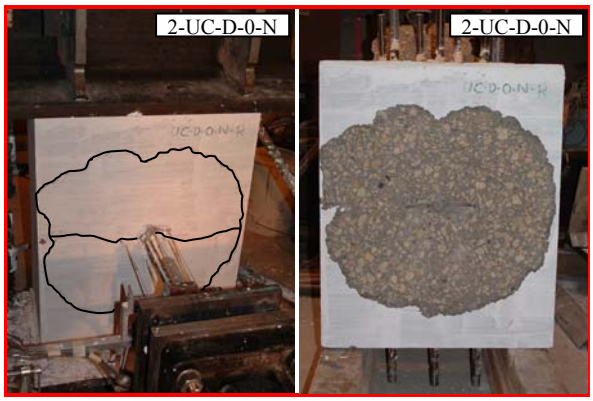

(a)

(b)

Fig. 3.11. Concrete cone breakout failures in unreinforced pull-out test specimens: (a) concrete breakout; (b) concrete breakout with radial cracking.

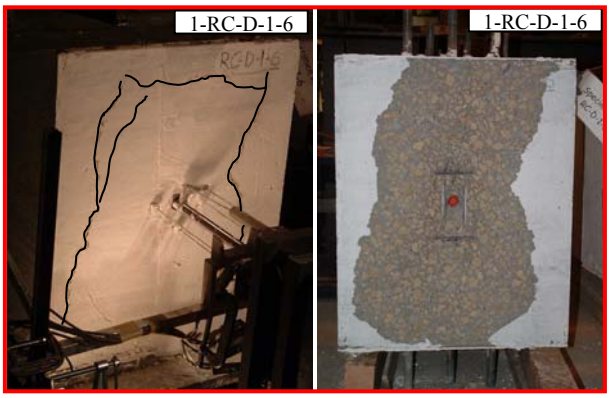

(a)

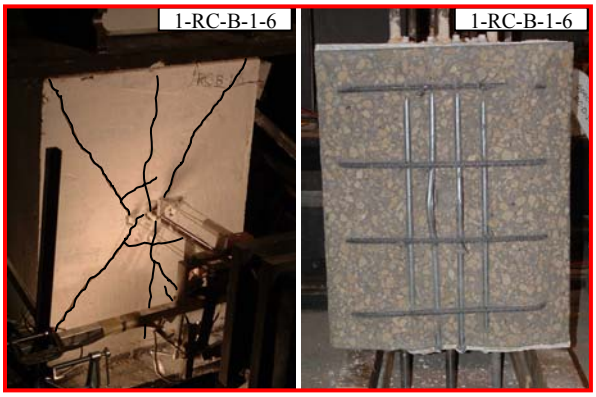

(b)

Fig. 3.12. Concrete cone breakout failures in reinforced center-insert pull-out test specimens: (a) irregular breakout area; (b) breakout of entire surface.

(a)

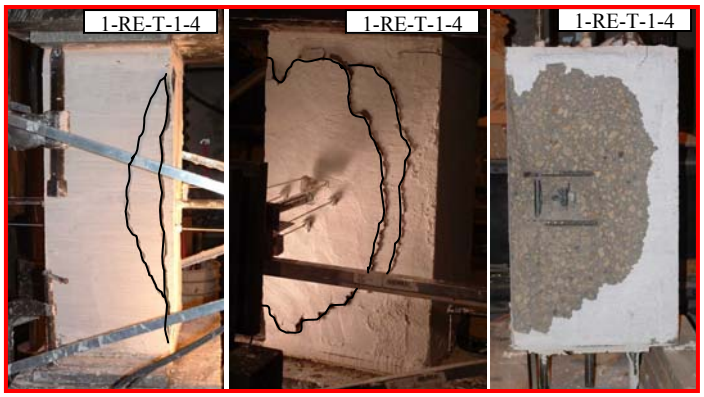

(b)

Fig. 3.13. Concrete cone breakout failures in edge-insert pull-out test specimens: (a) very shallow breakout; (b) regular cone breakout.

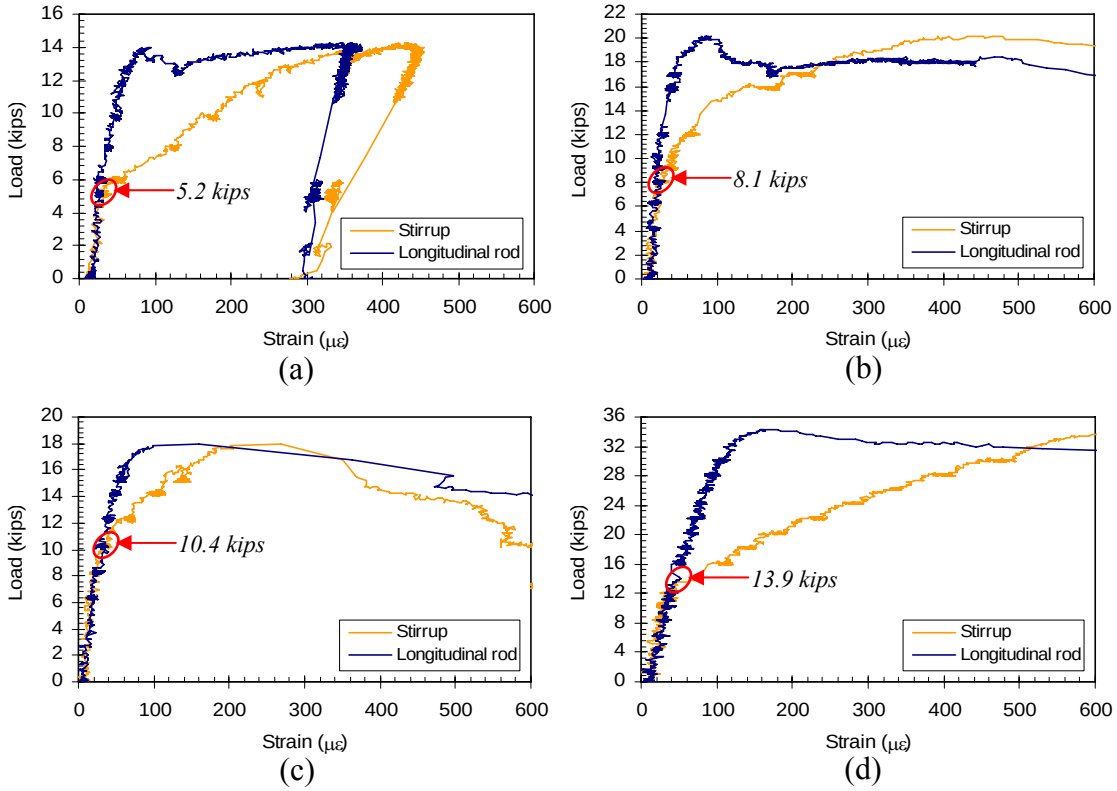

Fig. 3.14. Internal steel strains: (a) 2-RC-L-1-6; (b) 2-RC-T-1-6; (c) 2-RC-D-1-6; (d) 2-RC-B-1-6.

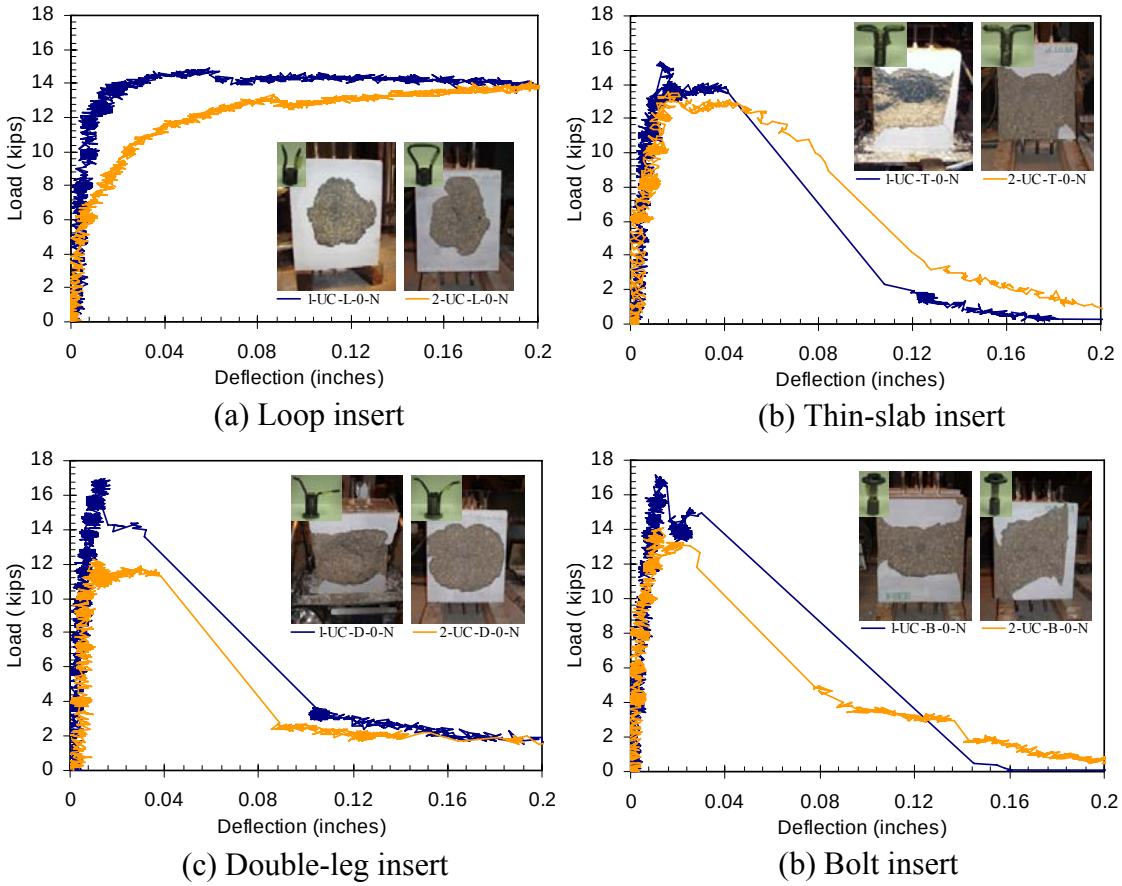

(a) Loop insert (b) Thin-slab insert

(c) Double-leg insert (b) Bolt insert

Fig. 3.15. Load-deflection curves for unreinforced pull-out test specimens.

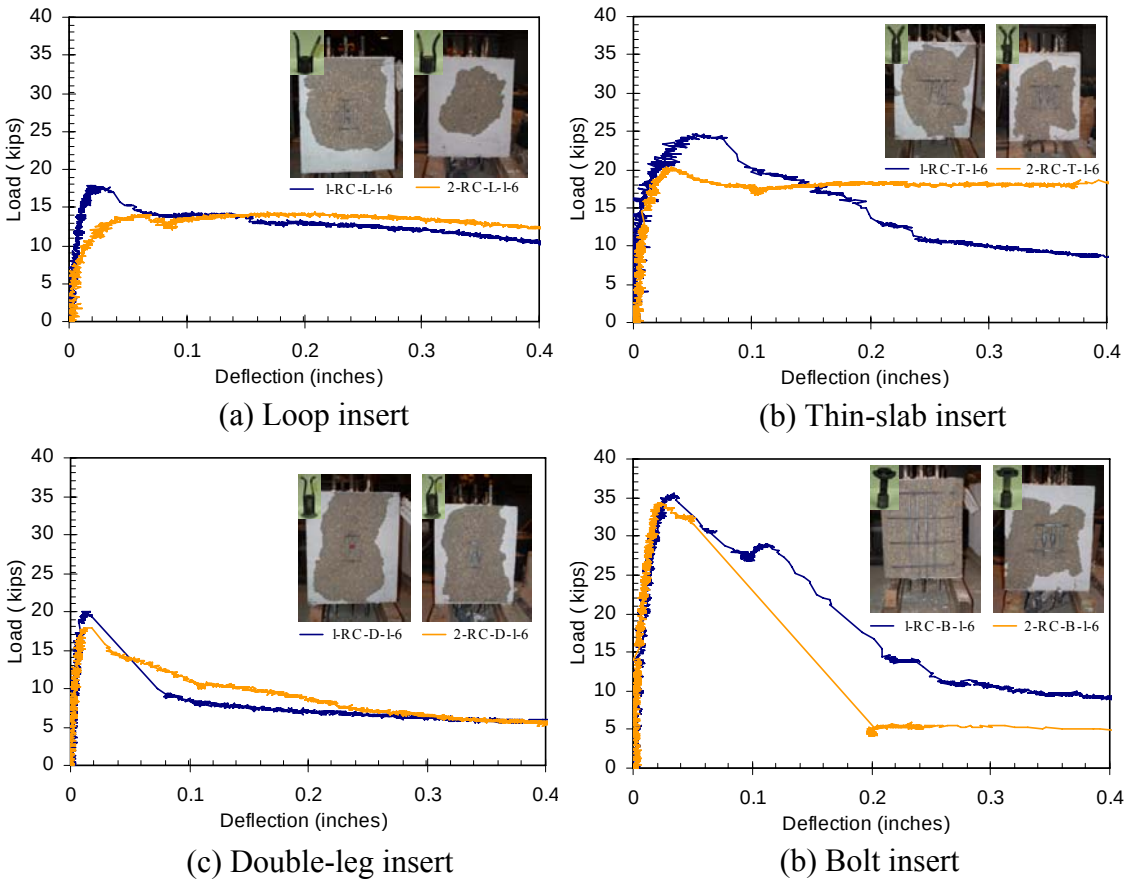

Fig. 3.16. Load-deflection curves for reinforced center-insert pull-out test specimens.

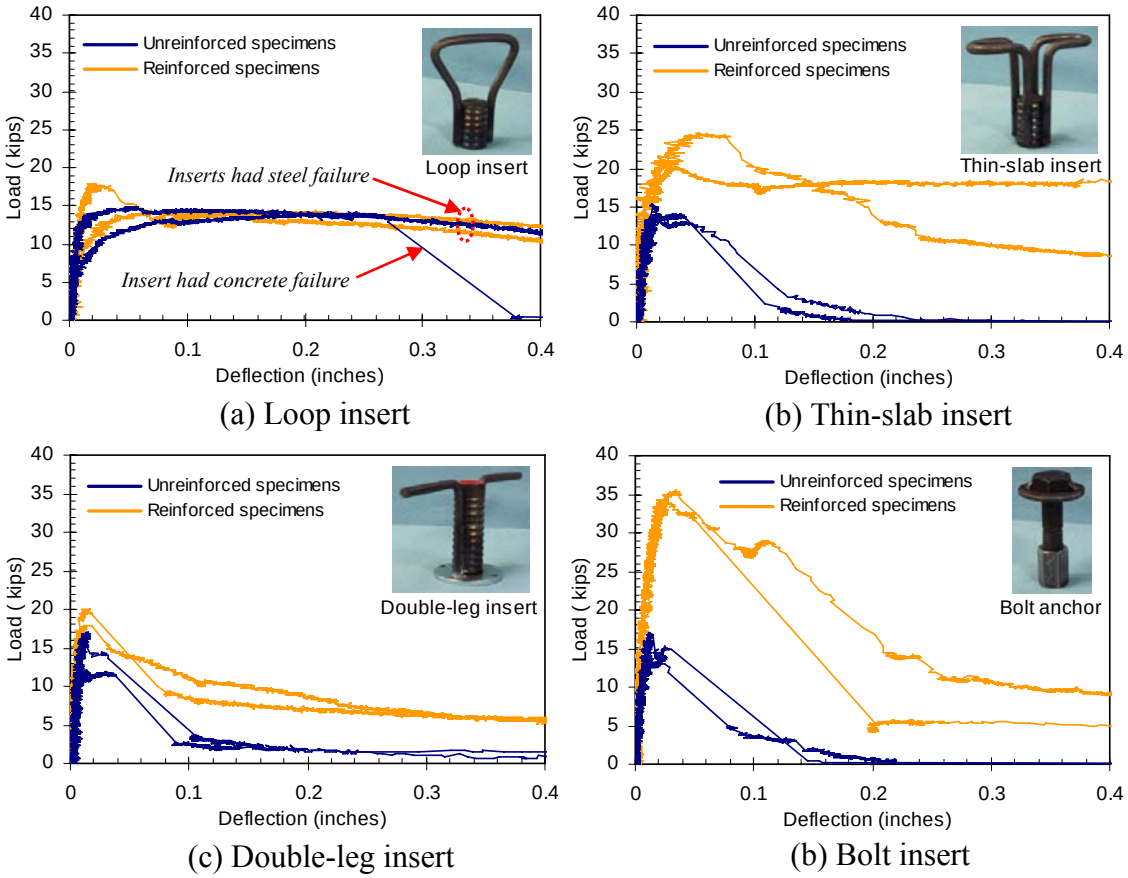

Fig. 3.17. Comparison of load-deflection curves for unreinforced and reinforced center-insert pull-out test specimens.

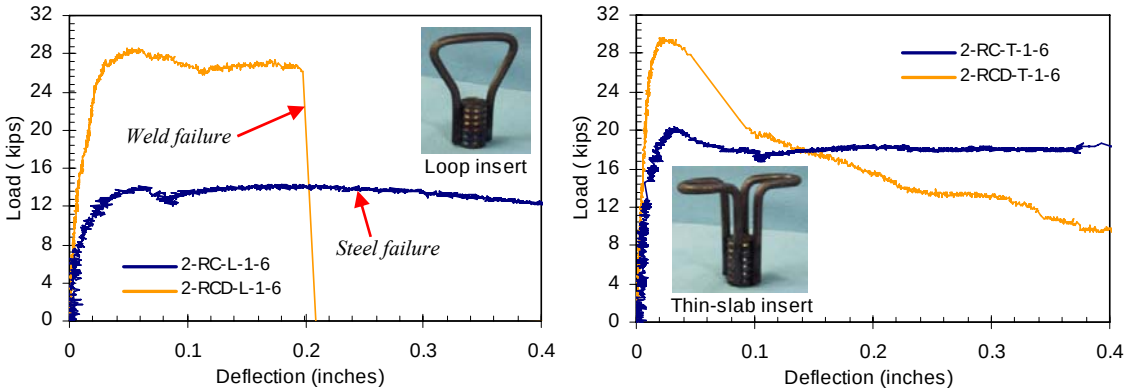

(a) Loop insert (b) Thin-slab insert

Fig. 3.18. Load-deflection curves for center-insert pull-out test specimens showing the effect of second insert.

(a)

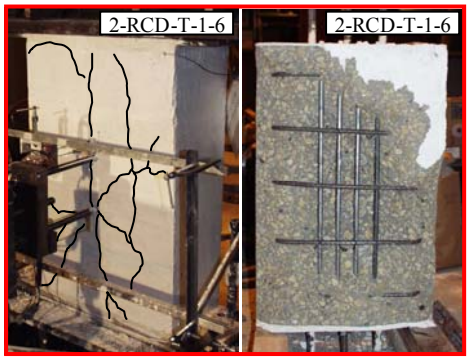

(b)

Fig. 3.19. Crack pattern of pull-out test specimens with thin-slab inserts: (a) 2-RC-T-1-6; (b) 2-RCD-T-1-6.

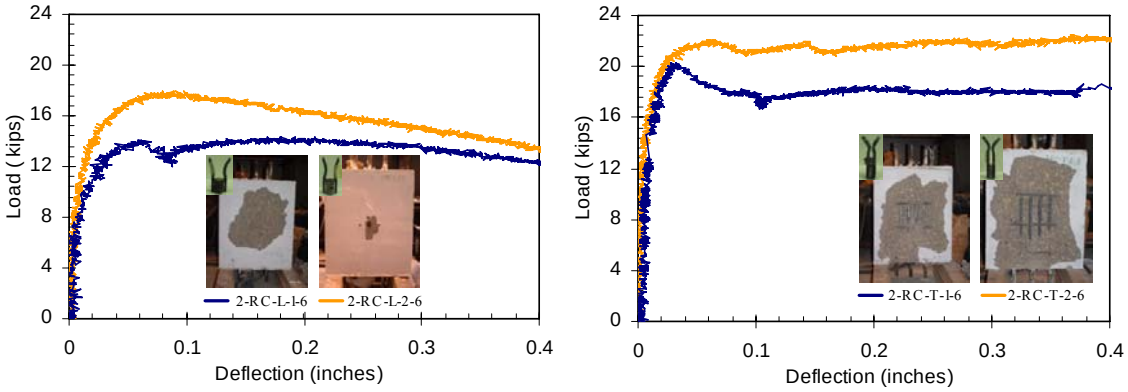

(a) Loop insert (b) Thin-slab insert

Fig. 3.20. Load-deflection curves for center-insert specimens showing the effect of axial compression.

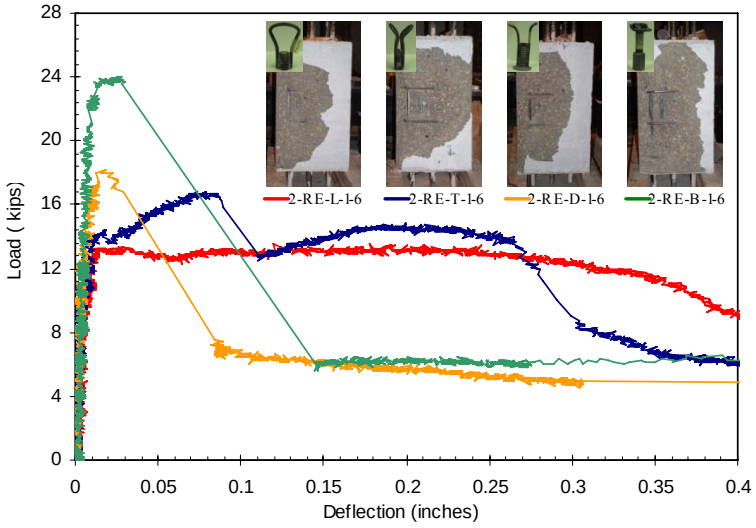

Fig. 3.21. Load-deflection curves for edge-insert specimens showing the effect of insert type.

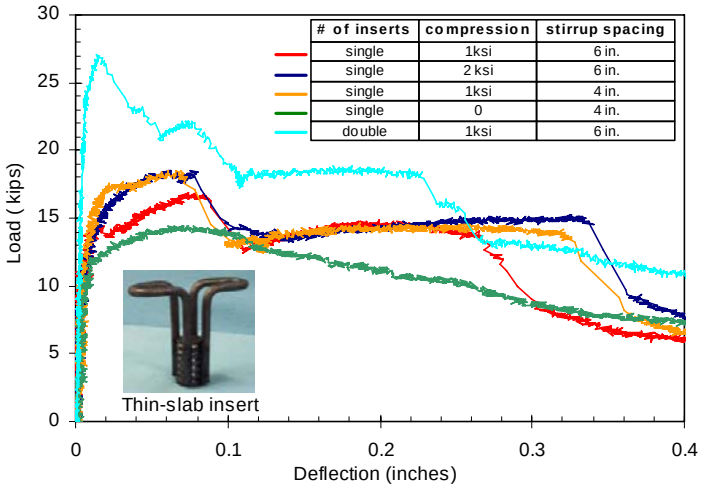

(a) Plots

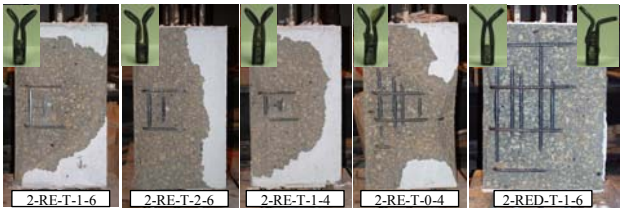

(b) Pictures of failed specimens

Fig. 3.22. Behavior of edge-insert specimens with thin-slab insert.

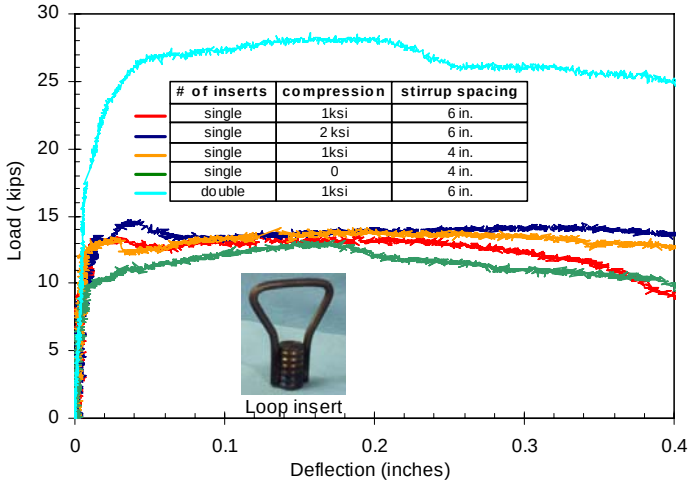

(a) Plots

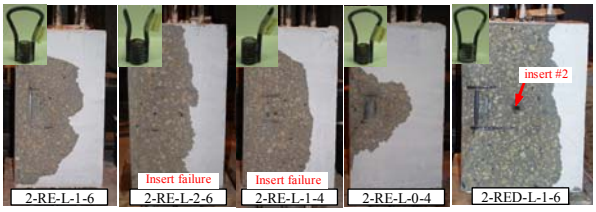

(b) Pictures of failed specimens

Fig. 3.23. Behavior of edge-insert specimens with loop insert.

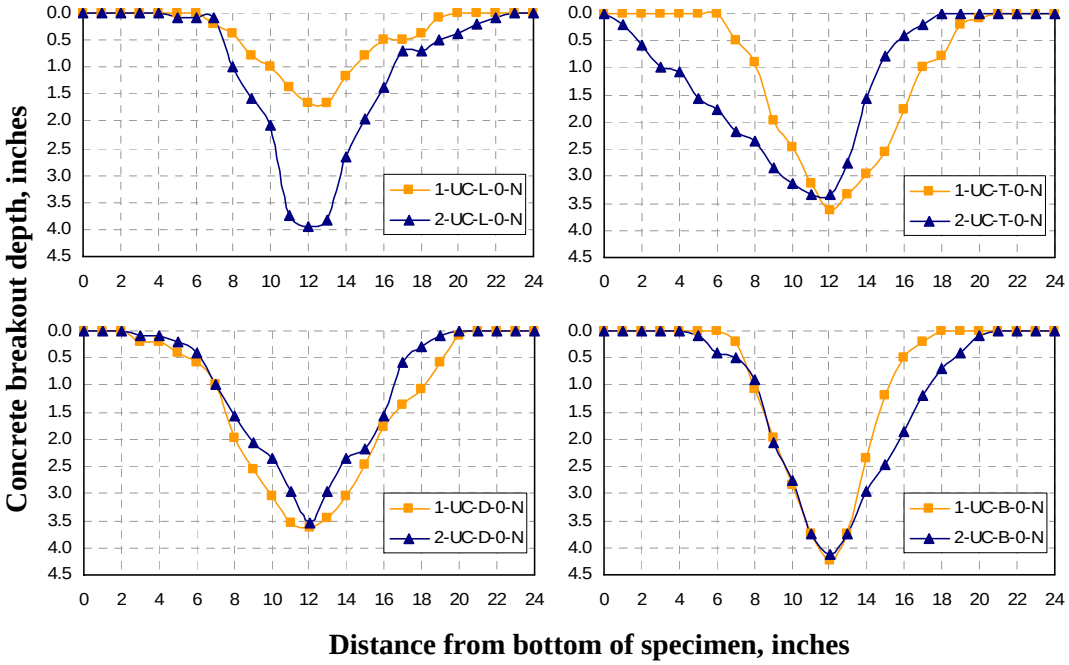

Fig. 3.24. Concrete breakout cone patterns observed in unreinforced specimens.

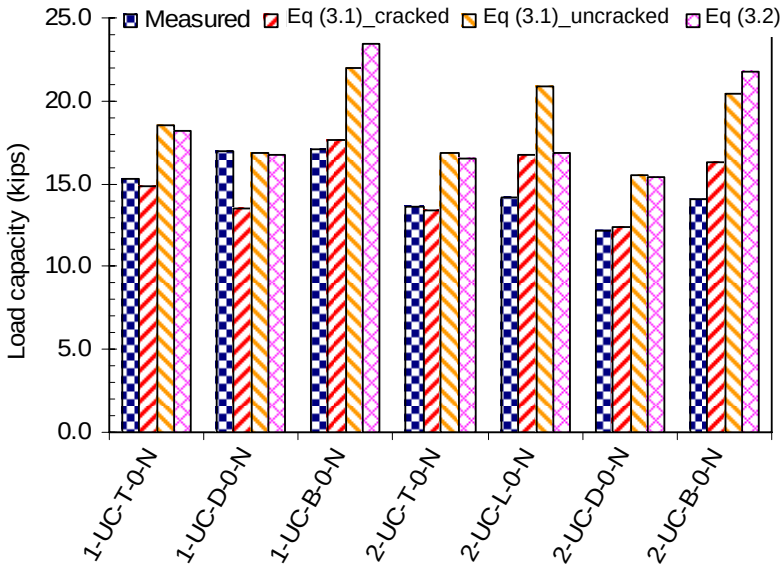

Fig. 3.25. Comparison of calculated and measured load capacities.

Chapter 4
Analysis of Girder-Floor Beam Connections

4.1. Introduction

As explained earlier, the results obtained from the reported experimental and numerical studies on the behavior of highway bridges under lateral impact loads show the ability of highway bridges to redistribute and transfer the locally-applied impact loads to other parts of the bridge to create alternate load paths. Unlike highway bridges, pedestrian bridges are of lighter construction and they do not have the high degree of redundancy exhibited by highway bridges. These characteristics make pedestrian bridges more vulnerable to collapse than highway bridges in the case of vehicular impact.

The main concern regarding the performance of prestressed concrete through-girder pedestrian bridges under lateral impact loading is limited strength and ductility of the connections between the prestressed concrete girders and the cast-in-place floor beams. In prestressed concrete through-girder type pedestrian bridge construction there is no connection between the deck and the prestressed concrete girders, and the only connection between the floor beams and the girders is through steel inserts embedded in the girders during fabrication. In such a bridge system, the connections between the girders and the floor beams would be subjected to large forces during the transfer of impact loads from the impacted girder to other parts of the bridge. Failure of these connections would reduce the structural integrity of the bridge, which compromises the stability of the structure.

The intent of the experimental and numerical analyses explained in this chapter was to study the behavior of girder-floor beam connections under load conditions representative of those that would occur when a typical bridge system is impacted in the transverse direction by an over-height vehicle. Results from static tests on full-scale, floor beam to prestressed girder subassemblage specimens, as well as a companion finite element analysis are presented. The experiments were conducted to investigate the behavior of the connection region with different types of steel inserts and under different loading conditions. Finite element models of the specimens were also prepared and calibrated with the data obtained from the load tests.

4.2. Pre-Test Finite Element Analyses

Two series of finite element analyses were conducted prior to the tests. A model of a complete through-girder pedestrian bridge system was prepared and analyzed under lateral static loading applied at various locations along both girders. The aim in these analyses was to determine the deformation patterns at the floor beam and girder connection interface under transverse loading. The second series of models consisted of the floor beam-girder connection subassemblages to be tested. Various loading combinations were explored with the subassemblage models to determine the loading configurations that would emulate the deformations observed in the entire-bridge model. The magnitude and orientation of loading used in testing of girder-floor beam subassemblage specimens were determined with this methodology.

4.2.1. Entire-Bridge Finite Element Models

Based on the plans of several prestressed concrete through-girder pedestrian bridges that had been constructed in Minnesota, a model of a typical bridge system was prepared using the general purpose finite element software MSC.Marc/Mentat [75]. As indicated in Fig. 4.1, dimensions of the bridge components used in the finite element model were representative of those shown on the bridge plans obtained from the Mn/DOT Bridge Office (see Table 1.1). The loading conditions used for testing of the connection subassemblage specimens were determined based on the deformations observed in these entire-bridge models.

The floor beams in the finite element model were assumed to be rigidly connected to the deck, while the girders were modeled as separate members. Contact surfaces were defined between the girders and floor beams as well as the girders and the deck. The contact surfaces defined at the connection interface allowed the transfer of bearing compressive stresses while allowing gap opening between the bodies whenever tensile stresses developed. In this way, the partially rigid behavior of the connection between the girders and the floor beams in through-girder construction was modeled.

The girders and floor beams in the model were connected by anchored reinforcemend represented by truss elements as illustrated in Fig. 4.2. At each girder-floor beam connection region, six sets of truss elements were defined with four of them in the girder web and two of them in the girder bottom flange. The locations of the truss elements were chosen to match those of the connector rods used in existing through-girder bridge construction.

The girders, floor beams, and the deck were modeled using 8-noded solid elements, while 2-noded truss elements were used for the connectors between the floor beams and the girders. Boundary conditions were defined at girder ends. Due to the lack of information on the resistance characteristics of the bearing assemblies when subjected to translational and rotational movement of the girder ends at the time, idealized pin and roller boundary conditions were used for the girder ends. With the pin boundary condition, girder end displacements in all three directions were assigned zero value, while the roller boundary condition allowed the girder end displacement along the longitudinal axis of the girders.

The material behavior for the connector elements were based on the load-displacement behavior obtained from the tension pull-out tests explained in Chapter 3. The pull-out test results indicated that the behavior of loop inserts was not significantly affected by the reinforcement detail, amount of edge distance, and the magnitude of axial compressive stress, therefore, the same material behavior was used for all six connectors in each girder-floor beam connection in the finite element model. Load versus deflection plots obtained from tension pull-out tests on loop inserts were converted into stress versus plastic strain plots using the appropriate length and cross-sectional area, and were assigned as the material behavior for the truss elements (Fig. 4.2).

Because of the large number of elements used in the model together with the nonlinearities in the model due to the contact surfaces and the highly nonlinear material behavior used for the connectors, the analyses were extremely time-consuming. In order to reduce the analysis time, the concrete material behavior used for the girders, floor beams, and the deck were simplified such that after reaching the concrete strength, the stress remained constant with no softening due

to crushing (i.e., perfectly plastic behavior). The effects of this simplification on the global behavior of the bridge system and the deformation at the girder floor beam connection interface were assumed to be minimal due to the configuration of the girder-floor beam connections which rely on the connector rods. Because of the flexibility of the connections, the regions of high compressive stress were greatly localized such that when transverse displacements were applied to the girders, the compressive stresses in other parts of the bridge remained relatively small.

Transverse displacement was applied to the entire model at four different locations along the length of both girders as shown in Fig. 4.2. At each location, the displacements were assigned to four nodes, two of which were 4 in. from the bottom of the girder and the other two were 7 in. from the bottom of the girder. Displacement loading was used in the analyses rather than applying forces in order to be able to obtain the load-deformation behavior of the bridge after reaching the peak load capacity. The loading patterns included application of transverse displacement at one face of the bottom flange of girders at floor beam locations (Locations 1 through 6) as well as in between the floor beam locations (Locations 2-3 and 5-6). The two distinct gap opening patterns observed to occur at the girder and floor beam connection interface are shown in Fig. 4.3. All of the deformation patterns that occurred under the eight loading conditions explained above were a combination of these distinct gap opening patterns. The deformation patterns shown in Figs. 4.3(a) and 4.3(b) were used for testing of the connection subassemblage specimens.

4.2.2. Connection Subassemblage Finite Element Models

Finite element models of the connection subassemblage specimens were prepared in order to determine the magnitude and orientation of displacements to be applied at the end of the floor beams. The models were analyzed under different combinations of loading location and magnitude in order to determine the combinations that would result in gap opening patterns at the girder-floor beam interface in these subassemblage models similar to those determined from the full-scale finite element models.

Similar modeling techniques explained earlier for the full-scale models were used to model the partially-rigid behavior of the girder-floor beam connection in the subassemblage models. All three translational degrees of freedom at the last two rows of nodes at the top and bottom of girder pieces at both ends were fixed, and displacement loading was applied at the end of the floor beam pieces, as indicated in Fig. 4.4.

Fig. 4.4 shows the two loading conditions applied to the subassemblage models, which produced similar gap opening patterns at the girder floor beam interface as those obtained from the entire-bridge model (Fig. 4.3). The first loading condition was a pure vertical displacement loading applied at the end of floor beam. The second gap opening pattern required application of displacements both in horizontal and vertical directions, with the magnitude of horizontal component of displacement being 30 percent of the magnitude of vertical component.

4.3. Description of Test Specimens

The experimental study included load testing of six girder-floor beam connection subassemblage specimens. As indicated in Table 4.1, the specimens included three different anchor types, each of which was tested under the two different types of loading. The specimen geometry mimicked

that of the girder-floor beam connection region in a typical through-girder bridge system, and comprised a 10 ft. length of prestressed concrete girder and a 5 ft. 2 in. length of cast-in-place reinforced concrete floor beam (see Fig. 4.5). The girder pieces had to be long enough to enable the transfer of the prestressing force from prestressing strands to the concrete, but at the same time they could not be too long because of easy handling in the lab. As a result, the 10 ft. length used for the girder pieces deemed to satisfy these two conditions. The 5 ft. 2 in. length was chosen for the floor beam pieces provided easy constructability and it enabled the use of the test setup that was consistent with the hole pattern in the strong-floor of the laboratory.

The girder and floor beam pieces were connected by means of steel inserts embedded inside the girders during fabrication and steel connection rods that were threaded into these inserts and which were cast inside the poured floor beams. Each connection specimen included six steel inserts, two of which were located in the bottom flange while the remaining four were located in the web of the girder section, as illustrated in Fig. 4.5.

Fig. 4.6 shows the three types of inserts used in the study. The two types of loop inserts tested in this study (national coarse (NC) thread loop insert and coil-thread loop insert) were the devices used in prestressed concrete bridge girders constructed in Minnesota, as mentioned in Chapter 3. Both the NC-thread and the coil-thread loop inserts had similar geometry except the coupler into which the connection rods were threaded. The bolt insert, which also had a NC-thread coupler, was included as the third type of insert in the girder-floor beam connection subassemblage specimens based on the results of pull-out tests performed on different types of inserts (Chapter 3). The pull-out test results indicated that bolt inserts had large tensile load capacity (as much as 216 percent larger than the loop insert) if there is reinforcement available to distribute the load from the insert to the surrounding concrete.

The Mn/DOT Type-54M girder section was used for the specimens (Fig. 4.5), even though the Type-63 girder section is more commonly specified for through-girder pedestrian bridges in Minnesota. The Type-54M section, which has a web that is 9 in. shorter than that in the Type-63 section (with the remaining dimensions being the same), facilitated test specimen construction and handling in the laboratory. The girder sections were prestressed with thirty-four ½ in. diameter straight prestressing strands with a nominal initial stress of either 130,000 or 172,000 psi. The initial stress and the location of prestressing strands in the girders were chosen such that the resultant prestressing force did not have eccentricity (see Fig. 4.5). This measure ensured a constant amount of prestress throughout the girder cross section so that all six steel inserts were subjected to the same uniform level of prestress. The nominal initial prestress in the girders was 1150 psi.

The girder segments were fabricated in one cast at a local prestressing yard and transported to the Structural Engineering Laboratory of the Department of Civil Engineering at the University of Minnesota, where the floor beams were constructed and load tests were performed.

During the fabrication of the girder segments, the steel inserts were placed at pre-determined locations and tied to the girder reinforcement, as shown in Fig. 4.7. Groups of inserts that had been welded to rebar pieces, as shown in Fig. 4.8, were tied to the girder stirrups with the help of #4 steel dowels with lengths of approximately 2 ft. After all the inserts were tied in position, the

side forms were attached and the concrete for the girder sections was cast using a concrete mix with 8200-psi nominal compressive strength. The concrete compressive strength measured at the time of load testing of specimens varied between 8650 and 9850 psi.

After each girder segment was placed in the testing frame, a reinforced concrete cast-in-place floor beam was constructed. The connection between the precast concrete girder pieces and the cast-in-place concrete floor beam pieces was through steel connection rods that were threaded into the steel inserts that had been embedded in the girders during fabrication. The four connection rods that were threaded into the web of the girder sections were 24 in. long and the two connection rods in the bottom flange were 18 in. long. In specimens with NC-thread steel inserts (NC-thread loop inserts and bolt inserts), #6 Grade-60 rebars with forged and threaded ends were used as connection rods. In specimens with coil-thread loop inserts, on the other hand, ¾ in. diameter high carbon steel coil rods were used as connection rods.

The 28 in. floor beam depth used in the test specimens represented two separate components of a through-girder pedestrian bridge: the bottom 21 in. of the 28 in. depth was included to account for the floor beam itself, while the top 7 in. depth was included to simulate the deck. The flange overhangs for the reinforced concrete deck were not included in the test specimens, because the analyses performed during the design stage of the test specimens indicated that they did not have a significant influence on specimen behavior, as no concrete crushing was expected to occur in the floor beam flange overhangs.

The concrete used to make the floor beam sections had a 4000-psi nominal compressive strength with the compressive strengths measured at the time of load testing of the specimens varying between 3500 and 5900 psi.

4.4. Test Setup, Instrumentation, and Testing of Specimens

The setup used for testing the specimens, shown in Fig. 4.9, required clamping the girder sections to the laboratory floor at both ends by means of steel sections and threaded rods. A monotonically increasing displacement was applied at the end of the floor beams. Specimens L-NC-V, L-C-V, and B-V were subjected to downward vertical displacement, while a combination of vertical upward and horizontal outward displacement loading was applied to the floor beams in Specimens L-NC-I, L-C-I, and B-I.

Vertical load was applied to the specimens with a 77-kip capacity hydraulic actuator. Two additional 77-kip capacity actuators were used for the horizontal load in Specimens L-NC-I, L-C-I, and B-I. These actuators were attached to a steel tube which was connected to the floor beams with four 1 in. diameter high-strength steel threaded rods that were embedded inside the floor beams (Fig. 4.9).

In all six specimens, the free ends of the floor beams were braced at the top and bottom on both sides to prevent any transverse displacement. The bracing system included threaded rods, turnbuckles between the threaded rods, and linear bearings attached to steel columns, which were bolted to the lab floor. The girder segments in specimens L-NC-I, L-C-I, and B-I were also braced to resist the force generated by the horizontal actuators using steel channels and plates to

transfer the horizontal reaction force to a pair of steel columns that were bolted to the lab floor, as shown in Fig 4.9.

The instrumentation used for the specimens included strain gages placed on the connection rods during the fabrication of the floor beams and linear variable differential transformers (LVDTs) placed at several locations on the girder segments and floor beams. Figs. 4.10(a) and 4.10(b) show the NC thread and coil thread connection rods, respectively, with strain gages attached to the rods. Mechanical protection and water proofing were applied to the gages to prevent any damage during casting of the floor beams. LVDTs were attached to the specimens (see Fig. 4.10(c)) to measure the deformation of floor beam and girder pieces as well as to monitor the opening of the gap at the girder-floor beam interface.

The specimens were whitewashed with a mixture of lime and water to facilitate visual detection of the cracks and monitoring of gap opening at the girder-floor beam interface. Displacement-controlled loading was applied to the specimens at a typical rate of 1 in./hr in the vertical direction. In specimens L-NC-I, L-C-I, and B-I, the horizontal actuators were programmed to develop a displacement at the end of floor beam equal to 30 percent of the vertical displacement. After reaching peak load and producing extensive damage in the specimens, the loading rate was first increased to 2 in./hour and then to 4 in./hour. The testing continued until failure of the specimens, which involved either fracture of the steel inserts embedded in the girder sections or concrete breakout failure around the inserts.

4.5. Test Results

4.5.1. Vertical Loading Specimens

The vertical load specimens (i.e., Specimens L-NC-V, L-C-V, and B-V)) developed the concrete breakout and cracking patterns shown in Fig. 4.11 at the end of testing. Because of the downward direction of loading applied to these specimens, the upper layer of inserts in the web of the girders were subjected to a larger magnitude of tensile loads than the other inserts. As a result, the first visually observed cracks in these specimens occurred in the girder web close to the location of the upper layer of web inserts. As the loading continued, more cracks developed in the girder web, and concrete breakout started at the location of the upper layer of web inserts. No sign of concrete crushing was observed in the floor beam and girder pieces during testing.

For Specimens L-NC-V and L-C-V, which had loop-type inserts, the failure of the specimens was due to fracture of the loop inserts. During testing of these specimens, fracture of inserts was accompanied by loud noises and sudden increases in gap opening at the girder and floor beam connection interface. For Specimen B-V, which had bolt-type inserts, no fracture of the inserts occurred. In this specimen, concrete breakout occurred around the two upper web inserts. After termination of the test, it was discovered that stripping of the threads in both the couplers and connector rods occurred for the remaining four inserts.

The load versus floor beam end displacement plots for the three vertical loading specimens are shown in Fig. 4.12. Table 4.2 summarizes the load capacities of the specimens, in addition to the load carried by the specimens at several floor beam end displacement levels during testing. As listed in Table 4.2, Specimen L-C-V had approximately 23 percent higher load capacity than Specimens L-NC-V and B-V. Even though all three specimens seemed to have very similar

initial stiffnesses, the amount of displacement to reach the maximum load levels was also larger for Specimen L-C-V.

4.5.1.1. Difference in Behavior between Loop Insert Specimens

As explained earlier, Specimens L-NC-V and L-C-V had loop-type inserts embedded in the girder pieces. The loop inserts in Specimen L-NC-V had a regular national coarse (NC) thread coupler at the end of the loop part of the insert, while the loop inserts in Specimen L-C-V had a coil-thread coupler. Behavior of these two specimens having the same type of inserts is compared in Fig. 4.13. After reaching the maximum load, Specimen L-C-V was able to maintain most of its load capacity at floor beam end displacement of 1.5 in. Specimen L-NC-V, on the other hand, suffered from a sudden loss of capacity almost immediately after reaching the maximum load. The reason for the difference in the behavior of these two specimens was due to the small difference in the deformation patterns of the inserts.

The coupler part of coil inserts in Specimen L-C-V were observed to uncoil under the effect of tensile loads transferred from the threaded rods embedded in the floor beam piece to the inserts. This extra deformation that occurred in coil-type loop inserts resulted in extra gap opening at the interface and hence extra floor beam end displacement in Specimen L-C-V as compared to Specimen L-NC-V.

Pictures of fractured NC-thread and coil-thread loop inserts are superimposed on Fig. 4.13. The NC-thread and coil-thread loop inserts shown in the pictures were one of the two upper web inserts embedded in the girder pieces, and the failure mode of these inserts were common to the other inserts in Specimens L-NC-V and L-C-V, respectively. As shown in the pictures, in addition to uncoiling of the coupler, the location of fracture in the coil-thread insert was slightly different from the fracture location in the NC-thread insert. Fracture of the coil-thread loop insert at the location away from the coupler part of the insert was likely to be another reason for the difference between the behaviors of Specimens L-NC-V and L-C-V.

In addition to the difference between the displacement behavior of Specimens L-NC-V and L-C-V, the load capacity of the two specimens was also different, as evident in Fig. 4.13. Tension tests were performed on wire pieces cut out from the NC-thread and coil-thread loop inserts in order to determine if the reason for the difference in the load capacity of Specimens L-NC-V and L-C-V was due to a difference in the material strength between the two types of loop insert (See Appendix D). These tension tests indicated almost identical load-deformation behaviors for the two inserts, suggesting that the difference in the measured load capacity of the two specimens was not due to the difference in insert strength itself.

Another possible reason for the difference in load capacity of Specimens L-NC-V and L-C-V was the difference in concrete strength of girder pieces for the two specimens. Even though the girder pieces for all specimens were cast at the same time, several concrete batches were used to cast the specimens. Because of this, the concrete strengths for girder pieces varied slightly among the specimens. As listed in Table 4.1, the measured girder concrete compressive strengths at the time of testing for Specimens L-NC-V and L-C-V were 8650 and 9800 psi, respectively, which corresponds to a 13 percent difference. The higher concrete strength of Specimen L-C-V

is likely to be part of the reason for the higher load capacity of this specimen compared to Specimen L-NC-V.

The points labeled on the plots in Fig. 4.13 show the progression of damage in Specimens L-NC-V and L-C-V. Points 1 and 2 correspond to the fracture of two upper layer inserts in the web of the girder in Specimen L-NC-V. Similarly, Points 4 and 5 mark the fracture of the upper layer of web inserts in Specimen L-C-V. As seen, for both specimens, fracture of the first insert was immediately followed by fracture of the second insert, resulting in a sudden drop in the load carried by the specimens.

Point 3 in Fig. 4.13 marks the initiation of concrete breakout around the two upper web inserts in Specimen L-C-V. Breakout of the cover concrete occurring at the peak load resulted in a decrease in the load carried by the specimen, even though no insert failure occurred yet. After this point, the total load in the connector rods was transferred to the loop part of the inserts as the contribution from the cover concrete diminished due to the concrete breakout.

It is interesting to note that fracture of the inserts in Specimens L-NC-V and L-C-V occurred at very similar load levels (Points 1 and 2 vs. Points 4 and 5), even though the two specimens had different load capacities. This suggests that the extra strength in Specimen L-C-V (difference between Points 3 and 4) as compared to Specimen L-NC-V was due to the concrete contribution, which vanished following the breakout of cover concrete.

Changes in strain in the connector rods during testing of Specimens L-NC-V and L-C-V are shown in Figs. 4.14(a) and 4.14(b), respectively. Each figure includes plots of three strain gages placed on one of the two upper web connector rods, as well as the plot of the load applied at floor beam end. Location of strain gages on the connector rods is also superimposed on the plots. It should be noted that the data in this figure were plotted against the actuator stroke, which is different than the net floor beam end displacements shown in the previous figures. The reason for the difference between the actuator stroke and net floor beam end displacements was the deformation of the load frame itself and the twisting of the girder pieces as a result of the flexibility of the mechanism used to clamp the girder ends. As evident in Figs. 4.14(a) and 4.14(b), fracture of the inserts caused a sudden drop in the connector rod strains. Fracture of the upper web inserts in specimen L-NC-V occurred almost immediately after reaching the peak load, while in Specimen L-C-V the first insert fracture was preceded by concrete breakout that occurred at the peak load. Fracture of the inserts marked in Figs. 4.14(a) and 4.14(b) corresponds to Points 1 and 2, and Points 4 and 5, respectively in Fig. 4.13. The increase in the connector rod strains that occurred at approximately 24 kips in Specimen L-C-V was due to a major vertical crack that initiated in the floor beam at this load at approximately 16 in. from the girder.

4.5.1.2. Influence of Construction Method on Insert Behavior

Results obtained from testing of the connection subassemblage specimens indicated that the behavior of the specimens was affected by the method used to position the inserts inside the girder pieces during fabrication. As explained earlier, during fabrication of the girder pieces, the inserts in the web and flange of the girder segments were connected by welding rebar pieces to the inserts (see Fig. 4.8). These insert groups were then tied to the reinforcement cages with the help of additional steel dowels, as shown in Fig. 4.7. The deformation pattern of inserts observed

during testing of the connection subassemblage specimens indicated that the process of welding rebar pieces affected the behavior of these inserts.

Influence on Loop Inserts

Fig. 4.15 shows the load-deflection behavior of NC-thread loop inserts and bolt inserts obtained from the pull-out specimens (Chapter 3). In the pull-out tests, no rebar pieces were welded to the inserts, and the inserts were tested without modifying their geometry. In the figure, results from two reinforced and two unreinforced pull-out specimens are presented for each insert type.

As evident in the load-deflection plots shown in Fig. 4.15(a), the loop inserts exhibited a very ductile behavior during the tension pull-out tests. After reaching the peak load, the inserts were able to maintain almost the full load capacity over large amounts of deflection until the fracture of the insert legs occurred. The inset picture on Fig. 4.15(a) shows a photograph of a loop insert after testing. As seen in the photograph, fracture of the loop part of the insert occurred at the corner locations during testing. This type of failure was typical of the majority of the pull-out specimens with loop inserts.

With the type of failure mode shown in Fig. 4.15(a), there was considerable amount of plastic deformation, including necking at several locations, taking place in the loop part of the inserts during testing. As a result of the large amount of plastic deformation of the inserts, pull-out specimens with loop inserts exhibited ductile behavior as shown in Fig. 4.15(a). In the connection subassemblage specimens, on the other hand, fracture of the loop inserts occurred at much smaller ductility levels than those obtained with the pull-out specimens (see Fig. 4.13). The reason for this major difference in behavior of the connection subassemblage specimens and the pull-out specimens can be clearly seen by comparing the pictures of fractured NC-thread and coil-thread loop inserts in Fig. 4.13 to that shown in Fig. 4.15(a).

As shown in the pictures in Fig. 4.13, fracture of the inserts in Specimens L-NC-V and L-C-V occurred at or near the locations where the rebar pieces had been welded to the inserts during fabrication of the girder pieces (see Figs. 4.8(a) and 4.8(b) for pictures of rebar pieces welded to the inserts). The welding process led to stress concentrations and embrittlement of the insert wire at welding locations, which promoted the premature fracture of insert wire at those locations. Welding of the rebar pieces near the coupler part of the loop inserts also caused the entire load coming into the insert to be transferred to the surrounding concrete through the coupler part of the insert and the welded rebar pieces. This mechanism considerably reduced the contribution of the loop part of the inserts in carrying load as they remained behind the welded rebar pieces, and resulted in a much smaller loop wire length to undergo plastic deformation under tensile loads.

The practice of welding rebar pieces to the inserts resulted in a very limited amount of plastic deformation taking place in the loop inserts in connection subassemblage specimens as compared to the loop inserts in the pull-out tests. As a result of this limited plastic deformation in the inserts, the global load-deflection behaviors of Specimens L-NC-V and L-C-V were not as ductile as they were expected to be based on the load-deflection plots of loop-type inserts obtained during the pull-out tests.

Influence on Bolt Inserts

Different from the case with loop inserts, the practice of welding rebar pieces to bolt inserts improved the behavior of these inserts. The effects of welding rebar pieces to the bolt inserts in Specimen B-V can be seen by comparing the plots in Figs. 4.15(b) and 4.16(a). Fig. 4.15(b) shows the behavior of bolt inserts obtained during tension pull-out tests of reinforced and unreinforced specimens. As shown in the figure, bolt inserts suffered from a sudden loss of tensile load capacity. Even though the existence of steel bars in the reinforced pull-out specimens resulted in an increase in the load capacity, the non-ductile behavior of the bolt inserts remained unchanged between the reinforced and unreinforced specimens.

The load-deflection behavior of Specimen B-V is shown in Fig. 4.16(a). The deformed position of the floor beam piece at several stages of testing are also indicated in the figure. The dashed lines in the inset drawings indicate the undeformed configuration of the floor beam piece, while the floor beam configurations determined from the displacements measured during testing are shown with the solid lines. The deformed floor beam configurations are shown for five locations in the load-deflection curve. Point 2 on the load-deflection plot corresponds to the occurrence of extensive cracking and breakout of concrete around the upper web inserts, while Point 4 denotes the failure of welds between the upper web inserts and the rebar pieces welded to the inserts during fabrication of the girder pieces (see Figs. 4.7 and 4.8(c)).

Fig. 4.16(a) shows that Specimen B-V, which had bolt inserts with rebar pieces welded during fabrication of the girder pieces, did not experience such capacity loss as shown in Fig. 4.15(b) for the pull-out specimens with bolt inserts, which did not have rebar pieces welded to the inserts. Following the extensive cracking and concrete breakout that occurred at the peak load (Point 2), the specimen was able to maintain a constant load until the fracture of the welds between the inserts and the rebar pieces (Point 4).

Between Points 2 and 4 in Fig. 4.16(a), the rebar pieces welded to the inserts were able to transfer the loads from the bolt inserts to the surrounding concrete. The rebar pieces also helped to transfer the loads from the floor beam piece to the girder piece by engaging the girder stirrups in resisting and transferring the loads. After termination of the test, bending of the girder stirrups, rebar pieces welded to the inserts, and the steel dowels that were used to tie the inserts to the reinforcement cage were observed, as illustrated in Fig. 4.16(b). As a result of the new load carrying mechanism caused by the existence of rebar pieces welded to the bolt inserts, Specimen B-V exhibited significantly more stable and ductile behavior than was expected based on the behavior of bolt inserts in the pull-out tests.

As mentioned earlier, stripping of the threads in the coupler part of the bolt inserts and also in the connector rods occurred for the lower web inserts and the flange inserts in Specimen B-V. The reason that this type of failure occurred in the web inserts was probably due to the fact that the 1-1/2 in. height used for the couplers placed at the end of bolts was not sufficient for full transfer of loads in the connection subassemblage specimens. The same type of couplers had also been used for the bolt inserts subjected to pull-out tests, and the inserts were able to carry a maximum of 35.5 kips tensile load in the reinforced pull-out specimens without any damage in the coupler.

The maximum load to which the inserts could be subjected in the connection subassemblage specimens was limited by the tensile capacity of the connector rods. Tension tests performed on connection rods indicated a tensile strength of 30.5 kips for the #6 Grade-60 rebar type connector rods used in Specimen B-V (See Appendix C). This indicates that the tensile load that the bolt insert in the connection subassembly specimen B-V was subjected to (smaller than 30.5 kips) was smaller than the load that the bolt inserts in the pull-out tests were subjected to (as much as 35.5 kips). It is, therefore, clear that the stripping of the threads in the couplers and in the connector rods occurred at smaller load levels than the capacity of the threads under pure tension loading. This observation suggests that the reason for the type of insert failure observed with Specimen B-V was due to the existence of bending exerted on the lower web and flange inserts in addition to the pure tensile loads.

The fact that stripping of the threads occurred in the lower web and flange inserts, but did not occur in the upper web inserts supports the idea of the role of bending on the stripping failure of the inserts. When the concrete breakout occurred near the upper web inserts, this caused additional rigid body rotation of the floor beam under increasing loading, which in turn, created bending of the connector rods for the lower web and flange inserts.

Even though four of the inserts suffered from stripping of the threads in the couplers and in the connector rods, the effect of this failure mode on the global behavior of Specimen B-V remained minimal. As explained earlier, concrete breakout around the upper web inserts was observed to occur at Point 2, and fracture of the welds connecting the rebar pieces to the upper web inserts occurred at Point 4 on the load-deflection curve in Fig. 4.16(a). Up to Point 4, the loads created on the lower web inserts and flange inserts were smaller than the loads on the upper web inserts because of the vertical downward direction of displacement loading applied at the end of floor beam piece. Therefore, stripping of threads in the lower web inserts and flange inserts could only occur after Point 4, and possibly at Point 5. This implies that the load-deflection curve shown in Fig. 4.16(a) would exactly be the same up to Point 5 even though none of the inserts had a stripping type failure.

4.5.2. Inclined Loading Specimens

The concrete cracking and breakout patterns obtained during testing of the inclined loading specimens (i.e., Specimens L-NC-I, L-C-I, and B-I) are shown in Fig. 4.17. Similar to what was observed with the vertical loading specimens, the inclined loading specimen with bolt-type inserts (i.e., Specimen B-I) had a larger concrete breakout area than the loop-type insert specimens (i.e, Specimens L-NC-I and L-C-I).

As mentioned earlier, during the fabrication of the girder pieces, rebar pieces were welded to the inserts and additional rebar dowels were placed around the inserts in order to position the inserts at the desired locations. The bolt-type inserts were able to engage a larger concrete area by engaging the girder stirrups in the girder web and flange through the welded rebar pieces and the rebar dowels, which resulted in a large concrete breakout area. The loop-type inserts, on the other hand, did not have enough strength to take full advantage of the welded rebar pieces and the dowels in engaging the girder stirrups in the load carrying mechanism.

During the load testing of the specimens, the first visual cracking in the girder pieces was observed to occur near the location of the lower layer of web inserts, followed by cracking in the girder flange near the insert locations. Major concrete breakouts occurred in the girder flange and web around the insert locations prior to failure of the individual inserts. Failure of the inserts was noticeable with loud breaking noises. Both concrete breakout and the insert fracture resulted in a sudden drop in the load carried by the specimens in the vertical and horizontal directions.

4.5.2.1. Load-Deflection Behavior

Fig. 4.18 shows the change of the resultant load with the resultant displacement applied by the hydraulic actuators at the floor beam end for the inclined loading specimens. As explained earlier, the displacement applied at the end of floor beams had horizontal and vertical components, with the horizontal component of the displacement being 30 percent of the vertical component and applied at 19 in. from the bottom of the floor beam (i.e., at the level of the upper layer of web connectors). The maximum loads attained by the specimens in the horizontal and vertical directions during the load tests and the value of displacements at these load levels are tabulated in Table 4.3. As seen, Specimens L-NC-I and L-C-I had comparable load capacities in both directions, while Specimen B-I had higher load capacities than those two specimens. Specimen B-I had 21 percent and 22 percent higher load capacity than Specimens L-NC-I and L-C-I, respectively in the vertical direction. In the horizontal direction, Specimen B-I had 39 percent and 25 percent higher capacity than Specimens L-NC-I and L-C-I, respectively. This trend is also seen in the load versus displacement plots of the resultant response shown in Fig. 4.18.

The load drops shown in the load versus displacement plots in Fig. 4.18 are due to either concrete breakout occurring near the insert locations or failure of the inserts themselves. In general, failure of the inserts caused larger decreases in the load resisted by the specimen than the concrete breakout. Following the completion of the load test, all six of the loop inserts in Specimen L-NC-I were observed to be fractured, while in Specimen L-C-I, the upper insert in the bottom flange of the girder remained unfractured. The insert fracture modes that occurred in these specimens were similar to those shown in the photographs in Fig. 4.13. As evident in the load-deflection plots, Specimen L-C-I, which had coil-thread loop insert, had slightly more ductile behavior than Specimen L-NC-I, which had NC-thread loop inserts. The reason for this small difference in behavior is probably the difference in the deformation pattern of the two types of inserts, as explained earlier for the vertical loading specimens.

Different from the loop insert specimens, only two of the inserts in Specimen B-I failed during testing. One of the lower web inserts suffered from stripping of the threads in the coupler part of the insert and in the connector rod. Fracture of the connector rod occurred at the other lower web insert in Specimen B-I. The fracture occurred at the end of the threaded part of the connector rod when the maximum resultant load was reached at a resultant floor beam end displacement of approximately 1.5 in. The remaining four inserts in this specimen remained undamaged when the test was terminated at a resultant floor beam end displacement of approximately 3 in. due to insufficient stroke capacity in the vertical actuator.

4.5.2.2. Behavior in Vertical and Horizontal Directions

Fig. 4.19(a) shows the change of the vertical and horizontal loads applied at the end of the floor beam with the resultant of the floor beam end displacement in Specimen L-NC-I. The maximum load attained by the specimen in the horizontal direction was 55.1 kips, while the vertical load capacity was only 29.5 kips (see Table 4.3). Several points on the resultant response curve are labeled to better explain the progression of the damage in the specimen. The measured floor beam configurations at some of these labeled points are shown in Fig. 4.19(b).

Point #2 on the resultant response curve corresponds to major concrete breakout that occurred around the lower flange insert. This point also marks the maximum vertical load capacity of the specimen. After this point, the vertical load started to decrease, while the load in the horizontal direction continued to increase after having a small drop. Failure of the lower layer of web inserts, which was in the form of fracture of the legs of the inserts, occurred at Point #3, while Point #4 corresponds to the failure of the lower flange insert. As seen, failure of the inserts caused sudden drops in the load capacity of the specimens and had more pronounced effect on the specimen behavior in the horizontal direction.

The major drop in the horizontal load capacity of the specimen that occurred at Point #5 was due to failure of the upper layer of web inserts. The reason that the failure of these inserts caused such a large drop in the horizontal load capacity was because the major part of the horizontal load being transferred from the floor beam piece to the girder piece was through the upper layer of web inserts just before Point #5, as these were the only web inserts that had not failed at this point. As a result, following the failure of these inserts, there were no inserts left in the girder web that could transfer the horizontal load effectively from the floor beam piece to the girder piece. The upper flange insert in Specimen L-NC-I failed at Point #7.

4.6. Post-Test Finite Element Analyses

4.6.1. Description of Finite Element Models

Additional finite element analyses were conducted following the connection subassemblage tests in order to determine the accuracy of the connection subassemblage finite element models in predicting the specimen response and to calibrate the models to the test data. The models used for this purpose were similar to the finite element models of the girder-floor beam connection subassemblages used for designing the test specimens, except that the finite element models used for post-test analyses had more realistic concrete material models.

More detailed material models were used for the concrete in the post-test connection subassemblage finite element models. The concrete stress-strain relations used for the girders and the floor beam pieces in the models are shown in Fig. 4.20(a). Compression portion of the concrete material model was proposed by Popovics, Thorenfeldt, and Collins [67]. Cracking in concrete was modeled by specifying cracking stress, tension-softening modulus, and shear retention values for the materials. A typical value of 0.5 was used for shear retention, while the value of cracking stress varied between 380 and 500 psi depending on the concrete strength. The tension-softening modulus was assumed to be 10% of the modulus of elasticity, and it varied between 330,000 and 430,000 psi depending on the concrete strength.

As mentioned earlier, the damage that occurred at the girder-floor beam interface during testing of the connection subassemblage specimens included two components: (1) cracking in the girder concrete and (2) plastic deformation in the steel inserts and also in the steel connection rods. The floor beam end displacement that occurred due to the deformation of the connection interface was simulated in the finite element models with the deformation of the truss elements connecting the girder and floor beam pieces. In other words, in the finite element models, all the deformation was forced to localize in the truss elements connecting the girder and floor beam pieces. The damage that occurred in the rest of the model was limited to minimal cracking in the floor beam and in the girder outside the connection region. In order to contain the damage in the truss connection elements in the models, cracking properties for the concrete were not assigned to the girder and floor beam elements around the connection interface, as illustrated in Fig. 4.20(b).

The contact surface at the floor beam-girder interface was assigned a coefficient of friction value of 1.2. Even though this value was 20 percent higher than the coefficient of friction specified in ACI 318-99 [7] for concrete placed against hardened concrete, it was used in order to obtain a stable numerical behavior.

During testing of the inclined-loading specimens (i.e., Specimens L-NC-I, L-C-I, and B-I) the magnitude of the horizontal component of the displacement applied at the end of the floor beam was 30 percent of the magnitude of the vertical component of the displacement. Analysis of the test results, however, indicated that due to unequal deformation of the horizontal and vertical loading frames, the ratio of the measured horizontal and vertical displacements at the end of floor beams changed continuously during load testing of the specimens. This ratio was much less than 30 percent at the beginning of testing and was observed to increase to approximately 30 percent toward the end of testing. Based on this observation, the displacement profiles that were applied at the end of floor beams in the connection subassemblage finite element models were adjusted such that the ratio of horizontal and vertical displacements was similar to those that were measured during the testing of the corresponding specimen.

4.6.2. Calibration of Finite Element Models with Test Data

As discussed earlier, analysis of the results obtained from the connection subassemblage tests and those obtained from the pull-out tests suggested that the behavior of the steel inserts in the connection subassemblage specimens could be different than the behavior of the inserts subjected to tension pull-out tests. As a result, the exact load-deflection behavior of the inserts in the connection subassemblage specimens was not known. Therefore, the calibration process of the finite element models included modifying the stress versus plastic strain behavior of the truss connector elements in the models and trying to match the global deflection and gap opening quantities from the models with those measured during testing of the connection subassemblage specimens.

During the calibration process, several stress-strain behaviors for the connector elements were used in the finite element models, including those corresponding to the measured load-deflection behaviors of the pull-out specimens with the loop and bolt-type inserts. For each finite element model with a certain stress-strain behavior for the connector elements, the predicted values of floor beam end deflection and the gap opening between the girder and the floor beam at the

connection interface were compared to the corresponding values measured during testing of the vertical and inclined loading connection subassemblage specimens. For each model, three types of responses were used for comparison between the predicted and measured quantities: (1) response of inclined-loading specimen in the vertical direction, (2) response of inclined-loading specimen in the horizontal direction, and (3) response of vertical-loading specimen.

4.6.2.1. Loop Insert Specimens

Fig. 4.21 presents the plots of measured and predicted load versus floor beam end displacement for specimens with NC-thread loop inserts (i.e., Specimens L-NC-V and L-NC-I), as well as the connector load-displacement behaviors assumed in the models. As shown, three sets of results predicted by the finite element models are included in the plots in Figs. 4.21(a)-4.21(c) together with the measured response of the connection subassemblage specimens.

Fig. 4.21(d) shows the load-deflection behaviors used for the connector elements in the models. It should be noted that the connector load-deflection behaviors shown in the figure were obtained from the stress-strain behaviors used in the finite element models by using proper element area and length. Two of the connector behaviors (i.e., Connectors #1 and #2) correspond to the measured load-deflection response of the two NC-thread loop insert tension pull-out specimens, while the third connector behavior (i.e., Connector #3) was obtained by modifying the measured load-deflection response of one of the tension pull-out specimens. As seen, Connector #3 had the same load capacity as Connector #1, but with a smaller value of displacement at failure, which was supposed to simulate the effect of reduced ductility of the loop-type inserts in the connection subassemblage specimens as compared to those in the tension pull-out specimens.

Figs. 4.21(a) and 4.21(b) show the results for Specimen L-NC-I in the vertical and horizontal directions, respectively. As shown in Fig. 4.21(a), the finite element model underpredicted the load capacity of Specimen L-NC-I in the vertical direction when the connector behavior labeled as Connector #2 in Fig. 4.21(d) was used. As mentioned above, the behavior of Connector #2 was extracted from the measured load-deflection response of one of the tension pull-out specimens with a loop-type insert. The models with Connectors #1 and #3 predicted similar response for the specimen. The model with Connector #3, which had smaller deformation capacity than those corresponding to the measured tension pull-out response of the loop-type inserts, followed the measured response more closely.

Regarding the response of Specimen L-NC-I in the horizontal direction, all three connector behaviors resulted in overprediction of the load capacity, as shown in Fig. 4.21(b). Among the three connector behaviors, Connector #3 had acceptable agreement with the measured response in terms of the load capacity and the shape of the load versus floor beam end deflection curve.

Fig. 4.21(c) shows the comparison of measured and predicted response of Specimen L-NC-V, which had NC-thread loop inserts and was subjected to vertical loading. The level of accuracy in predicting the measured load versus floor beam end displacement response was not as good as those of the inclined loading specimen. As shown in the figure, even for Connector #3, which had reduced deformation capacity as compared to the measured connector behavior of the tension pull-out specimens, overpredicted the displacement capacity of Specimen L-NC-V.

The relationships between the predicted and measured response of Specimens L-NC-I and L-NC-V explained above validated the previous observation that the loop inserts in the connection subassemblage specimens have smaller deformation capacity than those in the tension pull-out specimens.

4.6.2.2. Bolt Insert Specimens

Results of the calibration study for the bolt insert specimens are presented in Fig. 4.22. Figs. 4.22(a) and 4.22(b) show the measured and predicted response on the vertical loading and inclined loading specimens, respectively, while Fig. 4.22(c) shows the connector behavior used in the finite element models, as well as those measured during the pull-out tests. In order to obtain an acceptable agreement between the measured and predicted response of Specimen B-V and B-I, the connector behavior used in the finite element models needed to be modified significantly. Load capacity of the connector elements used in the models was larger than the measured load capacity of the plain concrete bolt insert pull-out specimens but not as high as that of the reinforced bolt insert pull-out specimens. The deformation capacity of the connector after reaching the peak load was also increased significantly for the connectors used in the finite element models.

As evident in Figs. 4.22(a) and 4.22(b), modifications of the connector behavior explained above resulted in good agreement between the measured and predicted response of the vertical loading and inclined loading bolt insert specimens. The finite element models accurately predicted not only the load capacity of the specimens, but also the overall shape of the load-deflection curves.

These results validated the previous hypothesis that the bolt inserts in the connection subassembly specimens had higher ductility than the bolt inserts in the pull-out specimens. As mentioned above, the load capacity of the connectors the finite element models had to fall in between the load capacities of bolt inserts in the unreinforced and reinforced pull-out specimens. The probable reason for this is that in the connection subassemblage specimens the inserts placed in the girder flange were placed between the prestressing strands while there were no prestressing strands around the inserts placed in the girder web. Because the same material behavior was used for connectors in the girder flange and girder web in the finite element models, the load capacity of these connectors had to fall between the load capacities from the unreinforced and reinforced pull-out specimens.

4.7. Summary, Conclusions, and Recommendations

The girder-floor beam connections rely on steel rods that are threaded into inserts which are cast into the bottom flanges and webs of the precast girders, and the exposed lengths of the rods are embedded in the cast-in-place floor beams. Non-prestressed reinforcement also connects the floor beams and deck, but no reinforcement is used to connect the deck and the girders, for which the only stress transfer possible is through bearing.

The investigation coupled the use of finite element analysis with physical testing to determine the load-deformation characteristics of the girder-floor beam connections. In the analyses, three-dimensional solid elements were used to represent the concrete, and the connectors were represented with two-dimensional truss elements. Two sets of concrete properties were used to differentiate between the higher strength plant-precast concrete in the girders and the lower

strength field-placed concrete in the floor beams. The concrete stress-strain behavior was represented using a nonlinear formulation that included compressive crushing and tension cracking properties.

Nonlinear static analyses using the finite element models of the entire bridge were used to determine the modes of deformation of the girder-floor beam connections and to identify the final configuration of the test specimens used to simulate these connections. In these entire-bridge analyses, the lateral loading was applied as a monotonically increasing displacement of a group of nodes on the precast girders on either the interior or exterior faces of the girders. From these analyses, the following observations and conclusions were drawn:

- Bridge response depends on the location of the application of load (with the girder subjected to exterior-face loading undergoing compression damage as the girder web bears against the deck and the girder subjected to interior-face loading undergoing extensive tensile distress in the connectors as this girder is locally pulled away from the bridge).

- A limited number of common deformation modes were identified for the girder-floor beam connection in spite of the large number of vehicle impact locations considered. Two of these deformation modes (Figs. 4.3(a) and 4.3(b)) featured primarily tensile response from the steel connectors, with the tension being generated from either rotation of the floor beam relative to the girder, or from separation of the two members.

- The demands on the steel rods and inserts were predominantly tensile, so that force-deformation models for these elements based on the tensile pull-out tests described in Chapter 3 were adequate for the finite element analyses.

Nonlinear finite element analyses of the girder-floor beam connection test specimens were conducted to verify that the previously identified deformation modes would be properly represented in the experiments. The following observations and conclusions were drawn from these analyses.

- The two common deformation modes for the girder-floor beam connection could be simulated using a subassemblage that included only segments of the girders and floor beams, as well as the fasteners which connect them.

- To achieve the desired deformation modes, the test specimen subassemblages were subjected to either a single vertical load (Fig. 4.3(a)) at the free end of the floor beam segment (which represented the midpoint of an actual floor beam), or a combination of vertical and horizontal loads (Fig. 4.3(b)). For the case of combined vertical and horizontal loading (i.e., inclined loading), the displacement of the horizontal degree-of-freedom was determined to be 30 percent of that for the vertical degree-of-freedom.

A series of six girder-floor beam connection subassemblage specimens were built and tested to determine the behavior of the connections. Three of the specimens were subjected to vertical loading at the free end of the floor beam segments, while the other three specimens had a combination of vertical and horizontal load. Three types of insert-steel rod combination were

investigated, including two types of loop inserts and one bolt insert. The test specimens were loaded in displacement control until the subassemblages lost a large fraction of peak load capacity. From these tests, the following observations and conclusions were made:

- Specimen response to load was initially closely linear, but the stiffness diminished gradually until peak load capacity was reached.

- There was no clear trend regarding which type of insert possessed the largest loading capacity, with the coil loop insert offering greater peak load for the vertical load specimens, and the bolt insert specimen exhibiting the largest load capacity for the case of combined vertical and horizontal load.

- Behavior of the inserts in the connection subassemblage specimens was significantly affected by the construction method followed during the fabrication of prestressed concrete girders. The welding of rebar pieces on the loop and bolt inserts changed the load-carrying mechanism of the inserts. The effect was beneficial in the case of bolt inserts, while the deformation capacity of the loop inserts was reduced. The welding of rebar pieces resulted in premature steel fracture at the weld locations in the loop inserts (due to stress concentration and steel embrittlement), while it provided improved anchorage to concrete and improved deformation capacity for the bolt inserts.

- Deterioration of specimen load capacity was associated with (a) concrete cracking, (b) formation of a cone breakout surface, (c) yielding of the threads on the steel rods, the inserts and/or the girder stirrups to which they were tied, and (d) fracture of the inserts.

- The subassemblages were able to resist large displacements after attaining peak load, even though post-peak load carrying capacity was undermined in most cases.

- The observed load-deformation behavior of the subassemblage specimens was reproduced using the nonlinear finite element models described earlier as long as accurate descriptions of the load-deformation characteristics of the inserts in the specimens were assumed.

The analyses and experiments described here suggest a complex and highly nonlinear behavior for through-girder pedestrian bridges that rely on embedded steel inserts and steel rods for fastening the floor beams to the precast girders. The post-peak deformation capacity of the girder-floor beam connections allow for redistribution of loads between the connected members. Therefore, failure of some inserts, or even some girder-floor beam connections do not necessarily imply collapse. Additional finite element analyses of an entire bridge system utilizing the information presented here on the response and modeling of the girder-floor beam connections were performed in an attempt to perform an assessment of a prestressed concrete through-girder pedestrian bridge system. These analyses, as well as load tests performed on the details used at the girder ends, are explained in the following chapters.

Table 4.1. Connection Subassemblage Test Variables and Concrete Strengths.

Specimen designation	Insert type	Loading direction	Concrete strength, psi	
			Girder	Floor beam
L-NC-V	Loop Regular thread	Vertical	8650	3500
L-C-V	Loop Coil thread	Vertical	9800	4400
B-V	Bolt	Vertical	9050	3500
L-NC-I	Loop Regular thread	Inclined	9300	3550
L-C-I	Loop Coil thread	Inclined	8900	4700
B-I	Bolt	Inclined	9850	5900

Table 4.2. Summary of Measured Response for Vertical Loading Specimens.

Specimen designation	Peak load kips	Displacement at peak load inches	Load at 1 in. displacement kips	Load at 2 in. displacement kips
L-NC-V	20.8	0.20	10.0	0.4
L-C-V	25.7	0.84	21.5	11.2
B-V	20.8	0.21	17.0	13.1

Table 4.3. Summary of Measured Response for Inclined Loading Specimens.

Specimen designation	Vertical Direction		Horizontal Direction		Resultant Response	
	Peak load kips	Displacement at peak load inches	Peak load kips	Displacement at peak load inches	Peak load kips	Displacement at peak load inches
L-NC-I	29.5	0.40	55.1	0.17	59.3	0.76
L-C-I	29.2	0.36	49.5	0.25	54.8	0.55
B-I	35.7	0.60	68.8	0.44	75.0	1.46

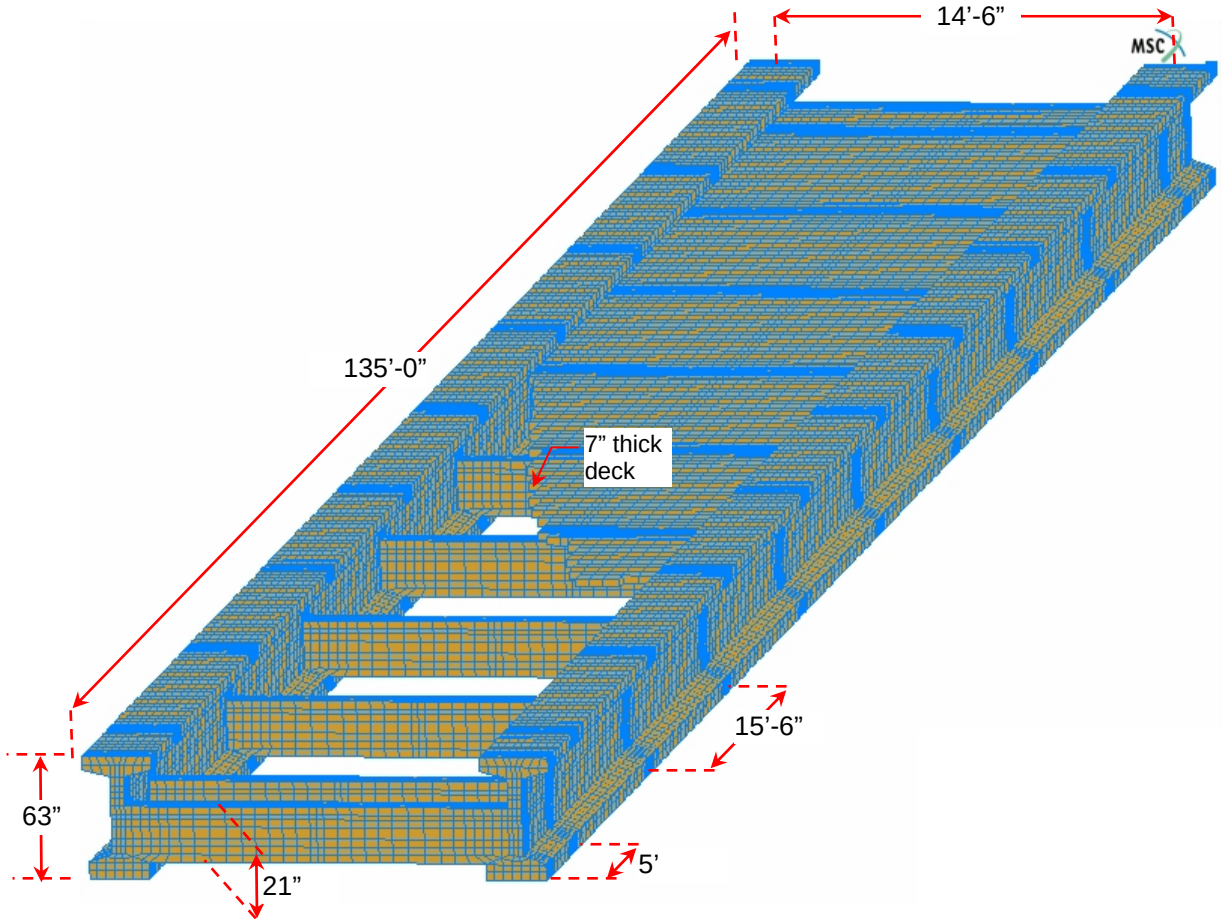

Fig. 4.1. Dimensions used in full-bridge finite element model.

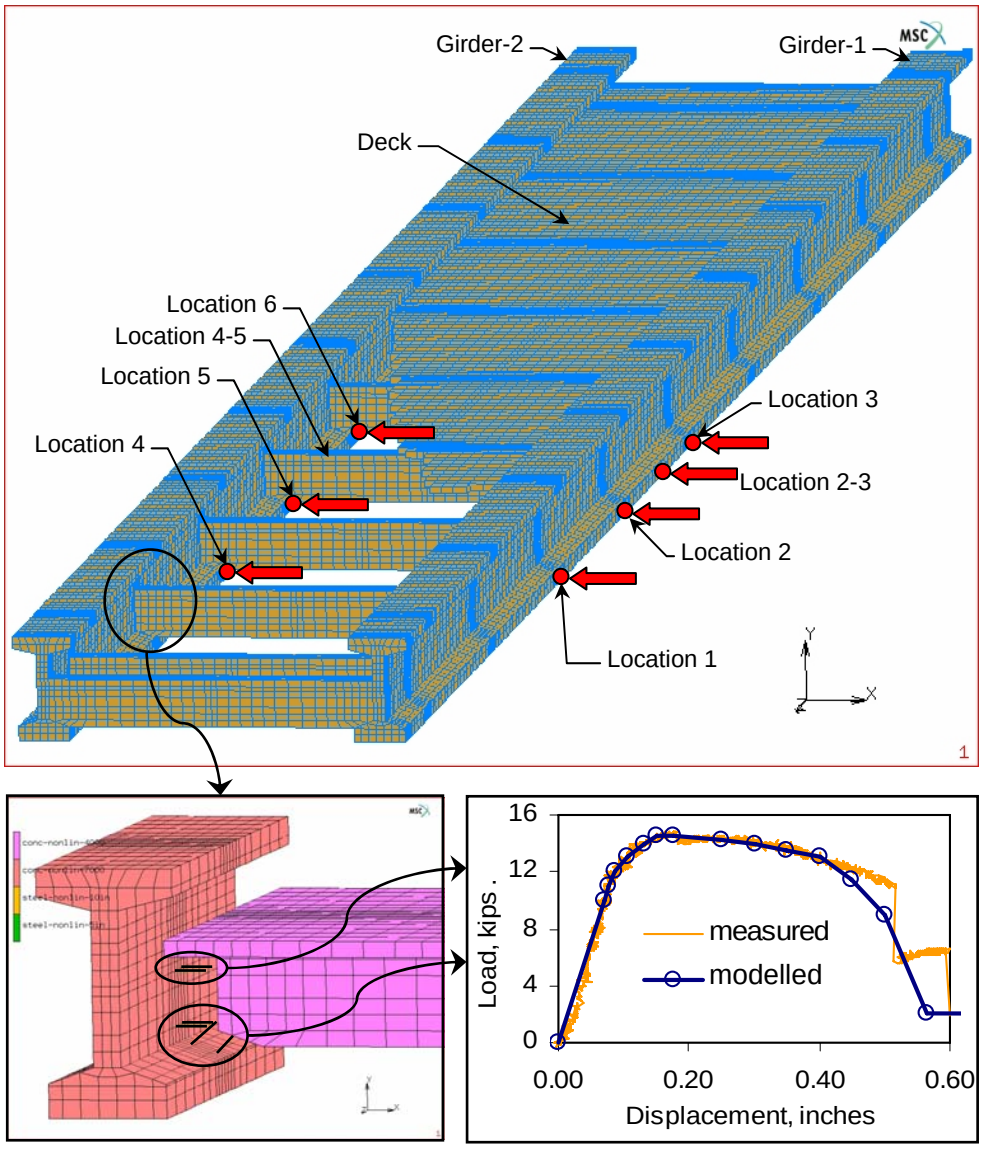

Fig. 4.2. Modeling of girder floor beam connection in full-bridge finite element model.

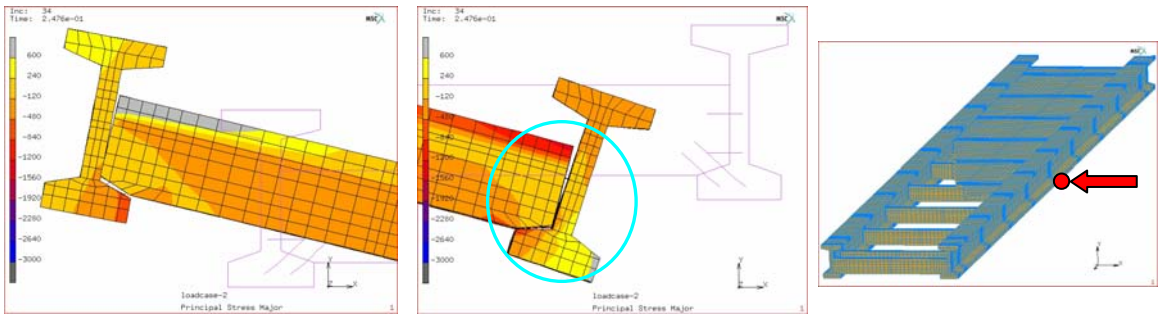

(a)

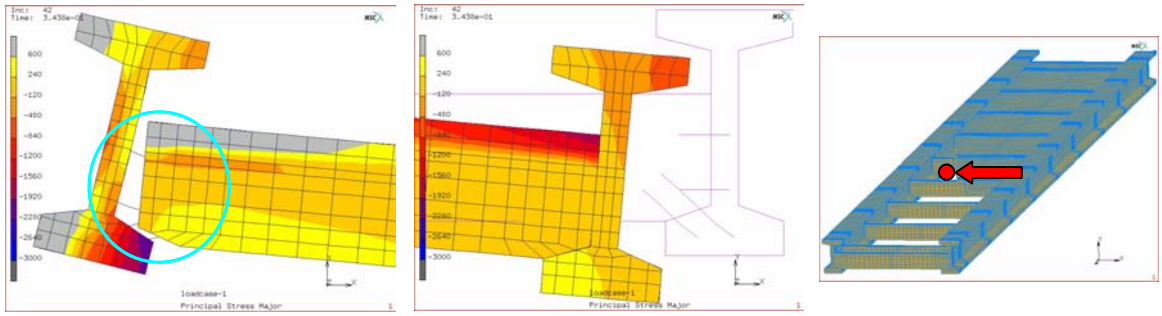

(b)

Fig. 4.3. Gap opening patterns observed in full-bridge models.

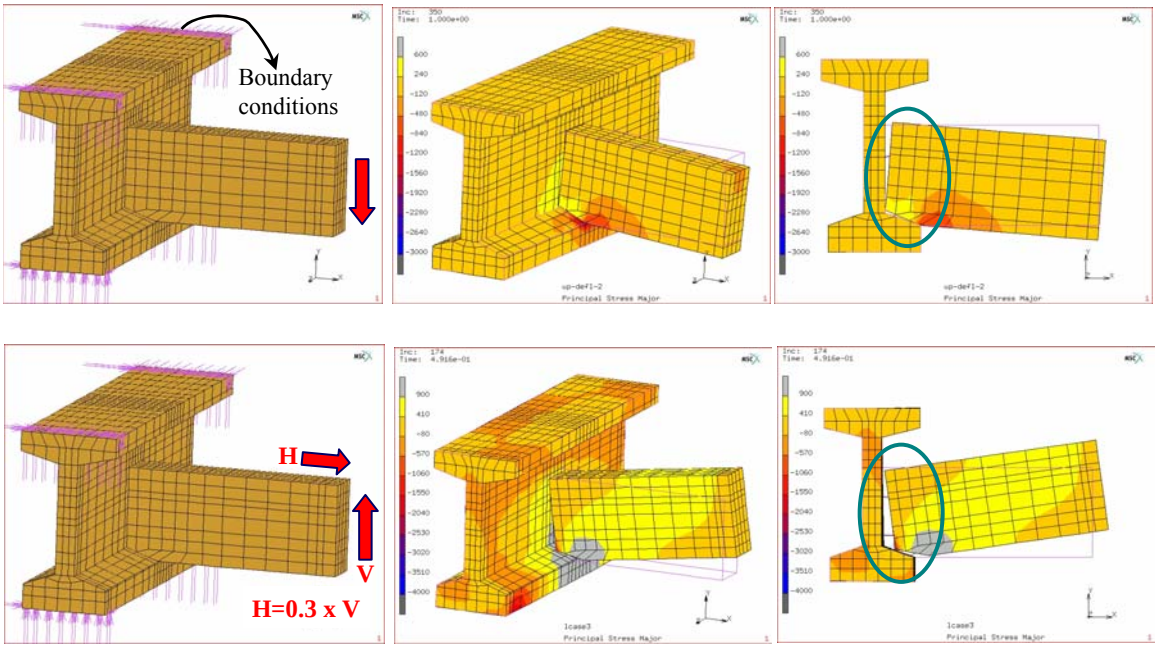

Fig. 4.4. Loading conditions determined from connection subassemblage models.

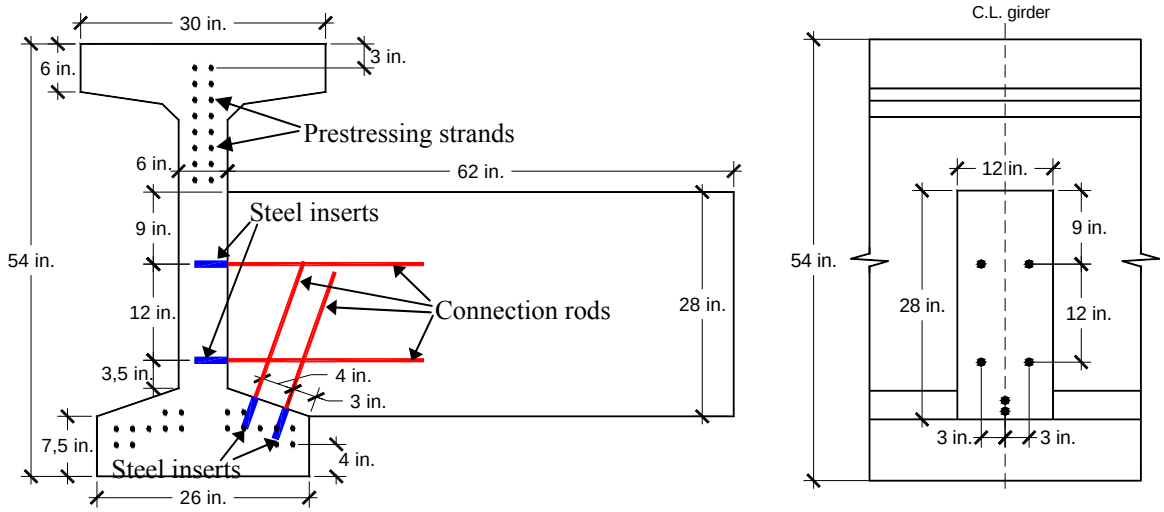

Fig. 4.5. Specimen dimensions and position of steel inserts.

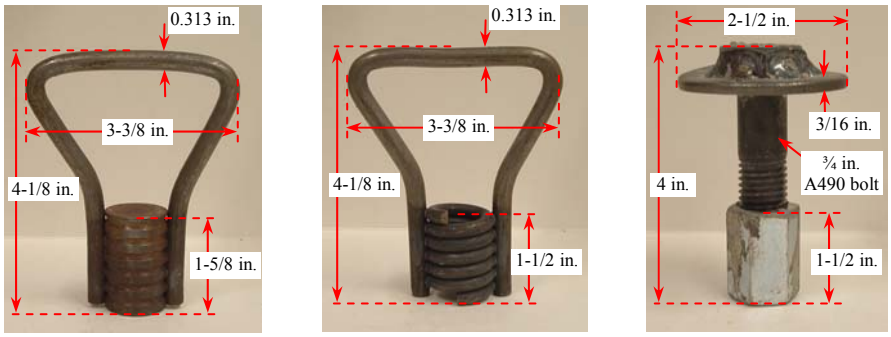

(a) NC-thread loop insert (b) Coil-thread loop insert (c) Bolt insert

Fig. 4.6. Inserts used in specimens.

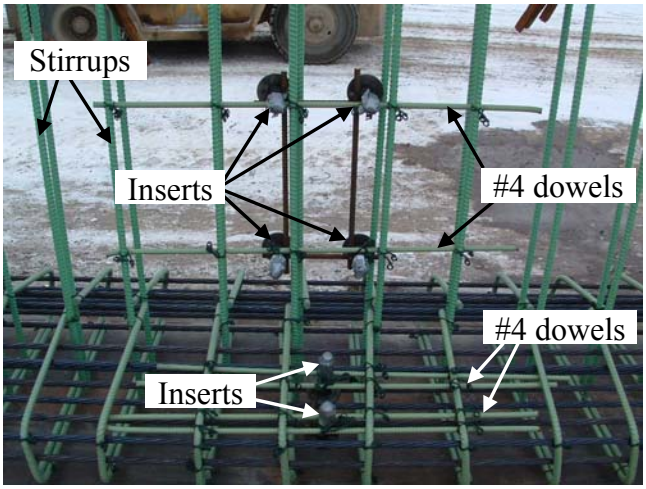

Fig. 4.7. Placement of steel inserts.

(a) (b) (c)

Fig. 4.8. Steel inserts to be placed in girder segments: (a) loop inserts to be placed in girder web; (b) loop inserts to be placed in girder flange; (c) bolt insert to be placed in girder web.

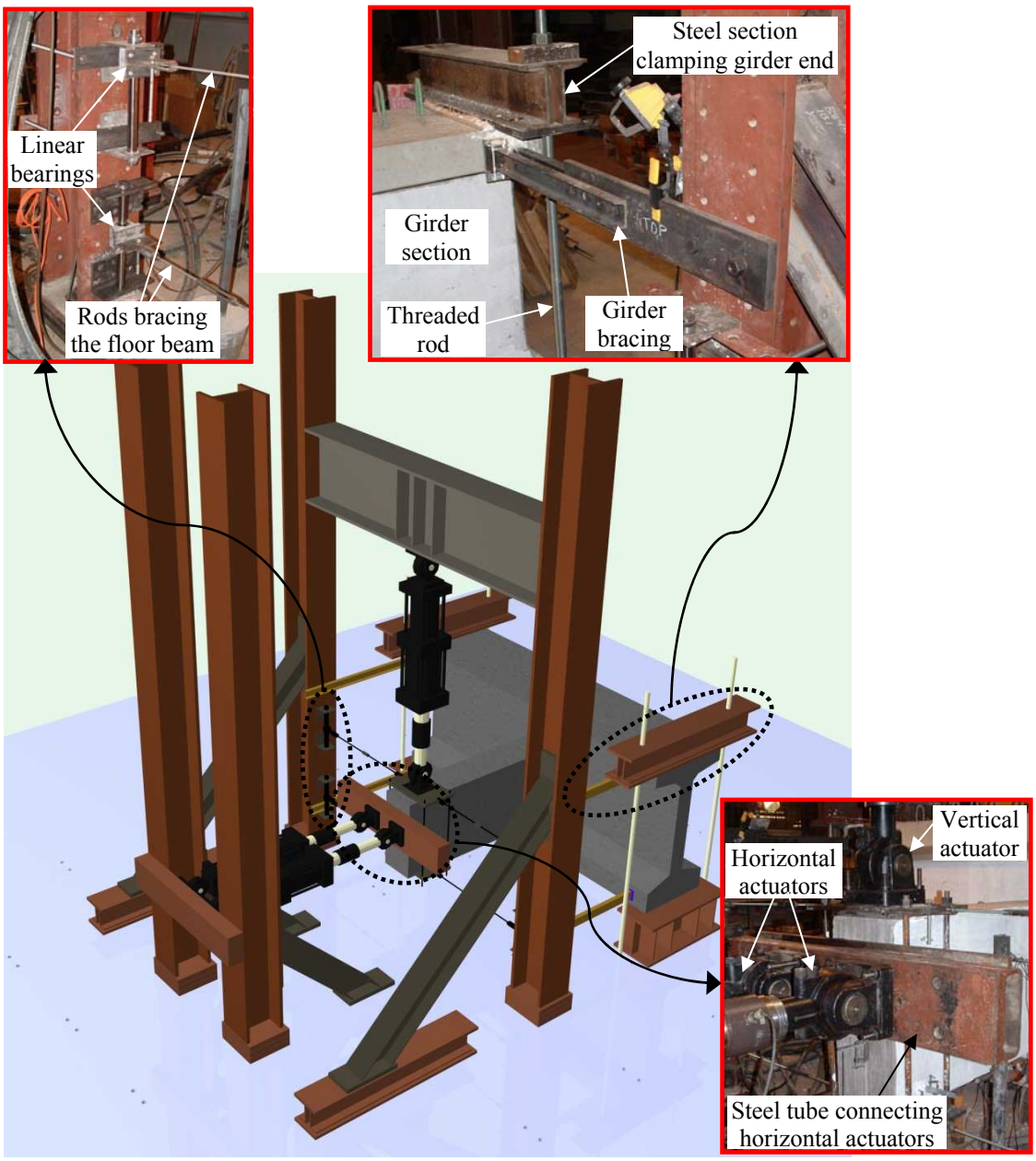

Fig. 4.9. Details of test setup.

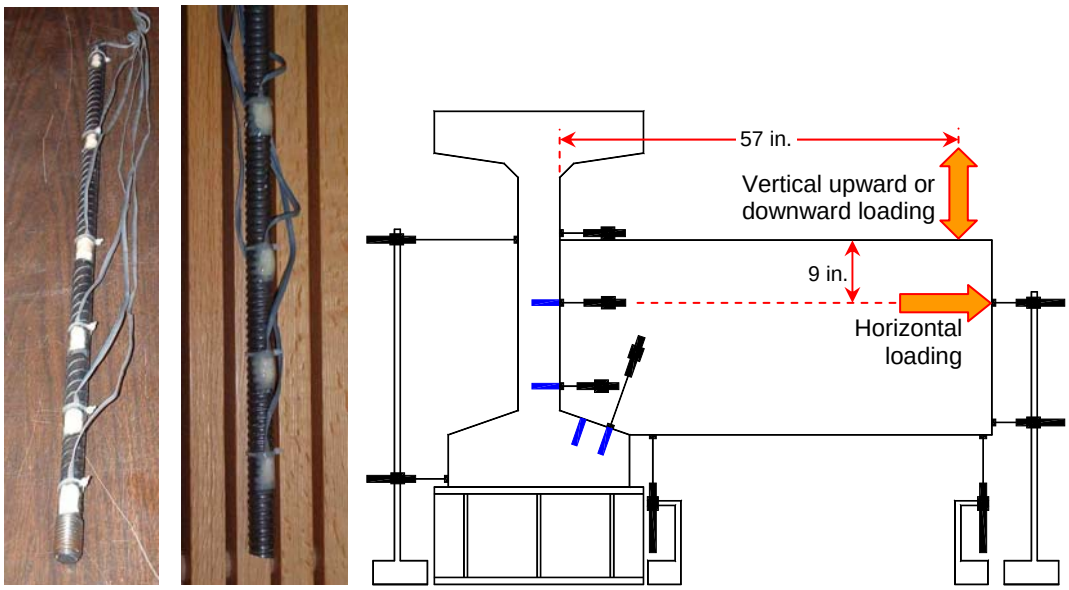

(a) (b) (c)

Fig. 4.10. Instrumentation used on specimens: (a) strain gages placed on NC thread rod; (b) strain gages placed on coil thread rod; (c) typical LVDT locations.

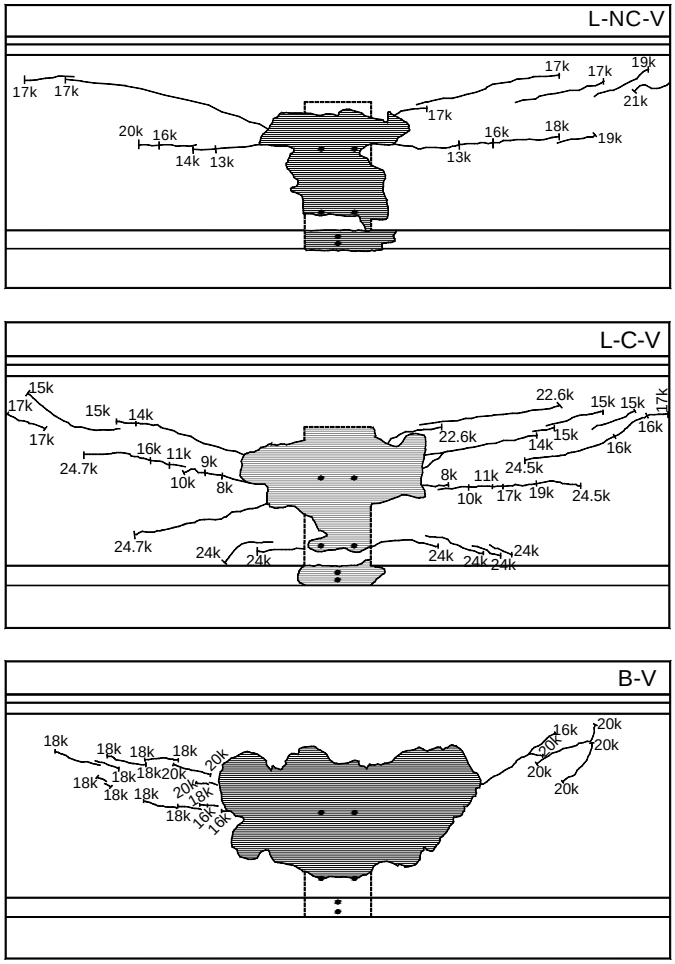

Fig. 4.11. Concrete breakout and cracking pattern in vertical loading specimens.

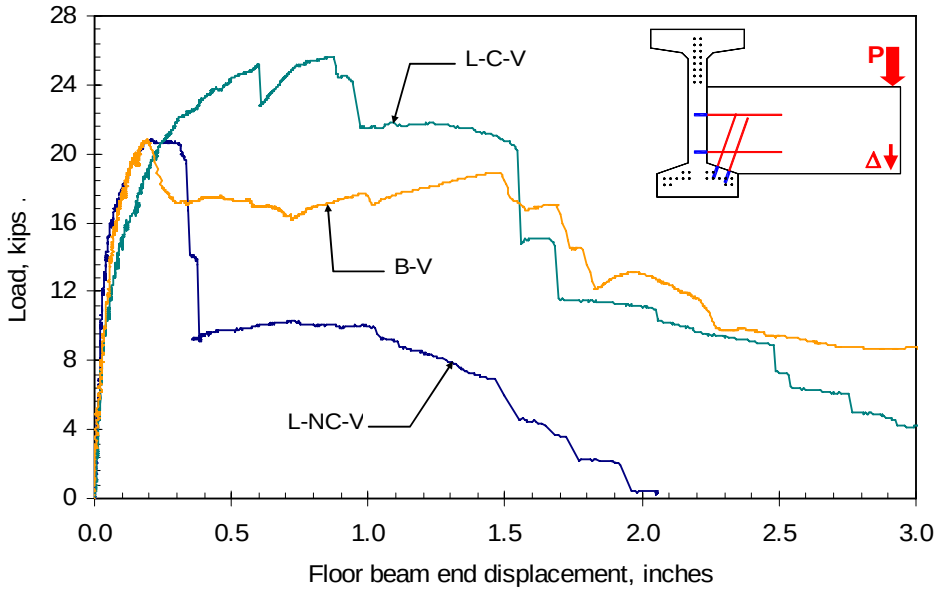

Fig. 4.12. Load-deflection behavior for vertical loading specimens.

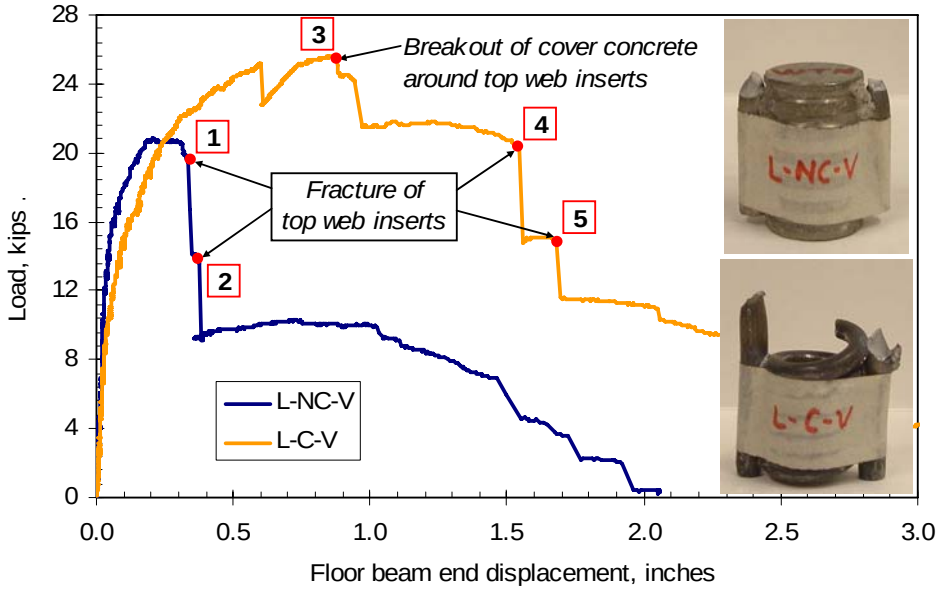

Fig. 4.13. Load-deflection behavior for vertical loading specimens with loop inserts.

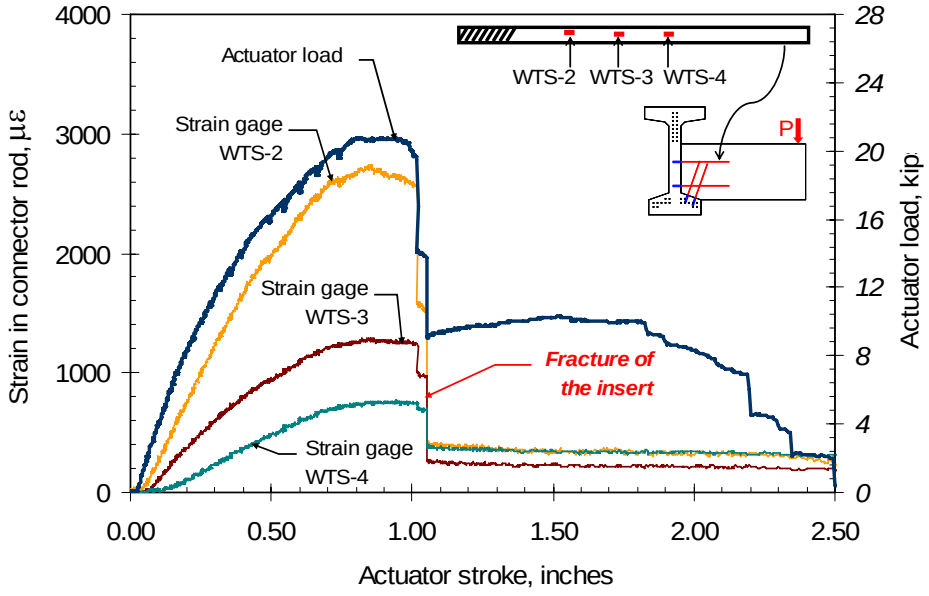

(a) Specimen L-NC-V

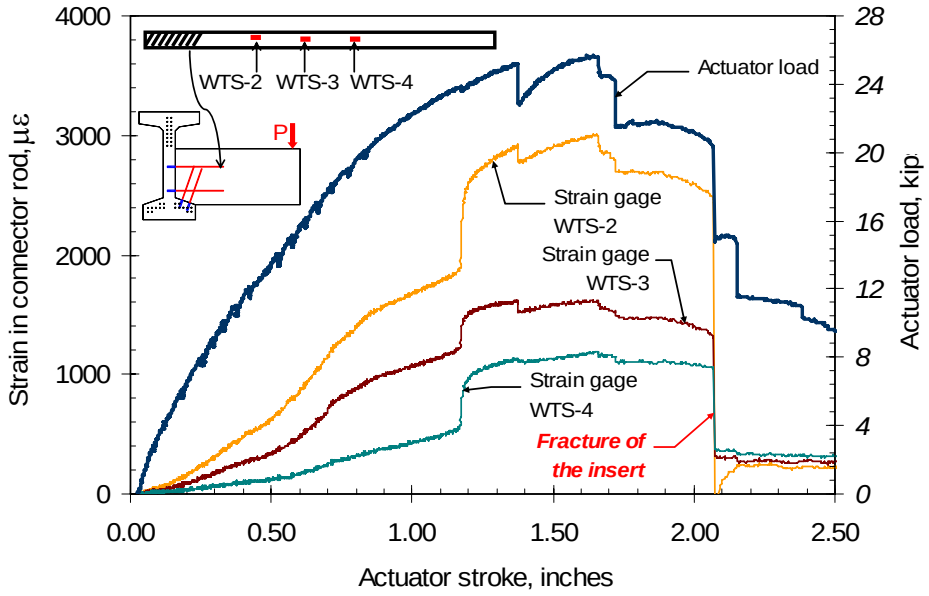

(b) Specimen L-C-V

Fig. 4.14. Strain in connector rods relative to actuator load and displacements.

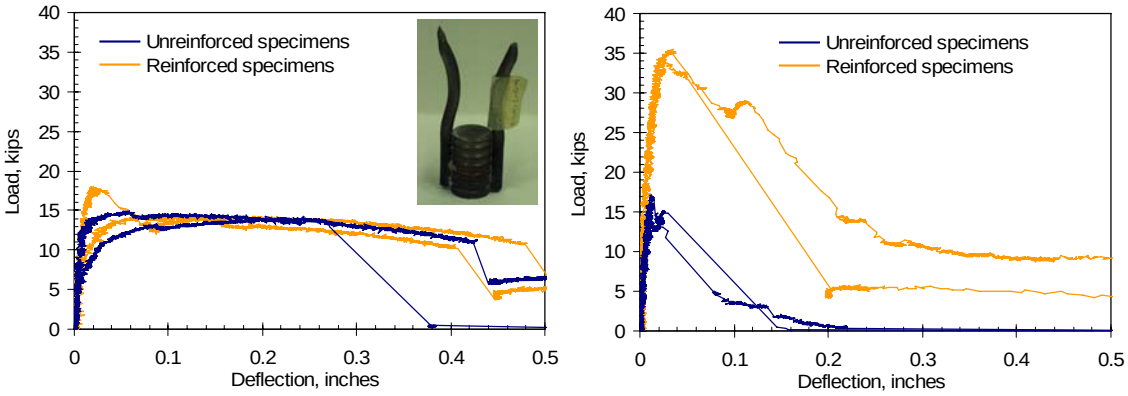

(a) NC-thread loop insert (b) Bolt insert

Fig. 4.15. Behavior of inserts from pull-out tests.

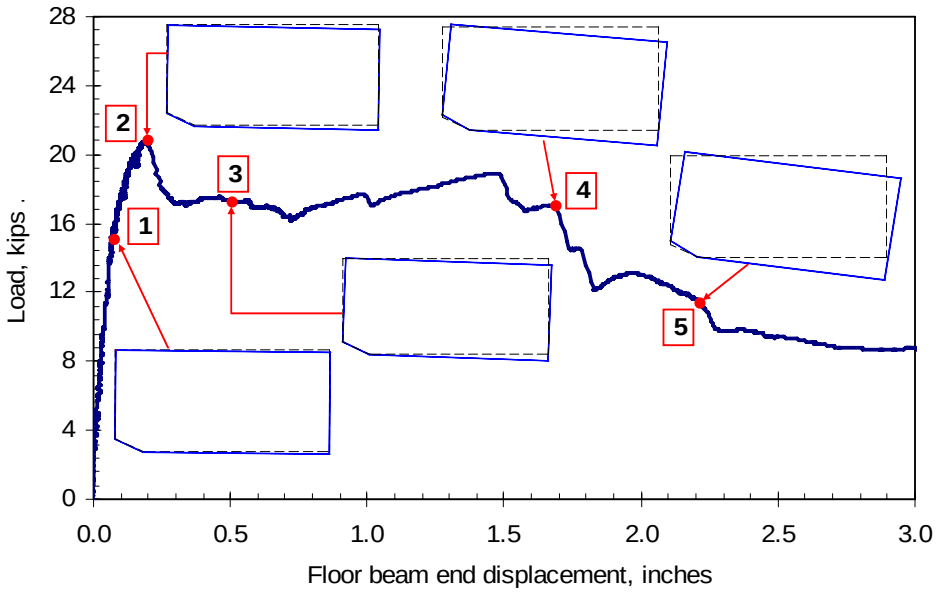

(a) Load-deflection behavior

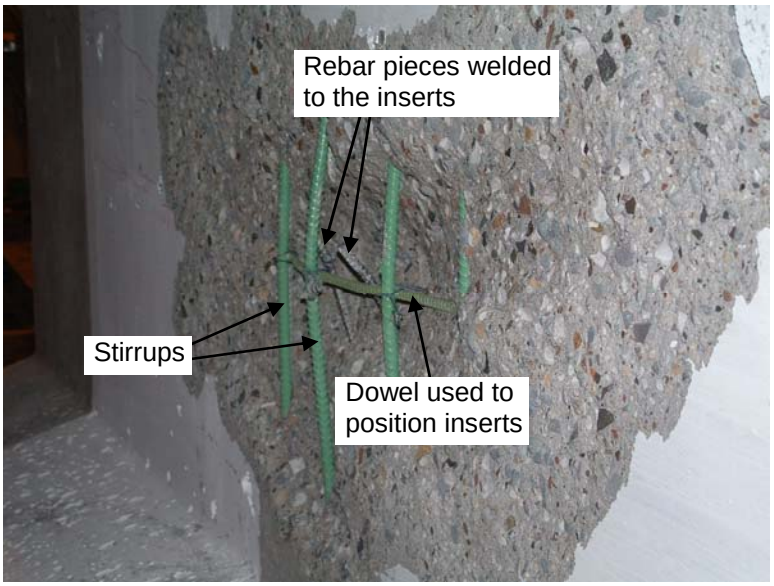

(b) Close-up view of top web insert location in girder

Fig. 4.16. Behavior of Specimen B-V.

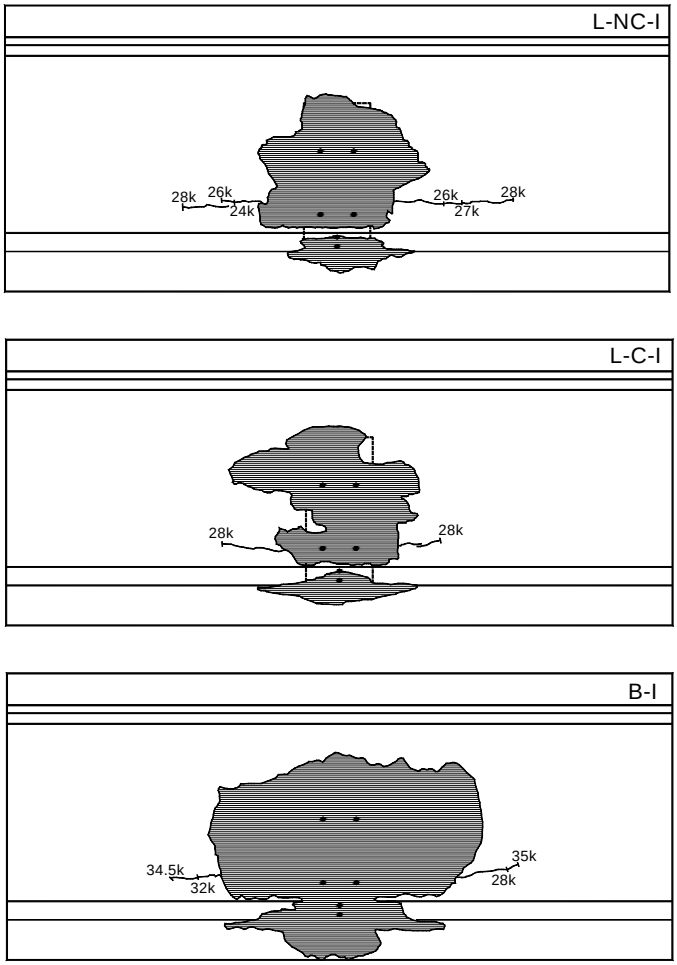

Fig. 4.17. Concrete breakout and cracking pattern in inclined loading specimens.

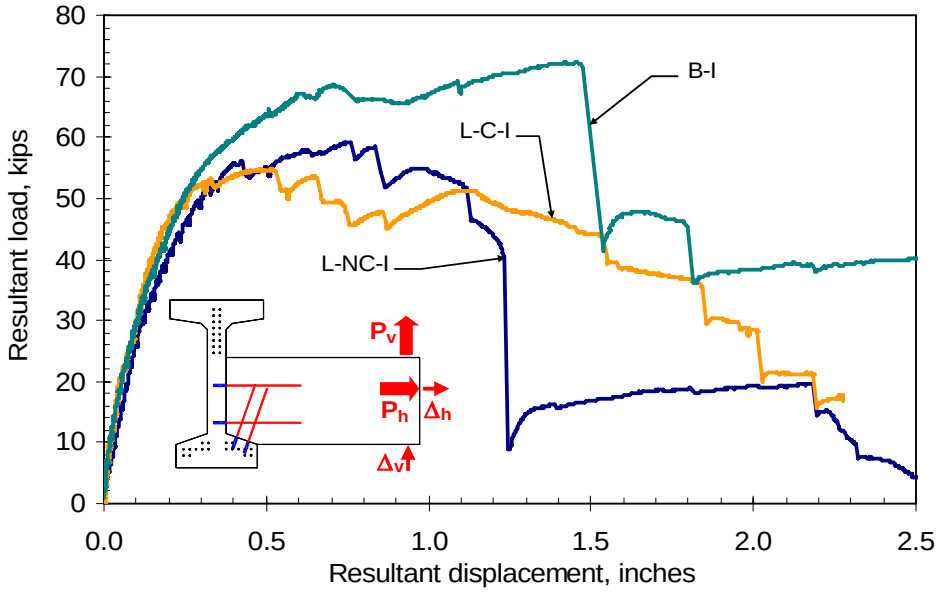

Fig. 4.18. Load-deflection behavior for inclined loading specimens.

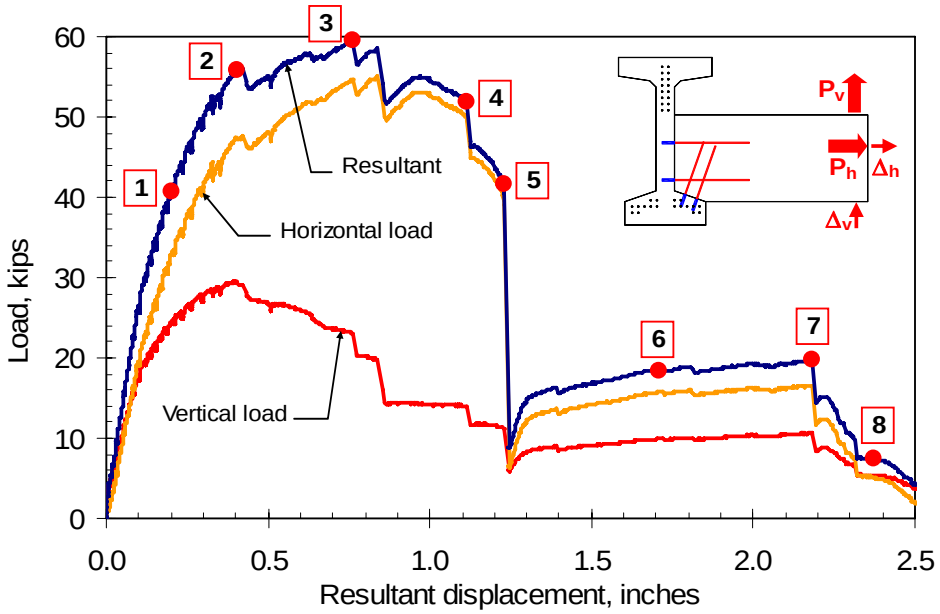

(a) Load-deflection plots

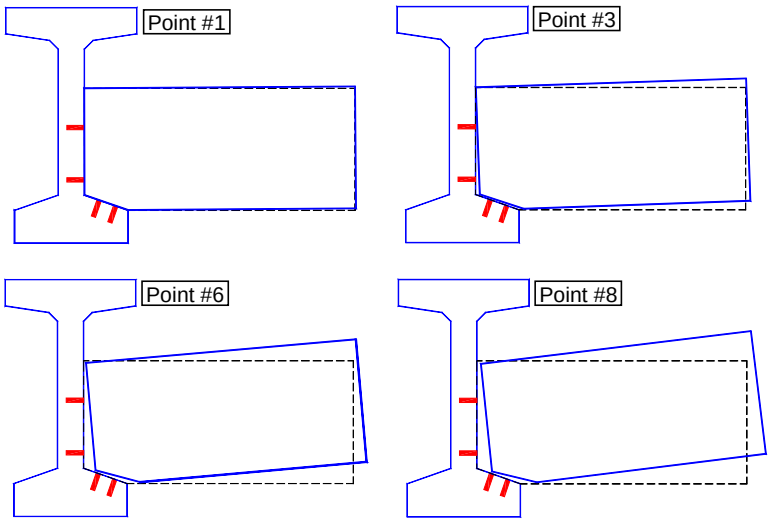

(b) Deformed shape of specimen during testing

Fig. 4.19. Behavior of Specimen L-NC-I.

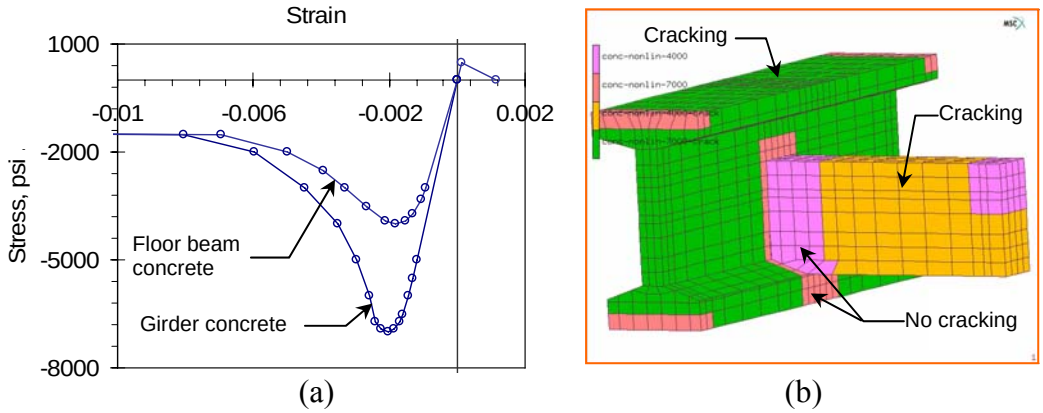

Fig. 4.20. Modeling of concrete material in finite element models: (a) concrete stress-strain behaviors used for girder and floor beam pieces; (b) Definition of cracking properties throughout the model.

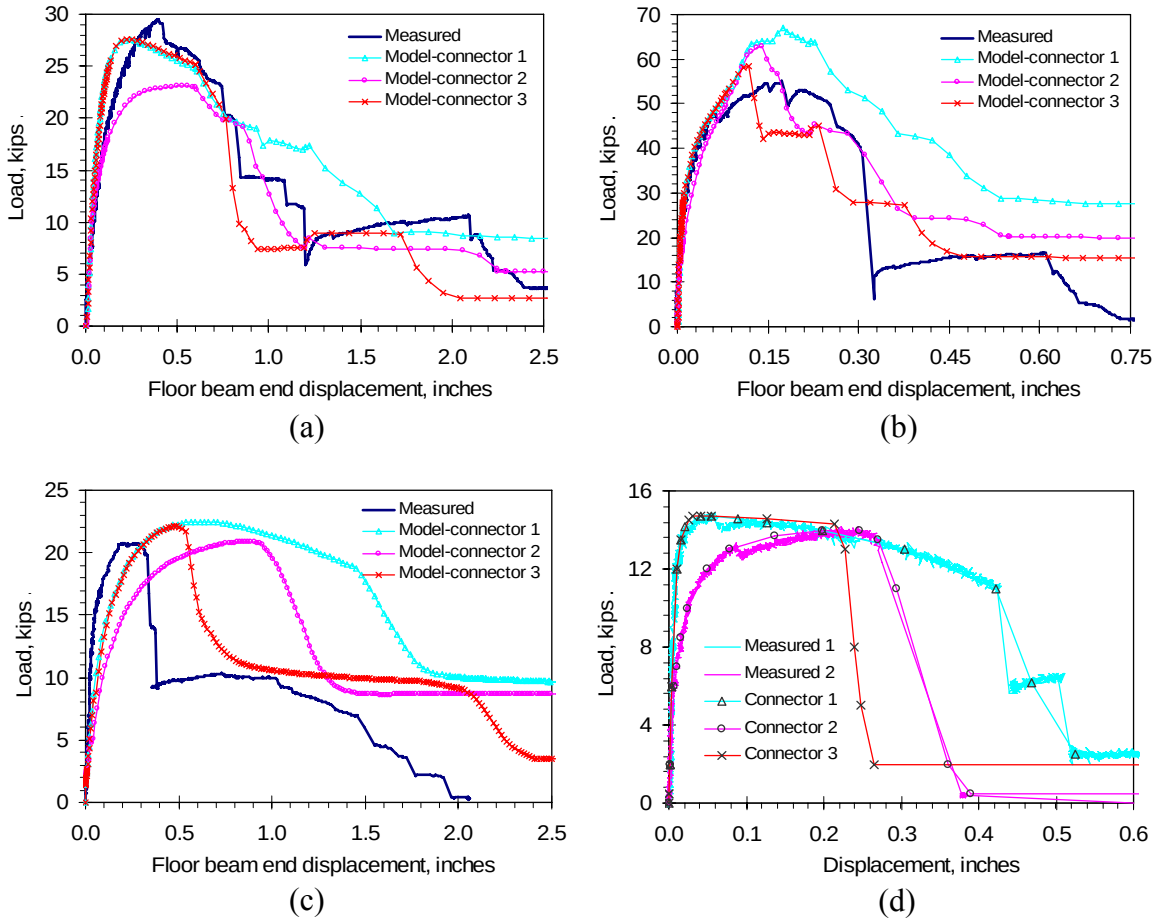

Fig. 4.21. Calibration of connection subassemblage models (NC-thread loop insert specimens): (a) overall response of Specimen L-NC-I in vertical direction; (b) overall response of Specimen L-NC-I in horizontal direction; (c) overall response of Specimen L-NC-V; (d) connector behavior.

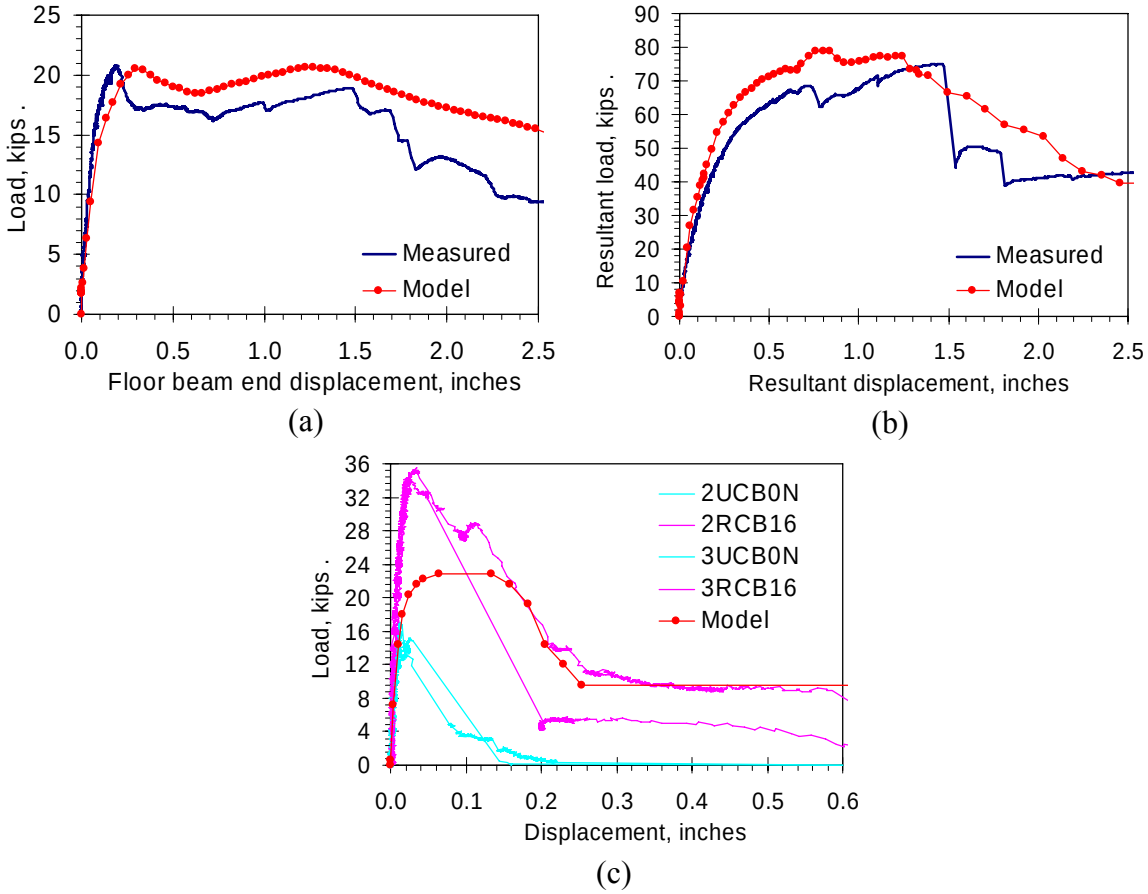

Fig. 4.22. Calibration of connection subassemblage models (bolt insert specimens): (a) Specimen B-V; (b) Specimen B-I resultant response; (c) connector behavior.

Chapter 5
Tests on Girder Support Details

5.1. Introduction

This chapter describes the static tests performed on the assemblies used to support the prestressed concrete girders at the bridge abutments and piers. Analysis of a bridge system under transverse impact loads that would cause extensive damage in bridge components and sliding of girders on the bridge supports requires an accurate modeling of the stiffness and strength of support details used at the girder ends. For the case of prestressed concrete through-girder pedestrian bridge systems, this requirement becomes more important as larger magnitudes of transverse displacements are expected to occur at the ends of girders because of the relatively small bridge self-weight, which results in smaller resistance against sliding of girder ends under transverse loads. Also, there are only two girders present to resist the transverse impact loads in these types of bridges, which increases the likelihood of support movements under transverse impact loads.

The aim in performing these tests was to evaluate the strength and stiffness properties of the support details used at the ends of prestressed concrete girders in through-girder pedestrian bridges. The significance of the support flexibility on the overall load-deformation behavior of the bridge system under dynamic and static loading is numerically investigated in Chapter 6. Data obtained from the tests explained in this chapter were incorporated in the finite element models of a complete bridge system, which were used to perform assessment of a typical bridge system with static, dynamic, and stability analyses.

5.2. Description of Test Specimens

The bridge plans indicated one end of the prestressed concrete girders as “fixed” and the other end as “expansion.” The expansion-end detail was intended to account for the longitudinal displacements at the girder ends caused mainly by thermal expansion and contraction of the bridge. Figs. 5.1(a) and 5.1(b) shows the support details used at the expansion end and fixed end, respectively, of prestressed concrete girders used in through-girder pedestrian bridges. Each support assembly consisted of an elastomeric bearing pad, a steel bearing plate, and a steel curved plate. The bearing pad was placed directly on the bridge seating. The bearing plate and the curved plate were attached to each other and they sat on top of the bearing pad.

Similar details were used at the fixed and expansion ends, except at the fixed end there were two 1-1/2 in. diameter anchor rods embedded into the bridge seating to provide restraint against movement of the bearing plate in the directions along and perpendicular to the longitudinal axis of the bridge. As seen in Figs. 5.1(a) and 5.1(b), the bearing plate at the fixed end was longer to accommodate the holes for the anchor rods. In order to allow the expansion end of the girders to move under the effect of thermal changes without much resistance, a thicker bearing pad was used at the expansion end of the girders compared to the fixed end.

Two specimens, one with an expansion-end detail and one with a fixed-end detail, were tested. The specimens were designed to simulate the details used at the fixed and expansion ends of the girders. The specimens consisted of a bottom concrete block simulating the bridge abutment, a

top concrete block simulating the girder bottom flange, and a support assembly placed in between the two concrete blocks, as shown in Figs. 5.2 and 5.3(a).

5.2.1. Design and Construction of Specimens

The specimens were constructed at the University of Minnesota Structural Engineering Laboratory. The specimen design was based on the details shown on plans for several prestressed concrete through-girder pedestrian bridges that had been constructed in Minnesota. The bottom concrete block simulated the details used at the bridge abutments, while the top concrete block simulated the girder bottom flange.

The bottom concrete block dimensions and the reinforcement layout for the specimens are shown in Fig. 5.3(b). The figure shows the details for the fixed-end specimen, while similar details were used for the expansion-end specimen, except for the use of anchor rods. Some of the dimensions shown in the figure were determined based on either the details shown in bridge plans or personal communication with the Mn/DOT Bridge Office personnel, while the rest of the dimensions were determined based on the constructability and testability of the specimens at the laboratory. The dimensions determined based on the bridge details or the request from the Mn/DOT personnel included the spacing between anchor rods, 5 in. edge dimensions for the anchor rods, 15 in. depth for the anchor rods, and the step shown at one of the top corners of the block. Similarly, the reinforcement layout used in the specimens was from the bridge details, except some of the modifications as requested by the Mn/DOT Bridge Office personnel. The main modification in the reinforcement layout was to provide one vertical stirrup on the exterior side of each anchor rod so that these rods were enclosed by the stirrups (for the case of fixed-end specimen). The reinforcement in the bottom part of the block was included to prevent excessive cracking in the concrete during testing of the specimen.

Fig. 5.4 illustrates the placement of bearing pad and bearing plate assembly on the bottom concrete block. Positioning of anchor rods in the fixed-end specimen was also shown in the figure. The bearing plate and curved plate assembly was supported by the bearing pad on the top surface of the bottom block. In the fixed-end specimen, lateral movement of the bearing plate was prevented with two 1-1/2 in. diameter anchor rods that were embedded inside the concrete block. The holes for the anchor rods were cast inside the test specimens, as opposed to the drilled holes used in the field. Hilti HIT HY 150 epoxy grout was used to secure the anchor rods in place. Similarly, three holes were cast in the bottom part of the concrete block on each side for the threaded rods that were used to clamp the concrete block to the laboratory strong floor for load testing of the specimen.

The reinforcement details and dimensions for the top concrete block are shown in Fig. 5.5(a). The details shown in this figure was common to both the fixed-end and expansion-end specimens. The 26 in. width used for the top block was the width of the bottom flange of Mn/DOT Type 63 section, which is the section used in through-girder pedestrian bridges. The 11 in. depth used in the specimen corresponds to the depth of the bottom flange of Mn/DOT Type 63 section (including the inclined portion of the bottom flange). The reinforcement layout used for the top concrete blocks in the test specimens was identical to the reinforcement layout in the bottom flange of prestressed concrete sections shown in bridge plans. The prestressing strands in the girders were simulated with #4 rebars placed inside the top concrete blocks. As indicated in

Fig. 5.5(a), each top concrete block had a sole plate that was cast with the block. Fig. 5.5(b) shows the details of the sole plates used in the test specimens. The studs that were welded to the sole plates allowed the transfer of lateral loads applied to the top concrete block to the sole plate. The loads were then transferred from sole plate to the curved plate and the bearing plate. The sole plates had two 1-3/4 in. diameter holes for the 1-1/2 in. diameter pintles that were attached to the curved plates. Load transfer from the sole plate to the curved plate occurred through these pintles.

Details of the curved plate and bearing plate assemblies used in the expansion-end and fixed-end specimens are shown in Figs. 5.6(a) and 5.6(b), respectively. As seen, both types of assemblies had two 1-1/2 in. diameter pintles connected to the curved plates. As explained above, these pintles fit into the holes in the sole plate, and the sole plate itself acts compositely with the top concrete block through the studs welded on the plate. The curved plates are connected to the bearing plates with continuous welds along four sides. As seen in Fig. 5.6, the assembly used for the fixed-end specimen had a longer bearing plate than the one used for the expansion-end specimen. Table 5.1 presents the dimensions of the curved plates, bearing plates, and bearing pads used in the fixed-end and expansion-end specimens. The extra length of bearing plate accommodated the 2 in. diameter holes for the anchor rods in the fixed-end specimen.

Beside the bearing plate and the anchor rods, the other difference between the fixed-end and expansion-end support assemblies was the thickness of the bearing pads used in the two types of assemblies. The fixed-end assembly included a ½ in. thick bearing pad, while the thickness of the bearing pad in the expansion-end assembly was 1-3/4 in. to allow longitudinal displacement of the girder ends with respect to the bridge abutment. The bearing pad used in the expansion-end specimen consisted three 1/8 in. thick steel plates sandwiched between layers of neoprene. The bearing pad used at the fixed-end specimen did not have steel plates because of the relatively small thickness of the neoprene pad.

The expansion-end and fixed-end specimens were cast separately at the University of Minnesota Structural Engineering Laboratory using commercial ready-mixed concrete. The measured concrete compressive strength at the time of testing was 4500 psi for the fixed-end specimen and 6200 psi for the expansion-end specimen. Considering that a concrete strength of 4000 psi was specified in the bridge plans, the concrete strength in the expansion-end specimen was 55 percent higher than the specified strength. As explained in the following section, the deformation mode of the expansion-end specimen was a combination of sliding between the components and shear deformation in the neoprene pad, without any concrete damage in the top and bottom concrete blocks. Therefore, the higher concrete strength used in the expansion-end specimen did not have any effect on the test results for this specimen.

5.3. Instrumentation, Test Setup, and Testing of Specimens

The specimens were instrumented with LVDTs prior to the load tests in order to determine the displacement of various components. The fixed-end specimen was also instrumented with external and internal strain gages. Fig. 5.7 shows the location of LVDTs and external strain gages placed on the fixed-end specimen. The LVDTs placed on the specimen are indicated with arrows while the strain gages are indicated with rectangles in the figure. The LVDT locations used in the expansion-end specimen were similar to those shown in Fig. 5.7. The vertically

positioned LVDTs were used to measure the vertical displacement of the top block during the vertical loading phase of load testing. Readings from these LVDTs were also used to determine the amount of vertical displacement of the top block during the horizontal loading phase. Lateral displacement of the top block, the bearing plate, and the bottom block during the horizontal loading phase was measured with the horizontally-positioned LVDTs.

The surface strain gages (indicated with rectangles in Fig. 5.7) placed on the front face of bottom concrete block were used to detect the initiation of concrete cracking during load testing of the fixed-end specimen. As shown in Fig. 5.7, the strain gages were placed in two rows centered with respect to the anchor rod. The specimens were also white washed with a mixture of lime and water to facilitate visual detection of concrete cracking during load testing. The load versus deflection behavior of the specimens was pen-plotted during load tests and continuously monitored for stiffness changes, which was an indication of damage progression in the specimens.

The sole plate in the fixed-end specimen was also instrumented with strain gages. One strain gage was placed on each of the six shear studs along the axis of the studs. The aim in providing these strain gages was to detect rupture of the studs during load testing of the fixed-end specimen.

The specimens were subjected to two-phase loading. In the first loading phase, vertical compressive loading was applied to the top surface of the top concrete block. This loading simulated the vertical reaction at the girder ends due to the self-weight of the bridge structure. The second loading phase simulated the transverse loading exerted on the girder ends due to impact loading caused by an over-height vehicle striking the bottom flange of the girder. The second loading phase consisted of application of a horizontal load on one side of the top concrete block.

In the first loading phase, the loading was applied by a vertically positioned 110-kip capacity hydraulic actuator in force-controlled ramp mode at a rate of 10 kips/min. After reaching the 90 kip load, the vertical loading was held, and this value of vertical load was maintained during the second loading phase, which consisted of application of horizontal loading to the top concrete block. The 90 kip vertical compression load approximately corresponded to one-fourth of the self-weight of a typical prestressed concrete through-girder pedestrian bridge.

In the second loading phase, horizontal loading was applied to the top concrete block with two 77-kip capacity hydraulic actuators in displacement-controlled ramp mode. The two horizontal actuators were master/slave connected to each other so that both actuators applied the same displacement to the specimens. A loading rate of 0.01 in./min was used at the beginning of the tests. After the specimens reached the post-peak load region of the load-deflection behavior, the loading rate was increased. At the end of testing, the loading rate was 0.025 in./min for the expansion-end specimen and 0.2 in./min for the fixed-end specimen.

The test setup used for load testing of the specimens is shown in Figs. 5.8(a) and 5.8(b). As indicated in the figure, the bottom concrete block was clamped to the laboratory floor at the front and back sides through an assembly of steel floor beams, and horizontal and vertical loading was

applied to the top concrete block. The load from the vertical actuator was transferred to the top concrete block through two steel bearing plates. A 3/4 in. thick horizontal bearing plate was placed on the top surface of the top concrete block and was leveled with hydrocal, i.e., gypsum cement. A 2 in. thick horizontal steel plate was attached to the head of the vertical actuator and transferred the vertical load from the actuator to the bottom bearing plate. Two layers of 1/8 in. thick Teflon sheets were placed in between the two bearing plates to reduce the friction when the bottom concrete block (and the bottom bearing plate) moved with respect to the top bearing plate under the effect of horizontally applied load.

As shown in Figs. 5.8(a) and 5.8(b), the top concrete block was clamped between a steel tube spreader beam on the east side and a steel plate on the west side with the help of two turnbuckles that were horizontally-positioned. The load from the horizontal actuators was transferred to the top concrete block through the spreader beam. The top concrete block and the head of the vertical actuator were braced against movement in the north-south direction. The 2 in. thick horizontal bearing plate, which was attached to the head of the vertical actuator, was also braced against movement in the west direction. The reaction against movement of the head of the vertical actuator in the west direction was also provided by the tie beam that was connected to the steel columns on the north and south sides of the specimens.

5.4. Test Results

5.4.1. Expansion-End Specimen

No concrete damage was observed in the top and bottom concrete blocks during testing of the expansion-end specimen. The resistance to the horizontally applied load was provided by the friction between the bearing pad and the bearing plate, and between the bearing pad and the top surface of the bottom concrete block. The load transferred to the bearing pad through this mechanism caused the bearing pad to undergo large amount of shear deformation during testing.

The lateral load versus lateral displacement plot of the expansion-end specimen is given in Fig. 5.9. The load values shown in the plot are the total net horizontal load applied to the top concrete block by the two horizontal actuators. A coefficient of friction of 0.04 with an axial compression load of 90 kips was used to determine the reaction force due to friction between the two bearing plates that was used to transfer the load from the vertical actuator to the top block. The friction force was assumed to increase linearly until first slip occurred between the bearing pad and the bearing plate, after which a constant value of friction force was assumed. The net force used in the plot in Fig. 5.9 was determined by subtracting the computed friction force from the total force applied to the top concrete block by the two horizontal actuators.

The displacement values shown in Fig. 5.9 were the horizontal displacement of the top concrete block with respect to the bottom concrete block. These displacement values were determined by subtracting the horizontal displacement of the bottom concrete block from the horizontal displacement of the top concrete block. Because of a problem with the data acquisition system that was encountered during testing of the expansion-end specimen, correct magnitude of displacements could not be measured with the LVDTs in this specimen. In order to determine the "correct" displacements, the horizontal LVDT readings were calibrated using the actuator stroke readings from the expansion-end specimen, which had the correct magnitude, and the relations

between the actuator stroke and horizontal LVDT readings from the fixed-end specimen. Therefore, the displacement values shown in Fig. 5.9 are the calibrated displacements.

As seen in Fig. 5.9, the maximum horizontal load carried by the specimen was 24.7 kips. The drop in the horizontal load that occurred at 15.8 kips was due to the slip between the bearing plate and the bearing pad. The specimen exhibited a linear load-deflection behavior prior to the bearing plate had slipped on the neoprene pad. The slope of this initial linear portion of the load-deflection curve depends on the shear stiffness of the bearing pad, and the maximum value of load that was attained in this portion was a function of the amount of static friction between the bearing pad and the bearing plate as well as between the bearing pad and the concrete surface.

Following the occurrence of slip, slope of the load-deflection plot decreased because of the relative movement between the bearing plate and the bearing pad in addition to the shear deformation of the bearing pad. The total load resisted by the specimen continued to increase until the contribution due to the shear stiffness of the bearing pad started to diminish. A close-up picture showing the shear deformation of the bearing plate as well as the slip between the bearing plate and the bearing pad near the end of load testing is given in Fig. 5.10.

5.4.2. Fixed-End Specimen

Fig. 5.11 shows the vertical load versus displacement plot obtained during the first loading phase of the fixed-end specimen. The figure shows measurements from three LVDTs placed on the north and south sides of the top concrete block, as well as the average of the three LVDTs. As seen, there was a nonuniform compression of the bearing pad due to an accidental eccentricity that occurred during the vertical loading phase.

The horizontal load carrying mechanism of the fixed-end specimen was different than that of the expansion-end specimen. In the fixed-end specimen, the applied horizontal load was mainly resisted by the two anchor rods that were embedded inside the bottom concrete block on the east and west sides of the specimen. The horizontal load-deflection plot of the fixed and specimen is shown in Fig. 5.11. The load capacity of the specimen was 78 kips, and it occurred at a horizontal displacement of 2.86 in. As evident in the figure, the load deformation capacity of the fixed-end specimen was much larger than the maximum load achieved by the expansion-end specimen. Different from the expansion-end specimen, the fixed-end specimen also experienced slow reduction in the load capacity with increasing magnitude of lateral displacement. The reason for this difference in behavior of the two specimens was because of the difference in lateral load-resisting mechanisms for the two specimens, as mentioned above.

As mentioned earlier, the holes in the bearing plate for the anchor rods were 1/2 in. oversized. Similarly, the holes in the sole plate for the pintles that were attached to the curved plate were 1/4 in. oversized. Because of the oversized hole in the bearing plate, the bearing plate did not come into contact with the anchor rods at the beginning of horizontal loading phase of the load test. As the horizontal loading was applied to the top concrete block, the bearing pad started to undergo shear deformation until the gap between the bearing plate and the anchor rods was closed. This behavior corresponds to the initial linear portion of the load-deflection curved with relatively low level of stiffness in Fig. 5.12. After the gap due to the oversized holes was closed and the bearing plate came into contact with the anchor rods, the horizontal load applied to the

top concrete block was transferred to the bottom concrete block through the front (west side) and rear (east side) anchor rods. This was evident with the increased stiffness of the horizontal load-deflection curve of Fig. 5.12. As shown in the figure, the horizontal load resisted by the specimen increased almost linearly with the increasing displacement until the occurrence of first cracking.

The first cracking during load testing of the specimen was visually detected at the load of 41.7 kips on the west face of the bottom concrete block near the front anchor rod location (see Fig. 5.13(a)). The effect of this crack was not observed on the load-deflection curve until 42.7 kips. As seen in Fig. 5.12, initiation of cracking on the front face of the bottom concrete block resulted in a drop in the horizontal load as well as a reduction in the stiffness of the specimen.

Initiation of first cracking was also detected by the strain gages placed on the front face of the bottom concrete block. Fig. 5.13(b) shows the reading from two of these strain gages. Initiation of cracking is indicated by the increase in the tensile strains recorded by the strain gage Top-Middle. The visually observed cracking load of the specimen is also indicated on the figure. As seen, initiation of the crack on the front face of the bottom block occurred earlier (around 30 kips) than the visually observed cracking load.

After the initiation of the first crack on the front face of the bottom concrete block, a new crack was observed at 43.9 kips on the north and south sides of the bottom block at approximately 3 in. from the front face of the block. This crack, which was going through the top surface of the bottom block from the north side to the south side of the block, continued to widen as the loading continued.

The second load drop that occurred in the horizontal load-deflection plot at 50.1 kips was due to sliding of the top concrete block on the curved plate. Because of the 1/4 in. oversized holes in the sole plate, at the beginning of the test the sole plate was not in contact with the pintles that were attached to the curved plate. In this case, the load was transferred from the top concrete block to the support assembly through the frictional resistance between the sole plate and the curved plate. At 50.1 kips load, the top concrete block slipped on the support assembly and the sole plate came into contact with the pintles. After this point, the horizontal load from the top concrete block was transferred to the support assembly through the bearing of pintles against the sole plate.

Fig. 5.14 illustrates the sliding between the sole plate and the curved plate. The figure shows the displacement readings recorded by the LVDTs attached to the top concrete block and to the bearing plate. The difference between the displacements measured by the two LVDTs following the load drop at 50.1 kips corresponds to the amount of slip between the sole plate and the curved plate. Considering that the holes on the sole plate were 1/4 in. oversized and that the pintles were approximately at the center of the holes at the beginning of load testing, the measured slip of approximately 0.1 in. is consistent with the mechanism explained above.

As the loading continued after the sliding of the top concrete block on the curved plate, the crack that was running from the north side to the south side of the bottom block continued to widen. Fig. 5.15 shows the location of this crack on the north side of the bottom concrete block. In

addition to widening of the crack on the bottom concrete block, the anchor rods were observed to bend as the loading continued. Bending and prying of the rear anchor rod resulted in circumferential cracking on the top surface of the bottom concrete cracking around the anchor rod location. The load resisted by the specimen increased up to 78 kips with increasing displacements applied by the horizontal actuator to the top concrete block. After reaching this load, the load-resisting mechanism of the specimen diminished slowly mainly because of the extensive damage occurred in the bottom concrete block and in the anchor rods (see Fig. 5.12). The damage in the bottom concrete block consisted of crushing of the concrete directly in front of the rear anchor rod and widening of the crack on the front face such that the reinforcement inside the block started to bend.

Following the breakout of the front face of the bottom concrete block see (Fig. 5.16), resistance by the front anchor rod to the applied horizontal load decreased considerably, which resulted in the major part of the applied load being resisted by the rear anchor rod. As a result, the rear anchor rod continued to bend such that the bearing plate started to ride on the anchor rod. Fig. 5.16 shows the extent of damage that occurred in the anchor rods. As evident in the figure, the rear anchor rod underwent extensive amount of bending and some level of local bearing damage caused by the load transferred from the bearing plate. The softening portion of the horizontal load-deflection curve in Fig. 5.12 that occurred after approximately 7 in. of horizontal displacement was due to sliding of the bearing plate on the bent portion of the rear anchor rod. The loading was continued until the bearing plate fell off the rear anchor rod.

Before load testing the fixed-end specimen, the top part of the rear anchor rod was flame-cut by approximately 1 in. in order to place the load spreader beam on the east face of the top concrete block. This modification did not have any effect on the behavior of the specimen until the portion of the test in which the bearing plate slid on the bent part of the rear anchor rod. Without this modification, the horizontal load-deflection plot of the specimen shown in Fig. 5.12 would have been the same except that the major load decrease that occurred at approximately 7 in. of horizontal displacement would have been expected to occur at a slightly larger displacement value.

The strain gages placed on the sole plate shear stud did not indicate any abrupt change in strain readings. This was an indication that none of the studs experienced steel fracture during the load tests.

5.5. Summary, Conclusions, and Recommendations

Idealized pin and roller girder boundary condition assumption used for the analysis of bridge structures under gravity loads, cannot be used for analyses under transverse impact loads. Instead, the strength and stiffness characteristics of the details used at the girder ends need to be determined and incorporated in to the analyses. This requirement becomes more critical for prestressed concrete pedestrian bridges due to the limited number of girders used in these types of bridges together with the smaller bridge self-weight.

The investigation presented in this chapter included the determination of the strength and stiffness properties of the support details used at the fixed and expansion ends of prestressed concrete girders through static load tests. The specimens used in these load tests simulated the

geometry and dimensions of the prestressed concrete girder ends and bridge abutments from through-girder pedestrian bridges constructed in Minnesota. The specimens were subjected to a combination of vertical and horizontal loads in an attempt to accurately simulate the loading conditions that girder end details are subjected to in the event of an over-height vehicle collision.

Two types of horizontal load resisting mechanisms were observed depending on the type of detail. The expansion-end detail resisted the horizontal applied load the friction between the bearing pad and the steel and concrete surfaces. The neoprene pad in this specimen was observed to undergo large amount of shear deformation. In the case of the fixed-end detail, the anchor rods that were used to prevent the transverse movement of the girder ends provided the main resistance against the horizontal loading. Concrete breakout and bending of the anchor rods resulted in the failure of the specimen with the fixed-end detail.

The fixed-end specimen resisted approximately 65 percent of the maximum load at a transverse displacement of 7.5 in. Even though the load testing of the expansion-end detail was terminated at a transverse displacement of approximately 3 in., this specimen would have withstood larger displacements with a certain level of residual load capacity if the loading had been continued.

The lateral load-deformation behavior of the fixed-end and expansion-end details determined through the load tests explained in this chapter were incorporated in the finite element models of a complete bridge system to simulate the flexibility of girder supports. As explained in the following chapter, these finite element models were used to perform assessment of a typical bridge system with static, dynamic, and stability analyses.

Table 5.1. Support Assembly Dimensions.

		Length inches	Width inches	Height inches
Expansion -end	Curved plate	26	5	1-3/8
	Bearing plate	27	14	1-3/8
	Bearing pad	22	9	1-3/4
Fixed-end	Curved plate	26	5	1-3/8
	Bearing plate	34	14	1-3/8
	Bearing pad	26	12	1/2

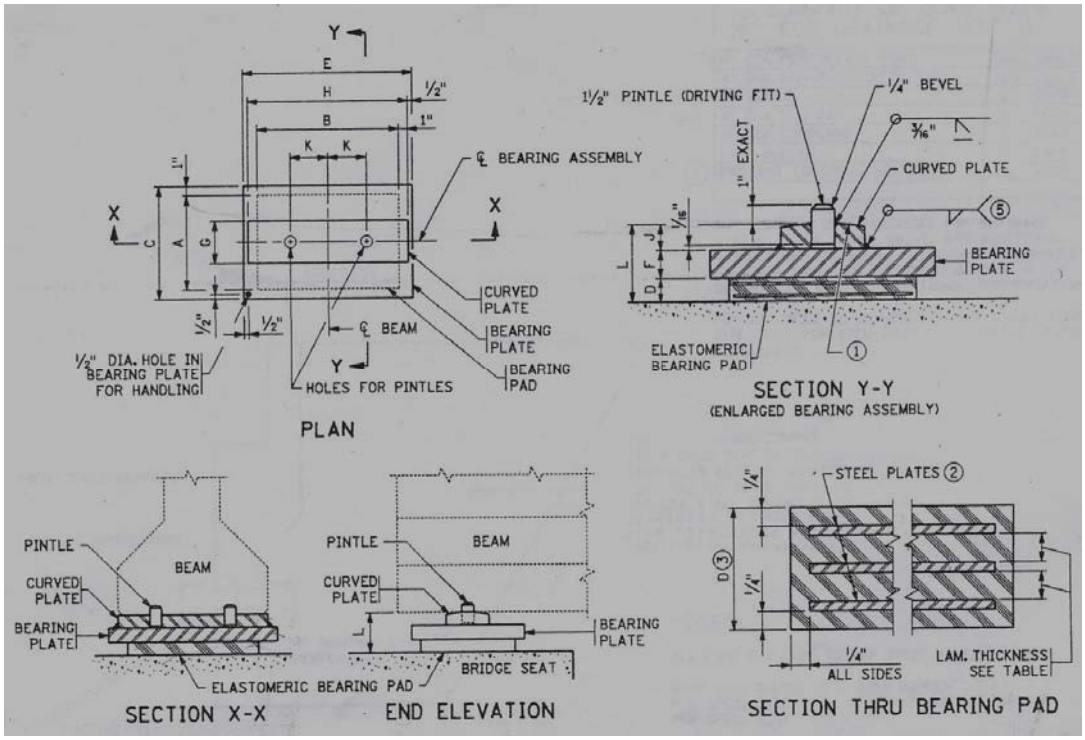

(a)

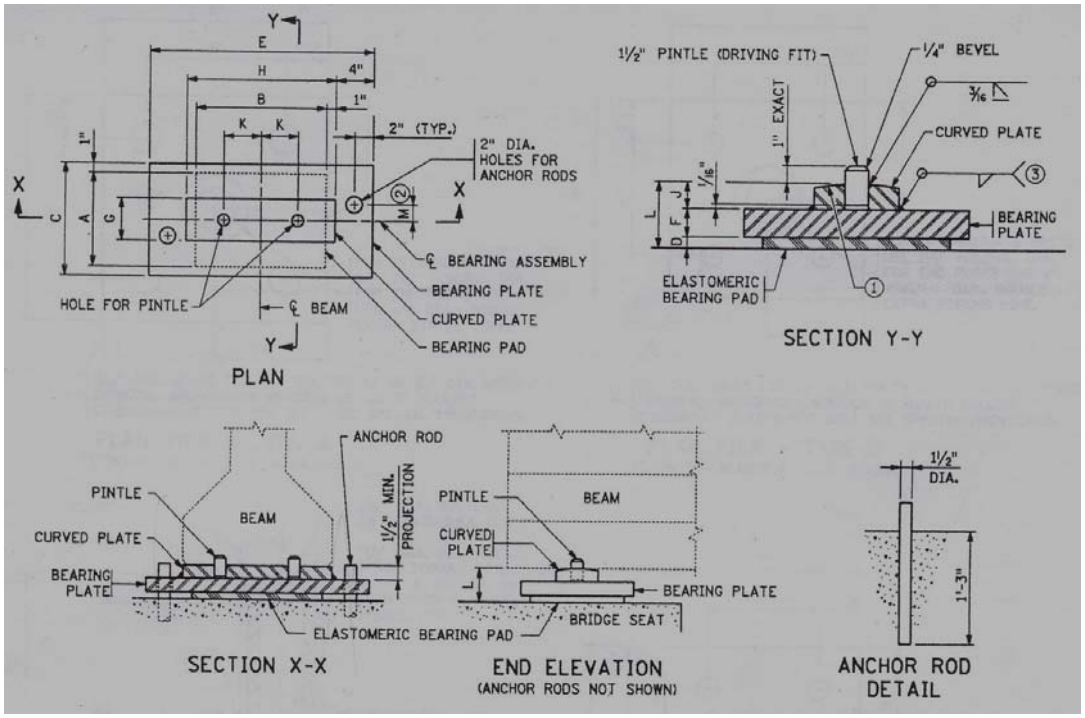

(b)

Fig. 5.1. Support details used at girder ends: (a) expansion end; (b) fixed end.

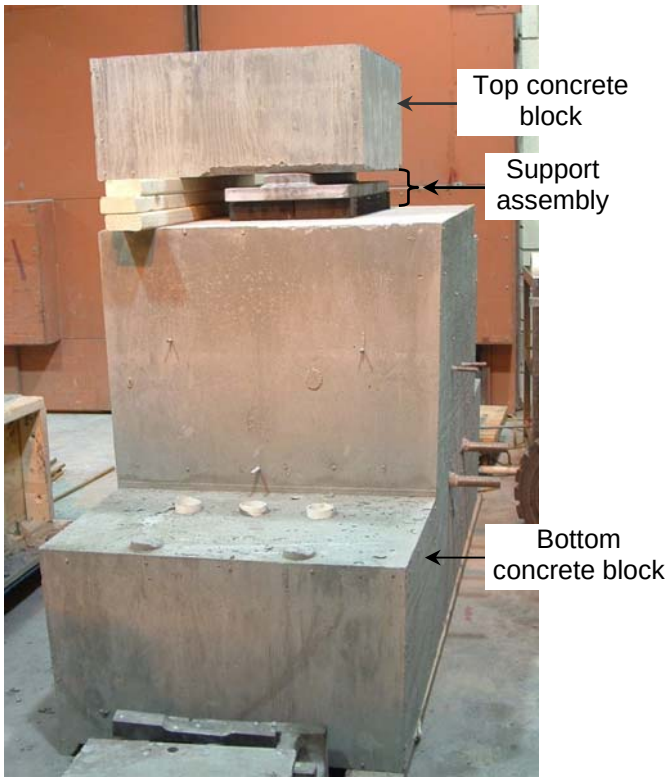

Fig. 5.2. Girder end detail test specimen.

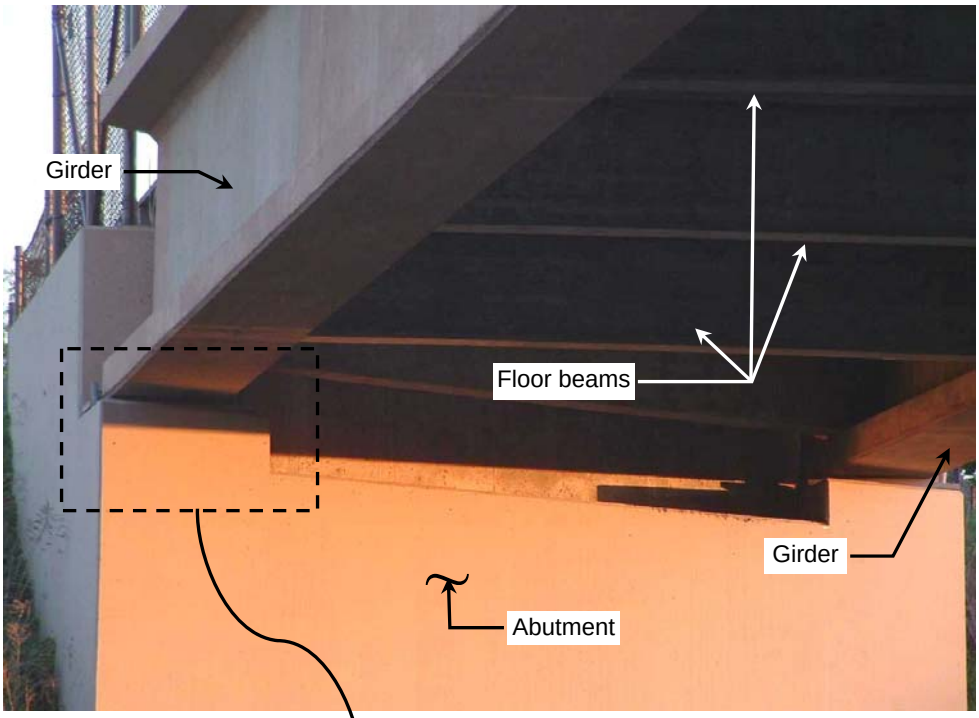

(a)

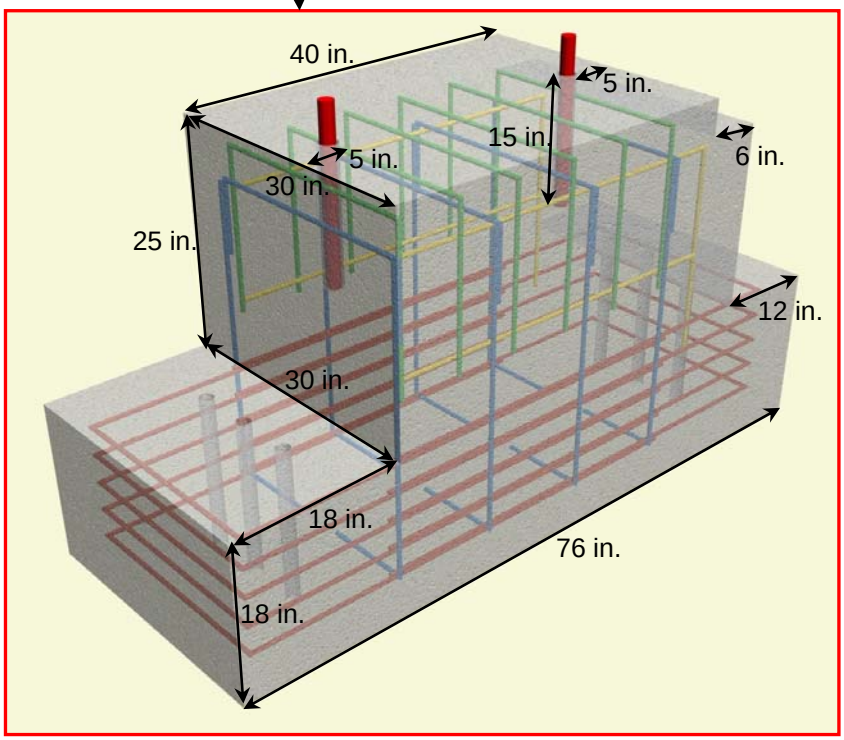

(b)

Fig. 5.3. Relation between a real bridge and girder end detail test specimen: (a) support detail in a bridge; (b) bottom concrete block dimensions.

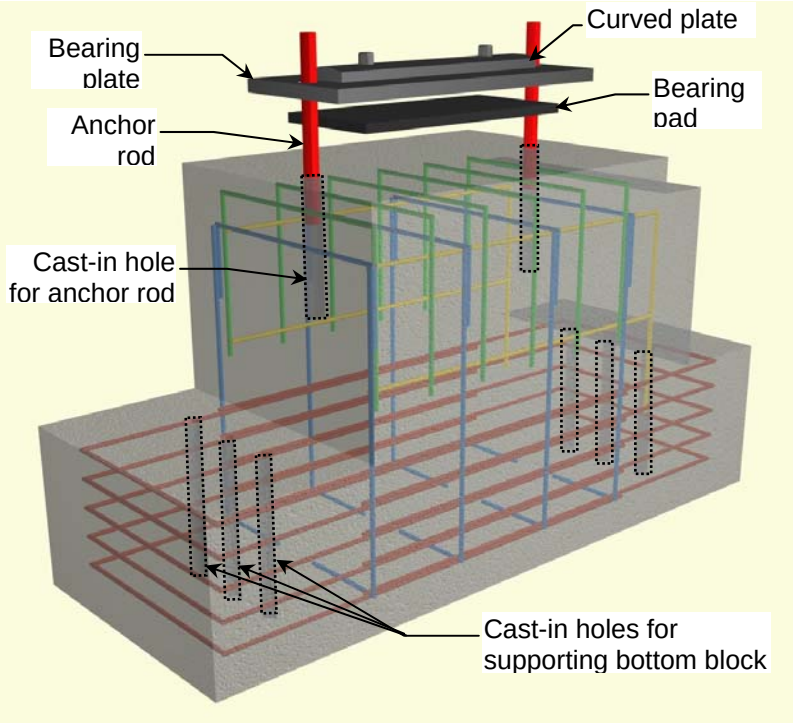

Fig. 5.4. Positioning of support assembly on bottom concrete block (fixed-end specimen).

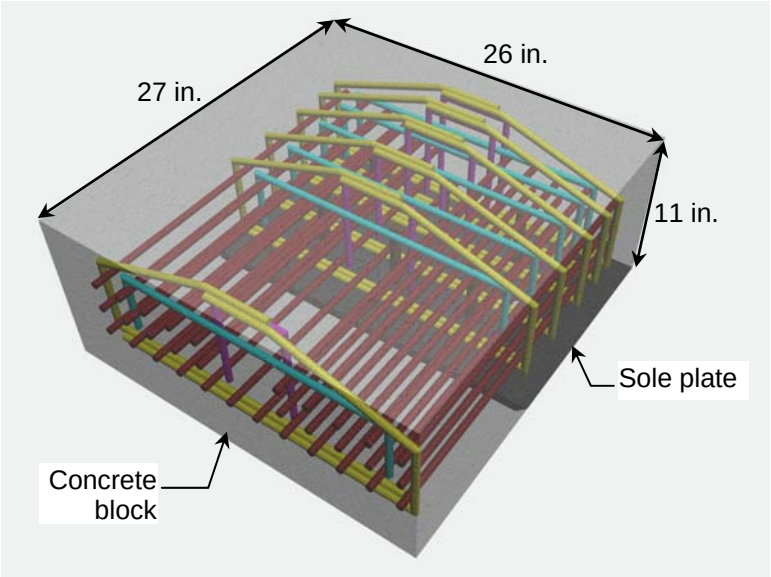

(a)

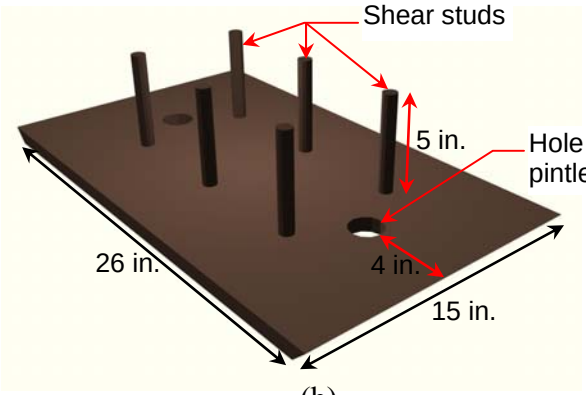

(b)

Fig. 5.5. Top concrete block details: (a) concrete block dimensions; (b) sole plate details.

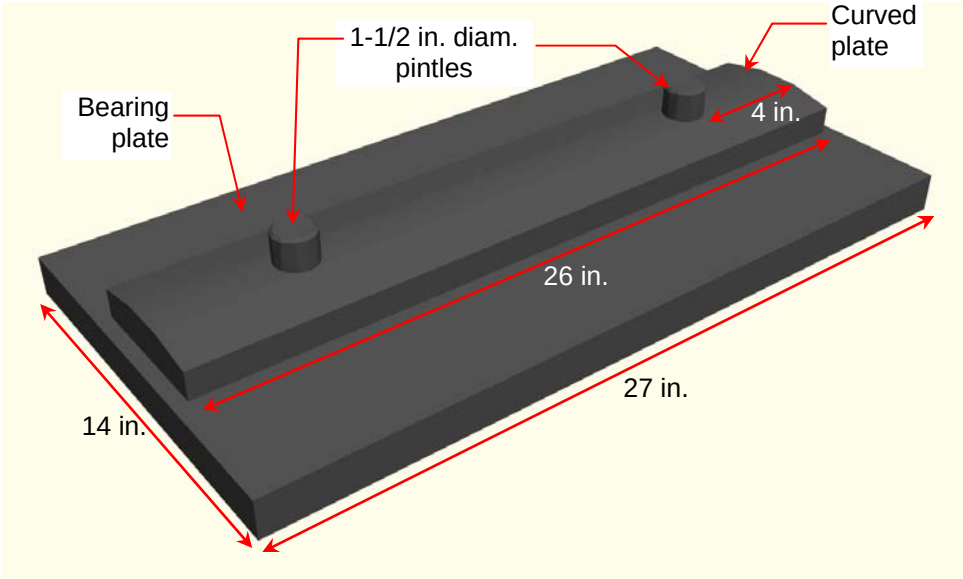

(a)

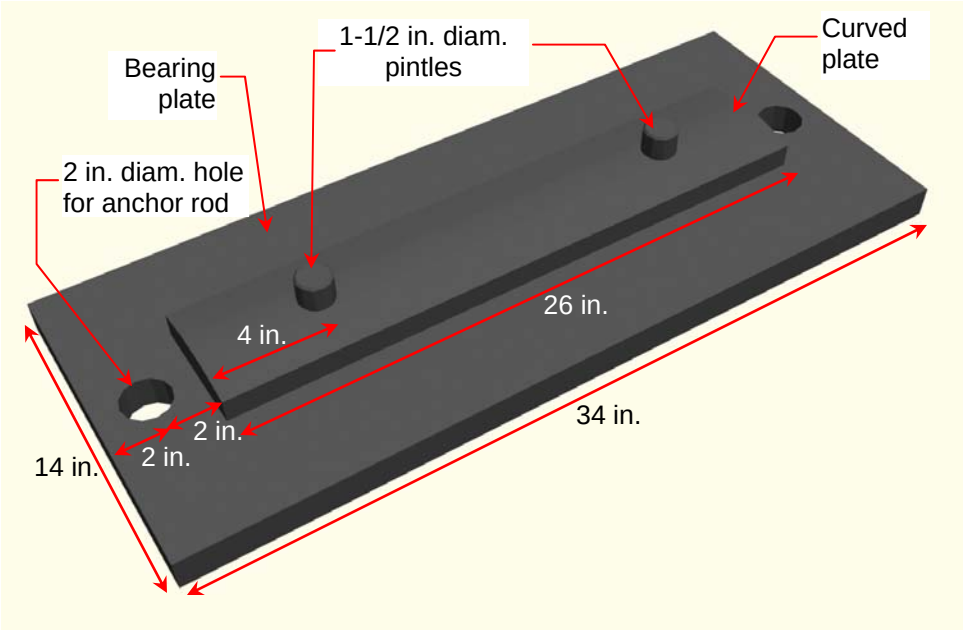

(b)

Fig. 5.6. Bearing plate details: (a) expansion end; (b) fixed end.

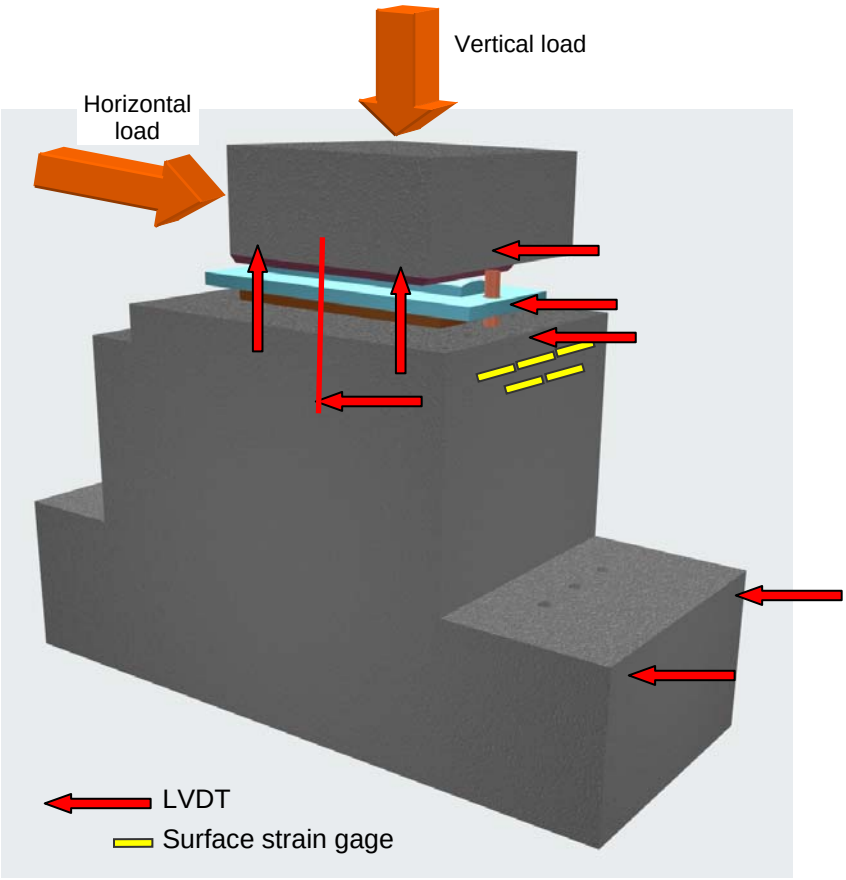

Fig. 5.7. External instrumentation used on fixed-end specimen (LVDTs on back face not shown).

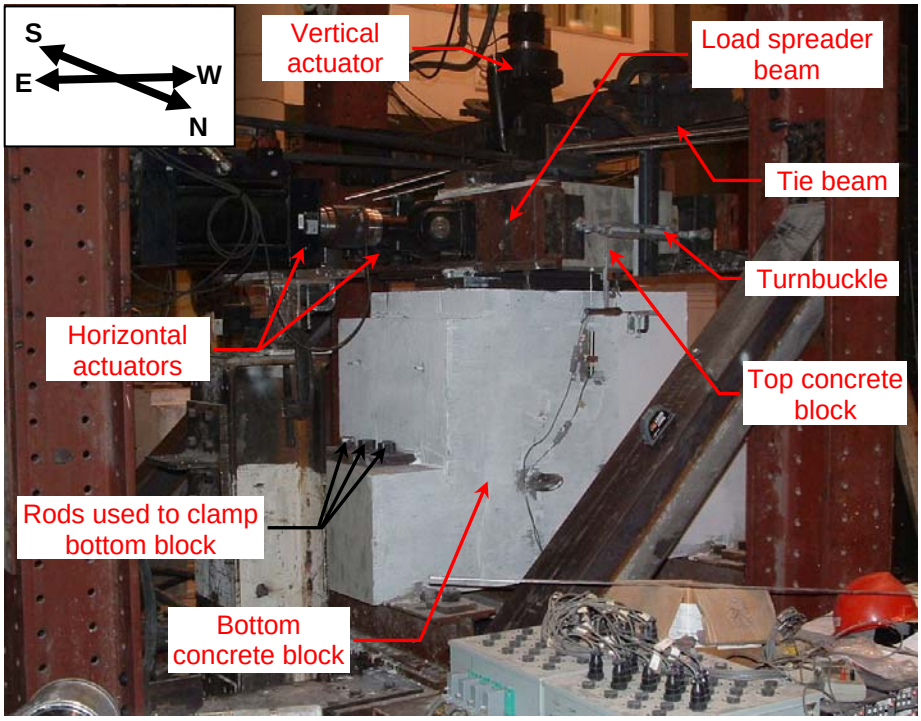

(a)

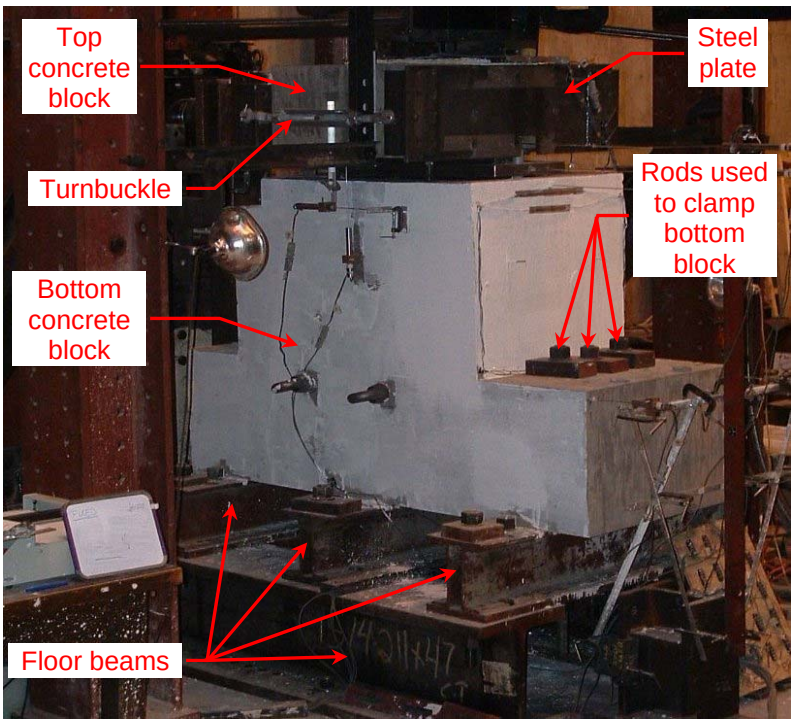

(b)

Fig. 5.8. Test setup: (a) North-East view; (b) North-West view.

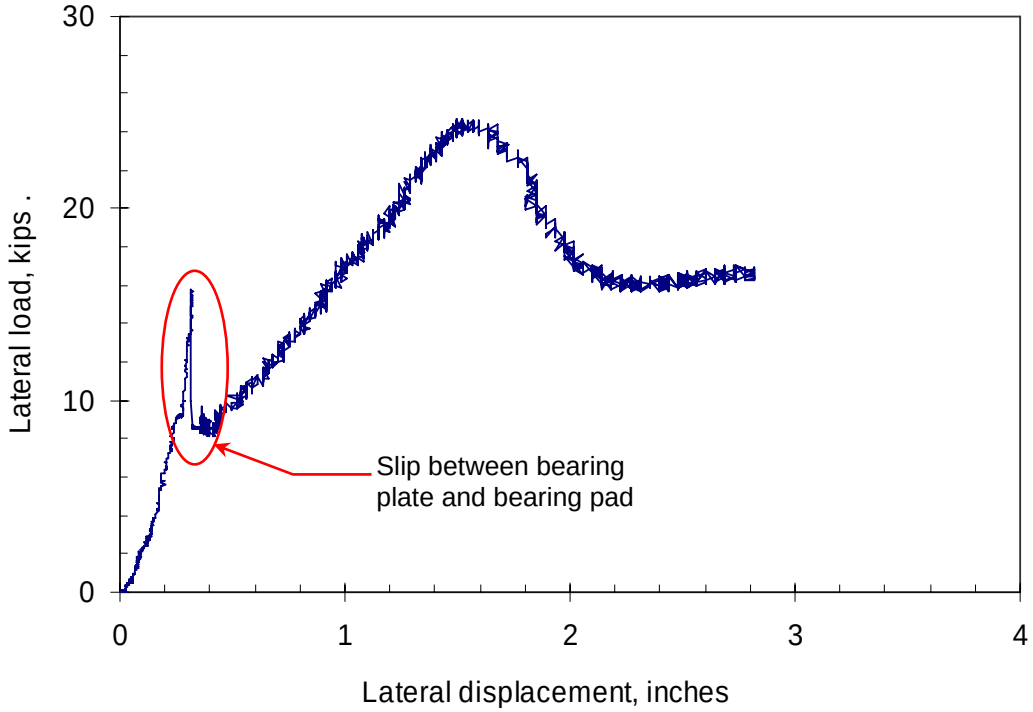

Fig. 5.9. Expansion-end specimen horizontal load-deflection behavior.

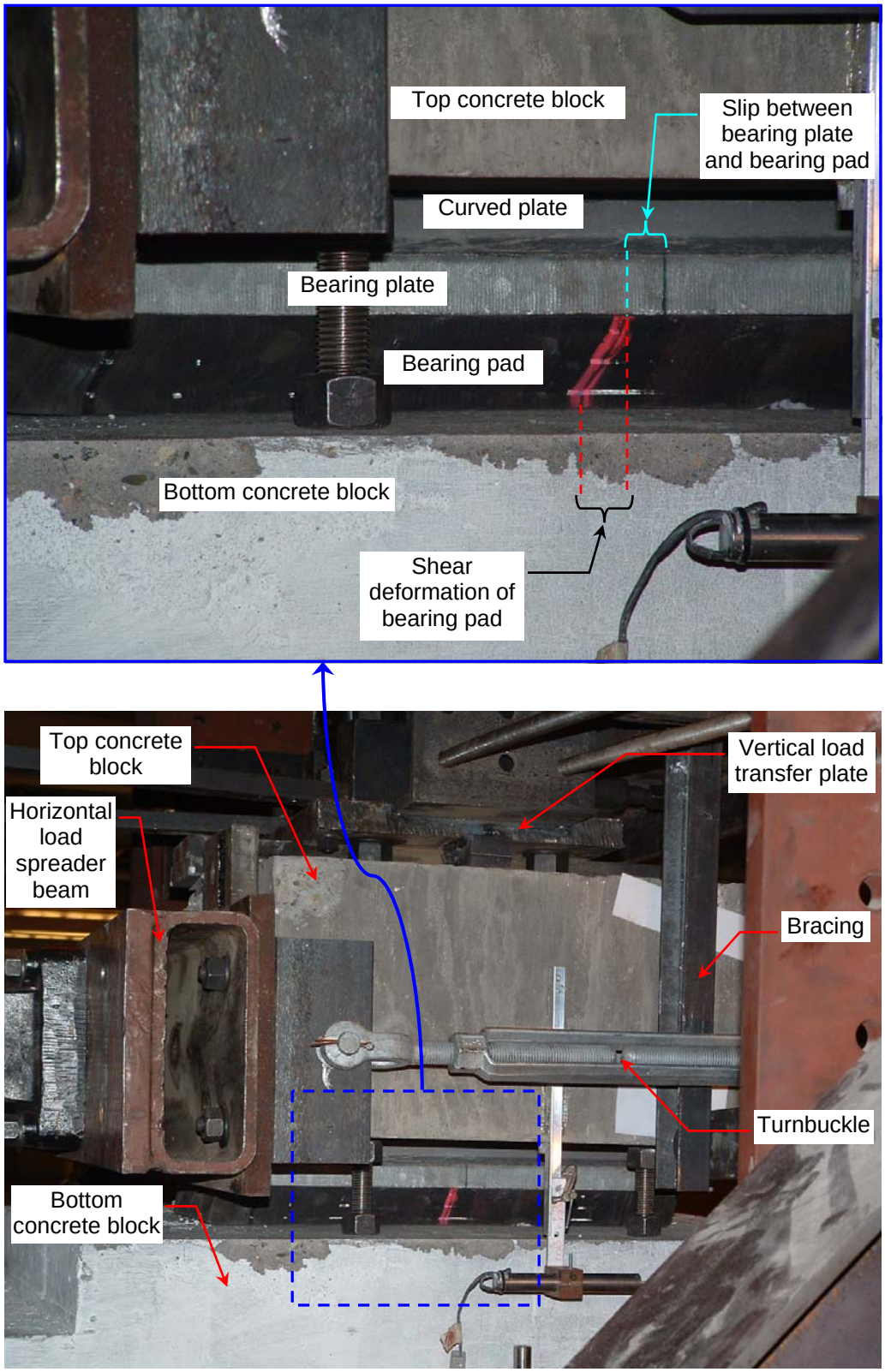

Fig. 5.10. Horizontal load resisting mechanisms in expansion-end specimen.

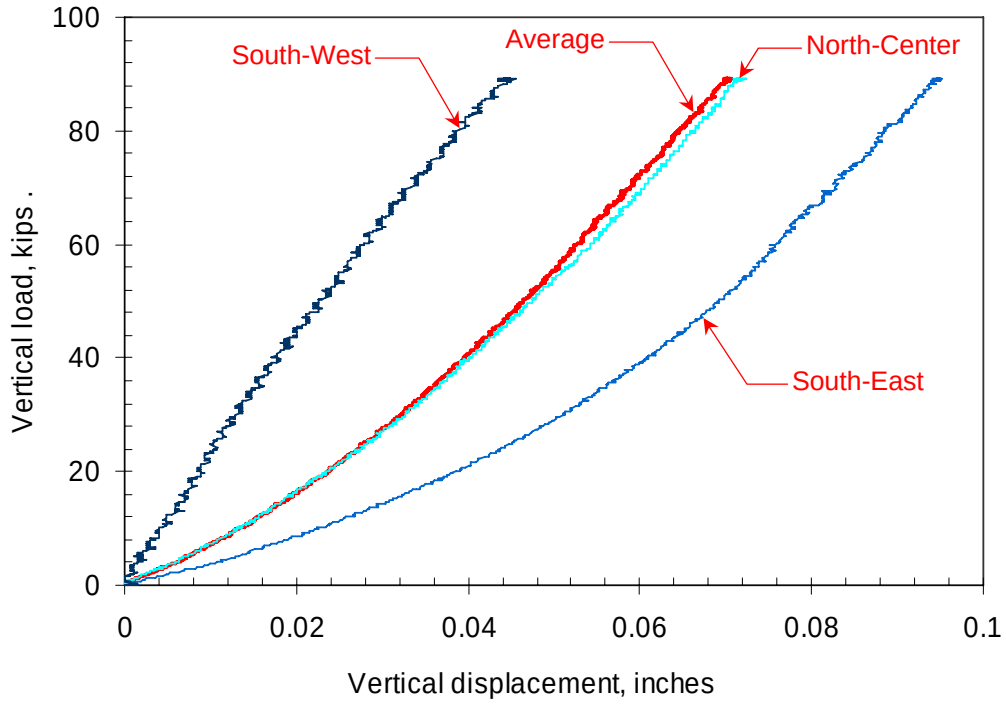

Fig. 5.11. Fixed-end specimen vertical load-displacement behavior.

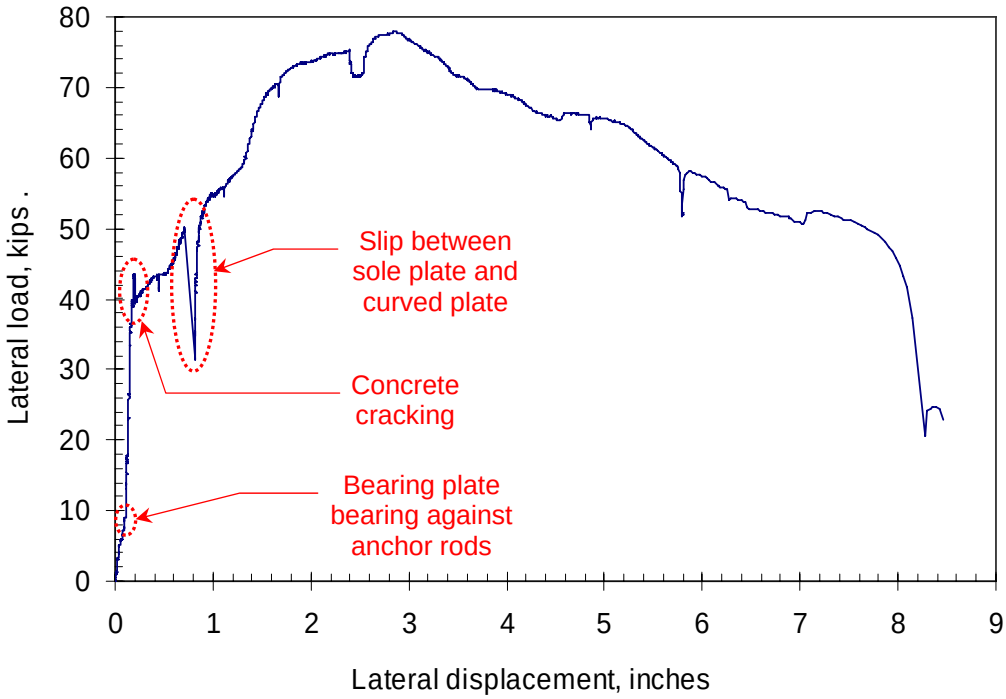

Fig. 5.12. Fixed-end specimen horizontal load-deflection behavior.

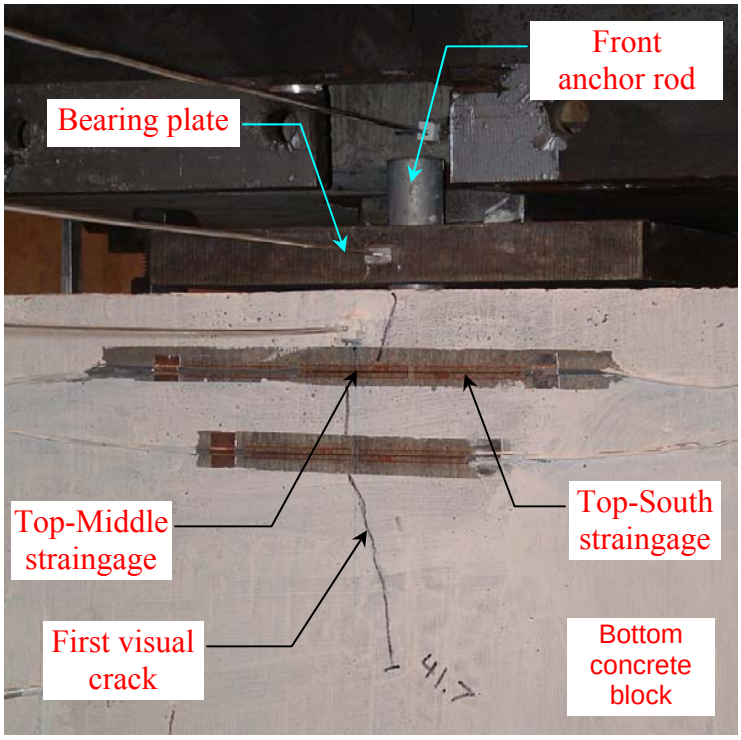

(a)

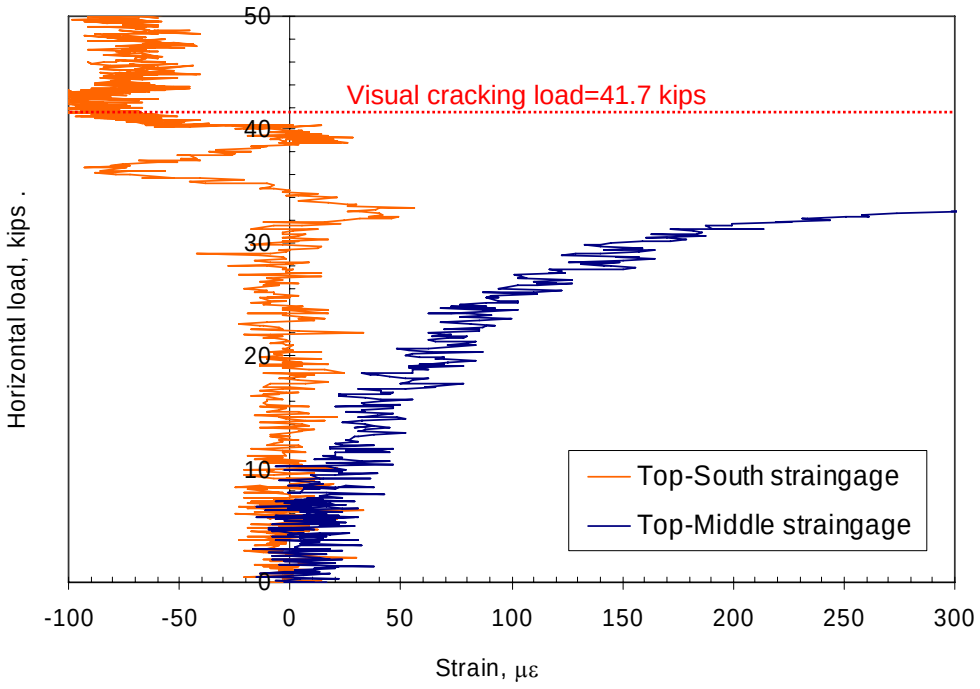

(b)

Fig. 5.13. Initiation of concrete cracking in fixed-end specimen: (a) strain gage locations; (b) variation of strain.

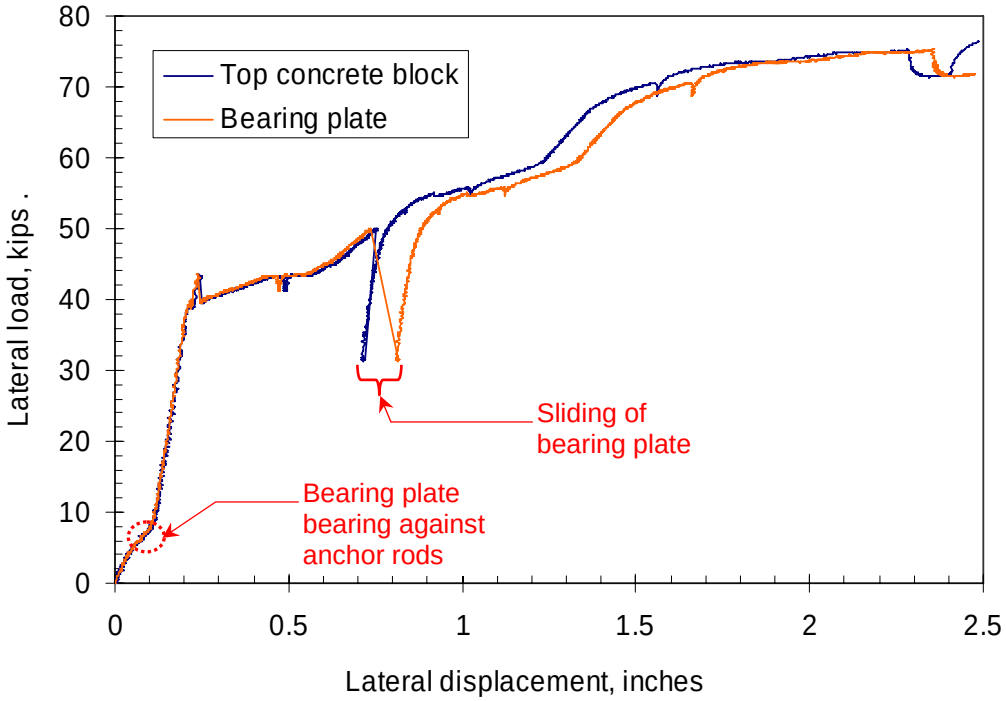

Fig. 5.14. Sliding of top concrete block on curved plate.

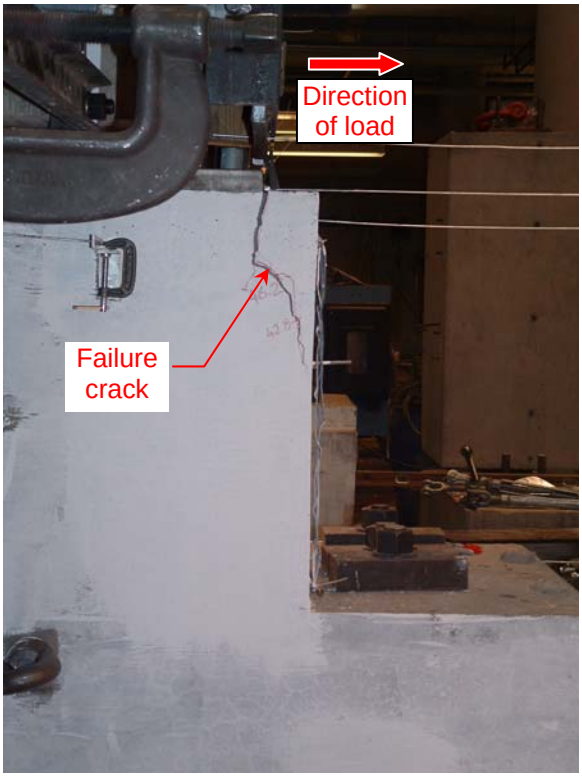

Fig. 5.15. Location of failure crack on North side of bottom concrete block.

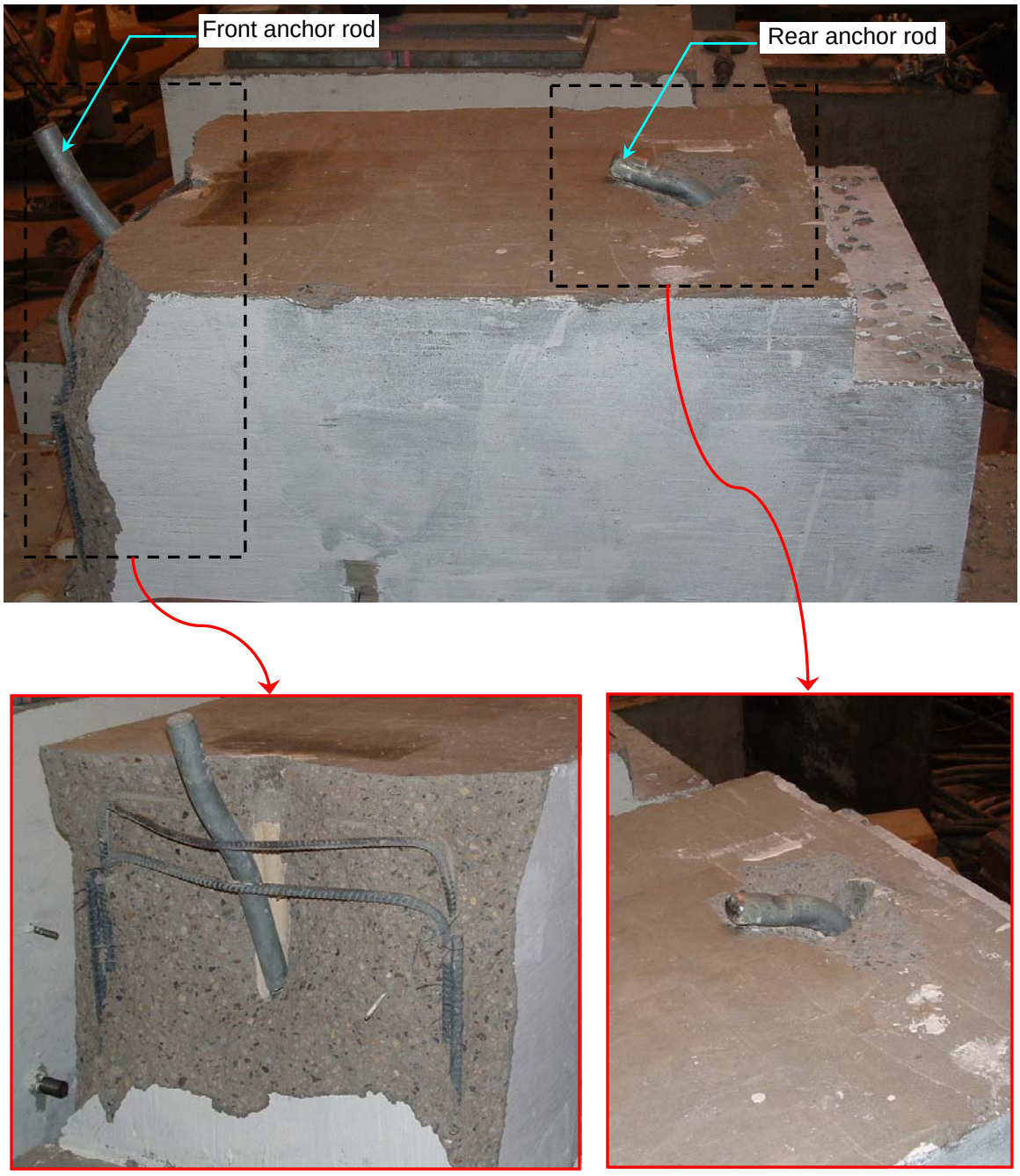

Fig. 5.16. Damage in bottom concrete block and anchor rods after load testing.

Chapter 6
Numerical Analysis of a Bridge System

6.1. Introduction

This chapter describes the finite element modeling of an entire prestressed concrete through-girder pedestrian bridge system. Information on deformation characteristics of various components of the bridge obtained through the experimental investigations described in the preceding chapters were incorporated in these models. By incorporating the measured load-deformation response of bridge components, it was assured that the finite element models predicted the response of the bridge system under the applied loads and deformations with a high level of accuracy.

The three series of analyses performed using the full-scale bridge models were (1) static lateral load analyses, (2) dynamic lateral impact analyses, and (3) static stability analyses under gravity loading. In the static lateral load analyses, the lateral displacement loading was applied to both girders of the bridge at different locations along the lengths of the girders. The aim in doing these analyses was to determine the response of the bridge system, including the strength, stiffness, and ductility characteristics, when it was subjected to lateral loads at different locations. Effects of parameters, such as location of load, behavior of connection between girders and floor beams, and girder support flexibility on the overall response of the bridge were studied in these analyses. Effectiveness of several modified connection details on the performance of the bridge system were also investigated with these analyses.

The dynamic lateral impact analyses were conducted in an attempt to determine the demand that would occur on a bridge system when it was subjected to striking of an over-height vehicle. These analyses included a rigid object impacting the bridge girders at several locations with changing amounts of initial velocities. The parameters studied with the dynamic lateral impact analyses included impact location, impact speed, and weight of the impacting object.

The last series of finite element analyses were conducted to study the stability of a bridge system following the occurrence of damage to the concrete girders as a result of dynamic impact of the striking vehicle. Different from the models used in the first two series of analyses, the models in this series were analyzed under the effect of self-weight of the bridge structure only. The effect of damage that would occur in the girders due to the dynamic impact loading was simulated by removing the concrete and prestressing strand elements in the bottom flange and bottom portion of the girder web in these models.

The models used in each analysis type are described below, followed by presentation of the results obtained from the analyses.

6.2. Description of Finite Element Models

The finite element analysis program MSC Marc/Mentat [75] was used to prepare the geometry of the models, to analyze the models, and to post process the analysis results. The models included three-dimensional full-scale simulations of an actual through-girder pedestrian bridge system. The models included material nonlinearities, such as nonlinear connector behaviors and concrete

crushing and cracking, as well as geometric nonlinearities, such as gap opening and friction between contact surfaces of different bridge members. Because of the relatively large size of the models together with the imposed material and geometric nonlinearities, the computer time required to analyze the models became excessive. The analyses were performed on IBM Power4 supercomputers using up to 5 processors for each run, and some of the models required up to 10 hours of computer time to complete the analyses. In order to reduce the time required for the analyses so that a larger number of parameters could be studied, simplifying assumptions had to be made in some of the models.

Fig. 6.1 (a) shows an overall view of the finite element model and the dimension of the components, while Fig. 6.1(b) illustrates the modeling of girder supports and girder-floor beam connection region. Mn/DOT Type 63 section was used for the girders as this was the section used in the prestressed concrete through-girder pedestrian bridges constructed in Minnesota. The girders in the finite element models were 135 ft. long with 14 ft.-6 in. spacing between the two girders. The end floor beams were placed at both ends of the girders, and nine intermediate floor beams were placed between the two end floor beams at 15 ft.-6 in. spacing.

The girders, floor beams, and the deck in the finite element models were modeled as independent bodies, and these bodies were connected together based on the connection details used in the actual bridge construction. In the bridge construction, stirrups were provided between the reinforced concrete cast-in-place floor beams and deck so that they would act monolithically. In order to simulate this condition, the deck and the floor beams in the finite element models were rigidly connected to each other. This was achieved by having the floor beam and deck elements share common nodes at the interface where the two sets of elements met.

6.2.1. Modeling of Connection Flexibility

The connection detail used at the girder and floor beam connection region in the through-girder pedestrian bridge construction did not allow a rigid connection in the finite element models. As explained earlier, because of the construction sequence a limited amount of connection exists between the girder and the floor beams in prestressed concrete through-girder pedestrian bridges. The connection between the reinforced concrete cast-in-place floor beams and the precast concrete girders is provided through steel anchors embedded inside the girders and connected to threaded rods cast inside the floor beams. This type of detail can provide only a “partially rigid” connection behavior.

A special modeling technique was used to simulate the partially rigid behavior of the girder and floor beam connections in the finite element models. In the models, the girder and floor beam elements were kept as independent bodies with two separate sets of nodes at the interface. In order to prevent the deformation of girder and floor beam elements independent from each other and to keep the bodies from penetrating into each other, contact surfaces were defined at the interface between the girder and floor beam elements. The contact surfaces defined at the connection interface allowed the transfer of bearing compressive stresses while allowing gap opening between the bodies whenever tension was generated. In this way, the partially rigid behavior of the connection between the girders and the floor beams in through-girder construction was modeled accurately. Because no connection is provided between the precast concrete girders and cast-in-place deck during construction, the partially rigid connection

modeling technique explained above was also used at the girder and deck connection region in the finite element models.

In order to simulate the frictional resistance between the concrete surfaces that would exist in actual construction, friction properties were assigned at the contact surfaces defined between the girders and floor beams and also between the girders and the deck. The contact surfaces were assigned a coefficient of friction value of 1.2. Even though this value is 20 percent higher than the coefficient of friction specified in ACI 318-05 [49] for concrete placed against hardened concrete, it was used in order to obtain a stable numerical behavior.

Steel truss elements were provided between the girder and floor beam elements in the finite element models in order to include the effect of the steel anchors and steel threaded rods present at the girder and floor beam connections in thorough-girder construction. For this purpose, six sets of truss elements were defined at each girder and floor beam connection region. As illustrated in Fig. 6.1, four of these connection elements were placed in the girder web and two of them in the girder bottom flange. The locations of the truss elements were chosen to match those of the connector rods used in actual through-girder bridge construction. No connection elements were used at the girder and deck connections, as none existed between the girders and deck in the actual system.

6.2.2. Material Models

The girders, floor beams, and the deck were modeled using 8-noded solid elements, while 2-noded truss elements were used for the connectors between the floor beams and girders.

The material behaviors used for the concrete elements are shown in Fig. 6.2. The higher concrete strength shown in the figure was used for the girder elements while the lower concrete strength was used for the floor beam and deck elements. As evident in the stress-strain plots shown in Fig. 6.2, the concrete material models were highly nonlinear with compression crushing and tensile cracking properties included. Compression portion of the concrete material model was proposed by Popovics, Thorenfeldt, and Collins [67]. Cracking in concrete was modeled by specifying cracking stress, tension-softening modulus, and shear retention values for the materials. A typical value of 0.5 was used for shear retention, while the value of cracking stress varied between 380 and 500 psi depending on the concrete strength. The tension-softening modulus was assumed to be 10% of the modulus of elasticity, and it varied between 330,000 and 430,000 psi depending on the concrete strength.

The material behaviors for the connector elements were based on the load-displacement behavior obtained from the pull-out tests of the loop-type inserts (see Chapter 3). The same material behavior was used for all six connectors in each girder and floor beam connection. Load versus deflection plots obtained from tension pull-out tests on loop inserts were converted into stress versus plastic strain plots using the appropriate length and cross-sectional area, and were assigned as the material behavior for the truss elements, as indicated in Fig. 6.1.

It should be noted that the load-deflection curves obtained from the pull-out tests included deformation of the steel inserts as well as deformation due to damage occurring in the concrete around the inserts. This latter type of damage was mostly in the form of cracking in the concrete.

Therefore, the concrete cracking around the steel inserts was already included in the load–deflection relations measured during the pull-out tests. In order to avoid double-counting the effect of concrete cracking on the load-deflection behavior of the inserts used in the finite element models, the concrete elements for the girders and the floor beams in the vicinity of connector elements were not assigned cracking properties (i.e., these elements had unlimited tensile strength).

6.2.3. Modeling of Prestressing

Two-noded truss elements were also used to model the prestressing strands inside the concrete girders. Because of difficulties in matching the locations of the nodes for the prestressing strands and the concrete girder, the prestressing strands were not draped in the models. Using a straight strand configuration would result in larger top fiber tensile stresses near the girder ends, than the case with draped strands. In order to take this difference into account, the truss elements were assigned a lower value of initial stress near the girder ends.

Prestressing strands in concrete girders that are in service are placed in a typical template of 2 in. vertical and horizontal spacing. Because a larger than 2x2 in. mesh size was used in the bottom flange of the girders in the finite element models, placement of the strands in the section in the models was different than that in actual girders. The prestressing strands in the models had to be lumped at the nodes in the bottom flange of the girders. As illustrated in Fig. 6.3, the bottom row of truss elements were assigned an area that was 3 times the area of a ½ in. diameter prestressing strand (0.153 sq. in.), while an area of the truss elements in the above row was twice the strand area. The total area of truss elements in the model was kept the same as the total area of strands in prestressed concrete girders used in through-girder pedestrian bridges.

The prestressing was defined using the "Initial Conditions" option available in MSC.Marc/Mentat [75]. The truss prestressing elements were assigned an initial stress of 162 ksi (60 percent of 270 ksi). As mentioned above, the value of initial stress was gradually lowered near the ends of the girders such that the top fiber concrete stress was kept below the concrete tensile strength. The material model used for the prestressing truss elements had perfectly elastic and perfectly plastic behavior with an initial stiffness of 29,000 ksi.

6.2.4. Boundary Conditions

Boundary conditions were defined at both ends of the girders. Two types of girder boundary conditions were used in the analyses. Initial analyses were conducted using idealized pin and roller boundary conditions defined at the ends of each girder. In this case, all three translational degrees of freedom were restrained at one end of the girders while only the translational degree of freedom along the bridge axis was allowed at the other end. The solid elements used in the models did not have any rotational degrees of freedom. By using these idealized boundary conditions, it was assumed that the girder ends were prevented from lateral movement under the effect of laterally applied loads during the analysis. From this respect, these boundary conditions reflect an extreme case that the details used at the girder ends had infinite stiffness in the direction transverse to the bridge axis.

The second set of boundary conditions used in the analyses included the flexibility of the girder supports. As mentioned previously, a bearing pad and bearing plate type assembly was used at

each end of the prestressed concrete girders to support the girders at the abutments and over the piers. Results obtained from the static tests performed on these bearing assemblies, as explained in Chapter 5, were incorporated into the finite element models to take into consideration the girder support flexibility on the behavior of the bridge components under transverse loads. As illustrated in Fig. 6.1, truss elements that were both parallel and perpendicular to the bridge axis were defined at the girder ends. These truss elements were assigned axial load-deflection relations that were extracted from the measured load-deflection relations of the girder end detail specimens (Chapter 5). Because there were four truss elements defined at each girder end for the directions parallel and perpendicular to the bridge axis, the axial stiffness of each truss element was one-fourth of that corresponding to the measured load-deflection behavior. Truss elements at each end of the girders were assigned load-deflection relation of either the fixed-end detail or the expansion-end detail.

6.3. Static Lateral Load Analyses

These analyses included application of transverse displacements at the bottom flange of the girders to study the force-deformation behavior of the bridge system in this direction. Prestress and self-weight of the bridge were applied to the models at the beginning of the analyses, followed by the statically applied displacement loading. A rigid block, 7.5 in. high and 12 in. wide, was defined at the loading location, and displacement loading with an increasing magnitude was assigned at the node that was at the center of this rigid block. Strength, stiffness, and ductility characteristics of the entire system with various parameters, such as location of loading, connection detailing, and support flexibility, were studied.

6.3.1. Effect of Loading Location

Fig. 6.4 shows the locations where the transverse displacements were applied in the model. The loading patterns included application of transverse displacement at one face of the bottom flange of the girders at floor beam locations (Locations 1 through 6) as well as in between the floor beam locations (Location 5-6). The loading applied to Girder-1 was to simulate the cases that the bridge would be impacted by an over-height vehicle on the exterior face of the first girder. Accidents of trucks striking highway bridges have indicated cases that interior girders of the bridge can also be impacted by over-height vehicles. In order to study this type of case, the displacement loading was applied to the interior face of Girder-2 in the finite element models as well, as indicated in Fig. 6.4. Behavior of the bridge system depended significantly on whether the loading was applied to Girder-1 or Girder-2, as explained in detail in the following sections.

6.3.1.1. Loading at Girder-1

In the cases that the displacement loading was applied to Girder-1, the loads were transferred through the floor beams and the deck to Girder-2. Because this type of load transfer caused bearing of contact surfaces at the connection regions of the bridge components, the steel connector elements joining the girders and floor beams did not have an effect on the behavior of the bridge. Consequently, the entire bridge acted similar to a deep beam under three-point bending in plan.

Fig. 6.5 shows the progression of damage on bridge components under the effect of loading applied to the exterior face of Girder-1 at the location of Floor Beam-6, which was at the mid-span of the bridge. The figure shows plan views of the middle portion of the bridge at four stages

during the analysis. The contours shown in the figure indicate different levels of equivalent cracking strain in the concrete elements. The figure clearly shows the progression of damage in the girders, deck, and floor beams as the magnitude of the displacement loading applied at the exterior face of Girder-1 increased. During the initial stages of loading, cracking occurred in Girder-2, as this was the portion of the bridge that was subjected to tensile stresses due to the loading applied as shown. Local concrete damage also occurred in Girder-1 in the vicinity of the applied loading, even though this damage is not visible in the plan views of the bridge shown in Fig. 6.5.

Comparison of bridge behavior when the loading was applied at different floor beam locations along Girder-1 is presented in Fig. 6.6. The figure includes the lateral load versus lateral deflection plots when the loading was applied at the locations of Floor Beam-4, -5, and -6. As mentioned earlier, Floor Beam-6 is located at the midspan of the bridge. The displacement values shown in the plots are the values of the transverse displacement applied at the center node of the rigid loading block, while the force values in the plots were the reaction forces reported for the same node in the direction of the applied displacement.

As shown in Fig. 6.6, the bridge exhibited nonlinear behavior under the transverse loading. The initial elastic portion of the load-deflection plots corresponds to the pre-cracked state of the girders. With the progression of cracking in Girder-2, deck, and floor beams, the transverse stiffness of the bridge was reduced. The softening portion of the load-deflection curve occurred following the extensive cracking of the deck and floor beams, and the progression of cracking into Girder-1.

Comparison of the plots in Fig. 6.6 also indicates that the behavior of the bridge did not differ much when the displacement loading was applied at midspan of the bridge and at locations 15 ft.-6 in. and 31 ft. away from the midspan. All three cases resulted in similar initial stiffness and maximum load values, as well as similar behavior in the post-peak region.

Fig. 6.7 shows the load-deflection behavior of the bridge when the loading was applied at the locations of Floor Beam-5 and -6 as well as at locations in between these two floor beams. The curve labeled as “FloorBeam_5-6” in the figure represents the case when the displacement loading was applied at mid-distance between Floor Beam-5 and -6. This corresponds to a location 7 ft.-9 in. away from both floor beams. The figure also shows the case when the loading was applied at a location 2 ft. away from Floor Beam-6 (the curve labeled as “FloorBeam_5-66”). Similar to the previous figure, there was no significant difference in the overall shape of the load-deflection plots of the bridge when the location of the loading varied between these two floor beams.

The plots in Fig. 6.7 also suggests that the maximum transverse load that the bridge could withstand was reduced when the loading was applied in between the floor beams, as opposed to the loading being applied at the floor beam locations. When the loading was applied in between the two floor beams, this caused additional bending deformation in the portion of Girder-1 between the two floor beams, which resulted in earlier cracking in Girder-1 near the location of loading.

6.3.1.2. Loading at Girder-2

A typical deformation pattern of the bridge and progression of damage when the loading was applied at the interior face of Girder-2 is shown in Fig. 6.8. This configuration of loading required the load transfer from Girder-2 to the floor beams and to Girder-2 through tensile forces in the connector elements between the girders and the floor beams. In this case, the overall behavior of the bridge is mostly dictated by the axial load versus elongation behavior of the connector elements in the finite element models. In other words, the transverse load capacity of the bridge system vanishes as the connector elements between Girder-2 and the floor beams started to fracture during the load transfer between the bridge components. As shown in Fig. 6.8, axial elongation and fracture of the connector elements caused gap opening between Girder-2 and floor beams. The reason that the cracking strain contours shown in the figure are not symmetric was because the loading location was not at the midspan of the bridge in this particular example.

The cracking strain contours in Fig. 6.8 show that the cracking damage in the bridge deck was localized at floor beam locations and at mid-distance between two adjacent floor beams. This happens because of the load transfer mechanism between Girder-2 and the floor beams. When the load transfer occurred between Girder-2 and floor beams through the connector elements, this caused tensile stresses, and hence cracking, in the floor beams and in the deck at floor beam locations. As the load was transferred from Girder-2 to the floor beams, a portion of the deck in between two adjacent floor beams became subjected to bending, and this caused compression stresses in the deck near Girder-1 and tensile stresses in the deck near Girder-2. In this case, the maximum value of tensile stresses occurs at mid-distance between two adjacent floor beams.

The difference in bridge response when the loading was applied at Girder-1 and Girder-2 is shown in Fig. 6.9. For the particular cases shown in the figure, the loading was applied at the location of Floor Beam-6. As explained earlier, the displacement values shown in the plots are the values of the transverse displacement applied at the center node of the rigid loading block, while the force values in the plots were the reaction forces reported for the same node along the direction of the applied load. As shown in the figure, the overall shapes of the load-deflection plots are significantly different when the displacement loading was applied at Girder-1 and Girder-2. For the case that the loading was applied at Girder-2, the shape of the overall load-deflection plots of the bridge resembles the axial load versus axial elongation plots of the connection elements used in the models (see Fig. 6.1). The load capacity of the bridge was also significantly reduced when the loading location was changed from Girder-1 to Girder-2.

The effect of the loading location on the behavior of the bridge when the loading was applied at Girder-2 is shown in Fig. 6.10. The figure shows the load-deflection plots when the displacement loading was applied at Girder-2 at locations of Floor Beam-5 and -6, as well as at mid-distance between the two floor beams. Varying the location of displacement loading between Floor Beam-5 and -6 caused a minor change in the load capacity of the bridge without changing the overall shape of the load-deflection plots. As seen in Fig. 6.10, among the three cases studied, the case with the loading applied in between Floor Beam-5 and -6 resulted in the largest load capacity. This was an expected result, because the bridge behavior was controlled by the connector elements and applying the displacement loading at the floor beam locations caused larger forces in the connector elements than the displacement loading being applied in between

the two adjacent floor beams. In the latter case, the load was distributed between the two adjacent floor beams, and the connectors that provided connection between Girder-2 and these floor beams were subjected to smaller forces than the former case.

6.3.2. Effect of Connector Type and Connection Detail

The results presented in the preceding sections were obtained from the finite element models with the connecter behaviors based on the measured response of pull-out specimens with loop-type inserts. In this section, behavior of the bridge system with loop-type and bolt-type inserts are compared in Fig. 6.11 for the case of loading applied at Girder-2. As explained earlier, when the loading was applied at Girder-1, the load transfer from Girder-1 to Girder-2 was through bearing of bridge components with respect to each other, and the effect of the connector behavior on the overall response of the bridge remained minimal. Therefore, analyses used to determine the effect of connector type on the bridge response was limited to the case of loading applied at Girder-2 only.

The material behavior of the connector elements used in the analyses were based on the load-deflection behavior labeled as "Connector 3" in Fig. 4.21(d) for the loop-type inserts and the load-deflection behavior labeled as "Model" in Fig. 4.22(c) for the bolt-type inserts. As shown in Fig. 6.11, both types of connector behavior resulted in similar overall bridge response. The larger load capacity obtained with the bolt inserts was due to larger tensile strength of the bolt inserts. Similarly, the larger post-peak load capacity of the bridge with bolt insert connectors was due to the larger post-peak strength of the bolt inserts. (see Figs. 4.21(d) and 4.22(c) for connector behaviors).

In the finite element models described so far in this chapter, the floor beams were connected to the girders with six steel connector elements at each connection location, and there was no connection between the deck and the girders. Different connection detail schemes were investigated in an attempt to improve the bridge performance under transverse loading. The new connection schemes were studied with the loading applied at Girder-2 only, because of the reason explained above.

Providing Additional Connector Elements between Deck and Girders

The idea behind the first connection scheme alternative was to provide connection between the deck and the girders, where connector elements similar to those between the floor beams and the girders were provided between the deck and the girders. The connector elements were placed in portions of the deck that were between two adjacent floor beams. One connector element was placed at every 18 in. in between two adjacent floor beams for each girder, as illustrated in Fig. 6.12. The material behavior used for the deck connector elements was assumed to be the same as the material behavior of the floor beam connector elements.

Load-deflection response of the bridge with the deck elements in addition to the floor beam elements is labeled as "Girder2_FloorBeam_5-6_Deckconn" in Fig. 6.13. In this particular example, the displacement loading was applied at Girder-2 at mid-distance between Floor Beam-5 and -6. Comparison of the bridge response with floor beam connectors only and with floor beam and deck connectors is shown in the figure. As evident in the figure, addition of deck connector elements resulted in an increase in the load capacity and post-peak load capacity of the

bridge without changing the overall shape of the load-deflection curve. The increase in load capacity for this particular example was approximately 50 percent.

Providing Tie-Rods between Girders through Floor Beams

In the second connection scheme alternative, steel tie-rods spanning between the exterior faces of the two girders and running through the floor beams were included in the models. A single tie-rod was placed at each floor beam location at the mid-height of floor beams. The rods were connected to steel plates that were attached to the two exterior faces of the girders. The tie-rods were modeled using 2-noded truss elements, and were assigned a perfectly elastic-perfectly plastic material model with 100 ksi strength. The models were analyzed with 1 in. and 1-1/2 in diameter rods. It should be noted that the tie-rods were placed in addition to the girder-floor beam connection elements that were already in the models.

Results obtained from the finite element models including the tie-rods are superimposed in Fig. 6.13. The figure includes the load-deflection curves for both the 1 in. (Rod-1) and 1-1/2 in. (Rod-2) diameter tie-rods. As evident in the figure, using the tie-rods resulted in a significant improvement in the overall behavior of the bridge as compared to the original connection detail and the first connection scheme alternative. With 1-1/2 in. diameter tie-rods, the increase in the load capacity was approximately 100 percent over the case with the floor beam connectors only, and was approximately 34 percent over the case with the floor beam and deck connectors. As the load-deflection curves in Fig. 6.13 indicate, the bridge models with tie-rods were able to maintain the maximum load capacity over the range of transverse displacement values studied. The point that the load-deflection plots for the models with tie-rods became horizontal corresponded to yielding of the rods. It was also determined that for the transverse displacement values shown in the plots, the total strain in the tie-rod elements remained below the fracture strain of 100 ksi tensile strength steel.

Fig. 6.14 shows results similar to those shown in Fig 6.13., but for the case that the loading was applied at Girder-2 at the location of Floor Beam-6. The observations explained for Fig. 6.13 are valid for this figure as well. As compared to the model with the original connection detail, the increase in the transverse load capacity of the bridge was approximately 19 percent when the deck connectors were included and was approximately 99 percent when the 1 in. diameter tie-rods were included.

6.3.3. Effect of Girder Support Flexibility

The analyses explained in the preceding sections included idealized pin and roller boundary conditions for the girders. As explained in Chapter 5, laboratory tests were performed on bearing pad-bearing plate type assemblies in order to determine the stiffness of the support details used at the ends of prestressed concrete girders. Results obtained from these test were incorporated in the finite element models to take into account the effect of girder support flexibility in the behavior of the bridge system under transverse loading.

Fig. 6.15 shows the deformed shape of the bridge and the cracking strain contours occurring when the girder support flexibility was introduced in the bridge model. The figure clearly shows that the overall deformation behavior of the bridge was controlled by the deformation of the girder supports. It is also evident from the cracking strain contours that limited deformation

occurred in Girder-2, while the rest of the bridge remained undeformed. Based on these observations it may be stated that the deformation mode of the bridge was a combination of pure rigid body translation and rotation.

The effect of support flexibility on the overall load-deformation response of the bridge system is presented in Fig. 6.16. The figure shows the load-deformation plots when the idealized pin-roller and flexible boundary conditions were used at the girder ends. The results are for the case where the loading was applied at Girder-1 at the location of Floor Beam-6. When the flexibility of the girder supports was included in the model, stiffness of the bridge was reduced. In this case, the overall load-deflection response of the bridge in the transverse direction was controlled by the stiffness of the girder supports. As shown in Fig. 6.16, load capacity of the bridge with flexible girder boundary conditions was reduced significantly compared to the case with idealized pin-roller boundary conditions. As explained in Chapter 5, the strength of support assemblies used at the girder ends under transverse loading was 24.7 kips for the "expansion" end and 78.0 kips for the "fixed" end detail. The load capacity of the bridge with flexible supports (see Fig. 6.16) was 88.0 kips based on the finite element analyses, and this capacity was a function of contribution of the expansion and fixed ends of the two girders in resisting the applied transverse loading.

6.4. Dynamic Lateral Impact Analyses

The response of a bridge system when subjected to vehicular impact varies depending on the magnitude of the demand exerted on the bridge structure due to the impact loading with respect to the load and deformation capacities of the structure. The analyses described in the preceding sections were useful in determining the capacity of a prestressed concrete through-girder pedestrian bridge system under statically applied lateral loading. The dynamic lateral impact analyses, which are described in the following sections, were conducted in an attempt to determine the demand that would occur on a bridge system when it was subjected to striking of an over-height vehicle. These analyses included a rigid object impacting the bridge girders at several locations with changing amounts of initial velocities. The parameters studied with the dynamic lateral impact analyses included impact location, impact speed, and weight of the impacting object.

6.4.1. Analysis Description

The finite element models used for the static lateral load analyses had to be modified for the dynamic impact analyses. Because of the limitations on the computer time required for analyses, the models included only linear-elastic concrete material models. Therefore, damage occurring due to tensile cracking and compression crushing of concrete elements were not captured in the models. The other simplification that needed to be made was to use perfectly rigid connections between the girders and floor beams, and also between the girders and deck. In other words, truss connector elements that were used in the static analysis models were removed, and the connection between the components of the bridge was achieved by using common nodes at the connection interfaces. These two modifications introduced an artificial stiffness to the bridge system in the dynamic analysis models. In order to compensate for this artificial stiffness and to account for damage that would occur in bridge components during the impact loading, the stiffness of the material models used for the girders, floor beams, and deck were decreased by 30 percent in the dynamic analysis models. A mass proportional damping corresponding to 5 percent of critical damping was used with the concrete materials.

Dynamic analyses were performed only with the impact load occurring on the exterior face of Girder-1. Because the models were linear-elastic, behavior of the bridge will be the same whether the loading is applied on the exterior face of Girder-1 or the interior face of Girder-2. As a result, the assumption of 30 percent less material stiffness (i.e., stiffness of the system is 70 percent of the stiffness of the linear-elastic system) used in the analyses was to emulate the impact on Girder-1. In the case that the impact occurs at interior face of Girder-2, the stiffness of the bridge system is likely to be smaller than 70 percent of the stiffness of the linear-elastic system, as this type of loading relies on steel connectors between the girders and floor beams for redistribution of forces.

Similar to the static analysis finite element models, two types of boundary conditions were defined at the girder ends. Effect of support flexibility on the dynamic response of the bridge was investigated by comparing the results with the idealized pin-roller boundary conditions and with the flexible boundary condition. The measured load-deformation response of the bearing plate-bearing pad assemblies were used to model the flexible supports, similar to the static analysis models.

A rigid body with 7x6x15 in. dimensions was used as the impacting object. The impacting body was positioned at the desired impact location with a small gap between the bridge and the body, as illustrated in Fig 6.17. The impacting body was then assigned an initial velocity in the direction perpendicular to the axis of the bridge. The rigid body impacted the bridge at the exterior face of Girder-1. As shown in Fig. 6.17, the impact location was at the bottom flange of the girder. For this purpose, a contact relation was defined between the impacting body and the bridge. The contact relation allowed the transfer of impact force from the impacting body to the bridge girder during the impact duration, and separation of the impacting body following the rebound of the bridge. The effect of the dimensions of the impacting body remains localized to the impact location. The overall response of the bridge system is a function of the initial impact speed as well as the mass of the impacting body, and not the volume of the body. As a result, the overall response of the bridge system to the impact loading may be assumed to be independent of the impacting body dimensions chosen.

Table 6.1 presents a summary of the variables investigated with the dynamic analyses. As seen, the analysis parameters were the impact location, impact speed, weight of impacting body, and the girder boundary condition. The peak dynamic force (PDF), Equivalent Impact Force (EIF), and Equivalent Static Force (ESF) quantities were used to evaluate the dynamic analysis results. A discussion of the determination of and relation between these force quantities is given in the following sections.

6.4.2. Analysis Results

The variation of dynamic quantities during a typical dynamic analysis is shown in Fig. 6.18. The figure shows the results from Model-2, which included a 30 kip body with 60 mph initial speed impacting Girder-1 at the location of Floor Beam-6, which is the mid-length of the bridge. Fig. 6.18(a) shows the variation of the speed of the impacting body. Speed of the body remained constant at 60 mph until t=0.001 sec, at which point the body came into contact with the bridge. During the impact duration, speed of the body decreased to zero and then increased in the opposite direction. Following the rebound, velocity of the impacting body was -10.6 mph.

The variation of the impacting force during the analysis is shown in Fig. 6.18(b). The force shown in the plot was the contact force between the impacting body and Girder-1. In other words, it was the force that the impacting body exerted on the bridge at the location of contact. As shown, the impact force increased at a fast rate at the beginning of the impact duration, and reached the PDF of 3649 kips at time t=0.0047 sec. After reaching the PDF, the impact force started to reduce, and became zero when rebound occurred at time t=0.0174. The duration between the time at which the impacting body came into contact with the bridge (t=0.001 sec for the model shown in Fig. 6.18) and the time at which the rebound occurred (t=0.0174 sec for the model shown in Fig. 6.18) is termed as "impact duration (Δt_{impact})" in the remainder of this document. It is important to note that the impact duration was not an input parameter, it was rather determined based on the analyses results.

The impact duration values for each model are tabulated in Table 6.1. As seen, the impact in all of the analyses occurred over a very short time interval. The possible reasons for this "fast" impact observed in the analyses are relatively high initial velocities used for the impacting bodies and relatively stiff models used for the bridge and the impacting body. As mentioned earlier, the damage that would occur in the bridge and also in the impacting body during the impact could not be modeled accurately in the analyses, because of restrictions of the program used for the analyses and also because of the excessive computation time required for the analyses. These restrictions resulted in smaller impact duration and larger impact force values than would be expected when an over-height vehicle strikes a bridge.

Fig. 6.18(c) shows the variation of cumulative impulse during the impact duration for Model-2. The cumulative impulse values were determined by calculating the area under the impact force versus time plot for each model, and are listed in Table 6.1. As shown in Fig. 6.18(c), the impulse started to increase when the impacting body came into contact with the bridge, and remained unchanged following the rebound of the impacting body. The load-deflection plot of the bridge as a result of the impact event is shown in Fig. 6.18(d). The load values shown in the vertical axis of the plot are the value of contact force transferred from the impacting body to the bridge, similar to Fig. 6.18(b). The displacement values on the plot are the transverse displacements (i.e., perpendicular to the bridge axis) of the bridge girder at the location of the impact.

Fig. 6.19 shows similar plots as Fig. 6.18 for Model-5f, in which the impact location was in between two adjacent floor beams. The overall bridge response obtained from this model was similar to that of Model-2. The fluctuations in the impact force shown in Figs. 6.19(b) and 6.19(d) were because of the vibration of the impacted girder during the impact duration. This type of vibration occurred because the girder in Model-5f was impacted in between two adjacent floor beams (see Table 6.1). In this case, the portion of Girder-1 spanning between the two floor beams acted like an independent beam supported by the two floor beams. When the impact force was transferred to Girder-1 by the impacting body in between the two floor beams, the portion of Girder-1 spanning between the two floor beams responded to the impact force locally in addition to the global response of the entire bridge system.

Progression of deformation in the bridge model during dynamic analysis is shown in Fig. 6.20 for Model-4f. The figure shows the deformed shape of the structure at different stages during the

dynamic analyses. The time corresponding to each of the deformed shapes shown are also indicated on the pictures. The impact duration determined for this model was 0.0246 sec (see Table 6.1). It can be seen in Fig. 6.20 that the damage occurred in the bridge due to the impact remained local to the portion of the bridge near the impact location until approximately half of the impact duration. After then, the effect of impact progressed rapidly towards the ends of the bridge in the forms of "damage waves". Another observation is that near the end of the impact duration, the ends of the bridge displaced in the opposite direction of the impact force, as opposed to what would be expected in the case of a statically applied transverse load.

6.4.2.1. Determination of PDF, EIF, and ESF Quantities

Three types of force quantities, namely the peak dynamic force (PDF), equivalent impact force (EIF), and equivalent static force (ESF), have been used to quantify the results of dynamic analyses. The PDF represents the maximum value of instantaneous contact force between the impacting body and the structure during the impact duration. Considering the impact duration values observed in this study (maximum of 0.038 sec), it is clear that the structure would be subjected to the PDF over a very short period of time. During such a short period, the structure would not have time to respond to the applied dynamic forces. In addition, as determined by the analytical results, the damage that occurs in the structure due to the impact force remains very local during a significant portion of the impact duration. Because of these reasons, the PDF is not the most suitable load quantity to be used in assessment of overall bridge system performance under impact loads.

The total impulse and impact duration values listed in Table 6.1 were used to determine the EIF value for each model. The EIF values were determined by dividing the total impulse exerted on the bridge by the impacting body with the corresponding impact duration. The total impulse values shown in Table 6.1 were determined by calculating the area under the impact force versus time plot for each model. This approach implicitly assumes that the impact force versus time plots (shown in Figs. 6.18(b) and 6.19(b)) are approximated by a plot that has a constant force with magnitude equal to EIF acting on the bridge during the impact duration (i.e., a rectangular impulse with magnitude EIF and duration Δt_{impact}). Even though the EIF values calculated for the bridge system were always smaller than the PDF values (see Table 6.1), the EIF still acts over a short period of time such that the bridge system would not be able to respond to this force. From this respect, EIF can still be considered as a "dynamic" load.

The ESF is a more appropriate method of representing the intensity of the dynamic loading. It is more appropriate to use ESF values than to use the PDF or EIF values for design and assessment of structures under impact loading. ESF represents force values that the structure would be subjected to over a sufficiently long period of time to which it could respond, but at the same time it is an equivalent of the dynamic impact forces in terms of structure displacement. The ESF values were related to the measured dynamic forces through the load-versus displacement plots of the bridge obtained from the dynamic and static analyses. Figs. 6.21(a) and 6.21(b) illustrate the method used to determine ESF for Model-3 and Model-3f, respectively. As shown, ESF is the force obtained from the static analysis corresponding to the displacement value at which the PDF occurs in the dynamic analysis.

Effect of Girder Support Flexibility on ESF

As evident in Figs. 6.21(a) and 6.21(b), ESF values for Model-3 and Model-3f were significantly different, even though dynamic analysis of the two models resulted in very similar load-deflection behaviors. The reason for the significant difference in the ESF values for Model-3 and Model-3f was the difference in the static load-deflection plots of the two models. As seen, the overall stiffness of the bridge in Model-3f was only approximately 10 percent of the stiffness in Model-3 based on the static analysis result. This difference in the load-deflection behavior of the bridge models was due to the way that the support flexibility was modeled in the finite element Model-3f. Including the flexibility of the girder supports did not cause an appreciable difference in the bridge response in the dynamic response, while it significantly reduced the stiffness of the bridge in the static analyses models. Effect of support flexibility on the dynamic behavior of the bridge system is further discussed in the following sections.

Fig. 6.22 shows the measured load-deformation response of the bearing pad-bearing plate assemblies used at the ends of prestressed concrete girders (see Chapter 5). Superimposed on the same figure are the linear load-deflection behaviors used for the truss elements to simulate the girder support flexibility in the dynamic finite element models and also in the static finite element models that were used in determining ESF values. Linear material behaviors were used in the static models because the companion dynamic models had linear material behaviors as well. As shown in Fig 6.22, the points of maximum load on the measured load-deflection plots of the support bearing assemblies (i.e., the fixed end and expansion end) were used to determine the corresponding load-deflection behaviors that were used in modeling the support flexibility in the static finite element models.

6.4.2.2. Effect of Impact Speed

The majority of the dynamic analyses were performed with an impact speed of 60 mph, except for Model-4f, which was analyzed with a 30 mph of impact speed. A comparison of impact force versus time profile of Model-3f and Model-4f is given in Fig. 6.23. The shapes of the impact force-versus time for the two models were similar, except that Model-3f had approximately 90 percent larger PDF than Model-4f. This resulted in a total impulse in Model-3f that was approximately 107 percent larger than that in Model-4f. The ratios of the EIF and ESF from Model-3f and Model-4f were approximately 1.89 and 2.53, respectively (see Table 6.1). These results suggest that severity of the impact increases with increasing impact speed.

6.4.2.3. Effect of Impacting Weight

Fig. 6.24 shows the impact force-versus time plots for Model-1f, Model-2f, and Model-3f, which included 10 kips, 30 kips, and 72 kips impacting objects, respectively, with the rest of the analysis parameters held the same. The 72 kips weight used in Model-3f corresponded to the weight of an AASHTO HS20 design truck. As evident in Fig. 6.24, increasing the weight of the impacting object resulted in increases in both the impact duration and the impact force. Between Model-1f and Model-2f (10 kips versus 30 kips impacting objects) the PDF increased by approximately 29 percent, while the increase in PDF between Model-1f and Model-3f (10 kips versus 72 kips) was approximately 65 percent. The increases in EIF and ESF were 15 percent and 42 percent, respectively, between Model-1f and Model-2f, and 97 percent and 175 percent, respectively, between Model-1f and Model-3f.

Variation of the impact force with the weight of the impacting body is plotted in Fig. 6.25. The plots shown in the figure include the results from Model-1f, Model-2f, and Model-3f. As seen, ESF increases almost linearly with the weight of impacting body, while the variation is close to linear for PDF and EIF.

6.4.2.4. Effect of Impact Location

The effect of the impact location on the impact force versus time behavior of the bridge system is presented in Fig. 6.26. In Model-3f the impact occurred at the midspan of the bridge, where there was a floor beam. In Model-5f, on the other hand, the impact location was at mid-distance in between two adjacent floor beams close to the midspan of the bridge (7 ft.-9 in. from the midspan). The fluctuations shown in the contact force from Model-5f were due to the portion of Girder-1 spanning between the two floor beams responding to the impact force locally in addition to the global response of the entire bridge system, as explained earlier. Moving the impact location from the midspan of the bridge to 7 ft.-9 in. off of midspan resulted in approximately 17 percent decrease in PDF, while increasing the impact duration. Model-5f also had approximately 25 percent and 42 percent, respectively, smaller EIF and ESF, as compared to Model-3f.

6.4.2.5. Effect of Girder Support Flexibility

Fig. 6.27 shows the results from Model-3 and Model-3f. Model-3 had idealized pin-roller girder boundary conditions while the girder boundary conditions in Model-3f were defined using truss elements at the girder ends to simulate the support flexibility. As explained earlier in the static analysis sections, including the girder support flexibility significantly affected the overall response of the bridge system under transverse loading. The flexible supports significantly reduced the overall transverse stiffness of the bridge and resulted in a decrease in the transverse load capacity. The contact force versus time plots shown in Fig. 6.27, on the other hand, indicate that there was almost no change between the dynamic behavior of the bridge when the support flexibility was included in the model. The reason for this was that the effect caused by the impacting body on the entire bridge remained very localized. In this case the entire bridge did not have time to respond to the dynamic forces exerted on the bridge girder by the impacting body. In the static analyses, on the other hand, the entire bridge responded to the transverse load that was applied statically to the bridge girders.

As shown in Fig. 6.27, Model-3 and Model-3f had almost identical PDF and impact duration. The difference between the EIF from the two models was only approximately 1 percent. However, there was a significant difference in the ESF for each model, as shown in Table 6.1. The ESF for Model-3, which had idealized pin-roller girder supports, was approximately ten times the ESF for Model-3f, which had flexible girder supports. The reason for this discrepancy was the excessive flexibility of static models with flexible girder supports, as explained in detail in Section 6.4.2.1.

Variation of Girder Support Reaction with Time

Fig. 6.28 shows the variation of the total transverse reaction (i.e., horizontal reaction perpendicular to the bridge axis) generated at the ends of girders for Model-3 due to impact on one of the girders. As indicated in Table 6.1, this model included a 72-kip impacting object that had an initial speed of 60 mph. Variation of the impact force during the impact duration is also

superimposed on the same plot. As seen, when the impact force reached its peak value (4591 kips) at time t=0.088 sec., there was still no reaction at the girder ends. This indicates that at this time, the "effect" of impact that occurred at the mid-span of the bridge has not reached the ends of girders, yet.

As the effect of impact reached the ends of girders in the form of damage waves, the reaction at the girder ends started to increase, as shown in the figure. The positive reaction indicates a reaction in the direction of the impact force. This is opposite to what would be expected in static loading, where the reaction is always in the opposite direction of the applied force. Fig. 6.28 also shows that the girder-end reaction changes direction at time t=0.027 sec. due to vibration of the girders caused by the impact. It is also important to note that the maximum value of support reaction (5158 kips) occurred after the rebound of the impacting object (i.e., during the free-vibration phase). The total girder support reaction of 5158 kips means a lateral reaction force of approximately 1300 kips at each girder end. Considering that the lateral load capacity of the support details used at the expansion and fixed ends of prestressed concrete girders were measured to be 24.7 and 78.0 kips, respectively, it is clear that the girder ends will undergo large amounts of displacements in the event of lateral vehicular impact.

Variation of Girder-End Displacements with Time

Fig. 6.29 shows the displacements that occurred at the girder ends in Model-3f. Because this model included the flexibility of girder supports, horizontal displacements of the girder ends were not fully restraint, which resulted in the girder ends to move under the effect of impact that occurred at midspan of the bridge. The displacements plotted in the figure are the horizontal displacements of the girder ends in the direction perpendicular to the longitudinal axis of the bridge. Superimposed on the same figure is the variation of the impact force during the impact duration. The positive displacements in the plot indicate that ends of the girders move in the opposite direction of the impact force. Similar to the case with the support reaction, movement of the girder ends in the opposite direction of the impact force is counter-intuitive considering static loading. When the impact force reached its maximum value, the girder ends still had zero displacements, indicating that the effect of impact has not reached the girder ends, yet. As seen, vibration of the girders resulted in 3 in. displacement of the girder ends in the opposite direction of the impact force and 7.1 in. in the direction of the impact force. These observations indicate that ends of prestressed concrete girders are expected to undergo large amounts of displacements under the effect of lateral impact force.

6.4.3. Summary of Results

The dynamic analyses revealed a different deformation pattern of the bridge system than the deformation patterns observed in the static analyses. The damage in the bridge caused by the impacting body was observed to remain very localized near the impact location until approximately half of the impact duration. After that time, the effect of impact progressed rapidly towards the ends of the bridge in the forms of "damage waves." Progression of these waves into the ends of the girders caused the girder ends to move in the opposite direction of the impact force, as opposed to what would be expected in the case of a statically applied lateral load.

The PDF and EIF values determined from the dynamic lateral load analyses were significantly higher than the lateral load capacity of the bridge system determined from the static lateral load analyses, for both the flexible and rigid girder support cases. The ESF values, on the other hand, were smaller than the static lateral load capacity of the bridge for the cases with flexible girder supports, while for the rigid supports the ESF values were still larger than the static lateral load capacities. Support flexibility of the girders did not have much effect on the dynamic behavior of the bridge, as opposed to the behavior observed in the static lateral load analyses. This was mainly because of the fact that the effect caused by the impacting body on the bridge system remained very localized in the dynamic analyses. The reason that the ESF values for the flexible and rigid girder support cases were different was because of the difference in the static load-deflection behavior of the bridge system for these two cases.

Even though the levels of force demand indicated by the dynamic analyses were higher than the lateral load capacity of the bridge system determined from static analyses, this does not necessarily imply collapse of the bridge structure. In the event of vehicular impact, the post-peak deformation capacity of the girder-floor beam connections is expected to allow for redistribution of loads between the connected members. Therefore, failure of some inserts, or even some girder-floor beam connections do not necessarily imply collapse. Moreover, because of the increase in material strengths associated with the high loading rates, the load capacity of the bridge system in the event of vehicular impact is expected to be higher than the load capacity determined from the static analyses.

Analysis of girder support reactions and girder end displacements determined, respectively, from the models with rigid and flexible girder supports indicate that in the case of lateral vehicular impact (1) force capacity of the girder support details are expected to be exceeded, and (2) large amounts of displacements are expected to occur at the girder ends. Providing concrete side-walls on both sides of prestressed concrete girders at the girder ends would prevent excessive lateral deformation of the girder ends and would eliminate a possible failure mode of falling of girders off the bridge supports. It is important, however, to note that increasing the rigidity of the girder end supports would make the bridge stiffer, which results in larger impact forces in the girders. Therefore, the side-walls should not be placed directly against the girder ends and some gap (e.g., 8 in.) should be provided. This would also allow the girder ends to slide on the bridge seating during the vibrating of girders and dissipate the energy generated by the vehicular impact.

Because of various limitations, the damage that would occur in the bridge components under the effect of impact loading could not be modeled in the dynamic analyses. In the event of a vehicle striking a bridge, the impact loading would cause damage in the girders, floor beams, and deck in the form of concrete cracking and crushing. The extent of damage would be highest near the location of the impact. It is likely that when an over-height vehicle impacts a bridge, a portion of the impacted girder will be broken out near the impact location. In this case, the amount of force delivered to the girder would depend on the resistance of the girder to the breakout force. Possible effects of losing portions of prestressed concrete girders on the overall stability of the bridge system are investigated in the following section.

6.5. Stability Analysis under Gravity Loading

As explained previously, when one of the girders in a typical prestressed concrete through-girder bridge is subjected to high-speed dynamic impact of an object, the damage that occurs in the girder remains very local to the impact location. The finite element models used in the dynamic impact analyses were unable to capture this type of damage in the girders because of the linear-elastic material models used for the girder elements in the models. As a result, any possible effect of local concrete damage at the bottom portion of prestressed concrete girders due to impact loading on the overall stability of the bridge system could not be investigated with the previous finite element models that were used for the static lateral load analyses and dynamic lateral impact analyses. Additional finite element analyses were conducted in an attempt to investigate the stability of the entire bridge structure under the bridge self-weight when bottom portions of the girders become damaged due to dynamic impact loading.

6.5.1. Analysis Description

The bridge geometry in the models used for the gravity stability analyses were similar to the geometry in the models that were used for the static lateral load and dynamic impact analyses. Following the application of the prestressing force and the self-weight of the bridge, the model was analyzed under the effect of these loads for the rest of the analysis. The effect of damage that would occur in the girders due to the dynamic impact loading was simulated by removing the concrete and prestressing strand elements in the bottom flange and bottom portion of the girder web, as shown in Fig. 6.30. The element deactivation feature in MSC.Marc/Mentat [75] was used for this purpose. Following the application of the prestressing force and the bridge self-weight to the model, several load cases were defined with one additional layer of elements being deactivated in each load case. The elements were deactivated gradually starting from the bottom of the girders towards the top until the bridge became unstable under its self-weight. The instability was evident in excessive deflection of the bridge and non-convergence of the analysis solution in some cases.

Different element removal schemes were investigated with the models. The elements were removed from a single girder as well as from both girders simultaneously. Element removal was also performed at different locations along the bridge length.

The element removal procedure that was utilized in the models is explained in Fig. 6.31. The figure shows the cross section and side view of a typical girder used in the models. Locations of the prestressing strands inside the girder sections are also shown in the figures. As indicated in the figure, elements were removed from the girders at the mid-distance between the two adjacent floor beam locations (Figs. 6.31(a) and 6.31(c)), as well as at the floor beam locations (Figs. 6.31(b) and 6.31(d)). The hatched areas in Fig. 6.31(c) and 6.31(d) indicate the elements removed along the length of the girders. Even though the shape and size of the areas from which the elements were removed were arbitrarily chosen, these areas were believed to be realistic considering the geometry of a backhoe or a boom truck (e.g., cherry picker), which are common types of vehicles involved in over-height vehicle collision incidents. The element mesh sizing at the location that the elements were removed was another parameter that controlled the shape and size of the area from which the elements were removed.

Progression of the element removal during the analysis is indicated in Figs. 6.31(a) and 6.31(b). The numbers shown in these figures indicate the order in which each element was removed during the analysis. As shown, at each analysis step, one layer of girder elements was removed starting from the bottom of the girders. For the cases that the element removal was performed at the floor beam locations, the floor beam elements, in addition to the girder elements, were removed as shown in Fig. 6.31(b). The steel strand elements at each level inside the girders were removed together with the concrete elements that were directly below the strand elements (i.e., the first layer of strand elements were removed together with the concrete elements numbered as #1 in Figs. 6.31(a) and 6.31(b), while the last layer of strand elements were removed together with the concrete elements #10).

Table 6.2 shows a summary of the stability analyses performed with the associated variables and the results. In Analysis 1, 2, 3, and 4 the elements were removed from both girders while in Analysis 5, 6, 7, and 8, the elements were removed from only one of the girders. In this way, the analyses covered both cases of one girder and two girders being damaged due to impact. The second variable shown in Table 6.2 was the location along the bridge that the elements were removed from the girders. In most of the analyses, the elements were removed at locations that were mid-distant between two adjacent floor beams. Analyses were also performed with the elements removed at floor beam locations (Floor beam numbering scheme is shown in Fig. 6.32).

The effect of the location of element removal was investigated with the models that had the original girder-floor beam connection detail. As mentioned in previous chapters, this detail included connectors between the girders and floor beams while no connection between the deck and the girders was provided. Some of the analysis cases including the original detail were repeated with two types of modified connection details. The first modified detail included threaded rod and anchor connectors between the girders and the deck in addition to those between the girders and the floor beams. In the second modified detail, steel rods going through each floor beam and spanning between the outside faces of the two columns were added to the original detail.

6.5.2. Analysis Results

As mentioned before, the elements at the girder bottom flange and at the bottom portion of the girder web (and at the floor beam ends in the cases that the element removal was done at the floor beam locations) were removed gradually until the bridge model became unstable under its self-weight. For all combinations of the analysis variables, the analysis step at which the structure became unstable was determined, and the results are presented in Table 6.2. The failure analysis step numbers in Table 6.2 are presented based on the element removal order numbering shown in Figs. 6.31(a) and 6.31(b).

As the elements were removed during analysis, cracking in the girders, floor beams, and the deck developed, and deflection of the girders increased gradually. Progression of damage in the girders due to removal of the elements in analysis #3 is shown in Fig. 6.33. As indicated in Fig. 6.33(a), in this particular analysis, the elements were removed from the girders at mid-distance between floor beams 3 and 4. The figure also shows the equivalent cracking strain contours in the girder elements as each layer of elements were removed from both girders. Removal of the girder elements caused development of cracking in the elements close to the region that the

elements were removed. Progression of cracking into the top flange of the girders resulted in failure of the bridge, which is evident with the excessive vertical deflection of the girders, as shown in Fig. 6.33(d).

Effect of Damage Location

The last column of Table 6.2 indicates that as the location along the length of the bridge that the elements were removed became closer to the mid-length of the bridge, failure of the bridge occurred sooner during the analyses. When the girder elements were removed from the girders between floor beams 5 and 6 (analysis #1 in Table 6.2), failure occurred at analysis step #8. When the location of the element removal was moved to between floor beams 4 and 5 (analysis #2) and between floor beams 3 and 4 (analysis #3), failure of the bridge did not occur until analysis step #9 and #10, respectively. This was an expected result, because the moment due to self-weight of the bridge is maximum at the mid-length of the bridge and it gets smaller towards the ends of the bridge. Therefore, locations near the midspan of the girders are more susceptible to failure than those near the girder ends.

Effect of Damage on Single versus Both Girders

The effect of removing the girder elements from a single girder versus from both girders can be seen when analyses #1 and #5 are compared. In analysis #1, the elements were removed from both girders at mid-distance between floor beams 5 and 6, while in analysis #5 the elements were removed from only one of the girders at the same location. As indicated in last column of Table 6.2, failure in analysis #1 occurred sooner than in analysis #5. The reason that the failure occurred later when the elements were removed from a single girder was due to the redistribution of loads from the damaged girder to the other girder. When the girder elements were removed from one of the girders and the girder started to deflect, the connectors between the girders and the floor beams allowed the transfer of loads from the deflecting girder to the floor beams and from floor beams to the other girder. In this way, the girder with elements removed was able to resist the gravity loading longer than the case when the elements were removed from both girders. The amount of load redistribution between the impacted girder and the other girder depends on the strength of connectors between the girders and the floor beams and also on the cracking strength of the floor beams.

Effect of Girder-Floor Beam Connection Detail

In order to investigate the effect of the strength of connections between the girders and the floor beams and also between the girders and the deck, analysis #5 was repeated with two types of modified connection details. In analysis #7, new connector elements were added between the girders and the deck in addition to the existing connectors between the girder and the floor beams. The connector elements were uniformly distributed along the bridge length at 18 in. spacing. Including these additional connector elements in the analysis did not change the behavior of the bridge significantly. Table 6.2 shows that in both analysis #5 and #7 the failure occurred at analysis step #9. This indicates that the addition of new connectors between the girders and the deck did not increase the amount of redistribution between the two girders, significantly.

The second connection modification that was investigated in an attempt to improve the load redistribution between the girders was to add steel rods that run through the floor beams and to

tie the two girders together. Truss elements were placed inside the floor beams to model the steel rods. Ends of these steel truss elements were connected to the steel solid elements that were attached to the outside face of the concrete solid elements simulating the girders. A single 1-in. diameter rod was used at each floor beam location. In the analysis including this connection detail (analysis #8 in Table 6.2), failure occurred at analysis step #10, as opposed to the failure occurring at analysis step #9 with the original connection detail and the first modified connection detail. The increased strength of the connections between the girders and the floor beams resulted in improved load redistribution between the two girders and hence delayed the failure of the bridge.

6.5.3. Summary of Results

Results of the analyses indicated that local girder damage that would occur in prestressed concrete through-girder pedestrian bridges due to striking of over-height objects may cause the failure of the bridge depending on the damage to which the girders would be subjected. In the finite element models, the damage in the prestressed girders was simulated by removing selected girder elements, which means that complete concrete crushing and fracture of prestressing strands at the damage location was assumed. Analysis results showed that in the case of both girders being impacted, failure of the bridge would occur when approximately 15 percent to 40 percent of the web, depending on the location of impact, was damaged in addition to the entire bottom flange. The bridge was more susceptible to failure when the impact damage occurred near the girder midspan than the girder ends.

When only one of the girders was impacted, failure of the bridge would require slightly larger amount of damage in the girder section. The amount of "additional capacity" between the cases of single girder damage and double girder damage was due to load redistribution from the impacted girder to the other girder. The amount of load redistribution depended on the strength of the connectors between the girder and the floor beams. One of the two modified connection details resulted in an improvement in the load redistribution between the girders while the behavior of the bridge with the other modified connection detail was not significantly different than the behavior with the original detail.

It should be noted that the analyses explained in Section 6.5 were performed under statically applied gravity loading. Therefore, all the damage caused in different portions of the bridge in the models was due to the gravity loads. In the case of an actual impact, the bridge components would be subjected to small-duration dynamic loads acting in the lateral direction. In this case, different portions of the bridge would undergo damage under the effect of these dynamic impact loads. In addition, the amount of redistribution between the bridge components would be affected by the ductility of the connectors as well as their strength.

Table 6.1. Summary of Dynamic Finite Element Analyses

Model	Impact location		Impact speed mph	Impacting weight kips	Boundary condition	Total impulse kips.sec	Impact duration seconds	*PDF kips*	*EIF kips*	*ESF kips*
	Girder	Floor beam								
1f	1	6	60	10	Flexible	11.28	0.0076	*2781*	*1484*	*81*
2	1	6	60	30	Pin & roller	32.75	0.0164	*3649*	*1997*	*1156*
2f					Flexible	33.20	0.0194	*3596*	*1711*	*115*
3	1	6	60	72	Pin & roller	81.68	0.0282	*4591*	*2896*	*2234*
3f					Flexible	78.76	0.027	*4598*	*2917*	*223*
4f	1	6	30	72	Flexible	37.99	0.0246	*2411*	*1544*	*88*
5f	1	5-6	60	72	Flexible	83.11	0.0378	*3807*	*2199*	*129*

Table 6.2. Summary of Gravity Loading Stability Analyses

Analysis number	Girder	Location of element removal	Girder-floor beam connection detail	Failure analysis step
1	Both girders	Between floor beams 5 and 6	Original	8
2	Both girders	Between floor beams 4 and 5	Original	9
3	Both girders	Between floor beams 3 and 4	Original	10
4	Both girders	At floor beam 6	Original	7
5	Single girder	Between floor beams 5 and 6	Original	9
6	Single girder	At floor beam 6	Original	8
7	Single girder	Between floor beams 5 and 6	Additional connectors in deck	9
8	Single girder	Between floor beams 5 and 6	Rods through floor beams	10

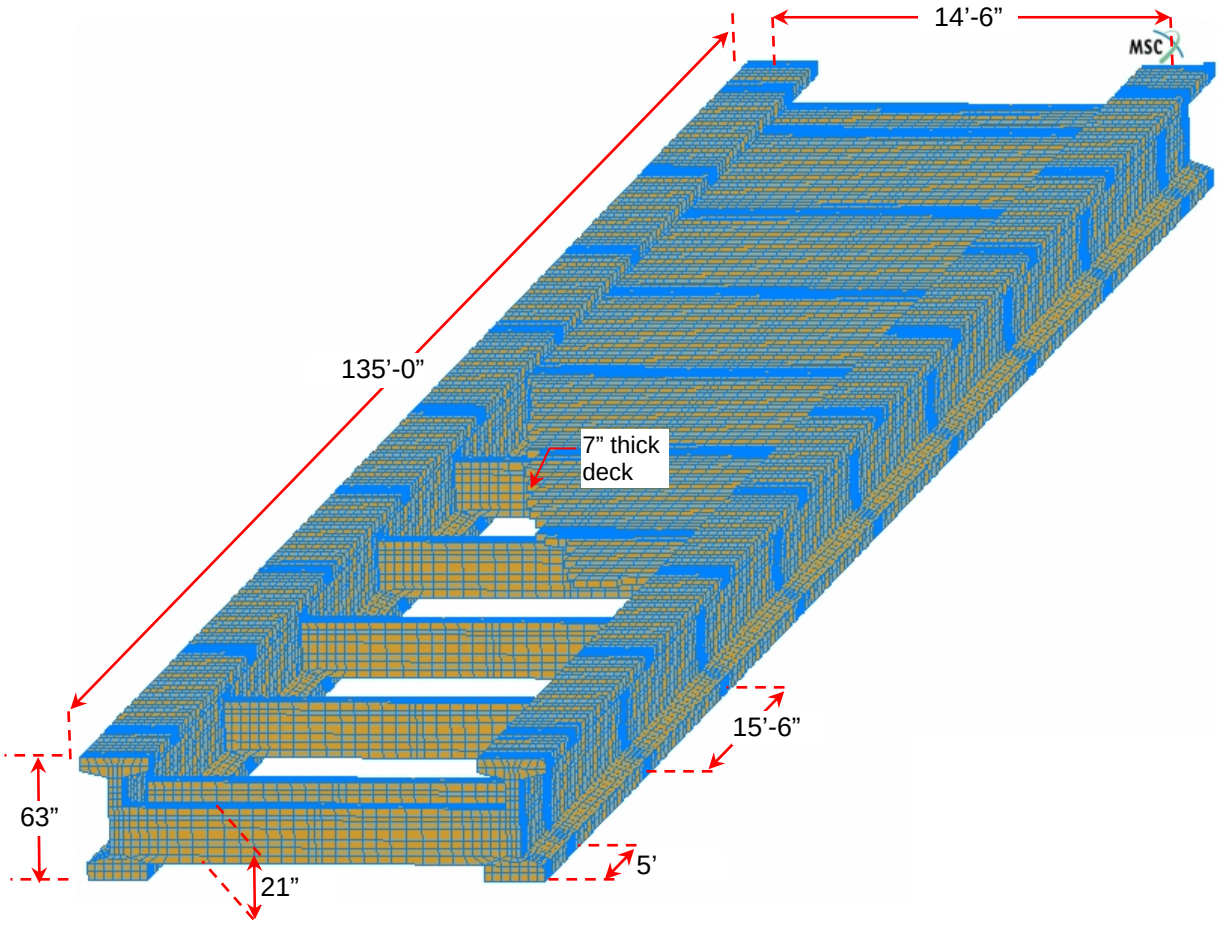

(a)

Fig. 6.1. Overall view of finite element model: (a) dimensions used in the models

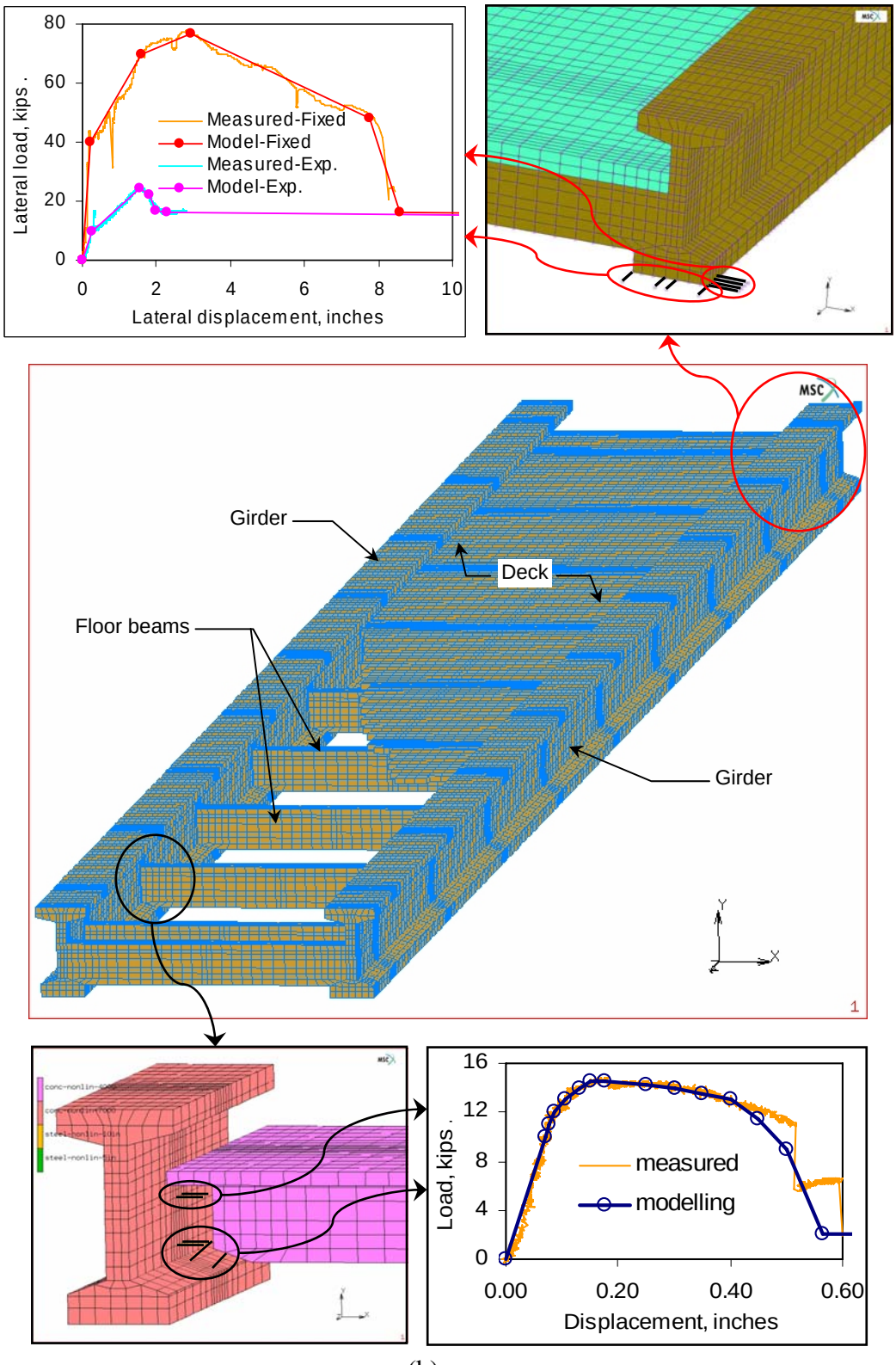

(b)

Fig. 6.1. Overall view of finite element model (continued): (b) modeling of components.

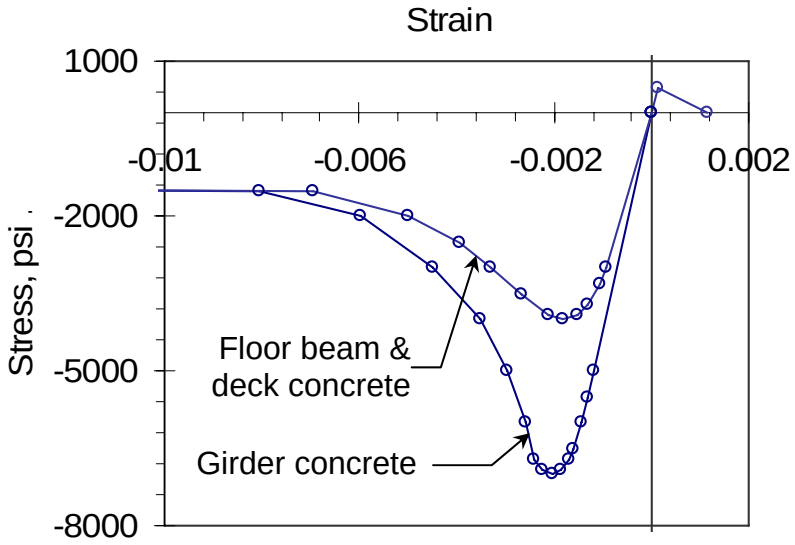

Fig. 6.2. Concrete material behaviors used in the models.

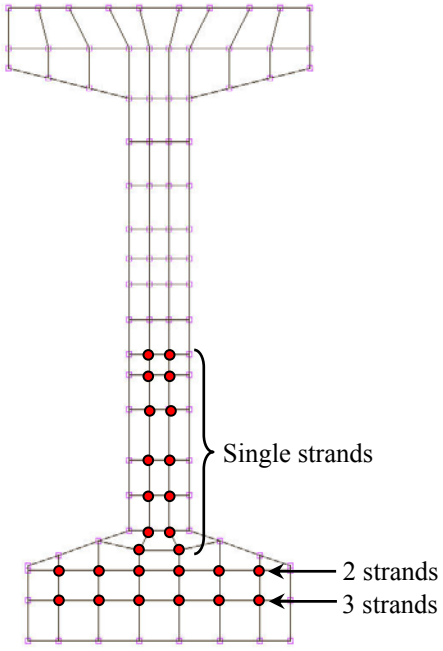

Fig. 6.3. Modeling of prestressing strands.

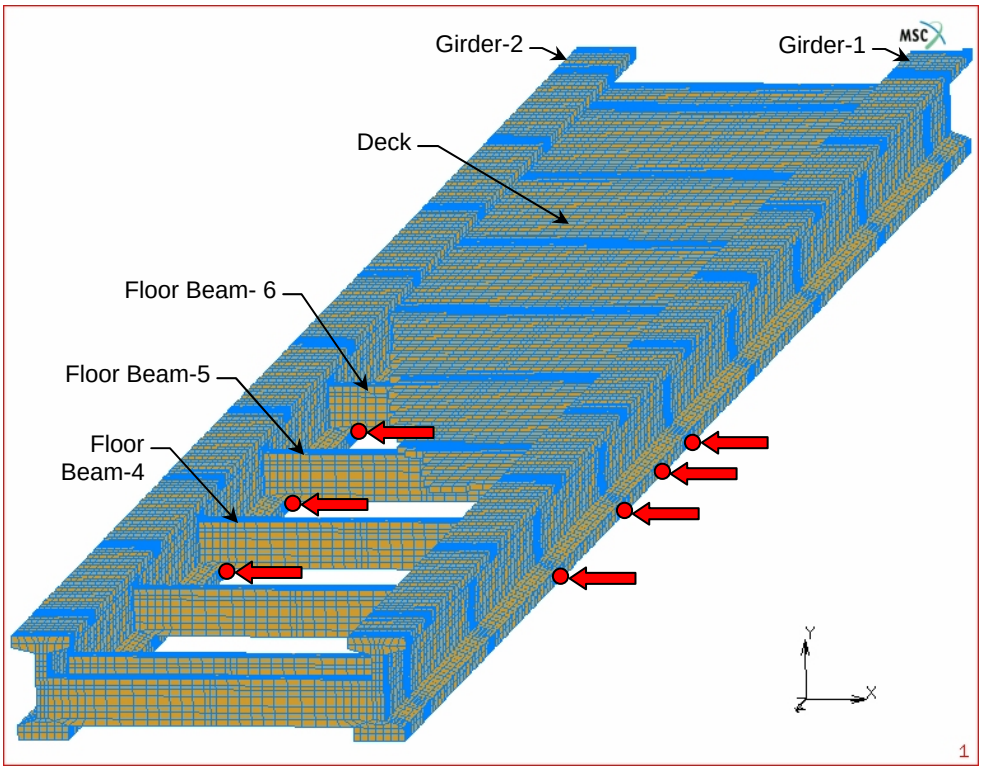

Fig. 6.4. Location of transverse displacements applied to the model.

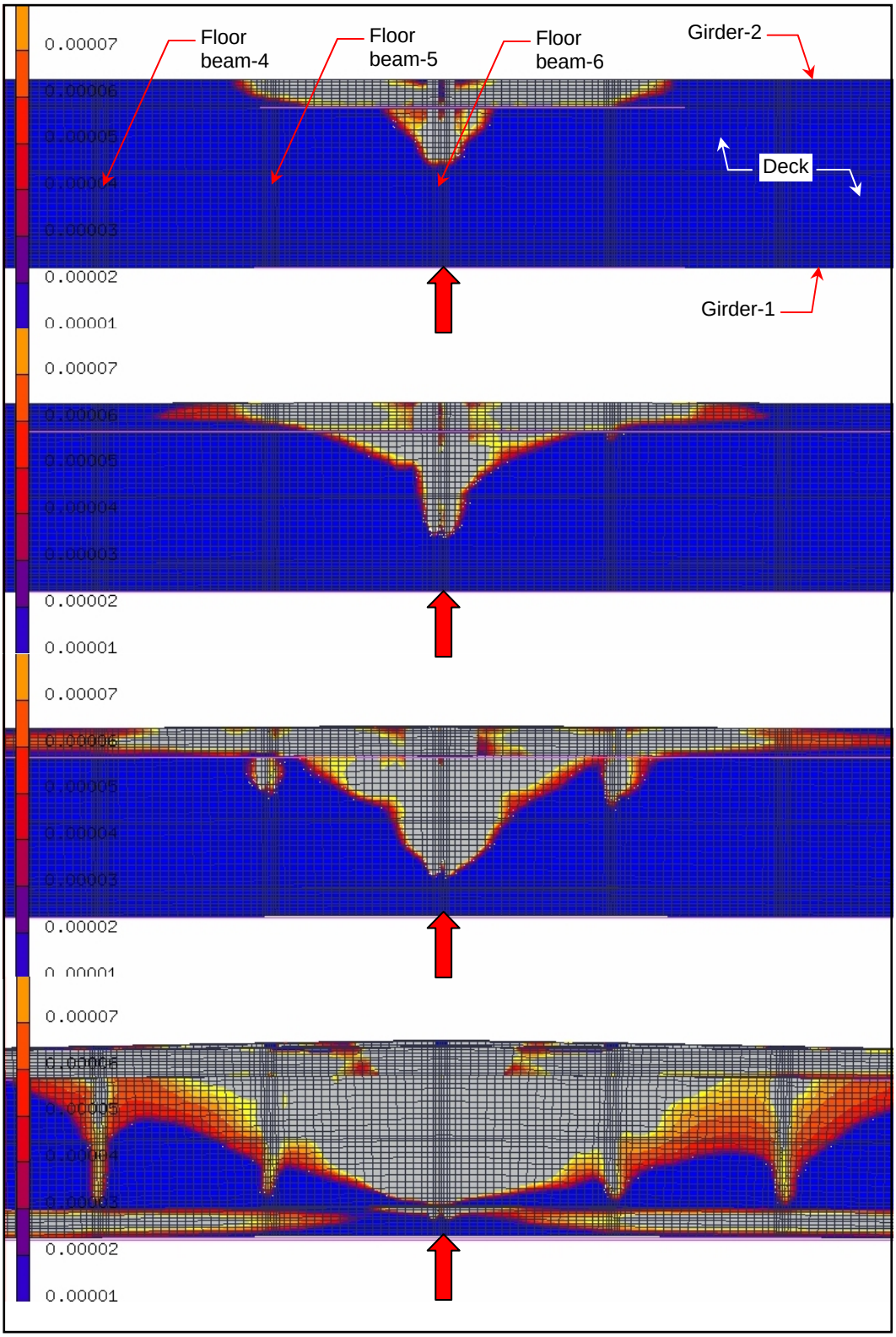

Fig. 6.5. Progression of damage with loading on Girder-1 (plan view).

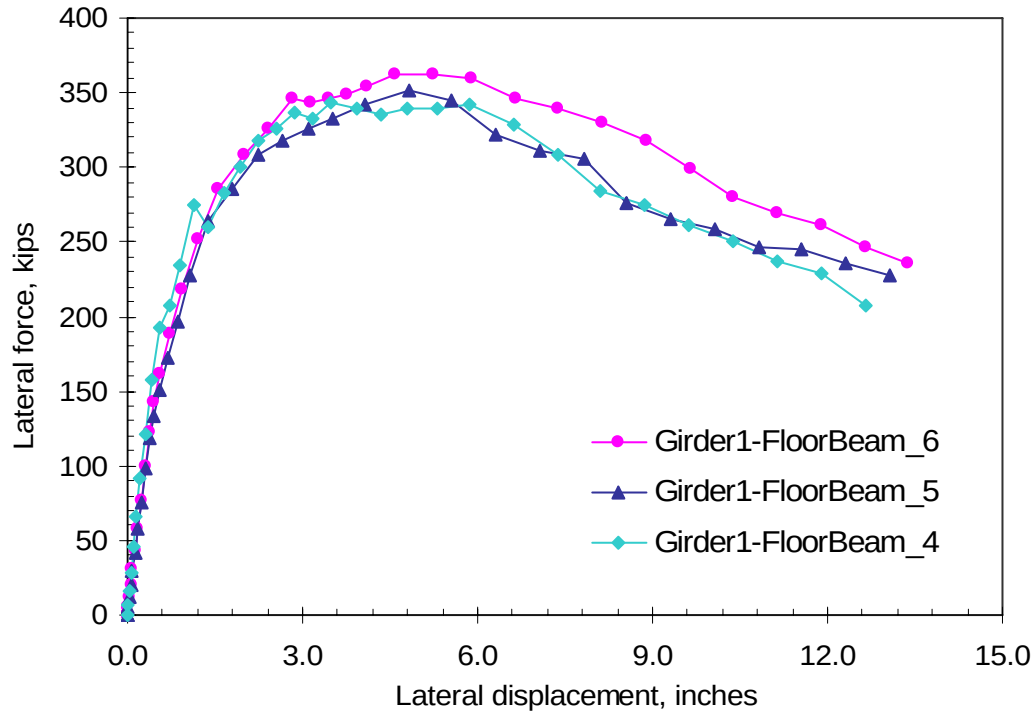

Fig. 6.6. Effect of loading location (loading at Girder-1 at Floor Beam-4, -5, and -6).

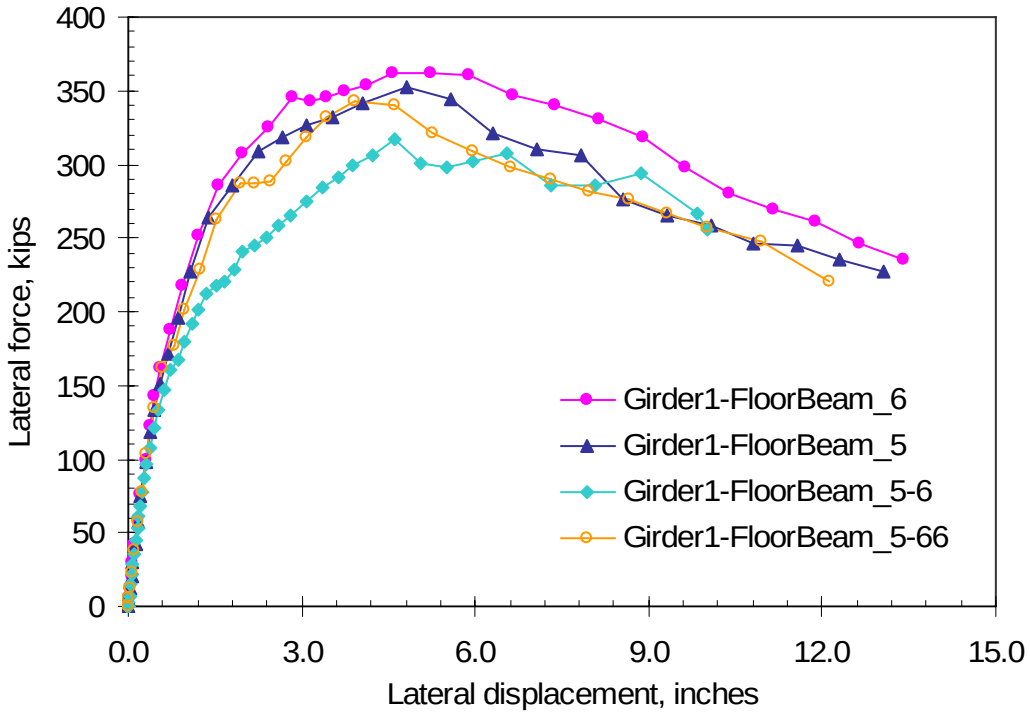

Fig. 6.7. Effect of loading location (loading at Girder-1 between Floor Beam-5, and -6).

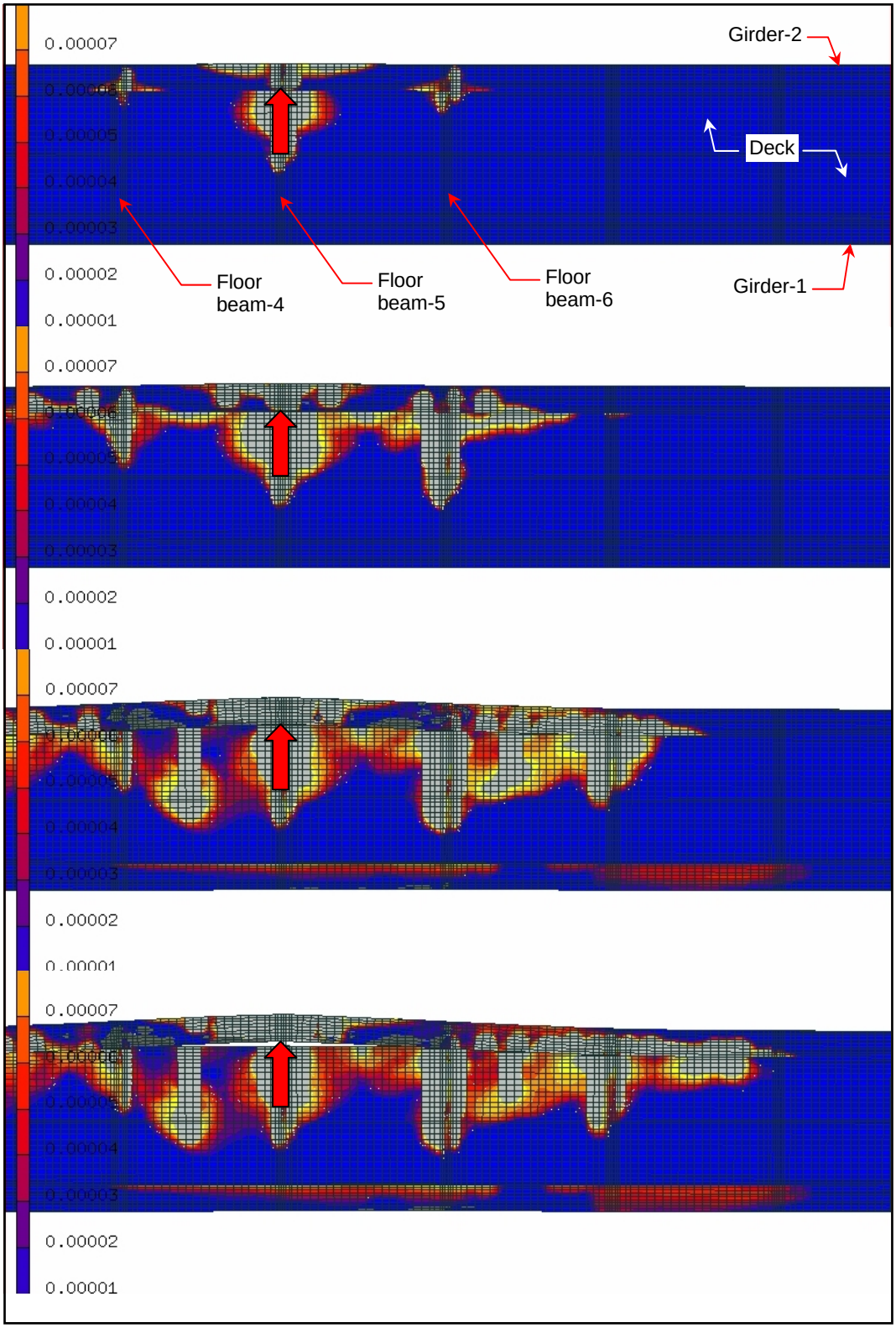

Fig. 6.8. Progression of damage with loading on Girder-2 (plan view).

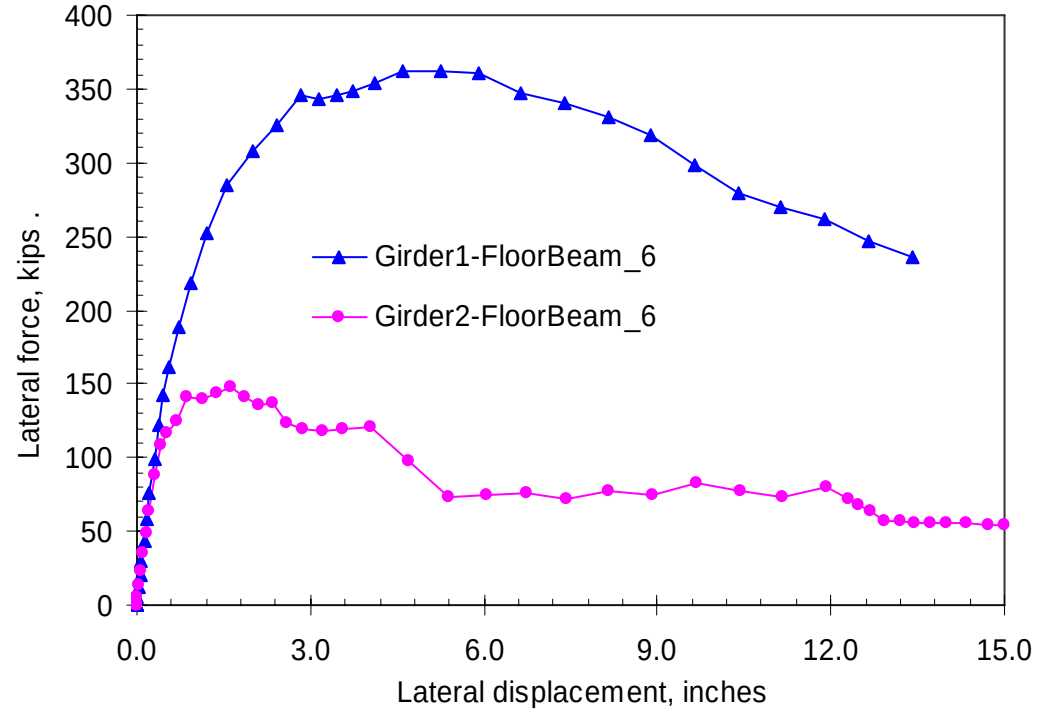

Fig. 6.9. Effect of loading location (loading at Girder-1 and Girder-2).

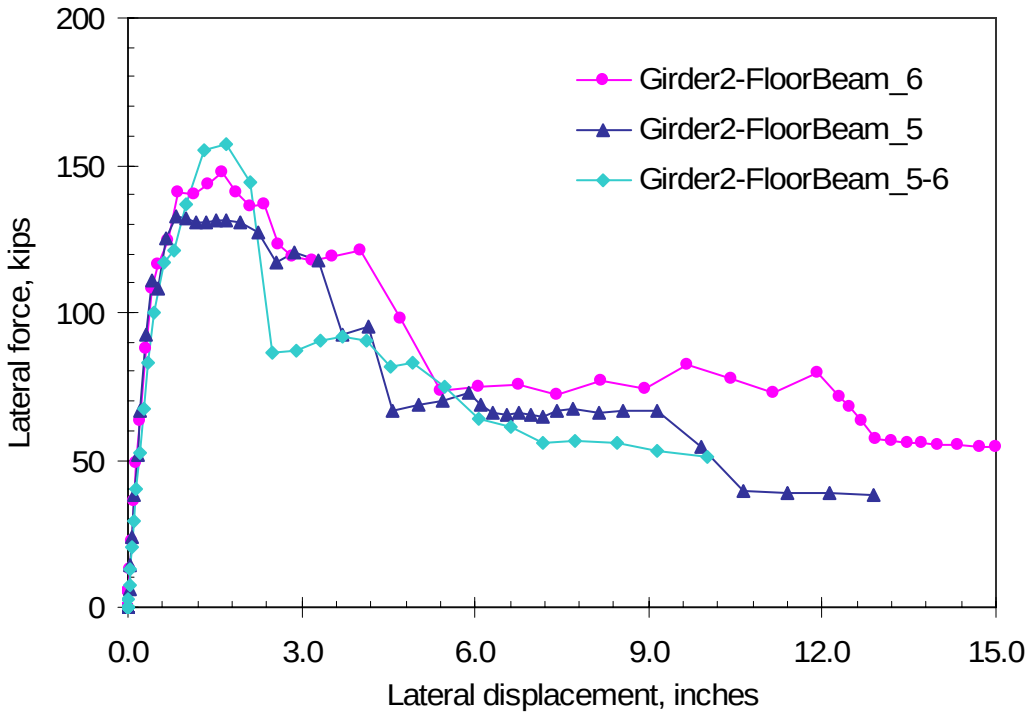

Fig. 6.10. Effect of loading location (loading at Girder-2 between Floor Beam-5, and -6).

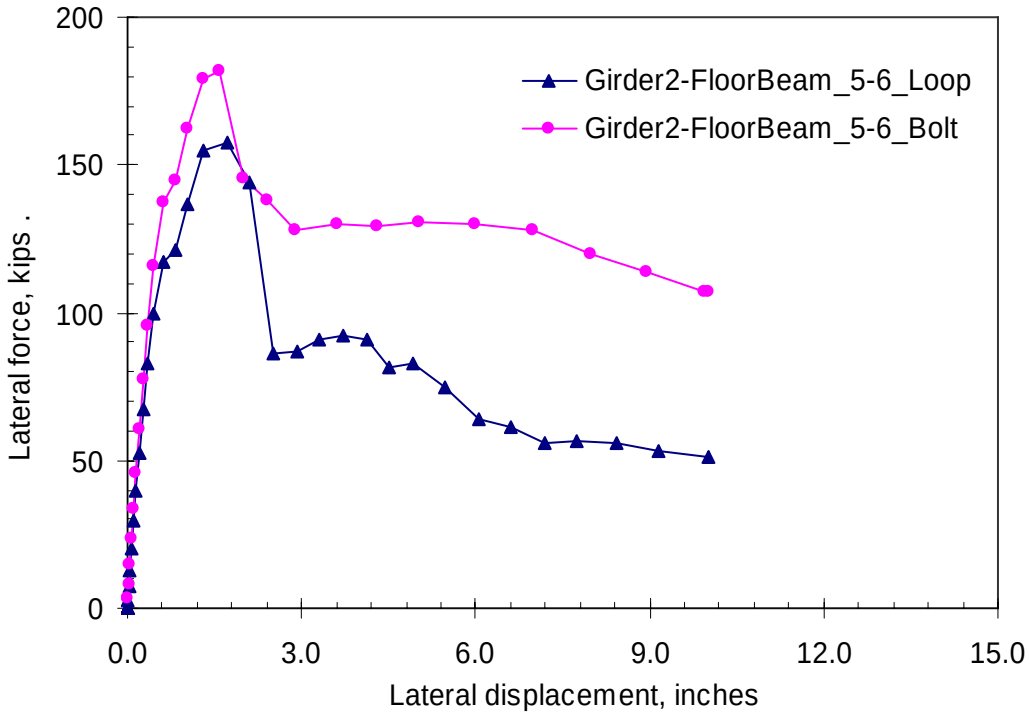

Fig. 6.11. Effect of connector type (loading at Girder-2 between Floor Beam-5, and -6).

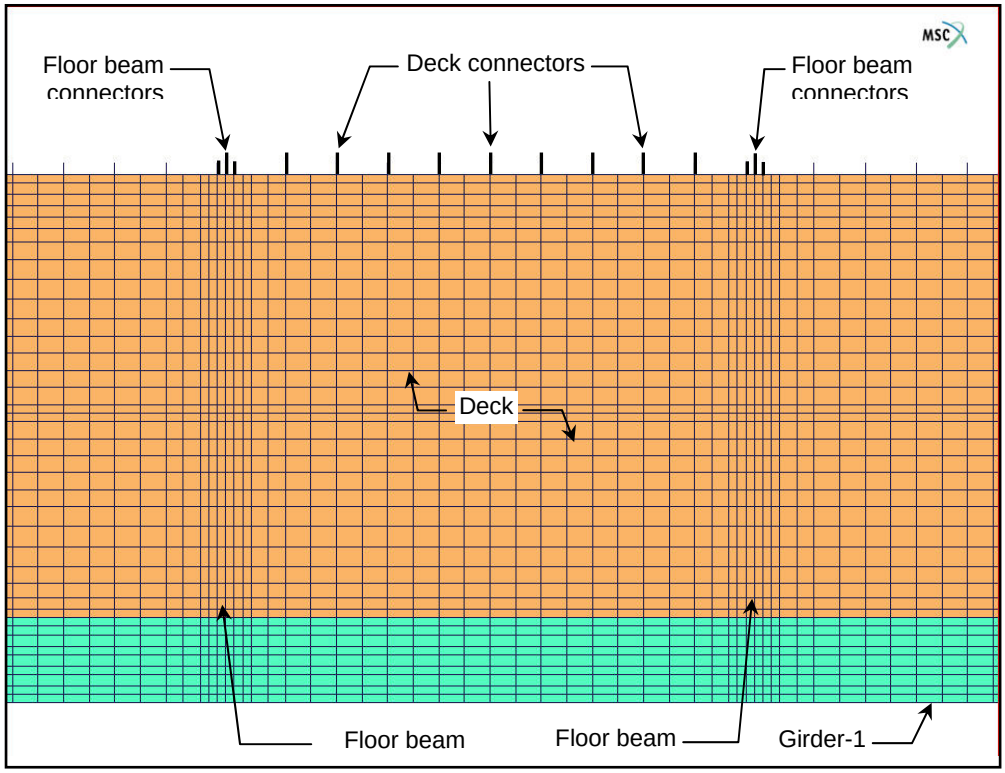

Fig. 6.12.Location of deck connectors (plan view) (Girder-2 not shown).

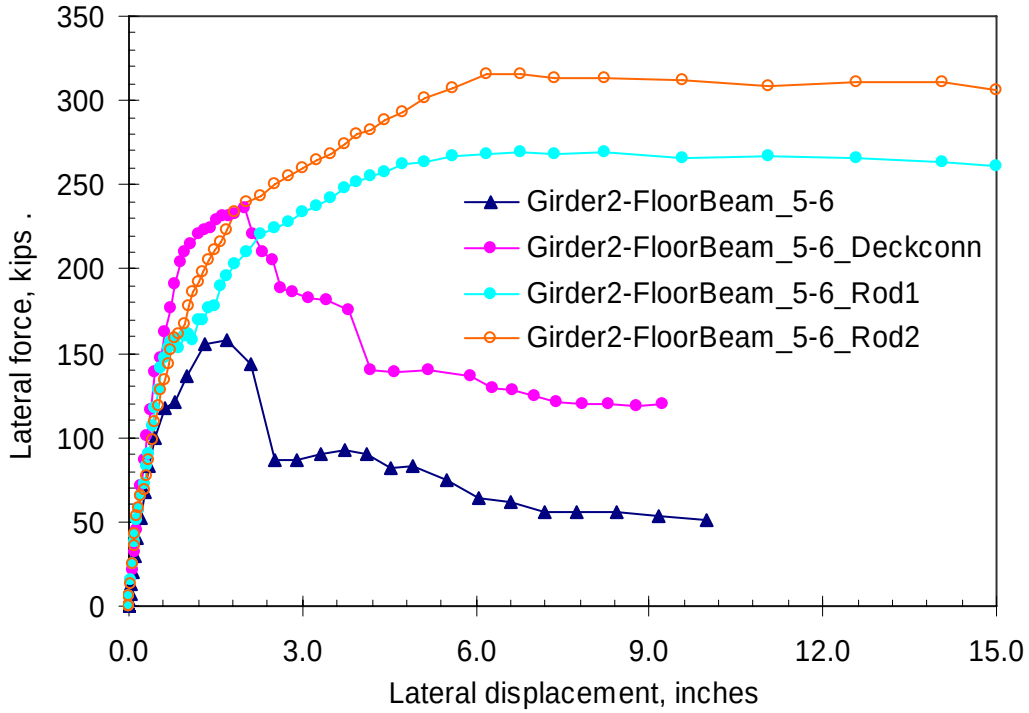

Fig. 6.13. Effect of connection detail (loading at Girder-2 between Floor Beam-5, and -6).

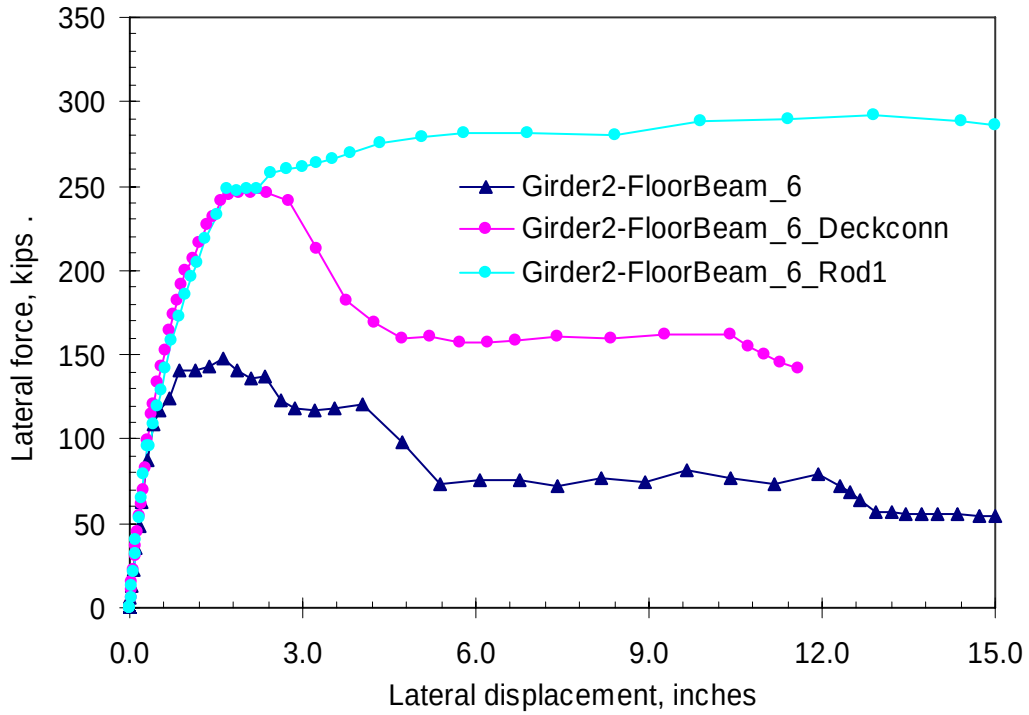

Fig. 6.14. Effect of connection detail (loading at Girder-2 at Floor Beam-6).

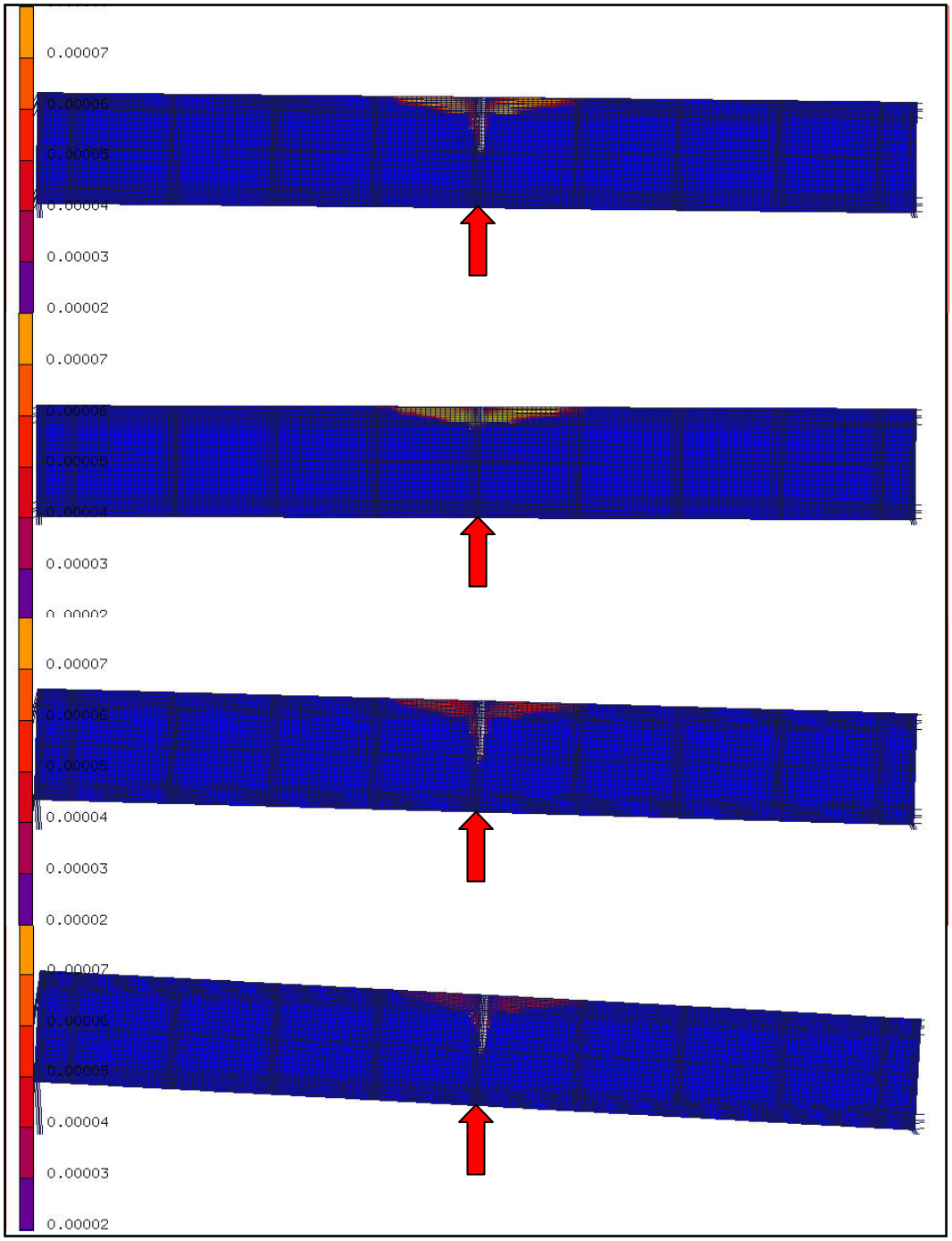

Fig. 6.15. Progression of damage with flexible girder supports (plan view).

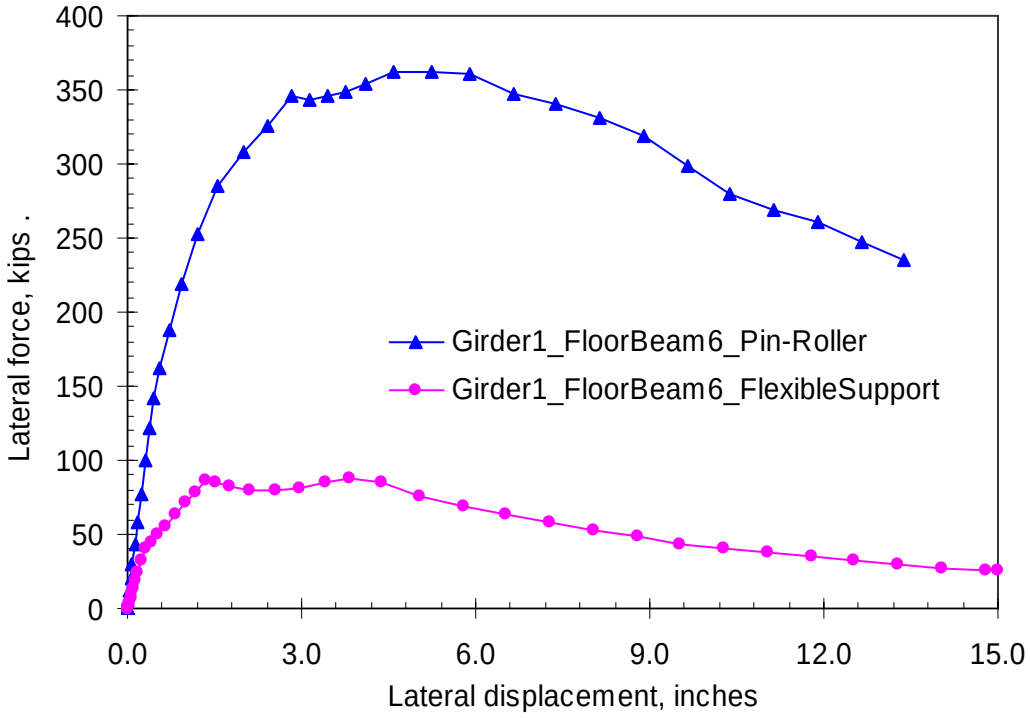

Fig. 6.16. Effect of girder support flexibility (loading at Girder-2 at Floor Beam-6).

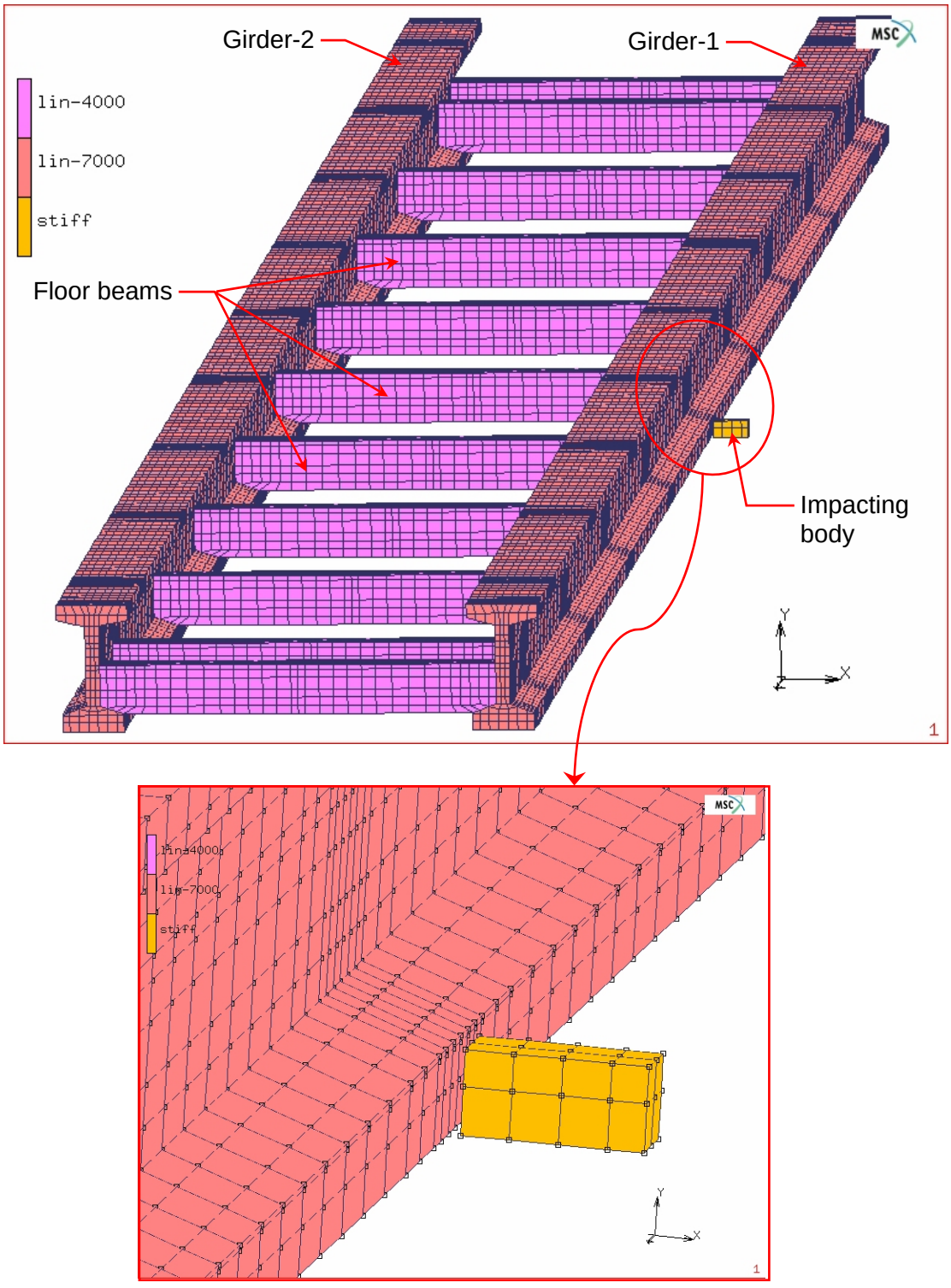

Fig. 6.17. Application of impact loading in finite element models (bridge deck not shown).

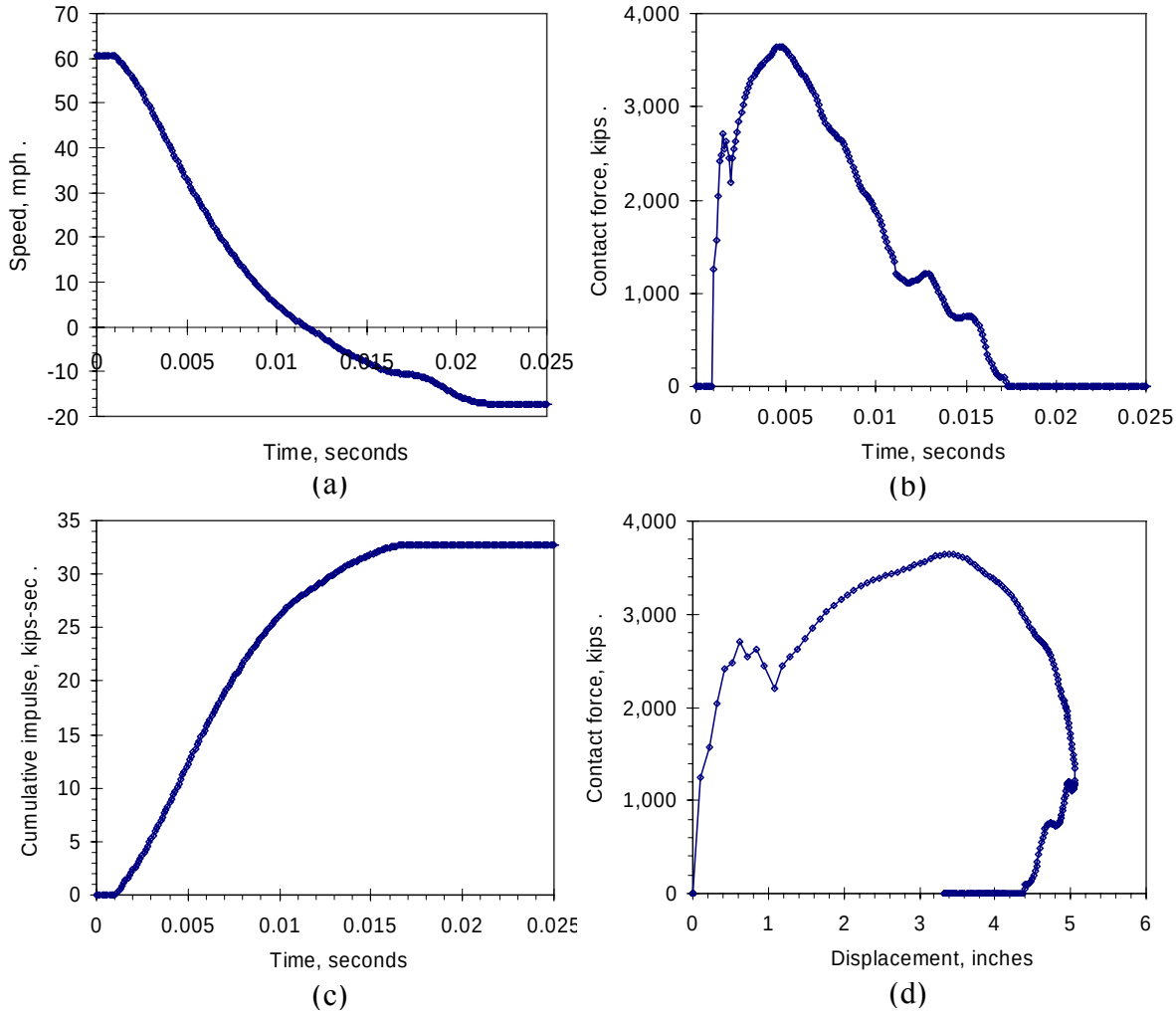

Fig. 6.18. Dynamic analysis results (Model-2)

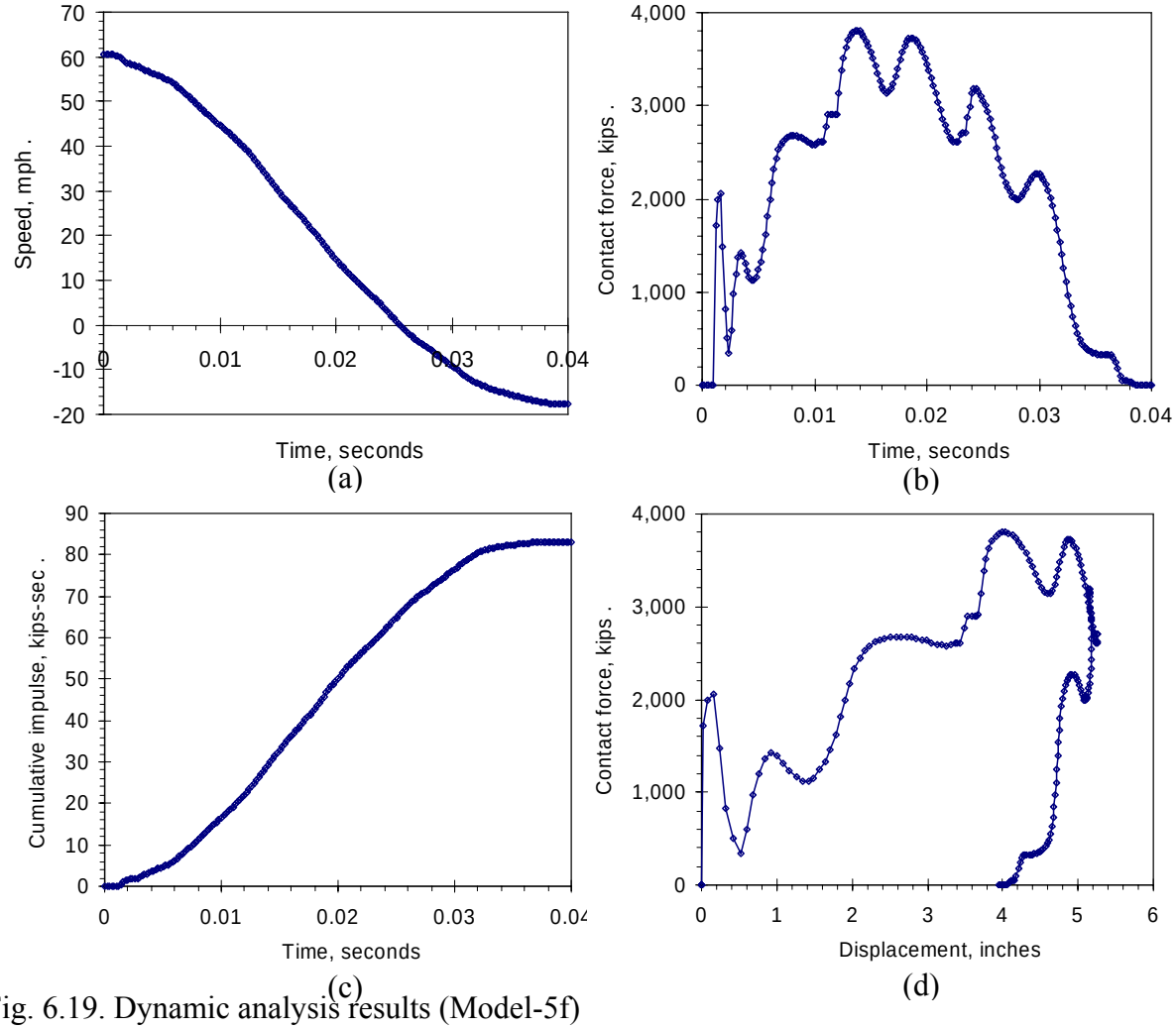

Fig. 6.19. Dynamic analysis results (Model-5f)

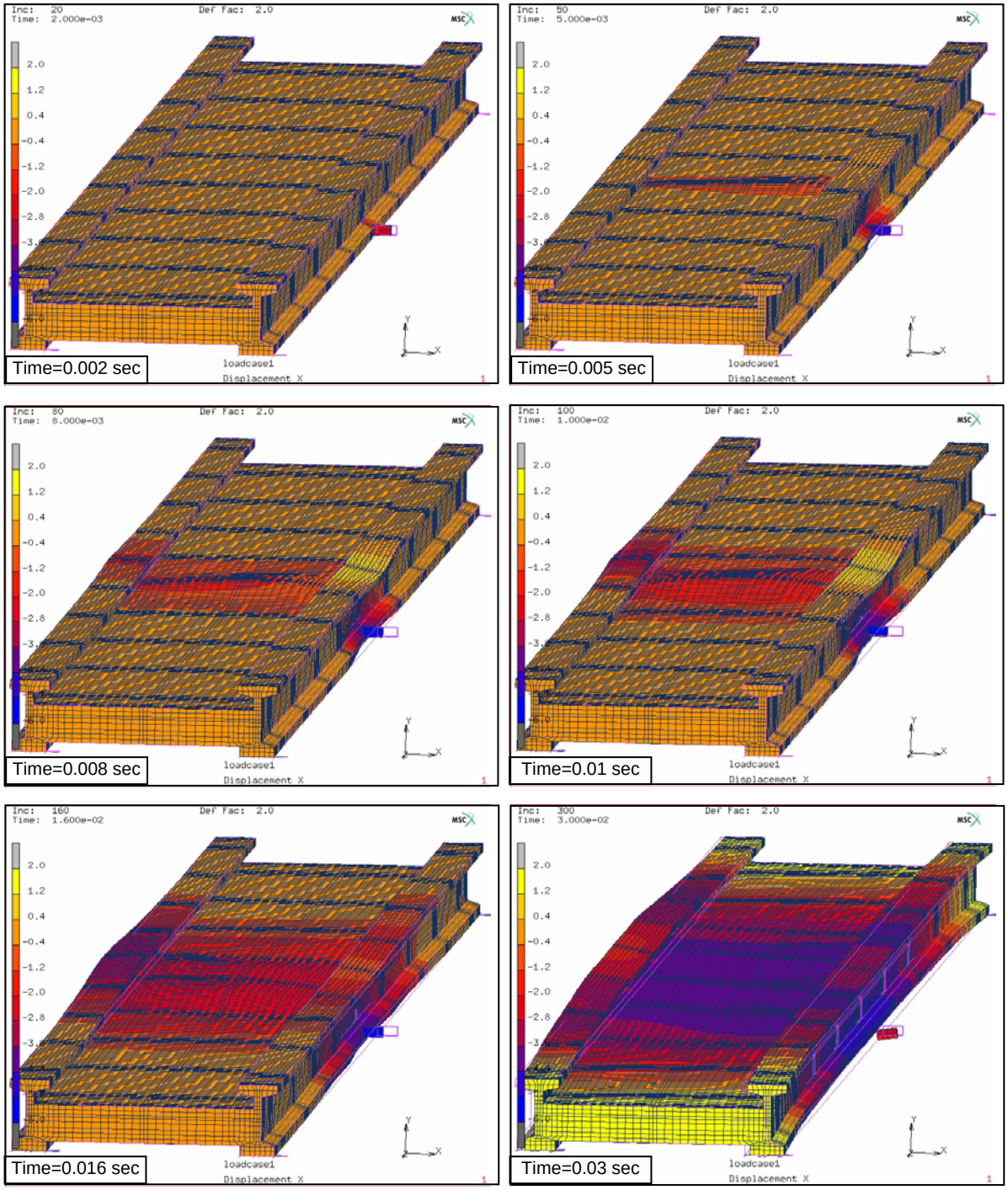

Fig. 6.20. Bridge deformations during dynamic analysis (Model-4f)

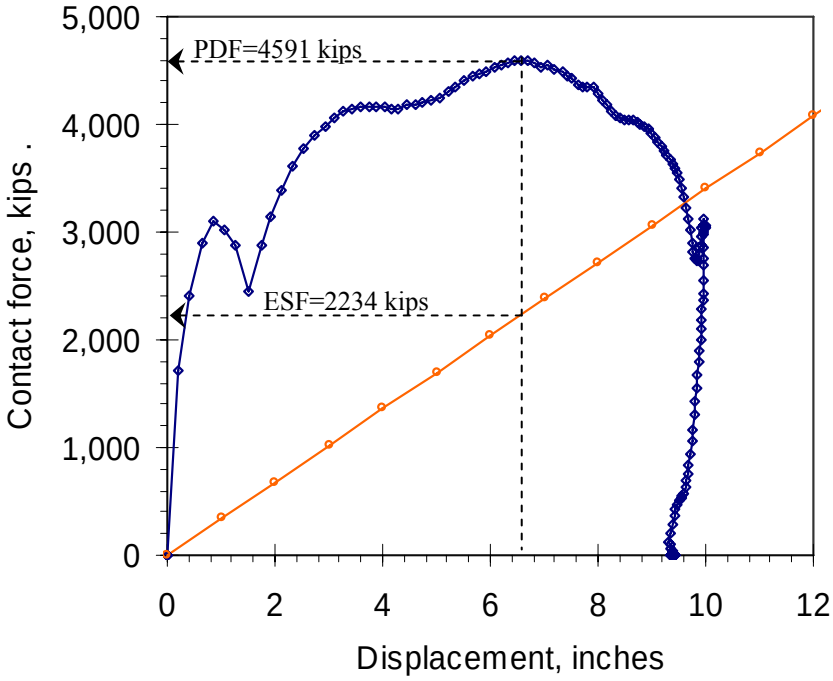

(a) Model-3

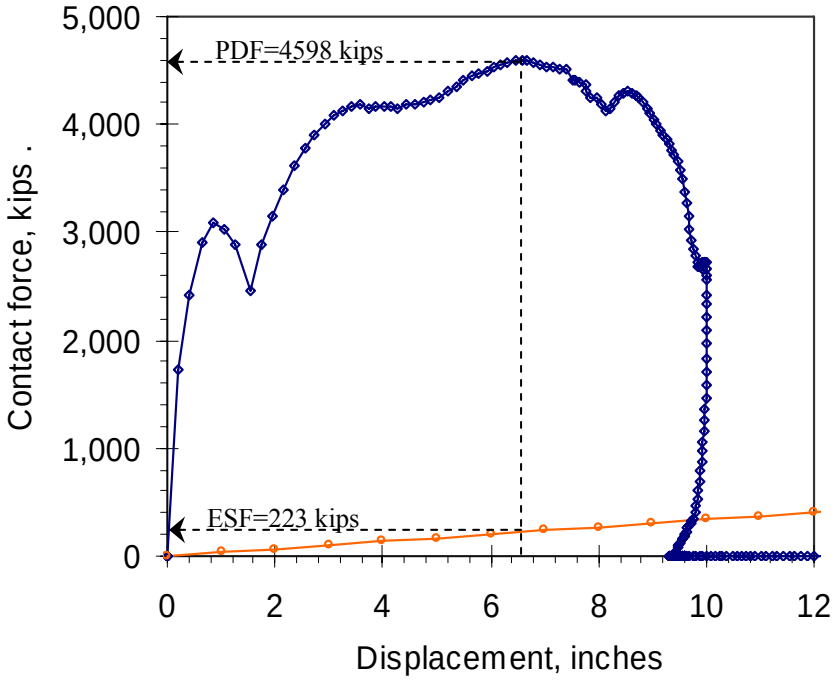

(b) Model-3f

Fig. 6.21. Determination of Equivalent Static Force (ESF).

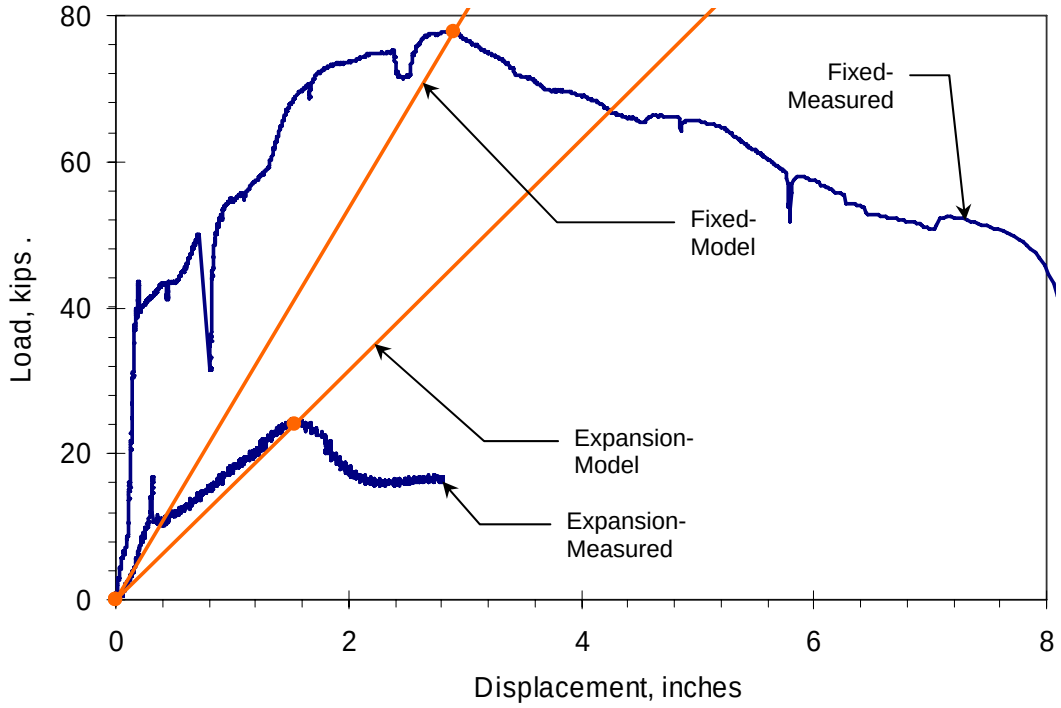

Fig. 6.22. Modeling of girder support flexibility in dynamic (and companion static) models.

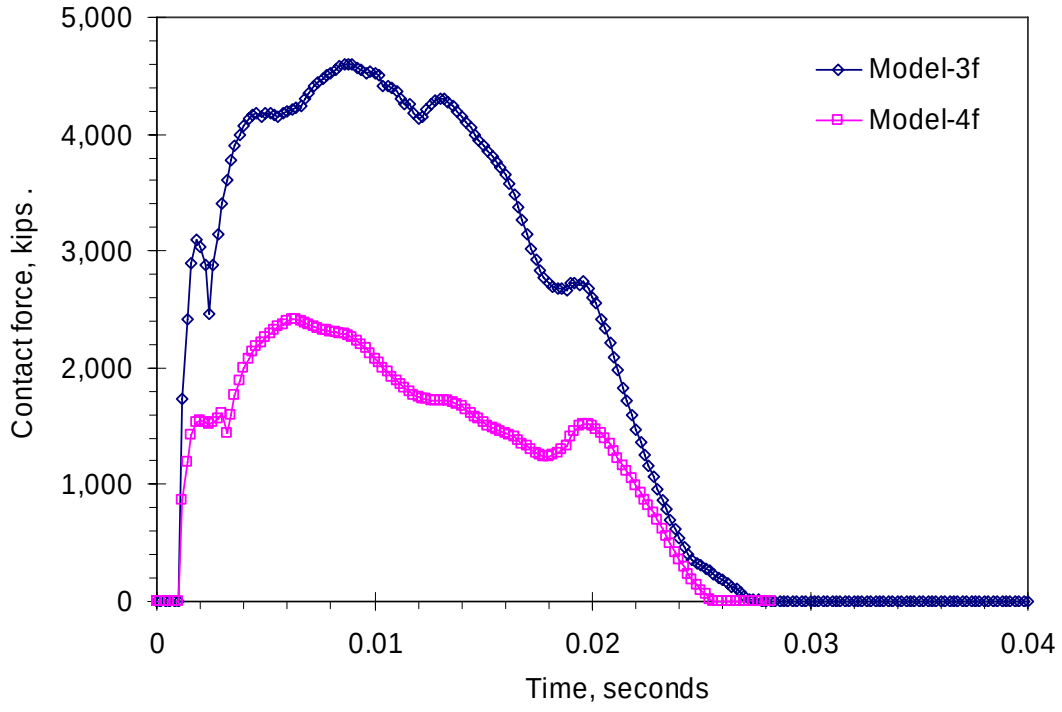

Fig. 6.23. Effect of impact speed.

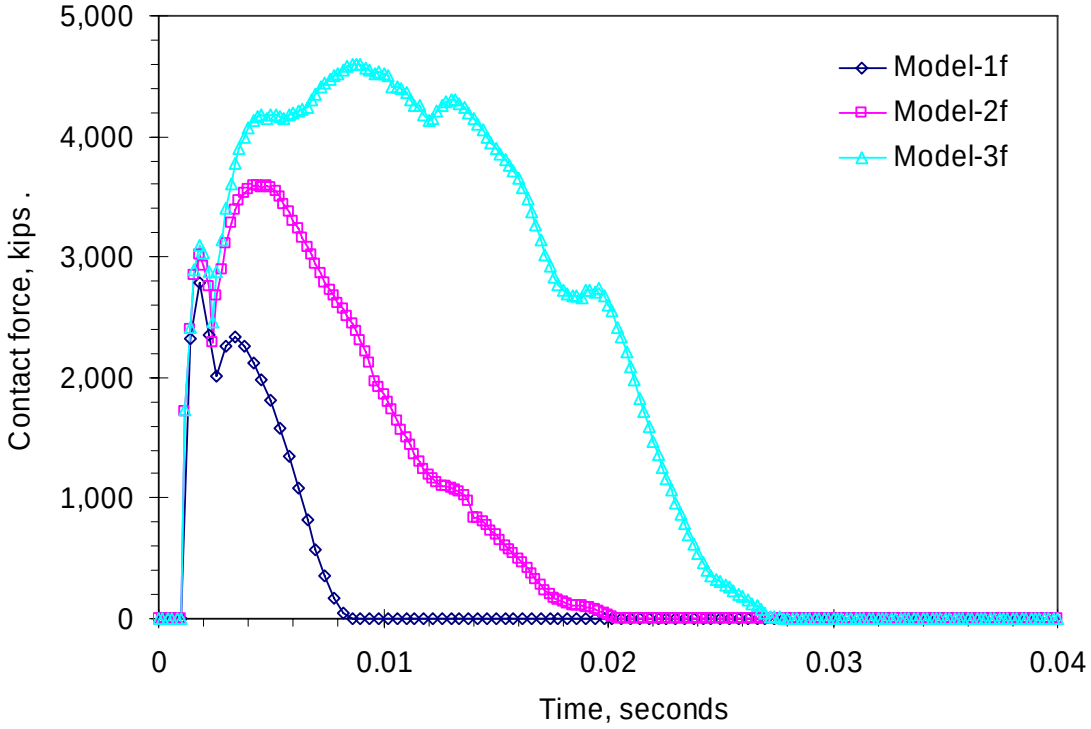

Fig. 6.24. Effect of impacting object weight.

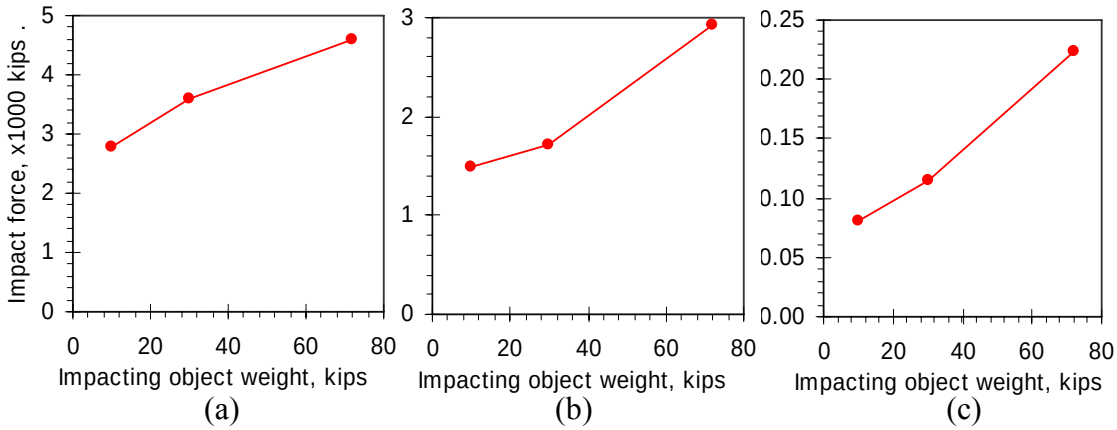

Fig. 6.25. Change of impact force with impacting object weight: (a) PDF; (b) EIF; (c) ESF.

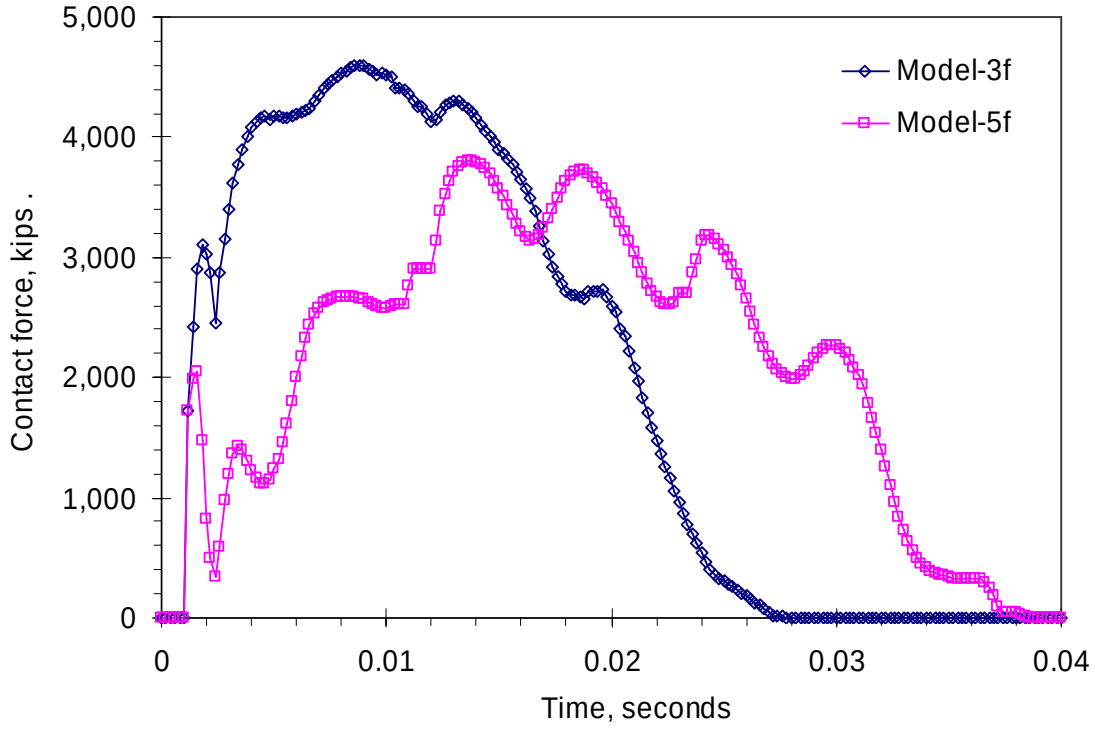

Fig. 6.26. Effect of impact location.

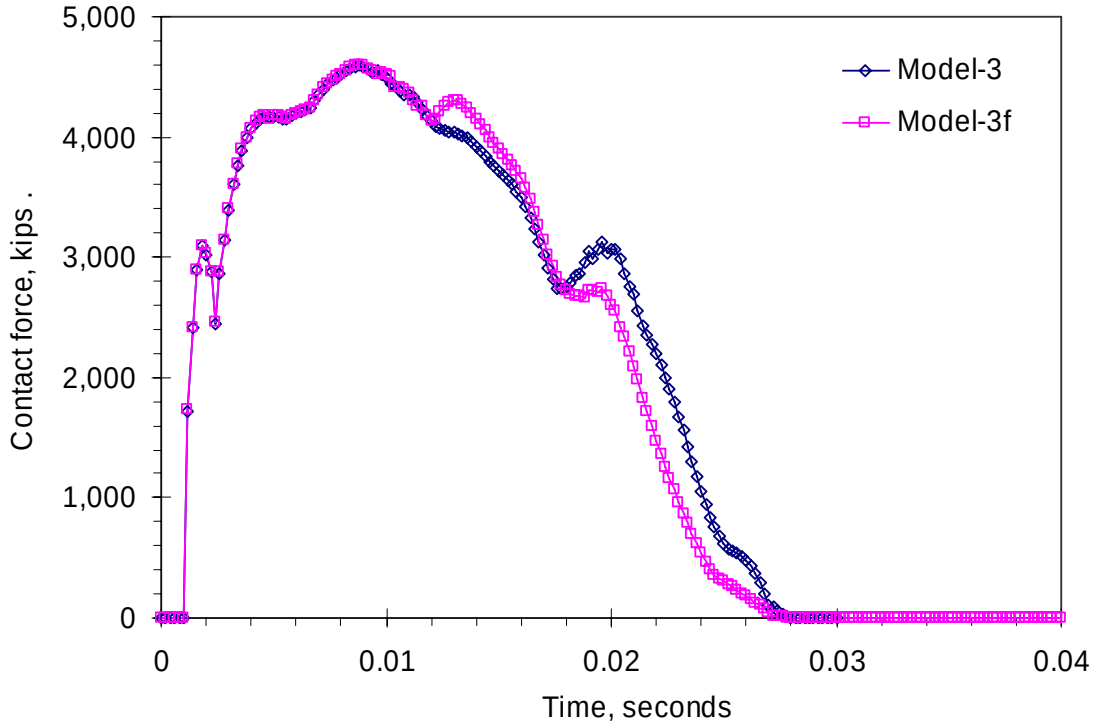

Fig. 6.27. Effect of girder support flexibility.

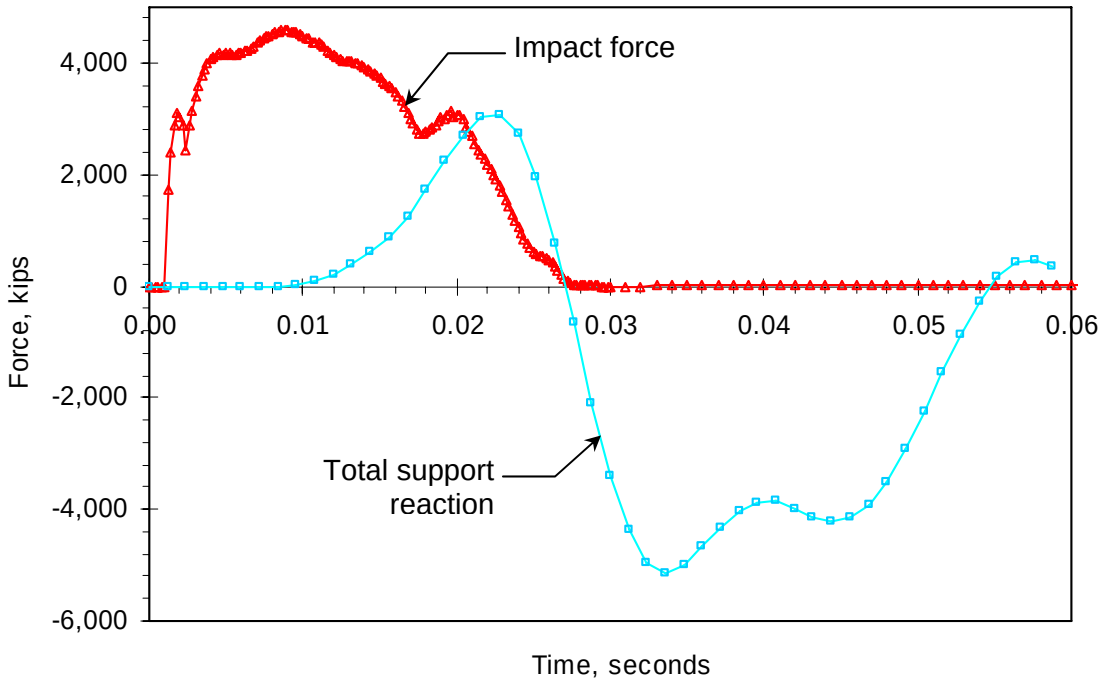

Fig. 6.28. Variation of girder support reaction (Model-3).

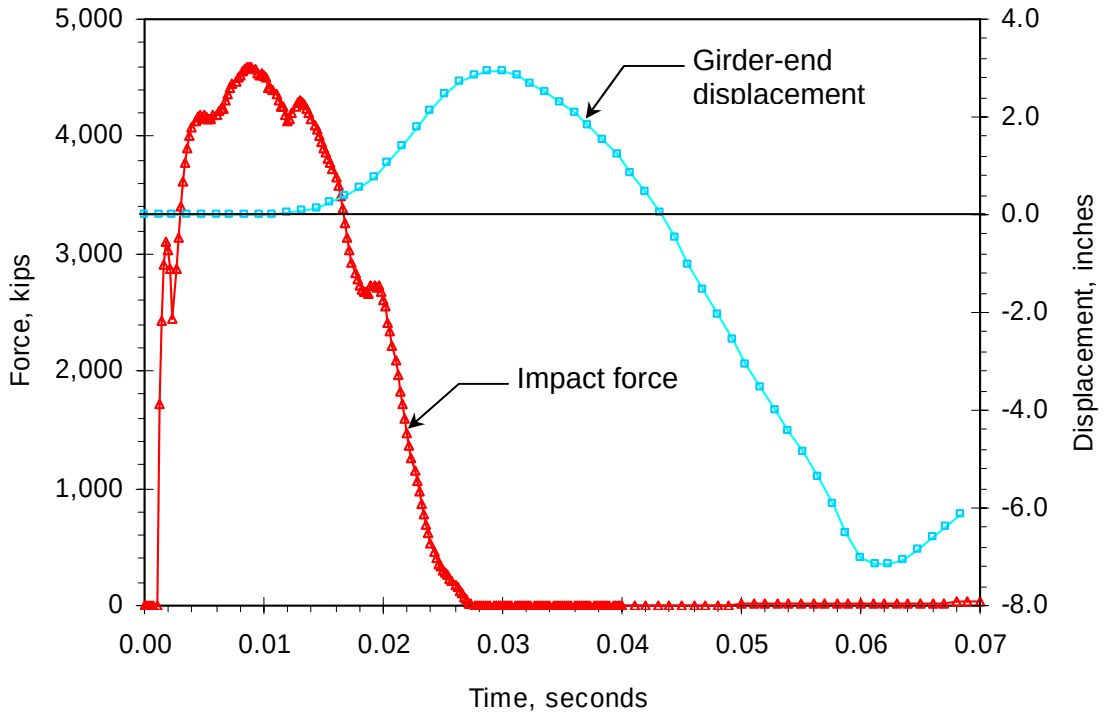

Fig. 6.29. Variation of girder-end displacement (Model-3f).

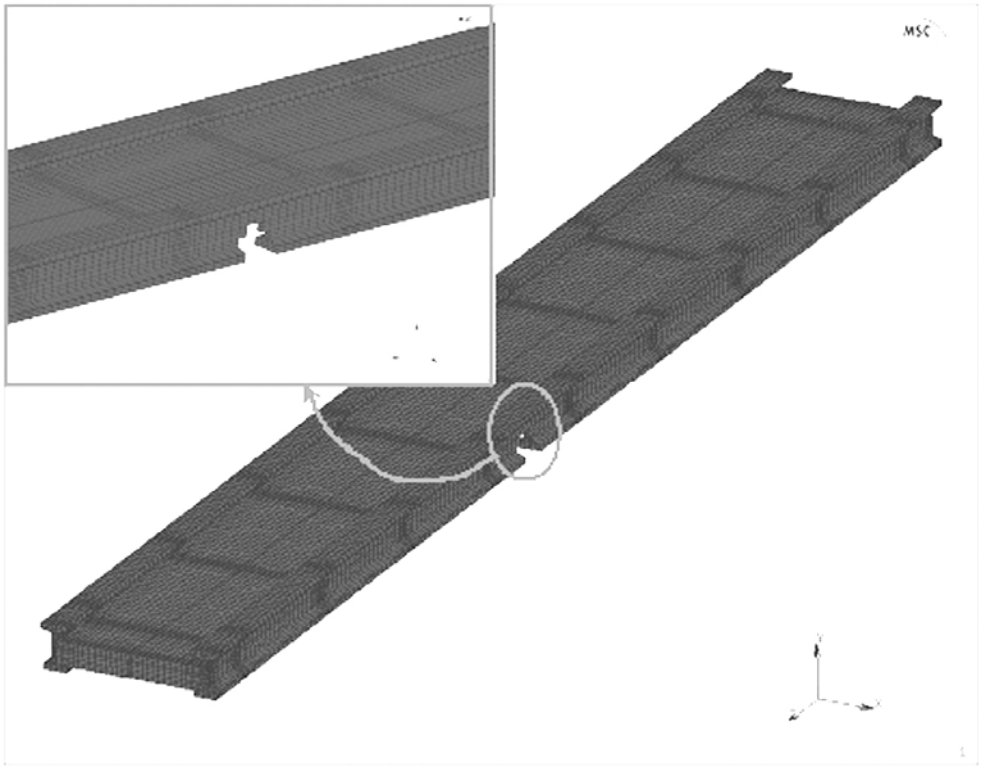

Fig. 6.30. Concrete elements removed from bottom part of a single girder.

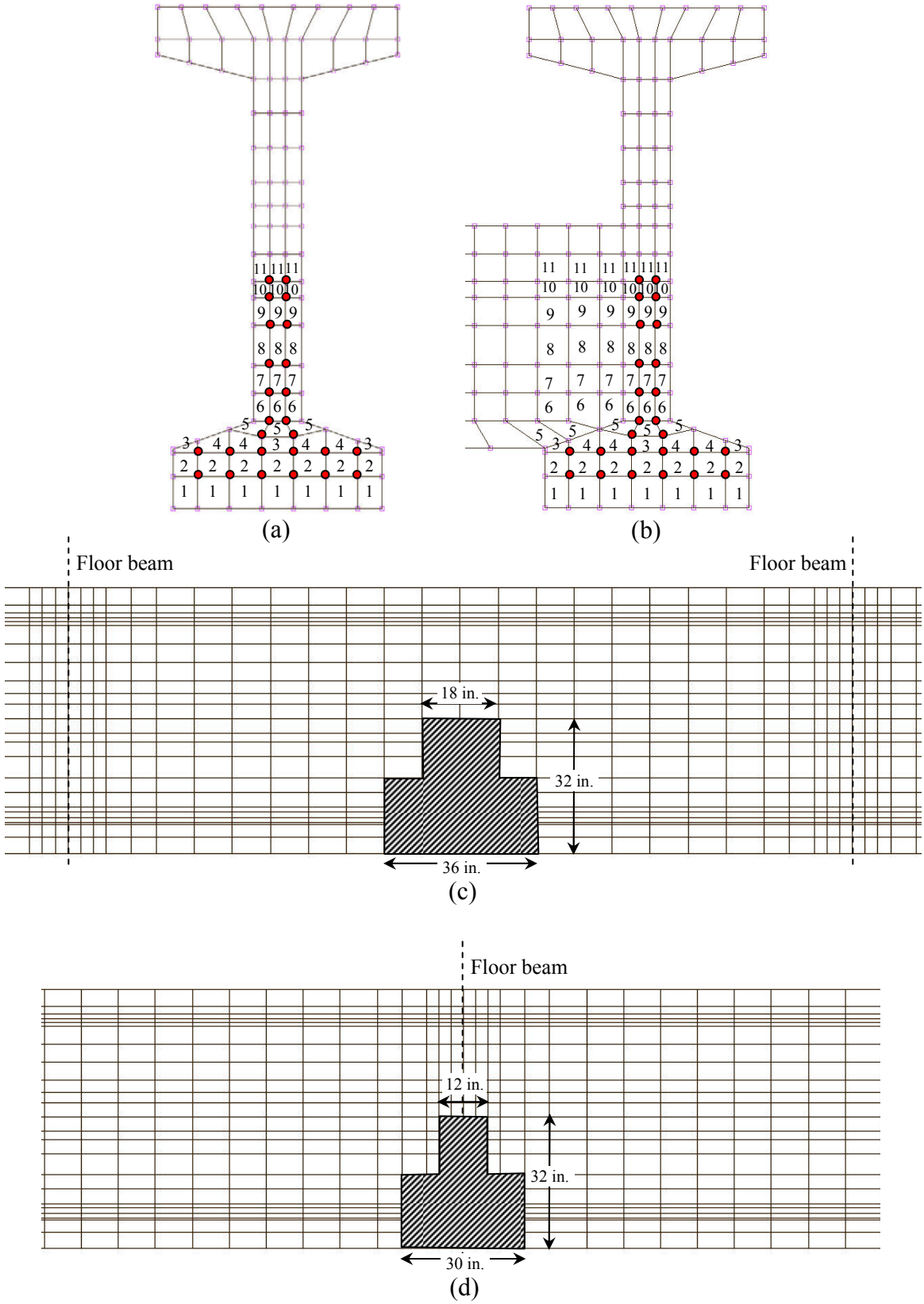

Fig. 6.31. Element removal procedure: (a) between floor beams; (b) at floor beam locations; (c) between floor beams side view, (d) at floor beam locations side view.

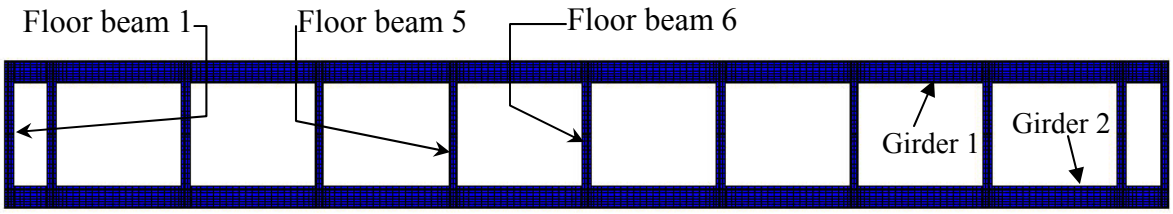

Fig. 6.32. Numbering of floor beams along bridge length (no deck shown).

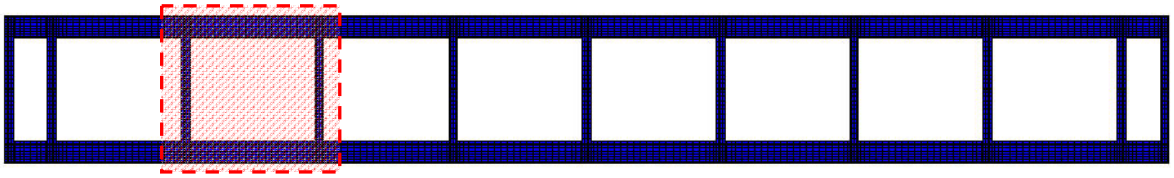

(a) Location of span that the elements were removed

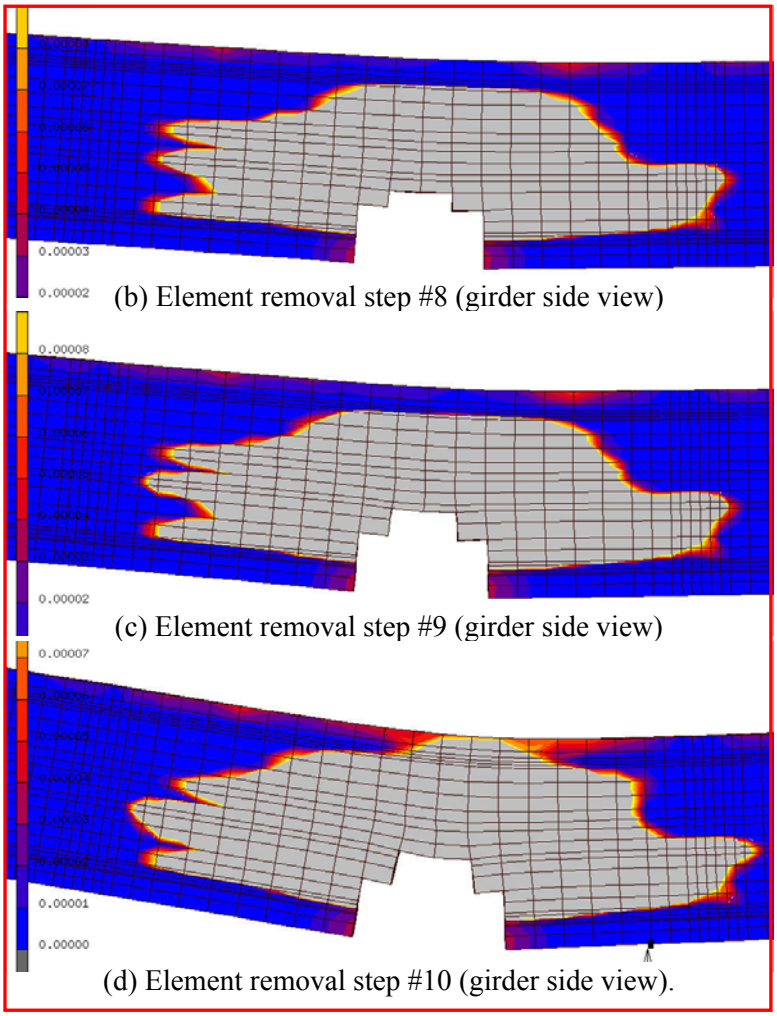

(b) Element removal step #8 (girder side view)

(c) Element removal step #9 (girder side view)

(d) Element removal step #10 (girder side view).

Fig. 6.33. Progression of damage due to element removal (analysis #3).

Chapter 7
Summary and Recommendations

7.1. Summary

Two issues have recently been raised regarding prestressed concrete through-girder pedestrian bridge systems widely used in the State of Minnesota. The first issue was related to the ductility of the prestressed concrete girders used in these types of bridges. The girders are reinforced with large amounts of prestressing strands in order to satisfy the deflection requirements with the relatively large span lengths (125-135 ft.). Moreover, the girders do not have a composite deck on top that would help to resist the relatively large internal tensile force provided by the prestressing strands. As a result, the section used in these bridges (Mn/DOT Type 63 section) is considered as over-reinforced according to the AASHTO LRFD Bridge Specifications and fails to meet the required flexural strength.

The first phase of the project included a nonlinear strain compatibility analysis of the Mn/DOT Type 63 section in order to identify the design procedures that accurately predict the section behavior. Response of the section, including the neutral axis location, strand stress at ultimate capacity, and the moment capacity of the section, predicted by the AASHTO Standard and AASHTO LRFD Specifications was compared with the sectional response determined from the strain compatibility analyses. Based on the analysis results, modifications were proposed to the procedure used by the LRFD Specifications in order to rectify the errors in predicting the sectional response.

The second issue investigated in the study regarded the strength and stability of prestressed concrete through-girder pedestrian bridges when subjected to striking of over-height vehicles. Three-dimensional full-scale finite element models of an entire bridge-system as well as bridge subassemblages were used to evaluate the strength, stiffness, and ductility characteristics of the bridge system and connection details. Accurate representation of the bridge details in the finite element models was assured utilizing experimentally determined load-deformation characteristics of these connections in the finite element models.

Three series of laboratory tests were conducted to investigate the performance of currently used and proposed details to be used in future construction. The laboratory tests included (1) pull-out tests on steel inserts used at the floor beam and girder connections, (2) tests on floor beam and girder connection subassemblages, (3) tests on support details used at the ends of prestressed concrete girders. Results obtained from the first series of tests were incorporated in the connection subassemblage finite element models in modeling of the connectors between the floor beams and the girders. Calibration of the connection subassemblage finite element models was performed using the data obtained from the tests on connection subassemblage specimens. Finite element models of an entire bridge system were produced using the calibrated connection subassemblage finite element models. Results obtained from the girder support detail tests were used in modeling the girder boundary conditions in the entire-bridge finite element models.

The three sets of analyses performed using the entire-bridge finite element models were (1) lateral static analyses, (2) lateral dynamic impact analyses, and (3) vertical stability analyses. In

the static lateral load analyses, lateral displacement loadings were applied at different locations along the lengths of the girders. The aim in doing these analyses was to determine the response of the bridge system, including the strength, stiffness, and ductility characteristics, when it was subjected to lateral loads at different locations. The effects of parameters, such as location of load, behavior of connection between girders and floor beams, and girder support flexibility on the overall response of the bridge were studied in these analyses. Effectiveness of several modified connection details on the performance of the bridge system were also investigated with these analyses.

The demand that would occur on a bridge system when it was subjected to striking of an over-height vehicle was determined through the dynamic lateral impact analyses. These analyses included a rigid object impacting the bridge girders at several locations with changing amounts of initial velocities. The parameters studied with the dynamic lateral impact analyses included impact location, impact speed, and weight of the impacting object.

The last series of finite element analyses were conducted in order to study the stability of a bridge system following the occurrence of damage in the concrete girders as a result of dynamic impact of the striking vehicle. The models were analyzed under the effect of self-weight of the bridge structure only. The effect of damage that would occur in the girders due to the dynamic impact loading was simulated by removing the concrete and prestressing strand elements in the bottom flange and bottom portion of the girder web in these models.

7.2. Results from Strain Compatibility Analyses

The analyses indicated that inconsistencies exist between the AASHTO LRFD and AASHTO Standard Specifications in predicting the response of prestressed concrete T-sections because of two reasons: (a) selection of the neutral axis depth at which transition from rectangular section behavior to T-section behavior occurs, and (b) selection of the amount of the top flange overhang contribution to the internal compressive force. Because of the underestimation of the contribution of top flange overhangs, the AASHTO LRFD Specifications overestimate the neutral axis depth of T-sections compared to the AASHTO Standard Specifications and nonlinear strain compatibility analyses. Overestimation of the neutral axis depth according to the AASHTO LRFD Specifications leads to the section being considered as over-reinforced at reinforcement ratios for which the AASHTO Standard Specifications and the strain compatibility analyses indicate otherwise. The tendency to prematurely classify some sections as over-reinforced results in large differences between the moment capacities predicted by the AASHTO LRFD Specifications and the other methods.

It was determined that limiting the maximum amount of tensile reinforcement to be used in determination of the moment capacity, as used in the AASHTO LRFD and Standard Specifications, is a means of providing an additional safety margin to account for the poor flexural ductility of sections with large amounts of tensile reinforcement. The provision in the AASHTO Standard Specifications yields similar maximum reinforcement limits as the strain compatibility analyses considering a limiting total prestressing steel strain of 0.01 at nominal capacity. Results of the AASHTO LRFD Specifications for maximum reinforcement limits are grossly conservative compared to those of the Standard Specifications and the strain compatibility analyses.

The inconsistencies between the sectional response and the maximum reinforcement limits predicted by the AASHTO LRFD Specifications and the other methods (AASHTO Standard Specifications and the strain compatibility analyses) is reduced by modifying the procedure of the AASHTO LRFD Specifications by changing the T-section limit from $c = h_f$ to $a = h_f$. With this modification, the $\beta_1 h_f$ maximum limit for the depth of the top flange overhang contribution to the internal compressive force in the LRFD Specifications is automatically removed.

The procedure outlined in the AASHTO Standard Specifications to determine the stress in prestressing steel at ultimate moment does not take into account the effect of changes in the neutral axis location caused by changes in top flange depth. In this respect, the LRFD procedure for strand stress provides more realistic sectional response. Thus, it is proposed that the LRFD strand stress relation be used with the modified procedure.

7.3. Results from Strength Evaluation of Through-Girder Pedestrian Bridge System

7.3.1. Experimental Results

The tensile pull-out tests performed on both the currently used and the alternative steel inserts indicated that the type of insert that has been used in prestressed concrete bridges in the State of Minnesota (i.e., loop-type insert) has the ability to undergo large amounts of plastic deformations without significant decrease in the load capacity. Even though, some of the other types of inserts included in the testing study exhibited larger load capacities than the loop-type inserts, the stable load-deflection behavior of the loop-type inserts makes it the most suitable type of insert when the bridge is subjected to impact loading. Failure of the steel parts of the loop inserts resulted in superior plastic deformation and energy dissipation capabilities. For the cases that the failure was controlled by concrete breakout, providing reinforcement near the insert locations and the failure planes improves the plastic deformation and energy absorption capacities of the inserts.

Connection Subassemblage Tests

Additional tests were performed on subassemblages of girder-floor beam connection region. Three types of inserts, two of which are the loop-type inserts used in prestressed concrete girders, were included in the test specimens. The girder-floor beam subassemblage tests indicated the ability of these specimens to attain large values of floor beam end displacements with some level of reduction in the peak load capacity. Deterioration of the capacity of the connection region following the peak load was associated with the deformation patterns of: (a) concrete cracking, (b) formation of concrete breakout surface, (c) yielding of the threads on the connector rods and inserts, (d) yielding of the girder stirrups, and (e) fracture of the inserts. No clear trend could be observed regarding which type of insert possessed the largest load and deformation capacities. The bolt insert specimen exhibited the largest load capacity for the case of combined vertical and horizontal load, while the coil loop insert specimen offered greater peak load for the vertical load specimen.

The connection subassemblage tests also revealed that the construction method followed during the fabrication of prestressed concrete girders significantly affected the behavior of the inserts. The welding of rebar pieces on the loop and bolt inserts changed the load-carrying mechanism of the inserts compared to the behavior obtained from the tension pull-out tests of these inserts. The

effect was beneficial in the case of bolt inserts, while the deformation capacity of the loop inserts was reduced (due to various effects from welding process including stress concentration, residual stresses, and steel embrittlement). The welding of rebar pieces resulted in premature steel fracture at the weld locations in the loop inserts, while it provided improved anchorage to concrete and improved deformation capacity for the bolt inserts.

Girder Support Detail Tests

Results obtained from the girder end detail specimens indicated two types of horizontal load resisting mechanisms depending on the type of detail. During testing of the specimens, large values of lateral displacements following the peak load capacities were measured with some level of residual load capacity. The expansion-end detail resisted the horizontal load through the friction between the bearing pad and the steel and concrete surfaces. The load transferred to the bearing pad through this mechanism caused the bearing pad to undergo large amount of shear deformation during testing. In the case of the fixed-end detail, the anchor rods that were used to prevent the transverse movement of the girder ends provided the main resistance against horizontal loading. Concrete breakout and bending of the anchor rods resulted in the failure of the specimen with the fixed-end detail. The static load capacities of the expansion-end and fixed-end details were approximately 25 kips and 78 kips, respectively, making the total horizontal static load capacity of the entire bridge approximately 210 kips. This indicates that, irrespective of the strength and ductility of other parts of the bridge system, the lateral static load capacity of a prestressed concrete through-girder pedestrian bridge is limited to 210 kips. In reality, however, the resistance of a bridge system subjected to vehicular impact would consist of inertial and damping forces in addition to the strength of the bridge components. The magnitude of the additional strength due to the inertial and damping forces would depend on the dynamic characteristics of the bridge system (i.e., mass and damping) as well as the intensity of the impact loading (i.e., velocity and acceleration).

7.3.2. Finite Element Study Results

Performance of a typical prestressed concrete through-girder pedestrian bridge system was analyzed through three sets of finite element analyses using the models of an entire bridge system. Each of these three sets of analyses was aimed at studying a different aspect of the bridge system behavior. The response of the bridge system, including the strength, stiffness, and ductility characteristics, when it was subjected to lateral loads at different locations was determined through the first series of analyses, which were static lateral load analyses. The second series of analyses, the dynamic lateral impact analyses, were conducted in an attempt to determine the demand that would occur on a bridge system when it was subjected to striking of an over-height vehicle. The third series of finite element analyses, which were the stability analyses under gravity loading, were conducted in order to study the stability of the bridge system following the occurrence of damage in the concrete girders as a result of dynamic impact of the striking vehicle.

The finite element model used for the static lateral load analyses included material and geometric nonlinearities. Moreover, the measured load-deformation characteristics of the connectors and the connection regions were also incorporated in these models. As a result, these models were able to predict the response of the bridge system to statically applied lateral loads with a high level of accuracy. However, several idealizations had to be made regarding the concrete material

models and the connection behaviors in the finite element model used for the dynamic lateral load analyses. Consequently, the accuracy of results obtained from these dynamic analyses including the magnitude of demand on the bridge system under lateral impact loads was not as high as those from the static lateral load analyses.

Static Analyses

Two cases of loading, representing the two possible scenarios that can happen when an over-height vehicle strikes the bridge, were used in the static lateral load analyses. The first case (loading applied at the exterior face of a girder) simulates the over-height vehicle striking the exterior face of the first girder in the direction of the traffic, while the second case (loading applied at the interior face of a girder) simulates the case that the over-height vehicle misses the first girder and strikes the second girder at the interior face. For both of these scenarios, the overall deformation behavior of the bridge was controlled by sliding of the girders at the supports when the flexibility of the girder supports was included in the models. In addition to translation and rotation of the bridge, a very limited amount of deformation was observed to occur in the loaded girder. In this case, the lateral load capacity of the bridge system is limited by the lateral load capacity of the girder support details in addition to the load capacity due to the dynamic effects (i.e., inertia and damping forces).

In order to investigate the bridge system response with the lateral sliding of the girder end supports prevented, the static lateral load analyses were repeated with idealized pin and roller girder boundary conditions. These analyses indicated that the behavior of the bridge system changes significantly depending on whether the loading was applied at the exterior face of one girder or the interior face of the other girder. This result was significantly different than what was observed with the flexible girder supports.

In the cases that loading was applied at exterior face of one of the girders, load transfer between different components of the bridge was through bearing of contact surfaces between these components. In this type of load transfer mechanism, the steel connector elements joining the girders and floor beams did not have an effect on the behavior of the bridge system. Consequently, the entire bridge acted similar to a deep beam under three-point bending, and the behavior of the bridge system was controlled by the concrete cracking in the girders, floor beams, and the deck. Because of nonlinear material response and gap opening at the girder and floor beam interface, a nonlinear lateral load versus lateral deflection behavior was observed. Extensive cracking in the deck and floor beams, as well as progression of cracking into both girders resulted in a gradual decrease in the load carrying capacity of the bridge system. Analyses also indicated that there was no significant difference in the response of the bridge when the loading was applied at different locations along the bridge length.

Different from the first loading case, when the loading was applied at the interior face of one of the girders, the overall behavior of the bridge system was dictated by the behavior of the steel connectors between the girders and floor beams. For this configuration of loading, the lateral load capacity of the bridge system was significantly reduced compared to the case of the loading applied at the exterior side of a girder. When the loading was at the interior side of a girder, load transfer among the bridge components was through tensile forces in the steel connectors, and fracture of these connectors resulted in reduction of the lateral load capacity of the bridge

system. Gap opening between the loaded girder and the floor beams was observed as a result of the axial elongation of the steel connectors. Extensive concrete cracking in the loaded girder, as well as localized concrete cracking in the deck at floor beam locations were also observed at later stages of loading. Varying the location of load along the bridge length did not cause a major change in the response of the bridge system.

For the cases of loading at the interior side of a girder, when the load-deformation characteristics of the connector elements between the girders and the floor beams were changed, the overall lateral load versus lateral deformation response of the bridge system also changed accordingly. For example, when the currently used connector was replaced by a connector with a larger load capacity, the lateral load capacity of the bridge was also observed to improve. This was an expected result, as for this configuration of loading, the overall bridge behavior was dictated by behavior of the steel connector elements.

The static lateral load analyses were also used to study the effect of different connection details than the one currently being used. The new connection details were investigated in an attempt to improve the bridge performance under lateral loading. The new connection details were studied with only the case of loading applied at the interior side of a girder, because the effect of connection detail had minimal effect on the overall bridge response in the case of loading applied at the exterior side of a girder.

Providing steel connectors between the girders and the deck in addition to those already present between the girders and floor beams improved the lateral load-deflection behavior of the bridge by increasing the load capacity and post-peak load capacity without changing the overall shape of the load-deflection curve. The level of improvement in the bridge behavior depends on how closely the new connectors would be spaced between the girders and the deck. With 18 in. connector spacing, the increase in lateral load capacity of the bridge was approximately 50 percent.

As a second alternative detail, steel tie-rods spanning between the exterior faces of the two girders were used to tie the girders and the floor beams. A single tie-rod was placed inside each floor beam. Using tie-rods resulted in significant improvement in the lateral load versus lateral deflection behavior of the bridge system as compared to the original connection detail and the first alternative detail. The amount of improvement in bridge response was dependent on the size of tie-rods used. With 1-1/2 in. diameter tie-rods, the increase in load capacity was approximately 100 percent over the case of original detail and was approximately 20-30 percent over the first alternative detail. As opposed to the case with the original detail and first alternative detail, the bridge was also able to maintain the maximum lateral load capacity over large levels of lateral deflections with the second alternative detail.

Dynamic Analyses

The dynamic lateral impact analyses that were performed in an attempt to determine the demand that would occur on the bridge system indicated considerably small impact durations (between 0.008 and 0.038 sec). These analyses were performed for various levels of impacting body weights (10, 30, and 72 kips) and initial impact speeds (30 and 60 mph). The possible reason for the “fast” impact observed in the dynamic analyses is the relatively high stiffness of the bridge

model, as well as the high stiffness of the impacting body. As explained earlier, the damage that would occur in the bridge structure and also in the impacting body during the event of a vehicular impact could not be modeled accurately because of limitations such as the excessive computation time required for the analyses and the ability of the computer program used for the analyses. The artificial stiffness of the models in these analyses would tend to result in smaller impact duration and larger impact force values than those that would occur in the event of an over-height vehicle striking a bridge.

The dynamic analyses revealed a different deformation pattern of the bridge system than the deformation patterns observed in the static analyses. The damage in the bridge caused by the impacting body was observed to remain very localized near the impact location until approximately half of the impact duration. After that time, the effect of impact progressed rapidly towards the ends of the bridge in the forms of "damage waves." Progression of these waves into the ends of the girders caused the girder ends to move in the opposite direction of the impact force, as opposed to what would be expected in the case of a statically applied lateral load.

Three types of force quantities, namely the peak dynamic force (PDF), equivalent impact force (EIF), and equivalent static force (ESF) were used to quantify the magnitude of impact in dynamic analyses. The PDF represents the maximum value of contact force between the impacting body and the bridge during the impact duration. Considering the very short impact duration values observed in this study, it is clear that the structure would be subjected to the PDF over a very short period of time. During such a short period of time, the structure would not have time to respond to the applied dynamic forces. In addition, the damage that would occur in the structure due to the impact force would remain very local during a significant portion of the impact duration. Because of these reasons, the PDF is not the most suitable load quantity to be used in the assessment of the overall bridge system performance under impact loads.

The EIF represents a constant value of impact loading that would produce the same amount of total impulse within the impact duration as exerted by the impacting body on the structure. Even though the EIF values are always smaller than the PDF values, the EIF still acts over a short period of time such that the bridge system would not be able to respond to this force. From this respect, EIF can still be considered as a "dynamic" loading.

The ESF is a more appropriate method of representing the intensity of the dynamic loading. It is more appropriate to use ESF values than to use the PDF or EIF values for design and assessment of structures under impact loading. The ESF represents force values to which the structure would be subjected over a sufficiently long period of time to respond, but at the same time it is equivalent to the dynamic impact forces. The ESF values were related to the measured dynamic forces through the load-versus displacement plots of the bridge obtained from the dynamic and static analyses.

The PDF and EIF values determined from the dynamic lateral load analyses were significantly higher than the lateral load capacity of the bridge system determined from the static lateral load analyses, for both the flexible and rigid girder support cases. The ESF values, on the other hand, were smaller than the static lateral load capacity of the bridge for the cases with flexible girder

supports, while for the rigid supports the ESF values were still larger than the static lateral load capacities. Support flexibility of the girders did not have much effect on the dynamic behavior of the bridge, as opposed to the behavior observed in the static lateral load analyses. This was mainly because of the fact that the effect caused by the impacting body on the bridge system remained very localized in the dynamic analyses. The reason that the ESF values for the flexible and rigid girder support cases were different was because of the difference in the static load-deflection behavior of the bridge system for these two cases.

Analysis of girder support reactions and girder end displacements determined, respectively, from the dynamic analyses with rigid and flexible girder supports indicate that in the case of lateral vehicular impact (1) force capacity of the girder support details are expected to be exceeded, and (2) large amounts of displacements are expected to occur at the girder ends. Providing concrete side-walls on both sides of prestressed concrete girders at the girder ends would prevent excessive lateral deformation of the girder ends and would eliminate a possible failure mode of falling of girders off the bridge supports. It is important, however, to note that increasing the rigidity of the girder end supports would make the bridge stiffer, which results in larger impact forces in the girders. Therefore, the side-walls should not be placed directly against the girder ends and some gap (e.g., 8 in.) should be provided. This would also allow the girder ends to slide on the bridge seating during the vibrating of girders and dissipate the energy generated by the vehicular impact.

Even though the levels of force demand indicated by the dynamic analyses were higher than the lateral load capacity of the bridge system determined from static analyses, this does not necessarily imply collapse of the bridge structure. The analyses and experiments suggest a complex and highly nonlinear behavior for the bridge system. The post-peak deformation capacity of the girder-floor beam connections allow for redistribution of loads between the connected members. Therefore, failure of some inserts, or even some girder-floor beam connections do not necessarily imply collapse. Moreover, because of the increase in material strengths associated with the high loading rates, the load capacity of the bridge system in the event of vehicular impact is expected to be higher than the load capacity determined from the static analyses.

Stability Analyses of Bridge

As explained earlier, the damage that would occur in the bridge components under the effect of impact loading could not be modeled in the dynamic analyses, because of various limitations. In the event of a vehicle striking a bridge, the impact loading would cause damage in the girders, floor beams, and deck in the form of concrete cracking and crushing. The extent of damage would be the highest near the location of the impact. It is highly possible that when an over-height vehicle impacts a bridge, a portion of the impacted girder will be broken out near the impact location. In this case, the amount of force delivered to the girder would depend on the resistance of the girder to the breakout force. Possible effects of losing portions of prestressed concrete girders on the overall stability of the bridge system were investigated with additional finite elements analyses.

Results of the stability analyses indicated that the local girder damage that would occur in prestressed concrete through-girder pedestrian bridges due to striking of over-height objects may

cause the failure of the bridge depending on the damage that the girders would sustain. In the finite element models, the damage in the prestressed girders was simulated by removing selected girder elements, which means that complete concrete crushing and fracture of prestressing strands at the damage location was assumed. Analysis results showed that in the case of both girders being impacted, failure of the bridge would occur when approximately 15 percent to 40 percent of the web, depending on the location of impact, was damaged in addition to the entire bottom flange. The bridge is more susceptible to failure when the impact damage occurs near the girder midspan than the girder ends.

When only one of the girders was impacted, failure of the bridge required slightly larger amount of damage in the girder section for failure than the damage level required for failure when both girders were damaged. The amount of "additional capacity" between the cases of single girder versus both girders being damaged was due to load redistribution from the impacted girder to the other girder. The amount of load redistribution between the girders depends on the strength of the connectors between the girders and the floor beams. The alternative connection detail with tie-rods between the exterior faces of the two girders resulted in an improvement in the amount of load redistribution between the girders. Behavior of the bridge system with the other alternative connection detail (additional connectors between girders and deck) was not significantly different than the behavior with the original detail.

It should be noted that the stability analyses were performed under statically applied gravity loading. Therefore, all the damage caused in different portions of the bridge in the models was due to the gravity loads. In the case of an actual impact, the bridge components would be subjected to small-duration dynamic loads acting in the lateral direction. In this case, different portions of the bridge would undergo damage under the effect of these dynamic impact loads. In addition, the amount of redistribution between the bridge components would be affected by the ductility of the connectors as well as their strength.

7.4. Recommendations

The following recommendations were drawn from this study:

- Based on the findings of strain compatibility analyses of prestressed concrete sections, it is recommended that the following modifications be applied to the procedure outlined in the AASHTO LRFD Specifications in order to accurately predict the sectional response: (1) initiation of T-section limit should be changed from $c = h_f$ to $a = h_f$,and (2) the $\beta_1 h_f$ limit on the depth of top flange overhang contribution should be removed.

- Loop-type inserts were determined to have a stable behavior with significant amount of deformation capacity. These characteristics make the loop-type inserts the most suitable insert type for applications that would involve impact loading, which requires superior energy dissipation ability. Based on this discussion it is recommended that the loop-type inserts be used in prestressed concrete bridge girders for connecting the bridge components.

- The connection subassemblage tests revealed that the construction method followed during the fabrication of prestressed concrete girders significantly affected the behavior of the inserts. The welding of rebar pieces on the loop-type inserts reduced the deformation capacity of the

inserts and resulted in premature steel fracture at the weld locations. Therefore it is recommended that no welding be used on steel inserts during production of prestressed concrete girders.

- The static finite element analyses indicated that the behavior of the bridge system could be improved by using new connection schemes together with the connection detail that is currently being used between girders and floor beams. The lateral load capacity of the bridge system could be improved by providing additional steel connectors between the girders and the deck in addition to those already present between the girders and floor beams. With 18 in. spaced connectors provided between the deck and the girders, the increase in lateral load capacity was approximately 50 percent.

- Significant improvements in the lateral load-deflection behavior of the bridge system could be obtained by providing steel tie-rods spanning between the exterior faces of the two girders and going through the floor beams. This type of connection scheme not only increases the lateral load capacity of the bridge system, it also results in significant improvement in the deformation capacity (i.e., ductility) of the bridge. The amount of improvement in bridge response will depend on the size and material grade of tie-rods used. With 1½ in. diameter tie-rods, the increase in load capacity was approximately 100 percent over the case of original detail and was approximately 20-30 percent over the first alternative detail.

- The dynamic impact finite element analyses indicate that the demand on the support details used at ends of the girders would exceed the force capacity of these details, and that large amounts of lateral displacements are expected to occur at the girder ends when the bridge system is subjected to lateral vehicular impact. Based in this observation, it is suggested that concrete side-walls be provided on both sides of prestressed concrete girders at the girder ends. This would prevent excessive lateral deformation of the girder ends and would eliminate a possible failure mode of falling of girders off the bridge supports. It is important, however, to note that increasing the rigidity of the girder end supports would make the bridge stiffer, which results in larger impact forces in the girders. Therefore, the side-walls should not be placed directly against the girder ends and some gap (e.g., 8 in.) should be provided between the girders and side-walls. This would also allow the girder ends to slide on the bridge seating during the vibrating of girders and dissipate the energy generated by the vehicular impact.

References

1. S. Sengupta and J. E. Breen (1973). "The Effect of Diaphragms in Prestressed Concrete Girder and Slab Bridges," The University of Texas at Austin Center for Highway Research, *Research Report 158-1F*, Austin, Texas.

2. R. E. Abendroth, F. W. Klaiber, and M. W. Shafer (1995). "Diaphragm Effectiveness in Prestressed Concrete Girder Bridges," *Journal of Structural Engineering*, V. 121, No. 9, pp. 1362-1369.

3. B. O. Andrawes (2001). "Lateral impact Response for Prestressed Concrete Girder Bridges with Intermediate Diaphragms," MS Thesis, Iowa State University, Ames, IA.

4. AASHTO (2001). *A Policy on Geometric Design of Highways and Streets*, American Association of State Highway and Transportation Officials, Washington, DC.

5. ACI Committee 318 (1971). "Building Code Requirements for Reinforced Concrete (ACI 318-71) and Commentary (ACI 318R-71)," American Concrete Institute, Farmington Hills, MI.

6. ACI Committee 318 (1983). "Building Code Requirements for Reinforced Concrete (ACI 318-83) and Commentary (ACI 318R-83)," American Concrete Institute, Farmington Hills, MI.

7. ACI Committee 318 (1999). "Building Code Requirements for Reinforced Concrete (ACI 318-99) and Commentary (ACI 318R-99)," American Concrete Institute, Farmington Hills, MI.

8. AASHTO (2002). *Standard Specifications for Highway Bridges*, 17th Edition, American Association of State Highway and Transportation Officials, Washington, DC.

9. AASHTO (2002). *LRFD Bridge Design Specifications*, American Association of State Highway and Transportation Officials, Washington, DC.

10. S. S. Badie and M. K. Tadros (1999). "Flexural Strength According to AASHTO LRFD Specifications," Open Forum: Problems and Solutions, *PCI Journal*, V. 44, No. 4, pp. 122-127.

11. S. J. Seguirant (2002). "Effective Compression Depth of T-Sections at Nominal Flexural Strength," Open Forum: Problems and Solutions, *PCI Journal*, V. 47, No. 1, pp. 100-105.
Also: Author's Closure (2002). *PCI Journal*, V. 47, No. 3, pp. 112-113.

12. A. E. Naaman (2002). "Reader Comments on: Effective Compression Depth of T-Sections at Nominal Flexural Strength," Open Forum: Problems and Solutions, *PCI Journal*, V. 47, No. 3, pp. 107-111.

13. A. E. Naaman (2003). "Rectangular Stress Block and T-Section Behavior," Open Forum: Problems and Solutions, *PCI Journal*, V. 47, No. 5, pp. 106-112.
Also: Author's Closure (2003). *PCI Journal*, V.48. No. 2, pp. 118-119.

14. A. P. Rabb (2003). "Reader Comments on: Rectangular Stress Block and T-Section Behavior," Open Forum: Problems and Solutions, *PCI Journal*, V. 48, No. 2, pp. 117.

15. A. Girgis, C. Sun and M. K. Tadros (2002). "Flexural Strength of Continuous Bridge Girders-Avoiding the Penalty in the AASHTO LRFD Specifications," Open Forum: Problems and Solutions, *PCI Journal*, V. 47, No. 4, pp. 138-141.

16. J. A. Weigel, S. J. Seguirant, R. Brice and B. Khaleghi (2003). "High Performance Precast, Pretensioned Concrete Girder Bridges in Washington State," *PCI Journal*, V. 48, No. 2, pp. 28-52.

17. ACI-ASCE Joint Committee 323 (1958). "Tentative Recommendations for Prestressed Concrete," *ACI Journal*, V. 54, No. 7, pp. 545-578.

18. J. Warwaruk, M. A. Sozen and C. P. Siess (1962). Investigation of Prestressed Reinforced Concrete for Highway Bridges: Part III-Strength and Behavior in Flexure of Prestressed Concrete Beams," *Bulletin No. 464*, Engineering Experiment Station, University of Illinois, Urbana, IL.

19. K. J. Thompson and R. Park (1980). "Ductility of Prestressed and Partially Prestressed Concrete Beam Sections," *PCI Journal*, V. 25, No. 2, pp.45-69.

20. M. Z. Cohn and M. Bartlett (1982). "Computer-Simulated Flexural Tests of Partially Prestressed Concrete Sections," *ASCE Structural Journal*, V. 108, No. 12, pp. 2747-2765.

21. A. Mattock (1984). "Modification of ACI Code Equation for Stress in Bonded Prestressed Reinforcement at Flexural Ultimate," *ACI Journal*, V. 81, No. 4, pp. 331-337.

22. A. E. Naaman, M. H. Harajli and J. K. Wight (1986). "Analysis of Ductility in Partially Prestressed Concrete Flexural Members," *PCI Journal*, V. 31, No. 3, pp. 64-87.

23. M. H. Harajli and A. E. Naaman (1985). "Evaluation of the Ultimate Steel Stress in Partially Prestressed Flexural Members," *PCI Journal*, V. 30, No. 5, pp. 54-81.

24. A. E. Naaman (1992). "Unified Design Recommendations for Reinforced, Prestressed, and Partially Prestressed Concrete Bending and Compression Members," *ACI Structural Journal*, V. 89, No. 2, pp. 200-210.

25. B. C. Skogman, M. K. Tadros and R. Grasmick (1988). "Ductility of Reinforced and Prestressed Concrete Flexural Members," *PCI Journal*, V. 33, No. 6, pp. 94-107.

26. M. Z. Cohn and P. Riva (1991). "Flexural Ductility of Structural Concrete Sections," *PCI Journal*, V. 36, No. 2, pp. 72-87.

27. R. F. Mast (1992). "Unified Design Provisions for Reinforced and Prestressed Concrete Flexural and Compression Members," *ACI Structural Journal*, V. 89, No. 2, pp. 185-199.

28. ACI Committee 318 (2002). "Building Code Requirements for Reinforced Concrete (ACI 318-02) and Commentary (ACI 318R-02)," American Concrete Institute, Farmington Hills, MI.

29. FHWA (2002). *National Bridge Inventory Report*, www.nationalbridgeinventory.com.

30. L. R. Feldman, J. O. Jirsa and E. S. Kowal (1998). "Repair of Bridge Impact Damage," *Concrete International*, V. 20, No. 2, pp. 61-66.

31. University of Maryland Bridge Engineering Software and Technology Center (2001). "Maryland Study, Vehicle Collisions with Highway Bridges," Maryland State Highway Administration, *Research Report SP907B1*, College Park, MD.

32. I. E. Harik, A. M. Shaaban, H. Gesund, G. Y. S. Valli and S. T. Wang (1990) "United States Bridge Failures, 1951-1988," *Journal of Performance of Constructed Facilities*, V. 4, No. 4, pp. 272-277.

33. K. Wardhana and F. C. Hadipriano (2003). "Analysis of Recent Bridge Failures in the United States," *Journal of Performance of Constructed Facilities*, V. 17, No. 3, pp. 144-150.

34. G. O. Shanafelt and W. B. Horn (1980). "Damage Evaluation and Repair Methods for Prestressed Concrete Bridge Members," National Cooperative Highway Research Program, *Report 226*, Transportation Research Board, Washington, DC.

35. S. El-Tawil, E. Severino and P. Fonseca (2005). "Vehicle Collision with Bridge Piers," *ASCE Journal of Bridge Engineering*, V, 10, No. 3, pp. 345-353.

36. AASHTO (1992). *Guide Specification and Commentary for Vessel Collision Design of Highway Bridges*, American Association of State Highway and Transportation Officials, Washington, DC.

37. D. L. Ivey, R. M. Olson, C. E. Buth and T. J. Hirsch (1971). "Breakaway Overhead Sign Bridges, Crash Testing," *Highway Research Record*, No. 346, pp. 35-46.

38. J. P. Cook and A. Bodocsi (1971). "Impact-Yielding Sign Supports," *Highway Research Record*, No. 346, pp. 58-66.

39. J. F. Kerkhoff, M. S. Varat, A. M. Busenga, K. Hamilton and S. E. Husher (1993). "An Investigation into Vehicle Frontal Impact Stiffness, BEV and Repeated Testing for Reconstruction," *Society of Automotive Engineers*, Paper No. 930899, pp. 227-254.

40. D. H. West, J. P. Gough and G. T. K. Harper (1993). "Low-Speed Rear-End Collision Testing using Human Objects," *Accident Reconstruction Journal*, V. 5, No. 3, pp. 22-26.

41. R. P. Howard, J. Bomar and C. Bare (1993). "Vehicle Restitution Response in Low Velocity Collisions", *Society of Automotive Engineers*, Paper No. 931842, pp. 227-254.

42. G. P. Siegmund, M. N. Bailey and D. J. King (1994). "Vehicle Restitution Response in Low Velocity Collisions", *Society of Automotive Engineers*, Paper No. 940916, pp. 333-371.

43. C. Ito and H. Ohnuma (1986). "Impact Behavior of PC Beams and Slabs," *Proceedings of the International Symposium on Intense Loading and Its Effects,*" Beijing, China, pp. 431-436.

44. J. Eibl, K. Kreuser, M. Feyerabend, F. Schluter and M. Curbach. (1986). "Impact on Concrete Structures," *Proceedings of the International Symposium on Intense Loading and Its Effects,*" Beijing, China, pp. 431-436.

45. N. Ishikawa, S. Katsuki and K. Takemoto (2000). "Dynamic Analysis of Prestressed Concrete Beams under Impact and High Speed Loadings," *Structures under Shock and Impact VI*, WIT Press, Southampton, UK, pp. 247-256.

46. T. Ando, N. Kishi, H. Mikami and K. G. Matsuoka (2000). "Weight Falling Impact Tests on Shear-Failure Type RC Beams Without Stirrups," *Structures under Shock and Impact VI*, WIT Press, Southampton, UK, pp. 247-256.

47. G. Hughes and D. M. Speirs (1982). "An Investigation of the Beam Impact Problem," Cement and Concrete Association, *Technical Report 546*, Slough, England.

48. Prestressed Concrete Institute (1999). *PCI Design Handbook*, 5th Edition, Chicago, IL.

49. ACI Committee 318 (2005). "Building Code Requirements for Reinforced Concrete (ACI 318-05) and Commentary (ACI 318R-05)," American Concrete Institute, Farmington Hills, MI.

50. ACI Committee 349 (1985). "Code Requirements for Nuclear Safety Related Concrete Structures (ACI 349-85) and Commentary (ACI 349R-85)," American Concrete Institute, Farmington Hills, MI.

51. R. Eligehausen, W. Fuchs and B. Mayer (1987). "Loadbearing Behavior of Anchor Fastenings in Tension, Part 1," *Betonwerk und Fertigteil Technik*, No. 12, pp. 826-832.

52. R. Eligehausen and W. Fuchs (1988). "Loadbearing Behavior of Anchor Fastenings under Shear, Combined Tension and Shear or Flexural Loading," *Betonwerk und Fertigteil Technik*, No. 2, pp. 48-56.

53. W. Fuchs, R. Eligehausen and J. E. Breen (1995). "Concrete Capacity Design (CCD) Approach for Fastening to Concrete," *ACI Structural Journal*, V. 92, No. 1, pp. 73-94.

54. A. F. Shaikh and W. Yi (1985). "In-Place Strength of Welded Headed Studs," *PCI Journal*, V. 30, No. 2, pp. 56-81.

55. R. Eligehausen and T. Balogh (1995). "Behavior of Fasteners Loaded in Tension in Cracked Reinforced Concrete," *ACI Structural Journal*, V. 92, No. 3, pp. 365-379.

56. Prestressed Concrete Institute (1985). *PCI Design Handbook*, 3rd Edition, Chicago, IL.

57. Prestressed Concrete Institute (1992). *PCI Design Handbook*, 4th Edition, Chicago, IL.

58. M. Rodriguez, D. Lotze, J. H. Gross, Y. G. Zhang, R. E. Klingner and H. L. Graves (2001). "Dynamic Behavior of Tensile Anchors to Concrete," *ACI Structural Journal*, V. 98, No. 4, pp. 511-524.

59. J. H. Gross, R. E. Klingner and H. L. Graves (2001). "Dynamic Behavior of Single and Double Near-Edge Anchors Loaded in Shear," *ACI Structural Journal*, V. 98, No. 5, pp. 665-676.

60. E. J. Primavera, J. P. Pinelli and E. H. Kalajian (1997). "Tensile Behavior of Cast-in-Place and Undercut Anchors in High-Strength Concrete," *ACI Structural Journal*, V. 94, No. 5, pp. 583-594.

61. P. J. Carrato, K. W. Krauss and J. B. Kim (1996). "Tension Tests of Heavy-Duty Anchors with Embedments of 8 to 19 Inches," *ACI Structural Journal*, V. 93, No. 3, pp. 360-368.

62. D. M. Collins (1988). "Load-Deflection Behavior of Cast-in-Place and Retrofit Concrete Anchors Subjected to Static, Fatigue, and Impact Tensile Loads," MS Thesis, University of Texas, Austin, TX.

63. R. E. Klingner and J. A. Mendonca (1982). "Tensile Capacity of Short Anchor Bolts and Welded Studs: A Literature Review," *ACI Journal*, V. 89, No. 4, pp. 270-279.

64. R. E. Klingner, J. A. Mendonca and J. B. Malik (1982). "Effect of Reinforcing Details on the Shear Resistance of Anchor Bolts under Reversed Cyclic Loading," *ACI Journal*, V. 89, No. 1, pp. 3-12.

65. P. J. McMackin, R. G. Slutter and J. W. Fisher (1973). "Headed Steel Anchor under Combined Loading," AISC Engineering Journal, V. 10, No. 2, pp. 43-52.

66. E. Bentz and M. Collins (2001). User Manual for RESPONSE-2000 Reinforced Concrete Sectional Analysis using the Modified Compression Field Theory.

67. M. P. Collins and D. Mitchell (1991). *Prestressed Concrete Structures*, Prentice Hall, Englewood Cliffs, NJ.

68. A. Mattock (1979). "Flexural Strength of Prestressed Concrete Sections by Programmable Calculator," *PCI Journal*, V. 24, No. 1, pp. 32-54.

69. Mathsoft (Internet). Mathcad Professional. Version 2001 (downloaded Sept. 2001), www.mathsoft.com.

70. E. Baran, A. E. Schultz and C. E. French (2005). "Analysis of the Flexural Strength of Prestressed Concrete Flanged Sections," PCI Journal, V. 50, No. 1. pp. 74-93.

71. G. Hernandez (1958). "Strength of Prestressed Concrete Beams with Web Reinforcement," Ph.D. Thesis, University of Illinois, Urbana, IL.

72. E. Baran, A. E. Schultz and C. E. French (2006). "Tension Tests on Cast-in-Place Inserts: Influence of Reinforcement and Prestress," *PCI Journal*, V. 52, No. 5, pp. 88-108.

73. ASTM (1996). *Standard Test Methods for Strength of Anchors in Concrete and Masonry Elements,* ASTM E488-96, American Society for Testing and Materials, West Conshohocken, PA, 1996.

74. W. C. Stone and N. J. Carino (1983). "Deformation and Failure in Large-Scale Pullout Tests," *ACI Journal*, Proceedings V. 80, No. 6, pp. 501-513.

75. MSC.Software Corporation (2001). MSC.Marc. Version 2001, Los Angeles, CA.

Appendix A
Notation

a = depth of equivalent rectangular stress block
A_o = area of concrete failure surface
A_{ps} = area of prestressing steel
A_s = area of nonprestressed tension reinforcement
A_{sf} = prestressing steel area required to develop the ultimate compressive strength of the overhanging portions of the top flange
A_{sr} = prestressing steel area required to develop the ultimate compressive strength of the web of the section
b = width of the compression face of the member
b_w = web width
c = distance from the extreme compression fiber to the neutral axis
C = resultant of the internal compressive force carried by the concrete at ultimate
d = distance from extreme compression fiber to centroid of the prestressing force
d_e = effective depth from extreme compression fiber to the centroid of the tensile force in the tensile reinforcement
d_h = head diameter of stud
d_p = distance from extreme compression fiber to the centroid of the prestressing tendons
f'_c = specified compressive strength of concrete
f_{ps} = average stress in prestressing steel at ultimate load
f_{pu} = specified tensile strength of prestressing steel
f_{py} = yield strength of prestressing steel
h_{ef} = effective anchor embedment depth
h_f = compression flange depth
k = factor for type of prestressing tendon
= 0.28 for low-relaxation steel
= 0.38 for stress-relieved steel
= 0.48 for bars
k = coefficient for basic concrete breakout strength in tension
l_e = embedment length
M_n = nominal flexural resistance
N_b = basic concrete breakout strength in tension of a single anchor in cracked concrete
P_c = nominal tensile strength of concrete element
β_1 = ratio of the depth of the equivalent uniformly stressed compression zone assumed in the strength limit state to the depth of the actual compression zone
γ, γ_p = factor for type of prestressing tendon
= 0.28 for low-relaxation steel
= 0.40 for stress-relieved steel
= 0.55 for bars
ρ = prestressed reinforcement ratio
$= A_{ps}/bd_p$
ω = reinforcement index (for flanged sections, b shall be the web width and reinforcement are shall be that required to develop compressive strength of web only in calculating the prestressed reinforcement ratio, ρ)
$=\rho f_{ps}/f'_c$

Appendix B
Nonlinear Sectional Analysis Mathcad Code

ORIGIN:= 1

fpc := 8000 bf := 30 hf := 6 bw := 6 nlayer := 100

nstrands := 30 **MAXIMUM NUMBER OF STRANDS IS 60 !** nstep := 100

steellayers :=
- $x \leftarrow 0$
- $x \leftarrow 2$ if nstrands ≤ 12
- $x \leftarrow 2$ if $12 < \text{nstrands} \leq 24$
- $x \leftarrow 3$ if $24 < \text{nstrands} \leq 36$
- $x \leftarrow 4$ if $36 < \text{nstrands} \leq 42$
- $x \leftarrow 4 + \frac{\text{nstrands} - 42}{2}$ if $42 < \text{nstrands}$
- x

steellayers = 3

Astrand := 0.153 εsinitial := 0.0056 εsinitial := 0.005234

Aslayers :=
- for $r \in 1..13$
  - $\text{Aslayers}_r \leftarrow 0$
- $\text{Aslayers}_1 \leftarrow \text{nstrands} \cdot \text{Astrand}$ if nstrands ≤ 12
- if $12 < \text{nstrands} \leq 24$
  - $\text{Aslayers}_1 \leftarrow 12 \cdot \text{Astrand}$
  - $\text{Aslayers}_2 \leftarrow (\text{nstrands} - 12) \cdot \text{Astrand}$
- if $24 < \text{nstrands} \leq 36$
  - $\text{Aslayers}_1 \leftarrow 12 \cdot \text{Astrand}$
  - $\text{Aslayers}_2 \leftarrow 12 \cdot \text{Astrand}$
  - $\text{Aslayers}_3 \leftarrow (\text{nstrands} - 24) \cdot \text{Astrand}$
- if $36 < \text{nstrands} \leq 42$
  - $\text{Aslayers}_1 \leftarrow 12 \cdot \text{Astrand}$
  - $\text{Aslayers}_2 \leftarrow 12 \cdot \text{Astrand}$
  - $\text{Aslayers}_3 \leftarrow 12 \cdot \text{Astrand}$
  - $\text{Aslayers}_4 \leftarrow (\text{nstrands} - 36) \cdot \text{Astrand}$
- if nstrands = 44

$Aslayers_1 \leftarrow 12 \cdot Astrand$

$Aslayers_2 \leftarrow 12 \cdot Astrand$

$Aslayers_3 \leftarrow 12 \cdot Astrand$

$Aslayers_4 \leftarrow 6 \cdot Astrand$

$Aslayers_5 \leftarrow 2 \cdot Astrand$

if $nstrands = 46$

$Aslayers_1 \leftarrow 12 \cdot Astrand$

$Aslayers_2 \leftarrow 12 \cdot Astrand$

$Aslayers_3 \leftarrow 12 \cdot Astrand$

$Aslayers_4 \leftarrow 6 \cdot Astrand$

$Aslayers_5 \leftarrow 2 \cdot Astrand$

$Aslayers_6 \leftarrow 2 \cdot Astrand$

if $nstrands = 48$

$Aslayers_1 \leftarrow 12 \cdot Astrand$

$Aslayers_2 \leftarrow 12 \cdot Astrand$

$Aslayers_3 \leftarrow 12 \cdot Astrand$

$Aslayers_4 \leftarrow 6 \cdot Astrand$

$Aslayers_5 \leftarrow 2 \cdot Astrand$

$Aslayers_6 \leftarrow 2 \cdot Astrand$

$Aslayers_7 \leftarrow 2 \cdot Astrand$

if $nstrands = 50$

$Aslayers_1 \leftarrow 12 \cdot Astrand$

$Aslayers_2 \leftarrow 12 \cdot Astrand$

$Aslayers_3 \leftarrow 12 \cdot Astrand$

$Aslayers_4 \leftarrow 6 \cdot Astrand$

$Aslayers_5 \leftarrow 2 \cdot Astrand$

$Aslayers_6 \leftarrow 2 \cdot Astrand$

$Aslayers_7 \leftarrow 2 \cdot Astrand$

$Aslayers_8 \leftarrow 2 \cdot Astrand$

if nstrands = 52

$Aslayers_1 \leftarrow 12 \cdot Astrand$

$Aslayers_2 \leftarrow 12 \cdot Astrand$

$Aslayers_3 \leftarrow 12 \cdot Astrand$

$Aslayers_4 \leftarrow 6 \cdot Astrand$

$Aslayers_5 \leftarrow 2 \cdot Astrand$

$Aslayers_6 \leftarrow 2 \cdot Astrand$

$Aslayers_7 \leftarrow 2 \cdot Astrand$

$Aslayers_8 \leftarrow 2 \cdot Astrand$

$Aslayers_9 \leftarrow 2 \cdot Astrand$

if nstrands = 54

$Aslayers_1 \leftarrow 12 \cdot Astrand$

$Aslayers_2 \leftarrow 12 \cdot Astrand$

$Aslayers_3 \leftarrow 12 \cdot Astrand$

$Aslayers_4 \leftarrow 6 \cdot Astrand$

$Aslayers_5 \leftarrow 2 \cdot Astrand$

$Aslayers_6 \leftarrow 2 \cdot Astrand$

$Aslayers_7 \leftarrow 2 \cdot Astrand$

$Aslayers_8 \leftarrow 2 \cdot Astrand$

$Aslayers_9 \leftarrow 2 \cdot Astrand$

$Aslayers_{10} \leftarrow 2 \cdot Astrand$

if nstrands = 56

$Aslayers_1 \leftarrow 12 \cdot Astrand$

$Aslayers_2 \leftarrow 12 \cdot Astrand$

$Aslayers_3 \leftarrow 12 \cdot Astrand$

$Aslayers_4 \leftarrow 6 \cdot Astrand$

$Aslayers_5 \leftarrow 2 \cdot Astrand$

$Aslayers_6 \leftarrow 2 \cdot Astrand$

$Aslayers_7 \leftarrow 2 \cdot Astrand$

$Aslayers_8 \leftarrow 2 \cdot Astrand$

$Aslayers_9 \leftarrow 2 \cdot Astrand$

$Aslayers_{10} \leftarrow 2 \cdot Astrand$

$Aslayers_{11} \leftarrow 2 \cdot Astrand$

if $nstrands = 58$

$Aslayers_1 \leftarrow 12 \cdot Astrand$

$Aslayers_2 \leftarrow 12 \cdot Astrand$

$Aslayers_3 \leftarrow 12 \cdot Astrand$

$Aslayers_4 \leftarrow 6 \cdot Astrand$

$Aslayers_5 \leftarrow 2 \cdot Astrand$

$Aslayers_6 \leftarrow 2 \cdot Astrand$

$Aslayers_7 \leftarrow 2 \cdot Astrand$

$Aslayers_8 \leftarrow 2 \cdot Astrand$

$Aslayers_9 \leftarrow 2 \cdot Astrand$

$Aslayers_{10} \leftarrow 2 \cdot Astrand$

$Aslayers_{11} \leftarrow 2 \cdot Astrand$

$Aslayers_{12} \leftarrow 2 \cdot Astrand$

if $nstrands = 60$

$Aslayers_1 \leftarrow 12 \cdot Astrand$

$Aslayers_2 \leftarrow 12 \cdot Astrand$

$Aslayers_3 \leftarrow 12 \cdot Astrand$

$Aslayers_4 \leftarrow 6 \cdot Astrand$

$Aslayers_5 \leftarrow 2 \cdot Astrand$

$Aslayers_6 \leftarrow 2 \cdot Astrand$

$Aslayers_7 \leftarrow 2 \cdot Astrand$

$Aslayers_8 \leftarrow 2 \cdot Astrand$

$Aslayers_9 \leftarrow 2 \cdot Astrand$

$Aslayers_{10} \leftarrow 2 \cdot Astrand$

$Aslayers_{11} \leftarrow 2 \cdot Astrand$

$Aslayers_{12} \leftarrow 2 \cdot Astrand$

$Aslayers_{13} \leftarrow 2 \cdot Astrand$

Aslayers

$Aslayers =$

	1
1	1.836
2	1.836
3	0.918
4	0
5	0
6	0
7	0
8	0
9	0
10	0
11	0
12	0
13	0

$$
\begin{aligned}
\text{Initial1} := \;& \text{fse} \leftarrow 29000000 \cdot \text{esinitial} \cdot \left[0.025 + \frac{0.975}{\left[1 + (118 \cdot \text{esinitial})^{10} \right]^{0.1}} \right] \\
& \text{Psteel} \leftarrow 0 \\
& \text{Eccmom} \leftarrow 0 \\
& \text{Ec} \leftarrow 40000 \cdot \sqrt{\text{fpc}} + 1000000 \\
& \text{for } \; j \in 1 .. \text{steellayers} \\
& \quad \text{hslayers}_j \leftarrow 2 \cdot j \\
& \quad \text{Psteel} \leftarrow \text{Psteel} + \text{fse} \cdot \text{Aslayers}_j \\
& \quad \text{Eccmom} \leftarrow \text{Eccmom} + \text{fse} \cdot \text{Aslayers}_j \cdot \left(\text{ybar\_bottom} - \text{hslayers}_j \right) \\
& \text{Uniformcomp} \leftarrow \frac{\text{Psteel}}{\text{Area}} \\
& \text{Ecccomp\_bottom} \leftarrow \frac{\text{Eccmom} \cdot \text{ybar\_bottom}}{\text{Inertia}} \\
& \text{Ecccomp\_top} \leftarrow \frac{-\text{Eccmom} \cdot (63 - \text{ybar\_bottom})}{\text{Inertia}} \\
& \text{Topstress} \leftarrow \text{Uniformcomp} + \text{Ecccomp\_top} \\
& \text{Bottomstress} \leftarrow \text{Uniformcomp} + \text{Ecccomp\_bottom} \\
& \text{Topstrain} \leftarrow \frac{\text{Topstress}}{\text{Ec}} \\
& \text{Bottomstrain} \leftarrow \frac{\text{Bottomstress}}{\text{Ec}} \\
& \text{Neutralaxis} \leftarrow \frac{-\text{Topstrain}}{\text{Bottomstrain} - \text{Topstrain}} \cdot 63 \\
& \text{Curvature} \leftarrow \frac{\text{Topstrain}}{\text{Neutralaxis}} \\
& \text{Output}_1 \leftarrow \text{Topstress} \\
& \text{Output}_2 \leftarrow \text{Bottomstress} \\
& \text{Output}_3 \leftarrow \text{Topstrain} \\
& \text{Output}_4 \leftarrow \text{Bottomstrain} \\
& \text{Output}_5 \leftarrow \text{Neutralaxis} \\
& \text{Output}_6 \leftarrow \text{Curvature} \\
& \text{Output}
\end{aligned}
$$

$$
\text{Initial1} = \begin{pmatrix} -608.908 \\ 2.513 \times 10^{3} \\ -1.33 \times 10^{-4} \\ 5.489 \times 10^{-4} \\ 12.29 \\ -1.082 \times 10^{-5} \end{pmatrix}
$$

$$\text{Geometric} := \left| \begin{array}{l} \text{Area} \leftarrow 0 \\ \text{Mom} \leftarrow 0 \\ \text{Inertia} \leftarrow 0 \\ \text{for } g \in 1..500 \\ \quad \left| \begin{array}{l} \text{hlayer}_g \leftarrow (2g-1)\cdot\frac{63}{1000} \\ b \leftarrow 26 \text{ if } \text{hlayer}_g < 9 \\ b \leftarrow 6 \text{ if } 9 \le \text{hlayer}_g \le 56 \\ b \leftarrow 30 \text{ if } \text{hlayer}_g > 56 \\ \text{Area} \leftarrow \text{Area} + b\cdot\frac{63}{500} \\ \text{Mom} \leftarrow \text{Mom} + b\cdot\frac{63}{500}\cdot\text{hlayer}_g \end{array} \right. \\ \text{ybar} \leftarrow \frac{\text{Mom}}{\text{Area}} \\ \text{for } v \in 1..500 \\ \quad \left| \begin{array}{l} \text{hlayer}_v \leftarrow (2v-1)\cdot\frac{63}{1000} \\ b \leftarrow 26 \text{ if } \text{hlayer}_v < 9 \\ b \leftarrow 6 \text{ if } 9 \le \text{hlayer}_v \le 56 \\ b \leftarrow 30 \text{ if } \text{hlayer}_v > 56 \\ \text{Inertia} \leftarrow \text{Inertia} + \left[b\cdot\frac{63}{500}\cdot(\text{ybar} - \text{hlayer}_v)^2 \right] \end{array} \right. \\ \text{Result}_1 \leftarrow \text{Area} \\ \text{Result}_2 \leftarrow \text{ybar} \\ \text{Result}_3 \leftarrow 63 - \text{ybar} \\ \text{Result}_4 \leftarrow \text{Inertia} \\ \text{Result} \end{array} \right.$$

$$\text{Geometric} = \begin{pmatrix} 726.264 \\ 31.364 \\ 31.636 \\ 3.901 \times 10^5 \end{pmatrix}$$

$\text{Area} := \text{Geometric}_1$ $\quad \text{Area} = 726.264$

$\text{ybar\_bottom} := \text{Geometric}_2$ $\quad \text{ybar\_bottom} = 31.364$

$\text{ybar\_top} := \text{Geometric}_3$ $\quad \text{ybar\_top} = 31.636$

$\text{Inertia} := \text{Geometric}_4$ $\quad \text{Inertia} = 3.901 \times 10^5$

Initial3 :=

$Ec \leftarrow 40000 \cdot \sqrt{fpc} + 1000000$

$\Delta TopStress \leftarrow InitialBottomStress \cdot \left(\frac{ybar\_top}{ybar\_bottom} \right)$

$\Delta TopStrain \leftarrow \frac{\Delta TopStress}{Ec}$

$\Delta BottomStress \leftarrow InitialBottomStress$

$\Delta BottomStrain \leftarrow \frac{\Delta BottomStress}{Ec}$

$TopStress \leftarrow InitialTopStress + \Delta TopStress$

$TopStrain \leftarrow \frac{TopStress}{Ec}$

$BottomStress \leftarrow InitialBottomStress - \Delta BottomStress$

$BottomStrain \leftarrow \frac{BottomStress}{Ec}$

for $s \in 1..steellayers$

- $hslayers_s \leftarrow 2 \cdot s$
- $\Delta\varepsilon slayer_s \leftarrow \Delta BottomStrain \cdot \left(\frac{ybar\_bottom - hslayers_s}{ybar\_bottom} \right)$

$Moment \leftarrow \frac{\Delta BottomStress \cdot Inertia}{ybar\_bottom}$

for $s \in 1..steellayers$

- $Output_s \leftarrow \Delta\varepsilon slayer_s$
- $Output_{s+1} \leftarrow Moment$
- $Output_{s+2} \leftarrow TopStrain$
- $Output_{s+3} \leftarrow BottomStrain$
- $Output_{s+4} \leftarrow \Delta BottomStrain$

Output

$$Initial3 = \begin{pmatrix} 5.139 \times 10^{-4} \\ 4.789 \times 10^{-4} \\ 4.439 \times 10^{-4} \\ 3.125 \times 10^{7} \\ 4.206 \times 10^{-4} \\ 0 \\ 5.489 \times 10^{-4} \end{pmatrix}$$

$InitialTopStress := Initial1_1$ $InitialTopStress = -608.908$

$InitialBottomStress := Initial1_2$ $InitialBottomStress = 2.513 \times 10^{3}$

$InitialTopStrain := Initial1_3$ $InitialTopStrain = -1.33 \times 10^{-4}$

$InitialBottomStrain := Initial1_4$ $InitialBottomStrain = 5.489 \times 10^{-4}$

$InitialNeutralAxis := Initial1_5$ $InitialNeutralAxis = 12.29$

$InitialCurvature := Initial1_6$ $InitialCurvature = -1.082 \times 10^{-5}$

$InitialTopStrain := Initial3_{steellayers+2}$ $InitialTopStrain = 4.206 \times 10^{-4}$

$InitialMoment := Initial3_{steellayers+1}$ $InitialMoment = 3.125 \times 10^{7}$

```
mom :=
  Ec ← 40000·√fpc + 1000000
  n ← 0.8 + fpc/2500
  εpc ← (fpc/Ec)·(n/(n − 1))
  k ← 0.67 + fpc/9000
  ed ← k
  k ← 1 if ed < 1
  ds ← 0
  dsa ← 0
  ds ← 61 if nstrands ≤ 12
  ds ← 63 − (12·2 + (nstrands − 12)·4)/nstrands if 12 < nstrands ≤ 24
  ds ← 63 − (12·2 + 12·4 + (nstrands − 24)·6)/nstrands if 24 < nstrands ≤ 36
  ds ← 63 − (12·2 + 12·4 + 12·6 + (nstrands − 36)·8)/nstrands if 36 < nstrands ≤ 42
  if 42 < nstrands
    m ← (nstrands − 42)/2
    for k ∈ 1..m
      dsa ← dsa + 2·(8 + 2·k)
    ds ← 63 − ((12·2 + 12·4 + 12·6 + 6·8 + dsa)/nstrands)
  C ← 0
  T ← 0
  for s ∈ 1..nstep
    εtop ← (InitialTopStrain + 0.00004·s)
    flag ← 0
    c ← 3
    tol ← 10
    while flag = 0
      c ← c + 0.01
      C ← 0
      T ← 0
      Mom_s ← 0
      Curv_s ← εtop/c
```

for $j \in 1..\text{steellayers}$

$\text{hslayers}_j \leftarrow 2 \cdot j$

$\text{eslayers}_j \leftarrow \frac{(63 - c - \text{hslayers}_j)}{c} \cdot \varepsilon\text{top} + \text{Initial3}_j + \varepsilon\text{sinitial}$

$\text{fslayers}_j \leftarrow 29000000 \cdot \text{eslayers}_j \cdot \left[0.025 + \frac{0.975}{\left[1 + (118 \cdot \text{eslayers}_j)^{10} \right]^{0.1}} \right]$

$\text{stress} \leftarrow \text{fslayers}_j$

$\text{fslayers}_j \leftarrow 270000 \text{ if } \text{stress} > 270000$

$\varepsilon s \leftarrow \text{eslayers}_j$

$fs \leftarrow \text{fslayers}_j$

$Ts_j \leftarrow \text{Aslayers}_j \cdot \text{fslayers}_j$

$T \leftarrow T + Ts_j$

$\text{Mom}_s \leftarrow (\text{Mom}_s - \text{hslayers}_j \cdot Ts_j)$

$\varepsilon\text{steelcentroid} \leftarrow \frac{(ds - c)}{c} \cdot \varepsilon\text{top} + \left[\left(\text{Initial3}_{\text{steellayers}+4} \right) \cdot \left(\frac{\text{ybar\_bottom} - 63 + ds}{\text{ybar\_bottom}} \right) \right] + \varepsilon\text{sinitial}$

$\text{fsteelcentroid} \leftarrow 29000000 \cdot \varepsilon\text{steelcentroid} \cdot \left[0.025 + \frac{0.975}{\left[1 + (118 \cdot \varepsilon\text{steelcentroid})^{10} \right]^{0.1}} \right]$

for $i \in 1..\text{nlayer}$

$\text{hlayer}_i \leftarrow i \cdot \frac{c}{\text{nlayer}}$

$\varepsilon c_i \leftarrow \varepsilon\text{top} \cdot \frac{\text{hlayer}_i}{c}$

$fc_i \leftarrow \left[\frac{n \cdot \frac{\varepsilon c_i}{\varepsilon pc}}{n - 1 + \left(\frac{\varepsilon c_i}{\varepsilon pc} \right)^{n \cdot k}} \cdot fpc \right]$

$\text{concstrain}_s \leftarrow \varepsilon c_i$

$\text{concstress}_s \leftarrow fc_i$

$b \leftarrow bf \text{ if } (c - \text{hlayer}_i) < hf$

$b \leftarrow bw \text{ if } (c - \text{hlayer}_i) \geq hf$

$$Fc_i \leftarrow fc_i \cdot b \cdot \frac{c}{nlayer}$$

$$C \leftarrow C + Fc_i$$

$$Mom_s \leftarrow \left[Mom_s + \left[Fc_i \cdot \left(63 - c + hlayer_i \right) \right] \right]$$

$$Output_{s,1} \leftarrow c$$

$$Output_{s,2} \leftarrow \varepsilon top$$

$$Output_{s,3} \leftarrow Curv_s$$

$$Output_{s,4} \leftarrow Mom_s$$

$$Output_{s,5} \leftarrow C$$

$$Output_{s,6} \leftarrow T$$

$$Output_{s,7} \leftarrow fsteelcentroid$$

$$tol \leftarrow \frac{C}{T}$$

flag ← 1 if $0.99 < tol < 1.01$

Output

Appendix C
Tension Tests on Connection Rods

Tension tests were performed on the connection rods embedded inside the floor beam pieces in the connection subassemblage tests. These rods were part of the system to transfer the loads between the girder and the floor beam pieces. One end of the connection rods were connected to the steel inserts embedded inside the girders while the rest of the rods were embedded inside the floor beams. As mentioned earlier, two types of connection rods were used in the connection subassemblage specimens depending on the type of steel insert used in the girder pieces. In specimens with NC-thread steel inserts, #6 Grade-60 rebars with forged and threaded ends were used as connection rods. In specimens with coil-thread loop inserts, on the other hand, ¾ in. diameter high carbon steel coil rods were used as connection rods.

Two samples from both types of rods were subjected to the tension test to determine the load capacity of the rods. As shown in Fig. C.1, the tensile loading was applied to the 12 in.-long pieces of rods with a 200-kip capacity MTS testing machine. Fig. C.2 shows the load-elongation plots obtained for the rebar and coil-type rods. The elongation values shown on the plots are the total deflection recorded by the testing machine. As depicted in Figs. C.2(a) and C.2(b), the coil rods had approximately 40 percent higher load capacity than the rebar rods, while the rebar rods had approximately 3.4 times higher overall deformation than the coil rods.

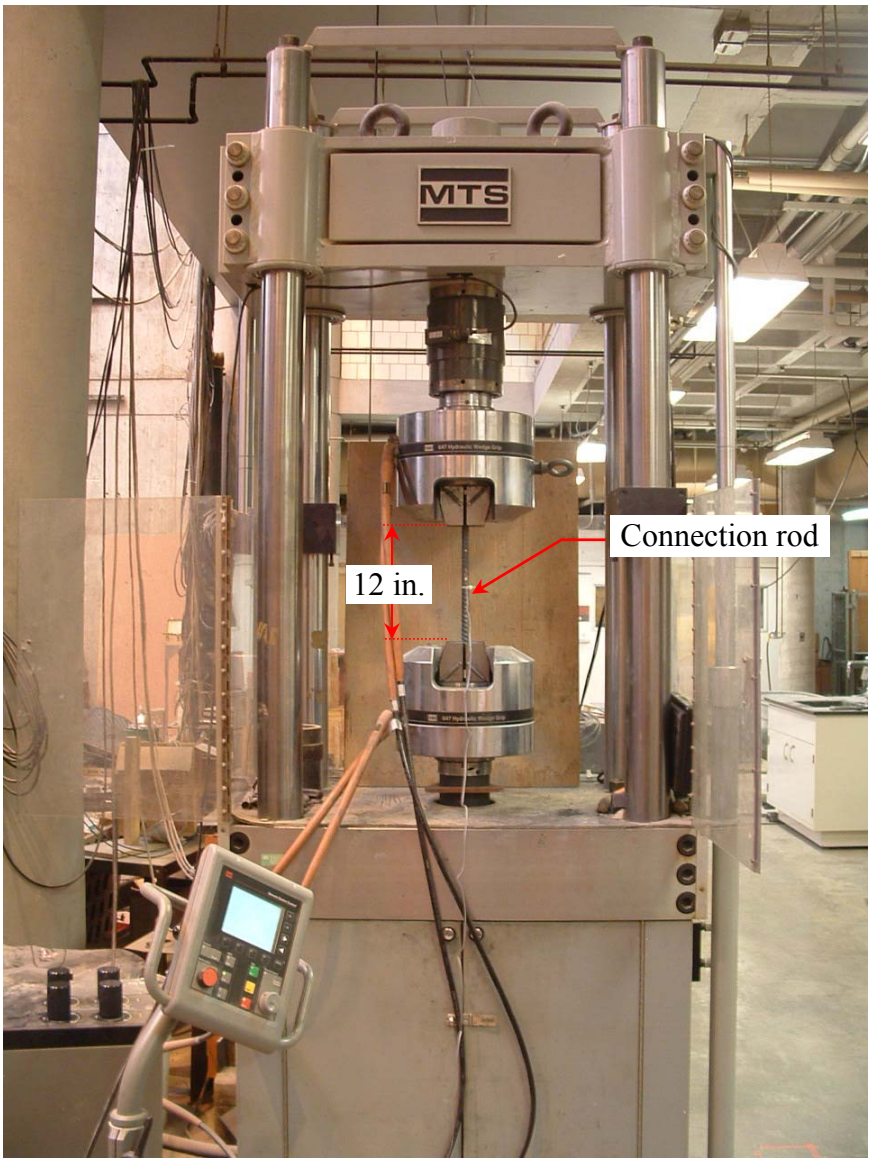

Fig. C.1. Connection rod test setup.

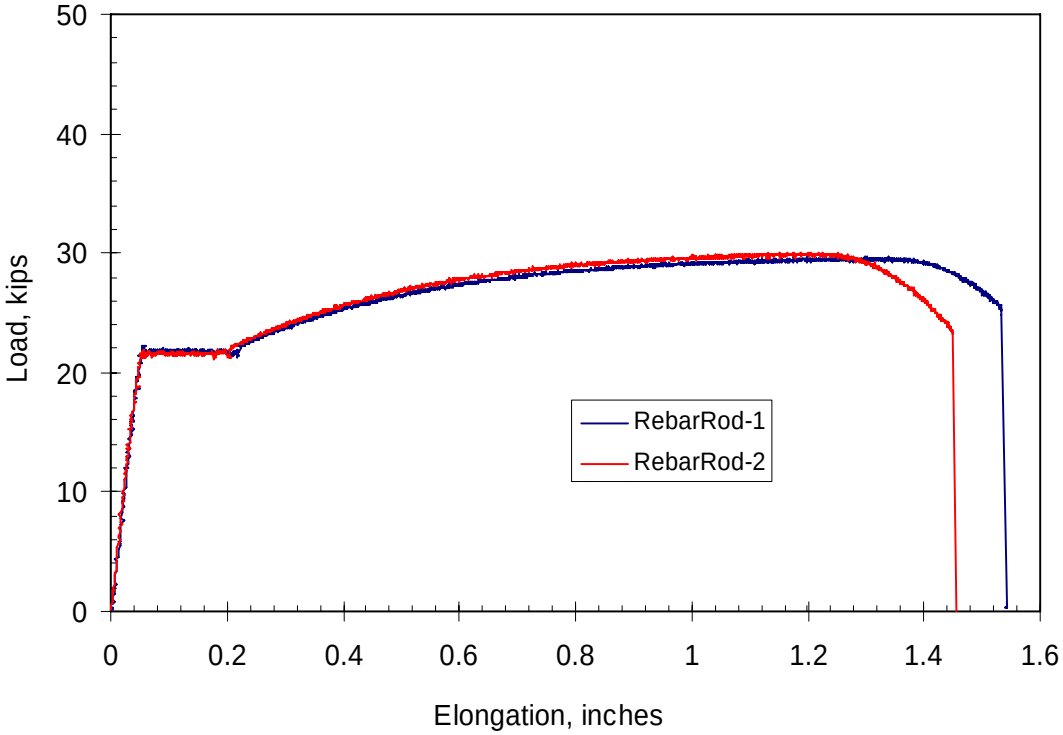

(a) Rebar rods

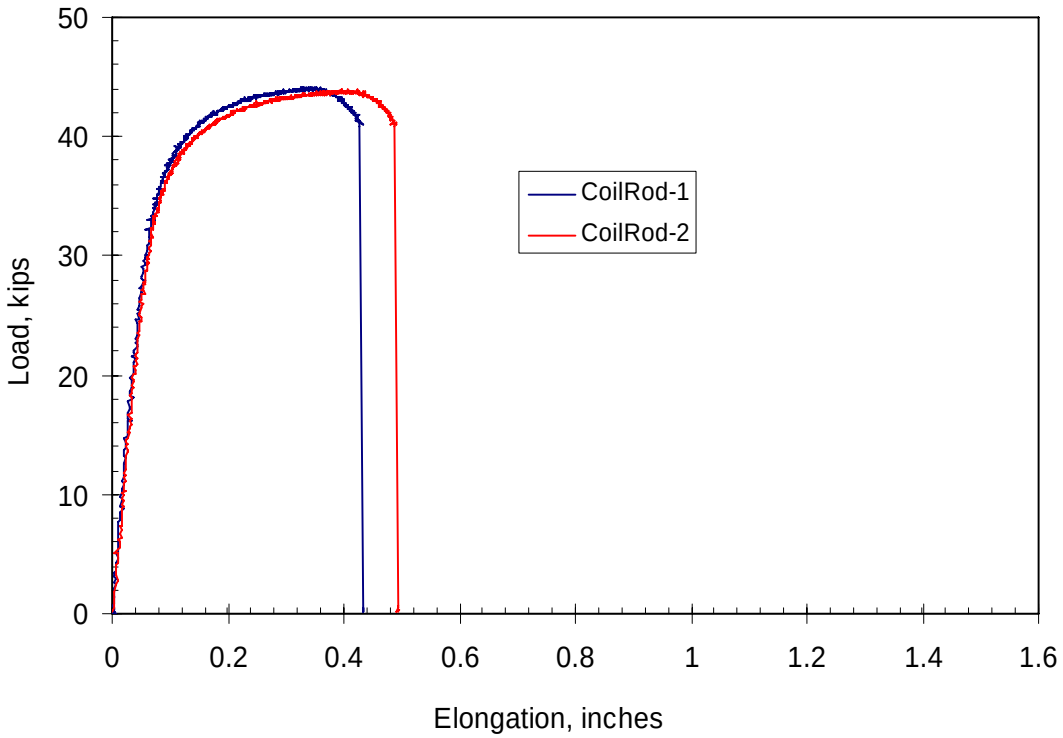

(b) Coil rods

Fig. C.2. Load-elongation behavior of connection rods.

Appendix D
Tension Tests on Loop Insert Wires

Tension tests were performed on steel wire pieces cut out from NC-thread and coil-thread loop inserts. These tests were performed in order to determine if the reason for the difference in the behavior of the connection subassemblage specimens with the NC-thread and coil-thread loop inserts was due to a difference in the material strength between the two types of inserts (See Chapter 4). In order to have straight wire pieces, the wires were straightened after they were cut out from the inserts, and tests were performed on approximately 10 in.-long pieces. One sample from each type insert was tested in a 200-kip capacity MTS testing machine. Each wire piece was instrumented with two electrical resistance strain gages placed at the mid-distance from both ends on opposite faces of the wires.

During the tension tests, both wires were observed to fail (i.e., wire fracture) at the locations corresponding to the corner location of the loop inserts. Fig. D.1 shows the load versus strain plots for the wires from the NC-thread and coil-thread loop inserts. The tests indicated almost identical load versus strain behaviors for the two wire pieces, suggesting that both the NC-thread and coil-thread loop inserts were probably made out of the same material.

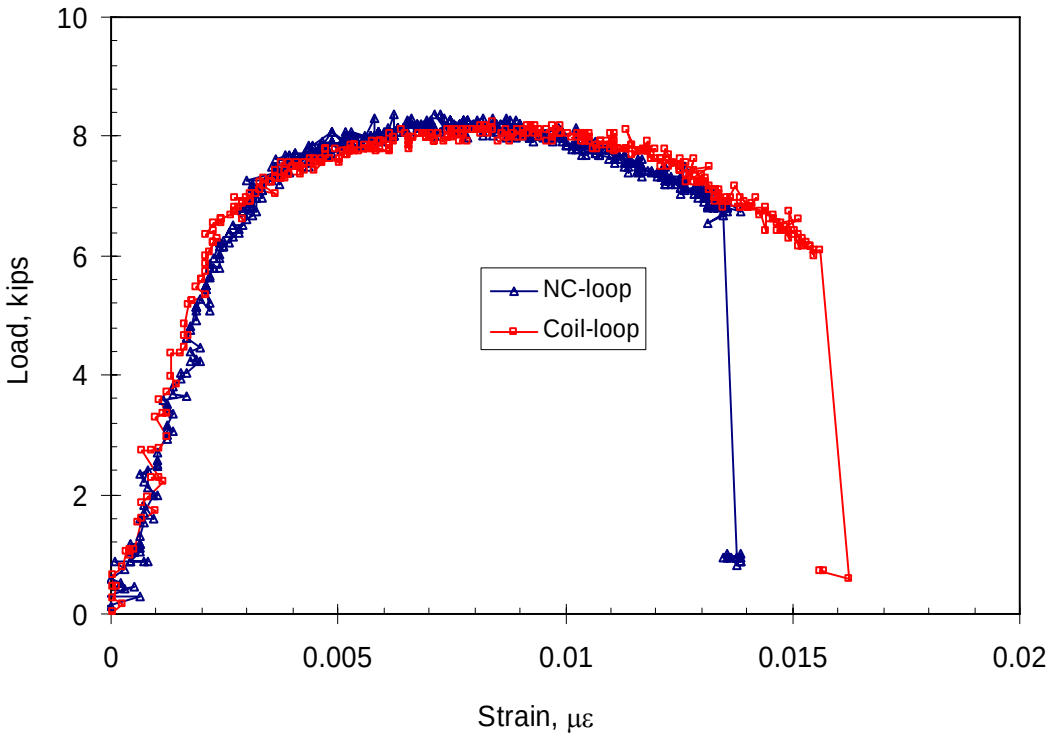

Fig. D.1. Load-strain behavior of loop insert wires.